

8-28-2017

# Diagenesis and Formation Stress in Fracture Conductivity of Shaly Rocks; Experimental-Modelling Approach in CO<sub>2</sub>-Rock Interactions

Abiola Olukola Olabode

*Louisiana State University and Agricultural and Mechanical College, olabode51@yahoo.com*

Follow this and additional works at: [https://digitalcommons.lsu.edu/gradschool\\_dissertations](https://digitalcommons.lsu.edu/gradschool_dissertations)

 Part of the [Environmental Engineering Commons](#), [Geotechnical Engineering Commons](#), and the [Petroleum Engineering Commons](#)

---

## Recommended Citation

Olabode, Abiola Olukola, "Diagenesis and Formation Stress in Fracture Conductivity of Shaly Rocks; Experimental-Modelling Approach in CO<sub>2</sub>-Rock Interactions" (2017). *LSU Doctoral Dissertations*. 4105.  
[https://digitalcommons.lsu.edu/gradschool\\_dissertations/4105](https://digitalcommons.lsu.edu/gradschool_dissertations/4105)

This Dissertation is brought to you for free and open access by the Graduate School at LSU Digital Commons. It has been accepted for inclusion in LSU Doctoral Dissertations by an authorized graduate school editor of LSU Digital Commons. For more information, please contact [gradetd@lsu.edu](mailto:gradetd@lsu.edu).

DIAGENESIS AND FORMATION STRESS IN FRACTURE CONDUCTIVITY OF SHALY  
ROCKS; EXPERIMENTAL-MODELLING APPROACH IN CO<sub>2</sub>-ROCK INTERACTIONS

A Dissertation

Submitted to the Graduate Faculty of the  
Louisiana State University and  
Agricultural and Mechanical College  
in partial fulfilment of the  
requirements for the degree of  
Doctor of Philosophy

in

The Craft & Hawkins Department of Petroleum Engineering

by

Abiola Olukola Olabode  
B.S., Obafemi Awolowo University, 2008  
M.S., Louisiana State University, 2012  
December 2017

To my mother, Adeyinka, who lived but for a while

## ACKNOWLEDGEMENTS

My sincere gratitude goes to the following; Dr. Craig M Harvey for graciously serving as chair of my doctoral research committee; my committee members, Dr. Mayank Tyagi, Dr. Paulo Waltrich, Dr. Dandina Rao and the graduate school Dean's Representative Dr. Chao Sun for their invaluable contributions and criticisms that have given shape to this work. I want to specially thank the Craft and Hawkins Department of Petroleum Engineering for availing me the multi-year resources that made this project a success. I appreciate Wanda LeBlanc, LSU AgCenter, Donmei Cao, and the LSU SIF staff members for assisting with post experimental data analysis. I also thank George Ohrberg for helping with computing needs in data acquisition and Fenelon Nunes for helping with laboratory ware purchases and maintenance. The financial support of the SPE and the GDL Foundation is kindly acknowledged. Thanks to LSU Graduate School for the Dissertation Year Fellowship that saw me through my final semesters.

I am appreciative of colleagues with whom I shared and gained useful ideas. They include Nnamdi Agbasimalo, Chukwudi Chukwudozie, Wei Wang, Gbola Afonja, Paulina Mwangi, Louise Smith, Arome Oyibo, Darko Kupresan, Kolawole Bello, Ruixuan Guo and Hui Du to mention a few.

Special thanks to my wife, Omoefe Kio-Olabode, for her unrelenting support throughout my graduate studies. Your children shall call you blessed. To our son, Mark Olayinka, thanks for beaming light on to our world at this junction in our lives.

I deeply appreciate the fervent prayers and support of my father and siblings; Oladepo Olabode, Titilola Akinyemi and Motunrola Olaiya. Thanks to my uncle, Jinmi Olabode and cousin, Tolu Olabode for always checking on us all these years. Also, special thanks to the Chapel on Campus for the edification of my inner man since I arrived at LSU.

## TABLE OF CONTENTS

ACKNOWLEDGEMENTS.....	iii
LIST OF TABLES .....	vi
LIST OF FIGURES .....	viii
NOMENCLATURE .....	xv
ABSTRACT .....	xvi
CHAPTER 1. INTRODUCTION .....	1
1.1 Background on Carbon Sequestration .....	1
1.2 Diagenesis and Fractures .....	8
1.3 Problem Definition .....	12
1.4 Objective of Research .....	13
CHAPTER 2. LITERATURE REVIEW .....	15
2.1 Diagenesis of Sedimentary Rocks .....	15
2.2 A Brief on Properties of CO <sub>2</sub> Saturated Brine .....	16
2.3 Shale Caprock Geochemical Alteration and Subsurface CO <sub>2</sub> Migration .....	20
2.4 Geomechanical Effects .....	43
2.5 Previous Experimental and Modeling Works .....	55
CHAPTER 3. EXPERIMENTAL SETUP AND PROCEDURE .....	62
3.1 Experimental Methods and Sample Preparation .....	62
3.2 Experimental Setup.....	66
3.3 Experimental Shale Rocks Geology .....	66
3.4 Mineralogical Composition of Shale Rock Samples.....	67
3.5 Experimental CO <sub>2</sub> -brine Fluid.....	70
3.6 Techniques in Rock and Fluid Analysis .....	71
3.7 Experimental Parameters .....	74
3.8 Experimental Matrix .....	76
CHAPTER 4. RESULTS FROM SHALE ROCK/FLUID INTERACTIONS EXPERIMENTS .....	81
4.1 pH Measurement .....	81
4.2 Inductively Coupled Plasma-Optical Emission Spectroscopy (ICP-OES) Analysis.....	82
4.3 Total Carbon Analysis .....	94
4.4 X-Ray Diffraction (XRD) Analysis .....	96

4.5 Electron Micro-Probe Analysis (EMPA) of Bulk Rock.....	106
4.6 Micro-Indentation of Rock Samples .....	120
4.7 Differential Pressure Analysis .....	124
4.8 Fracture Conductivity Estimation .....	128
CHAPTER 5. DISCUSSION OF RESULTS ROCK/FLUID INTERACTIONS EXPERIMENTS .....	134
5.1 General Discussion of Experimental Results .....	134
5.2 Integrated Experimental Observations .....	141
CHAPTER 6. CONCLUSIONS AND RECOMMENDATIONS .....	143
6.1 Conclusions .....	143
6.2 Recommendations .....	146
REFERENCES.....	147
APPENDICES .....	166
A: EQUIPMENT AND MATERIALS USED FOR SHALE ROCK/CO <sub>2</sub> BRINE EXPERIMENTS .....	166
B: EXPERIMENTAL PROCEDURE FOR ROCK-FLUID INTERACTION EXPERIMENTS .....	172
C: pH DATA .....	175
D: INDUCTIVELY COUPLED PLASMA EMISSION SPECTROSCOPY (ICP-OES) DATA.....	176
E: MICRO-INDENTATION OF SHALE ROCKS DATA .....	179
F: ADDITIONAL DATA FOR ELECTRON MICROPROBE ANALYSIS (EMPA).....	180
G: FLOW/PRESSURE DATA .....	188
H: FRACTURE CONDUCTIVITY DATA AND CALCULATIONS .....	196
VITA .....	197

## LIST OF TABLES

1.1: Worldwide potential CO <sub>2</sub> sequestration capacities and risks .....	2
2.1: Mineralogy of typical shale rock samples showing percentage composition .....	22
2.2: Geochemical model for reaction of shale, sandstone and cement with CO <sub>2</sub> and Na, Ca, Mg Chloride brines .....	26
3.1. Geological properties of shale rock samples used in the experiment .....	67
3.2: Mineralogical composition of shale samples in percentages as captured by the ternary diagram of figure 3.5 .....	70
3.3: Experimental brine composition for Shale/CO <sub>2</sub> -brine flooding experiment based on flowback fluid composition from hydraulically fractured shale .....	71
3.4: Experimental Matrix for CO <sub>2</sub> -brine/shale interaction at conditions of 50°C temperature and 1,000 psi pressure stated in A above .....	76
3.5: Experimental Matrix for CO <sub>2</sub> -brine/shale interaction at conditions of 50°C temperature and 1,000 psi pressure stated in B above .....	77
3.6: Micro-indentation; Hardness and Young Modulus at different temperature and pressure conditions of rock fluid interaction .....	78
3.7: Pre-injection and Post-injection analyses for each CO <sub>2</sub> -brine flooding experimental run including rock and fluid sampling procedure .....	79
4.1: Bulk rock compositional change for the shale rock samples. These values were computed from the pre- and post-XRD quantitative analysis using the bulk and clay XRD methods. There were slight changes in quartz, carbonates and clay contents .....	104
4.2: Percentage composition of the mineralogical components of precipitates that were recovered from the effluent during the shale/CO <sub>2</sub> -brine flooding experiment. The analysis indicated diagenetic quartz and carbonates as new minerals that were formed .....	105
B.1: Pre-injection and Post-injection analysis for each CO <sub>2</sub> -brine flooding run .....	172

G.1: Data for differential pressure across 25 $\mu$ m fractured core for flow-through experiment using Mancos shale .....	188
G.2: Data for differential pressure across 25 $\mu$ m fractured core for flow-through experiment using Marcellus shale .....	189
G.3: Data for differential pressure across 25 $\mu$ m fractured core for flow-through experiment using Pottsville shale.....	190
G.4: Data for differential pressure across 25 $\mu$ m fractured core for flow-through experiment using Wilcox shale .....	191
G.5: Data for differential pressure across 150 $\mu$ m fractured core for flow-through experiment using Mancos shale .....	192
G.6: Data for differential pressure across 150 $\mu$ m fractured core for flow-through experiment using Marcellus shale .....	193
G.7: Data for differential pressure across 150 $\mu$ m fractured core for flow-through experiment using Pottsville shale .....	194
G.8: Data for differential pressure across 150 $\mu$ m fractured core for flow-through experiment using Wilcox shale .....	195
H.1: Steps, equations and assumptions were made in calculating the fracture conductivity of the cores used during the experiments .....	196

## LIST OF FIGURES

1.1: CO <sub>2</sub> emission sources, potential utilization and sequestration sites .....	3
1.2: United States electric power generation by fuel over the next 25 years .....	4
1.3: Projected carbon dioxide (CO <sub>2</sub> ) emission in the United States .....	5
1.4: Schematic of CO <sub>2</sub> diffusive loss and other leakages through caprock .....	8
1.5: Representation of a possible CO <sub>2</sub> migration pathway from the reservoir through the caprock via fractures that have been opened during CO <sub>2</sub> injection .....	10
2.1: Phase diagram of CO <sub>2</sub> showing the pressure and temperature envelope for most sedimentary basins worldwide .....	17
2.2: the isothermal compressibility of CO <sub>2</sub> at 35°C and 50°C .....	19
2.3: Quartz precipitation rate in micrometers per million years for a range of temperature from 25°C to 250°C. The three curves represent the range of expected growth rate in a fracture .....	25
2.4: Mineral dissolution rate as function of pH, 1/T, $a_{Al^{3+}}$ , oxalate concentration, and $f(\Delta G_r)$ .....	32
2.5: Schematic drawing of pressure solution. Compaction by pressure solution reduces the porosity and permeability of a rock .....	39
2.6: Schematic of precipitation/dissolution reaction in finite length single fracture .....	46
2.7: Fracture shape with precipitation of cemented minerals leading to aperture loss .....	46
2.8: Fracture production simulation illustrating the impact of conductivity on long-term production .....	48
2.9: illustration of the pressure solution and compaction mechanism. High stress at the contact points increases the solubility of silica .....	48
2.10: Modification of calculated steady-state effective permeability for a generic fracture pattern showing reduction in effective permeabilities, $k_x$ and $k_y$ , caused by diagenetic cementation .....	52
3.1: Detailed process flow diagram of the experimental setup showing critical devices .....	63

3.2: Visual design of composite core made of kaolinite, cement and microtubings .....	64
3.3: Sample design of composite core made of kaolinite, cement and microtubings .....	64
3.4: Samples of composite core made of kaolinite, cement and microtubings mimic fractures ...	65
3.5: Initial mineralogical composition of four shale rock samples used in rock-fluid interaction experiment. The ternary diagram shows carbonates, quartz, feldspar, pyrite and clay .....	68
3.6: Initial mineralogical composition of four shale rock samples used in rock-fluid interaction experiment when compared to other plays .....	69
4.1: pH measurement of effluent for the four different shale rock samples used for the rock-fluid interaction experiment .....	81
4.2: Dimensionless elemental concentration of the effluent fluids showing the fraction of Calcium that were leached out from the shale rock samples .....	83
4.3: Dimensionless cationic concentration of the effluent fluids showing the fraction of Magnesium that were leached out from the shale rock samples .....	86
4.4: Dimensionless cationic concentration of the effluent fluids showing the fraction of Potassium that were leached out from the shale rock samples .....	86
4.5: Dimensionless cationic concentration of the effluent fluids showing the fraction of Selenium that were leached out from the shale rock samples .....	87
4.6: Dimensionless cationic concentration of the effluent fluids showing the fraction of Sulphur that were leached out from the shale rock samples .....	87
4.7: Dimensionless cationic concentration of the effluent fluids showing the fraction of Silicon that were leached out from the shale rock samples .....	88
4.8: Dimensionless cationic concentration of the effluent fluids showing the fraction of Aluminum that were leached out from the shale rock samples .....	90
4.9: Dimensionless cationic concentration of the effluent fluids showing the fraction of Arsenic that were leached out from the shale rock samples .....	91

4.10: Dimensionless cationic concentration of the effluent fluids showing the fraction of Boron that were leached out from the shale rock samples ..... 91

4.11: Dimensionless cationic concentration of the effluent fluids showing the fraction of Iron that were leached out from the shale rock samples ..... 92

4.12: Dimensionless cationic concentration of the effluent fluids showing the fraction of Manganese that were leached out from the shale rock samples. .... 92

4.13: Dimensionless cationic concentration of the effluent fluids showing the fraction of Nickel that were leached out from the shale rock samples ..... 93

4.14: Dimensionless cationic concentration of the effluent fluids showing the fraction of Phosphorus that were leached out from the shale rock samples. .... 93

4.15: Dimensionless cationic concentration of the effluent fluids showing the fraction of Zinc that were leached out from the shale rock samples ..... 94

4.16: Total Carbon measurement of bulk shale rocks for the four different samples analyzed. It shows major increase in carbon content for the Marcellus shale ..... 95

4.17: XRD Analysis of bulk rock Mancos before and after CO<sub>2</sub>-brine flooding at moderate temperature and pressure conditions along with the mineralogical composition of the associated precipitates recovered from the effluent ..... 97

4.18: XRD Analysis of bulk rock Marcellus before and after CO<sub>2</sub>-brine flooding along with the mineralogical composition of the associated precipitates recovered from the effluent ..... 98

4.19: XRD Analysis of bulk rock Pottsville before and after CO<sub>2</sub>-brine flooding at moderate temperature and pressure conditions along with the mineralogical composition of the associated precipitates recovered from the effluent ..... 99

4.20: XRD Analysis of bulk rock Wilcox before and after CO<sub>2</sub>-brine flooding at moderate temperature and pressure conditions along with the mineralogical composition of the associated precipitates recovered from the effluent ..... 99

4.21: XRD Analysis of clay components Mancos before and after CO<sub>2</sub>-brine flooding at moderate temperature and pressure conditions along with the mineralogical composition of the associated precipitates recovered from the effluent ..... 101

4.22: XRD Analysis of clay components Marcellus before and after CO<sub>2</sub>-brine flooding at moderate temperature and pressure conditions along with the mineralogical composition of the associated precipitates recovered from the effluent ..... 101

4.23: XRD Analysis of clay components Pottsville before and after CO<sub>2</sub>-brine flooding at moderate temperature and pressure conditions along with the mineralogical composition of the associated precipitates recovered from the effluent. Significantly higher clay content is present in precipitates compared to previous samples .....102

4.24: XRD Analysis of clay components Wilcox before and after CO<sub>2</sub>-brine flooding at moderate temperature and pressure conditions along with the mineralogical composition of the associated precipitates recovered from the effluent .....102

4.25: 20µm Electron Micro-Probe maps for Mancos shale showing the Calcium surface geochemical profile of the CO<sub>2</sub>-reacted sample compared to control specimen ..... 107

4.26: 20µm Electron Micro-Probe Analysis for Mancos shale showing Magnesium and Aluminum surface geochemical profile of the CO<sub>2</sub>-reacted sample compared to control specimen ..... 108

4.27: 20µm Electron Micro-Probe Analysis for Mancos shale showing Iron and silicon surface geochemical profile of the CO<sub>2</sub>-reacted sample compared to control specimen ..... 109

4.28: 20µm Electron Micro-Probe Analysis for Marcellus shale showing the Calcium surface geochemical profile of the CO<sub>2</sub>-reacted sample compared to control specimen ..... 110

4.29: 20µm Electron Micro-Probe Analysis for Marcellus shale showing Mg and Al surface geochemical profile of the CO<sub>2</sub>-reacted sample compared to control specimen .....111

4.30: 20µm Electron Micro-Probe Analysis for Marcellus shale showing Iron and Silicon surface geochemical profile of the CO<sub>2</sub>-reacted sample compared to control specimen ..... 112

4.31: 20µm Electron Micro-Probe Analysis for Pottsville shale showing the Calcium surface geochemical profile of the CO<sub>2</sub>-reacted sample compared to control specimen ..... 114

4.32: 20µm Electron Micro-Probe Analysis for Pottsville shale showing Magnesium and Aluminum surface geochemical profile of the CO<sub>2</sub>-reacted sample compared to control specimen .....115

4.33: 20µm Electron Micro-Probe Analysis for Pottsville shale showing Iron and Silicon surface geochemical profile of the CO<sub>2</sub>-reacted sample compared to control specimen .....116

4.34: 20µm Electron Micro-Probe Analysis for Wilcox shale showing the Calcium surface geochemical profile of the CO<sub>2</sub>-reacted sample compared to control specimen ..... 117

4.35: 20µm Electron Micro-Probe Analysis for Wilcox shale showing Magnesium and Aluminum surface geochemical profile of the CO<sub>2</sub>-reacted sample compared to control specimen .....118

4.36: 20µm Electron Micro-Probe Analysis for Wilcox shale showing Iron and Silicon surface geochemical profile of the CO<sub>2</sub>-reacted sample compared to control specimen ..... 119

4.37: the Vickers’ micro-hardness measurement taken on multiple samples of the experimental shale rocks. The results indicated reduction in geomechanical hardness of the rocks ..... 121

4.38: Young’s Modulus plots showing across the board decreases in measured values for the shale caprocks after flooding with CO<sub>2</sub>-brine at 50°C and 1,000psi ..... 122

4.39: Combined Hardness and Young’s Modulus plots showing across the board decreases in values for the caprocks after flooding with CO<sub>2</sub>-brine at 50°C and 1,000psi ..... 122

4.40: A correlation between the hardness of the shale rock and quantifiable mineralogical change in percentages. The graph shows that formation of diagenetic quartz can improve the hardness of the shale rock as observed in the Pottsville shale ..... 123

4.41: Average differential pressure profile across the 25µm composite core, with embedded micro-tubings to mimic fractures. The injected fluid was directly from the outlet of the packed bed of crushed shale rock samples .....125

4.42: Average differential pressure profile across 150µm composite core, with embedded micro-tubings to mimic fractures. The injected fluid was directly from the outlet of the packed bed of crushed shale rock samples ..... 126

4.43: Average first derivative of differential pressure drop across the 25µm composite core, with embedded micro-tubings to mimic fractures. The injected fluid was from directly from the outlet of the packed bed of crushed shale rock samples ..... 127

4.44: Average first derivative of differential pressure drop across the 150µm composite core, with embedded micro-tubings to mimic fractures. The injected fluid was from directly from the outlet of the packed bed of crushed shale rock samples ..... 128

4.45: Calculated dimensionless fracture conductivity profile from experimental differential pressure using fractured core parameters with 25 $\mu$ m micro-tubings embedded. The profile indicated a rapid reduction in the conductivity of the artificial fractured core .....	132
4.46: Calculated dimensionless fracture conductivity profile from experimental differential pressure (dP) data using fractured core parameters with 150 $\mu$ m micro-tubings embedded .....	132
4.47: Comparison of calculated dimensionless fracture conductivity profile from experimental differential pressure (dP) data using fractured core parameters with 25 $\mu$ m and 150 $\mu$ m embedded micro-tubings .....	133
5.1. The integration schematics of the geochemical, geomechanical and micro-fracture conductivity in shale rock-aqueous CO <sub>2</sub> interactions .....	142
A.1: Core flooding setup showing core holder and instrumentation.....	166
A.2: Helium porosimetry unit for estimation of porosity of fractured cores.....	166
A.3: Core flooding control unit.....	166
A.4: Automated oven for temperature control.....	166
A.5: Piston pump.....	167
A.6: PEEK micro-tubing used in composite cores.....	167
A.7: Micro-indentation fixture.....	167
A.8: Example of shale fragment and the indentation points.....	167
A.9: Crushed shale samples, pre-flooding with CO <sub>2</sub> -brine; Mancos.....	168
A.10: Crushed shale samples, pre-flooding with CO <sub>2</sub> -brine; Marcellus .....	168
A.11: Crushed shale samples, pre-flooding with CO <sub>2</sub> -brine; Pottsville.....	168
A.12: Crushed shale samples, pre-flooding with CO <sub>2</sub> -brine; Wilcox.....	168
A.13: Crushed shale samples, post-flooding with CO <sub>2</sub> -brine; Mancos .....	169

A.14: Crushed shale samples, post-flooding with CO <sub>2</sub> -brine; Marcellus .....	169
A.15: Crushed shale samples, post-flooding with CO <sub>2</sub> -brine; Pottsville .....	169
A.16: Crushed shale samples, post-flooding with CO <sub>2</sub> -brine; Wilcox .....	169
A.17: Recovered effluent precipitates, post-flooding with CO <sub>2</sub> -brine; Mancos .....	170
A.18: Recovered effluent precipitates, post-flooding with CO <sub>2</sub> -brine; Marcellus .....	170
A.19: Recovered effluent precipitates, post-flooding with CO <sub>2</sub> -brine; Pottsville .....	170
A.20: Recovered effluent precipitates, post-flooding with CO <sub>2</sub> -brine; Wilcox .....	170
A.21: Process schematics of experimental setup showing materials and equipment used for CO <sub>2</sub> -brine flooding and composite core conductivity measurement .....	171

## NOMENCLATURE

$C_r$  = Dimensionless Fracture Conductivity

$F_{cdn}$  = Normalized Dimensionless Fracture Conductivity

$w_f$  = Fracture Width,  $\mu\text{m}$

$k_m$  = Matrix Permeability, D

$k_f$  = Fracture Permeability, D

$L_f$  = Fracture Length

$\phi$  = Porosity, %

$P$  = Pressure, psi

$\Delta P$  = Differential Pressure (psi)

$T$  = Temperature,  $^{\circ}\text{C}$

$q$  = Flow Rate, ml/min

$R_T$  = Flow Rate (ml/min) at Temperature  $T$  ( $^{\circ}\text{C}$ )

$k_r$  = reaction rate, m/s

$v$  = velocity, m/s

$\mu$  = Viscosity, cp

$A$  = Cross-sectional Area

$YM$  = Young's Modulus

$SD$  = Standard Deviation

$HV$  = Vickers' Hardness

## ABSTRACT

In large scale subsurface injection of carbon dioxide (CO<sub>2</sub>) as obtainable in carbon sequestration programs and in environmentally friendly hydraulic fracturing processes (using supercritical CO<sub>2</sub>), long term rock-fluid interaction can affect reservoir and seal rocks properties which are essential in monitoring the progress of these operations. The mineralogical components of sedimentary rocks are geochemically active particularly under enormous earth stresses, which generate high pressure and temperature conditions in the subsurface. While geomechanical properties such as rock stiffness, Poisson's ratio and fracture geometry largely govern fluid flow characteristics in deep fractured formations, the effect of mineralization can lead to flow impedance in the presence of favorable geochemical and thermodynamic conditions. Simulation results suggested that influx-induced mineral dissolution/precipitation reactions within clay-based sedimentary rocks can continuously close micro-fracture networks, though injection pressure and effective-stress transformation first rapidly expand the fractures. This experimental modelling research investigated the impact of in-situ geochemical precipitation at 50°C and 1,000 psi on conductivity of fractures under geomechanical stress conditions. Geochemical analysis were performed on different samples of shale rocks, effluent fluid and recovered precipitates both before and after CO<sub>2</sub>-brine flooding of crushed shale rocks at high temperature and pressure conditions. Bulk rock geomechanical hardness was determined using micro-indentation. Differential pressure drop data across fractured composite core were also measured with respect to time over a five a day period. This was used in estimating the conductivity of the fractured core. Three experimental runs per sample type were carried out in order to check the validity of observed changes. The results showed that most significant diagenetic changes in shale rocks after flooding with CO<sub>2</sub>-

brine reflect in the effluent fluid with calcium based minerals dissolving and precipitating under experimental conditions. Major and trace elements in the effluent fluid (using ICP-OES analysis) indicated that multiple geochemical reactions are occurring with almost all of the constituent minerals participating. The geochemical composition of precipitates recovered after the experiments showed diagenetic carbonates and opal (quartz) as the main constituents. The bulk rock showed little changes in composition except for sharper peaks on XRD analysis, suggesting that a significant portion of amorphous content of the rocks have been removed via dissolution by the slightly acid CO<sub>2</sub>-brine fluid that was injected. However total carbon (TOC) analysis showed a slight increase in carbon content of the bulk rock. Micro-indentation results suggested a slight reduction in the hardness of the shale rocks and this reduction appear dependent on quartz content. The differential pressure drop, its 1<sup>st</sup> derivative and estimated fracture conductivity suggests that reactive transport of dissolved minerals can possibly occlude fracture flow path at varying degree depending on equivalent aperture width, thereby improving caprock integrity with respect to leakage risks under CO<sub>2</sub> sequestration conditions. An exponential-natural logarithm fit of the fracture conductivity can be obtained and applied in discrete fracture network modelling. The fit yielded lower and upper boundary limits for fracture conductivity closure. Higher temperature and pressure conditions of experimental investigations may be needed to determine the upper limit of shale rock seal integrity tolerance, under conditions that are similar to sequestration of CO<sub>2</sub> into deep and hot sedimentary rocks.

## CHAPTER 1

### INTRODUCTION

#### 1.1 Background on Carbon Sequestration

Sequestration of anthropogenic carbon dioxide (CO<sub>2</sub>) into geologic subsurface sinks has gained much attention from the science and engineering community in recent years. As fossil fuel is expected to continue to play a significant role in meeting worldwide energy demand, environmental considerations require some form of mitigation for the CO<sub>2</sub> being emitted- a prominent greenhouse gas [1-3]. Carbon cycle is one of the most complex geochemical cycles of the Earth as it involves atmosphere, hydrosphere, biosphere and lithosphere. Among these different geochemical spheres, mechanisms and reaction rates governing migration and fixation of carbon (i.e. fluxes), such as the stability of the different carbonates minerals under specific conditions in crustal reservoirs, are still matter of detailed studies [4].

Development of fossil fuels, emission of greenhouse gases, and changing climate have been at the forefront of geopolitical discussions in recent years. The challenge is to produce enough energy to maintain the current standard of living while simultaneously reducing greenhouse gas (GHG) emissions. Considerable amount of experimental and simulation studies in carbon dioxide sequestration have been carried out in investigating the geochemical and geomechanical stability of porous subsurface storage reservoirs such as saline aquifers, depleted oil and gas reservoirs, and coal bed seams for this purpose [5-20]. Table 1.1 below shows some estimates of the capacities available for each of these repositories worldwide. These capacities assume that variable solubility of CO<sub>2</sub> due to depth is insignificant. A particular risk is for CO<sub>2</sub> to migrate from the storage and leak into an overlying formation or back to the atmosphere.

Table 1.1: Worldwide potential CO<sub>2</sub> sequestration capacities and risks [1]

<b>Storage Option</b>	<b>Capacity (Gt-CO<sub>2</sub>)</b>	<b>Storage Integrity</b>	<b>Environmental Risk</b>
<b>Depleted oil and gas reservoirs</b>	25 – 30	High	Low
<b>Unmineable coal seams</b>	5 – 10	Average	Average
<b>Deep saline aquifers</b>	1 – 150	Average	Average
<b>Ocean (global)</b>	1,000 – 10,000	Medium	High

More recently geothermal utilization of CO<sub>2</sub> is gaining attention in addition to its high potential for enhanced hydrocarbon recovery projects serving as both a sweeping and swelling fluid [21-23]. Saline aquifers are considered to be one of the best options for CO<sub>2</sub> sequestration due to their large storage capacity, high injectivity and nearness to CO<sub>2</sub> sources. Depleted oil and gas reservoirs, unmineable coal seams and ocean sinks are the other subsurface repositories that can be used for sequestering CO<sub>2</sub> [1, 24-27]. Conventional sandstone reservoirs and possibly carbonates reservoirs are the most favored depleted oil and gas reservoirs considered in CO<sub>2</sub> sequestration. Experiments reacting supercritical CO<sub>2</sub> in synthetic and natural brines in the presence and absence of limestone and plagioclase-rich arkosic sandstone reveal that there are significant compositional, mineralogical and porosity changes in aquifer fluid and rock properties [28-30]. Under the impact of pressure and temperature (P&T) the aqueous species of the CO<sub>2</sub>-acidified brine diffuse through the cap rock where they trigger CO<sub>2</sub>-water-rock interactions. Characterizing the time-dependent fluid flux along a fractured wellbore and what phenomena might alter the leak path conductivity over time is vital for risk assessment. These geochemical reactions result in mineral dissolution and precipitation along the CO<sub>2</sub>

migration path and are responsible for a change in porosity and therefore for the sealing capacity of the cap rock [31, 32]. Figure 1.1 shows the network of potential sequestration sites and the CO<sub>2</sub> emitting industries that could be involved [14].

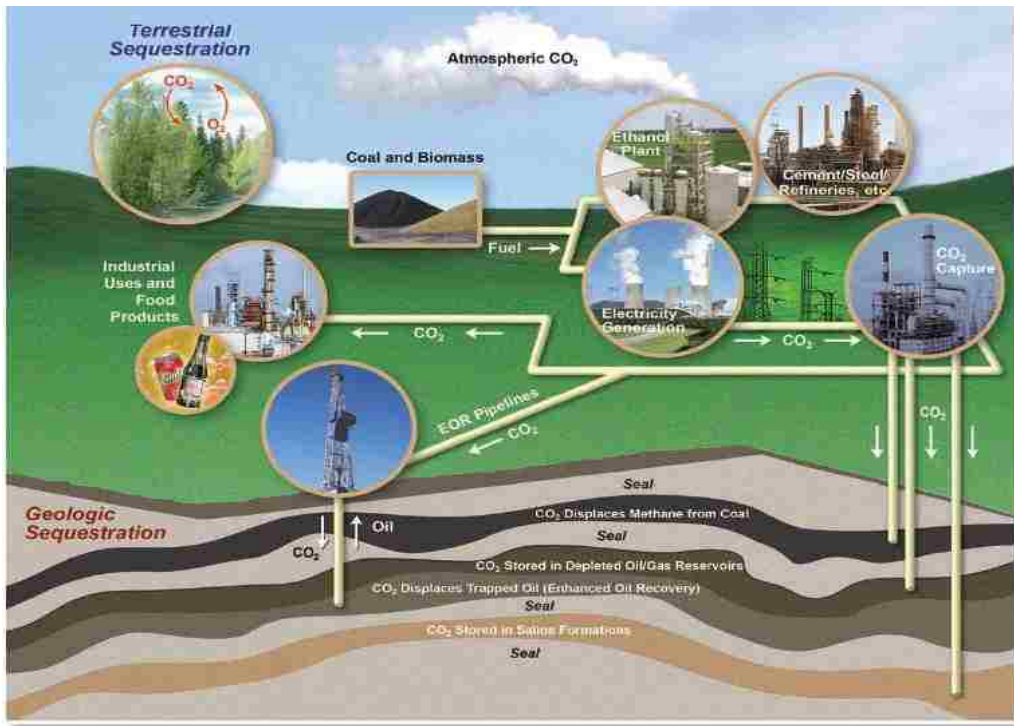


Figure 1.1: CO<sub>2</sub> emission sources, potential utilization and sequestration sites (Courtesy of the Department of Energy [14])

Meanwhile the emission of anthropogenic CO<sub>2</sub> is expected to continue into the future at an increasing volumetric rate. Figure 1.2 depicts the trend in CO<sub>2</sub> emissions in the United States by fuel type over the next 25 years and beyond. Figure 1.3 shows long term emission data for anthropogenic CO<sub>2</sub> in the United States. Industrialized societies which continue to use fossil fuel energy sources are considering adoption of Carbon Capture and Storage (CCS) technology to meet carbon emission reduction targets. Long-term security of performance of engineered CO<sub>2</sub> storage is a principle concern, as seepage of injected CO<sub>2</sub> to the surface is economically and

environmentally unfavorable, and can present a human health hazard. In Italy, natural CO<sub>2</sub> degassing to the surface via seeps is widespread, providing an insight into the various styles of subsurface ‘plumbing’ as well as surface expression of CO<sub>2</sub> fluids.

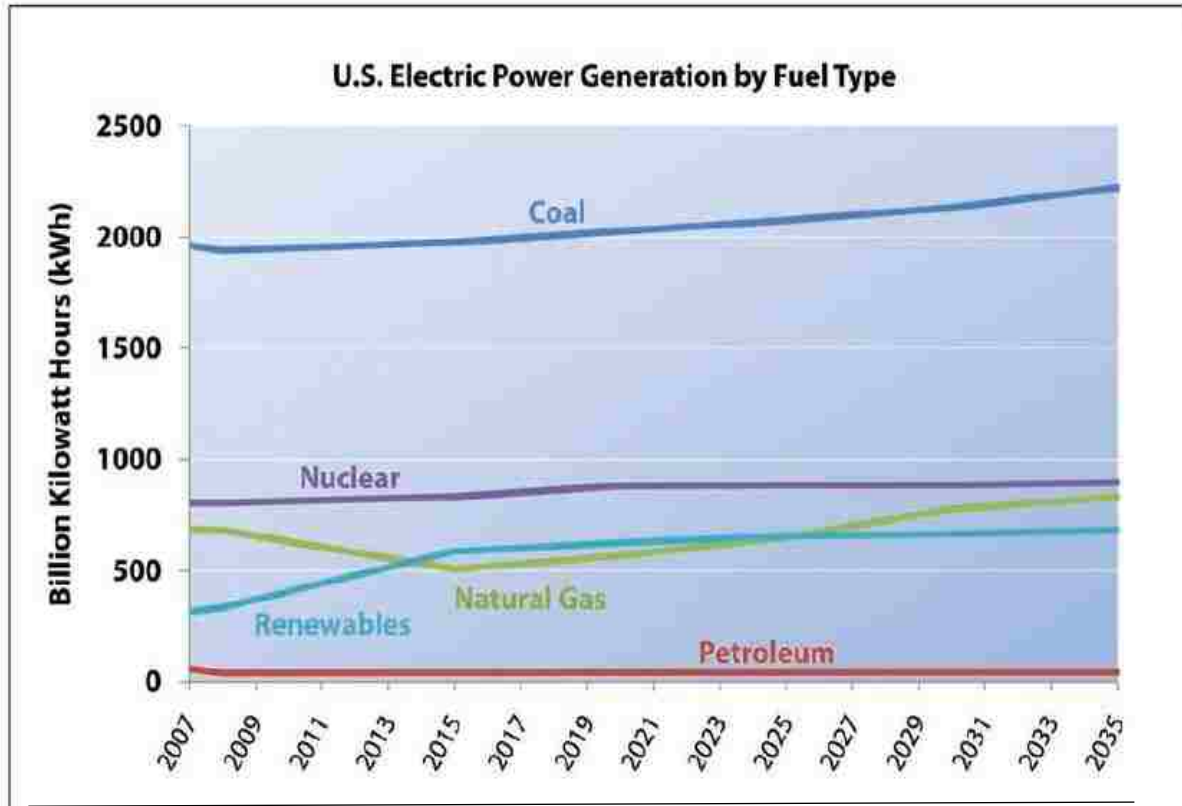


Figure 1.2: United States electric power generation by fuel over the next 25 years (Courtesy of the Department of Energy [14]).

Geological storage of CO<sub>2</sub> depends on the contribution of multiple CO<sub>2</sub> trapping mechanisms that includes: 1) physical trapping of CO<sub>2</sub> in a gaseous, liquid, or super critical state, 2) solubility trapping through dissolution of CO<sub>2</sub> within brine, 3) hydrodynamic trapping as a result of residual saturation of disconnected CO<sub>2</sub> within individual pore spaces and 4) mineral trappings- an insitu process of interstitial carbonate minerals formation from CO<sub>2</sub>, the host rock and formation waters [3, 33-35].

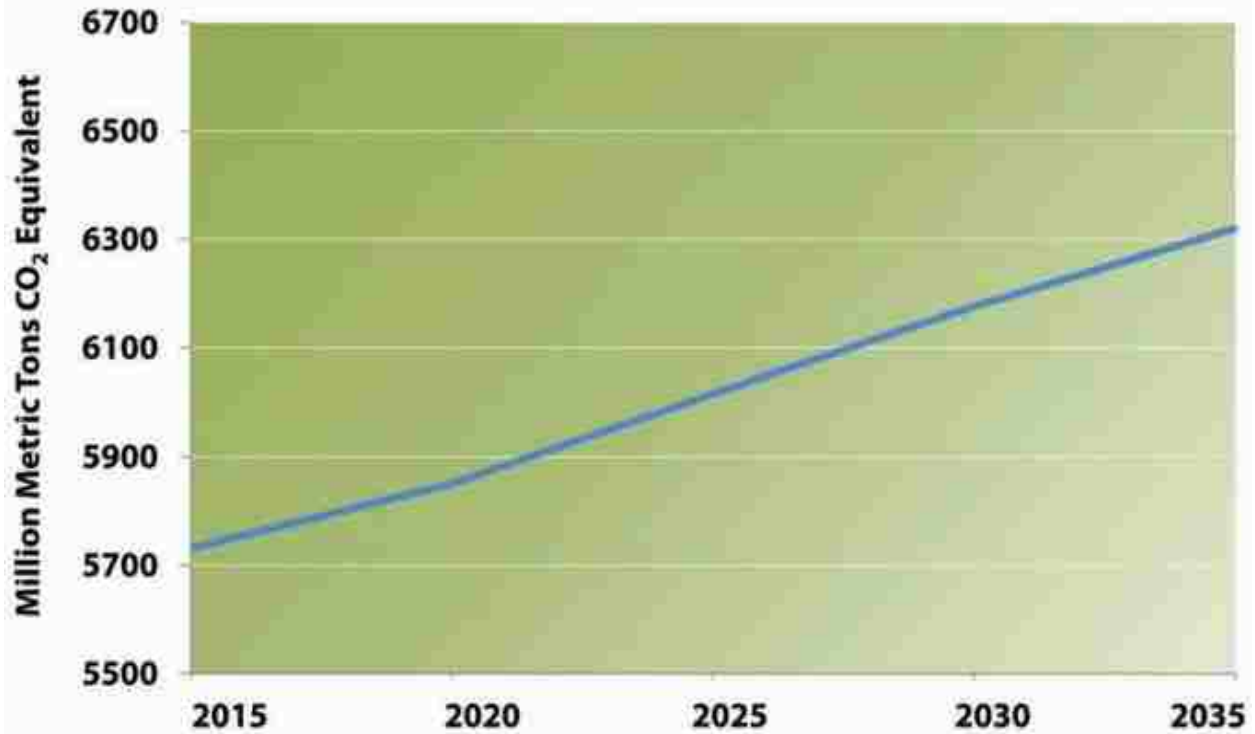


Figure 1.3: Projected carbon dioxide (CO<sub>2</sub>) emission in the United States. The model is based on point source industries (Courtesy of the Department of Energy [14]).

The process of carbon capture and sequestration include monitoring, verification, accounting and risk assessment of emission units and storage sites. At Sleipner in Norway, seismic monitoring combined with seabed gravimetric technologies have been used to constrain reservoir simulation models and to acquire insight into the flow behavior of CO<sub>2</sub> plumes in the Utsira sandstone reservoir [5, 6, 8, 36-38]. Extensive economic and cost analysis are required for projects that involve commercial entities and government budgetary appropriations.

Successful implementation of geological CO<sub>2</sub> sequestration depends on many factors including the ability to predict the extent of underground CO<sub>2</sub> movement and storage as a function of specific target formation that will enable the identification of optimal sites and evaluate their long term isolation performance while asserting the results through experimentation [1, 39, 40].

Geomechanical, geochemical and hydrological impact of engineered CO<sub>2</sub> storage into these geological storage options have been well researched with the conclusion that accurate estimation of maximum sustainable injection pressure plays a significant role on wellbore stability, wettability parameters, possible dormant fault reactivation among other concerns. The presence of impurities in the CO<sub>2</sub> stream raises the question of possible underground water and aquatic life contamination. This requires factoring the effects of trace impurities from large emission sources into CO<sub>2</sub> transport, injection and storage modeling [41-43].

While appreciable efforts have been expended in the scientific evaluation of CO<sub>2</sub> storage feasibility in conventional underground repositories, significant experimental research efforts are yet to be devoted to the seal rocks that cap most of these reservoirs. The reason might be their complexity, not just in terms of mineralogy and fluid flow behavior but also due to the lengthy laboratory measurements required for meaningful investigation. The rock-fluid interaction processes that are observed in most conventional CO<sub>2</sub> repositories with high permeability and porosity are to a limited extent applicable to sedimentary caprocks. Most effective caprock lithologies are fine-grained siliciclastics (clay-based rocks) and evaporites (anhydrites, gypsum, halites). An effective caprock usually has capillary entry pressure that exceeds the upward buoyancy pressure exerted by an underlying hydrocarbon or CO<sub>2</sub> column [33, 44, 45]. The capillary pressure of the caprock is largely a function of its pore sizes and this may be laterally variable. The buoyancy pressure is determined by the density of the reservoir fluid and column height. A caprock of extremely small pore size, in the order of nanometers, is required to prevent the buoyant rise of an underlying gas column [39, 46, 47]. The injection of CO<sub>2</sub> leads to CO<sub>2</sub>-water-rock interactions that result in the precipitation and dissolution of minerals which in turn

result in a change in porosity and permeability of the cap rock. This change leads to the improvement or deterioration of the sealing capacity of the cap rock. Mineral dissolution results in an increase in porosity and enables the creation of pathways for CO<sub>2</sub> migration. Mineral precipitation leads to a decrease in porosity and increases the sealing effect [31, 48-50].

Geochemistry and geomechanics affect caprock effectiveness and loss of gas through caprock may take place if the integrity of the caprock is breached, although transport processes are usually not rapid and may be in the nano-darcy permeability range. Recent field tests such as in Sleipner (Norway), showed that experience on in-situ caprock integrity characteristics can only be obtained in decades. CO<sub>2</sub> plume development and the required geophysical monitoring methods (seismic, gravity, and satellite data) can only yield valuable geological information in years as evident from the 15 years of operating the Sleipner project. Existing geologic discontinuities, fractures and faults also add to the uncertainty that may compromise seal effectiveness [37, 38]. The effectiveness of natural shale rock seals and other tight rocks are dependent on the absence of discontinuities.

The quantitative assessment of leakage risks and leakage rates is a basic requirement for site approval, public acceptance and the awarding of potential credits for sequestered CO<sub>2</sub> quantities.

Leakage through caprocks may occur in three different ways [51-54]:

- i.) rapid leakage by seal-breaching or wellbore failure (corrosion of pipes and cements), resulting in gas flow through a micro-fracture network.
- ii.) long-term leakage controlled by the capillary sealing efficiency and permeability (after capillary breakthrough pressure is exceeded).
- iii.) diffusive loss of dissolved gas through the water-saturated pore spaces.

Figure 1.4 below depicts 1) Wellbore failure 2) Capillary breakthrough 3) Diffusive loss phenomena that can aid CO<sub>2</sub> leakage through the caprock. These are relevant on reservoir/basin scale in processes that involve resource extraction and subsurface disposal of anthropogenic gases from emission sources. The permanent storage of carbon dioxide in the subsurface will surely pose challenges as the integrity of the various pinch points that are highlighted can be compromised. The choice of sequestration site and the engineering of the injection process will play a significant role in long term containment.

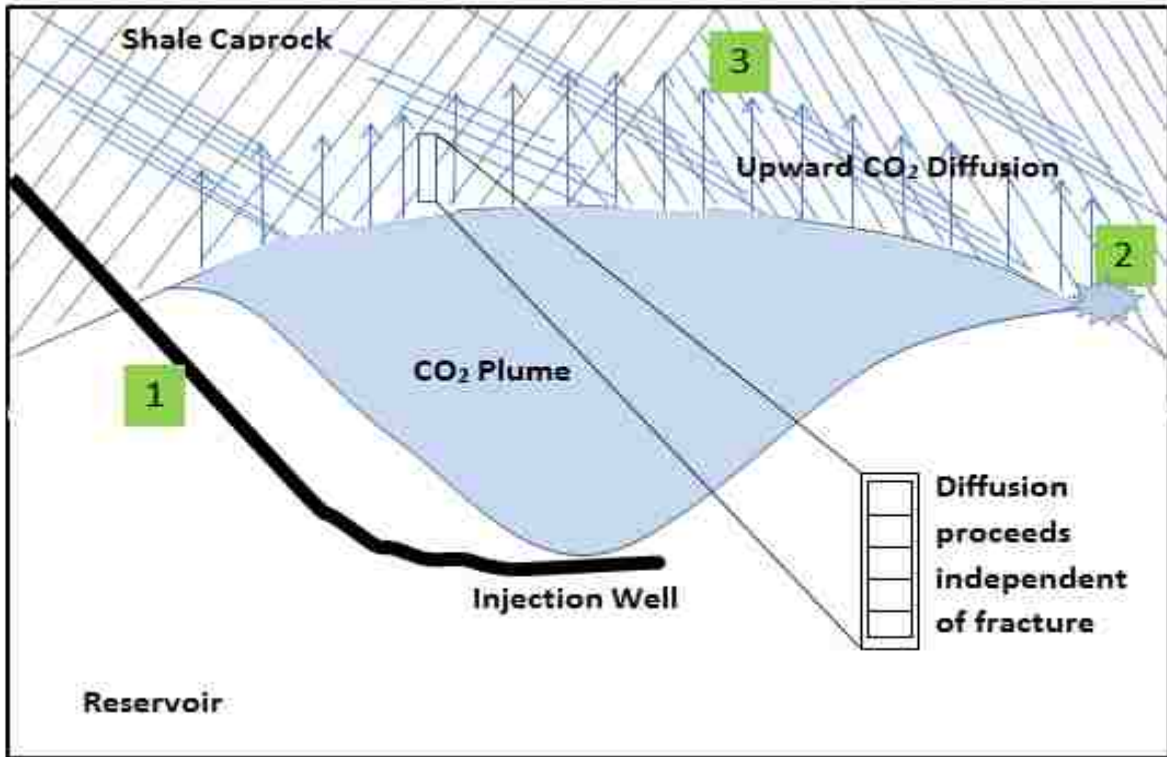


Figure 1.4: Schematic of CO<sub>2</sub> diffusive loss and other leakages through shale caprock [55].

## 1.2 Diagenesis and Fractures

In naturally fractured geologic formations, conductivity of fractures is important in fluid extraction and injection. The role of mineralization in the loss of fracture conductivity due to

aqueous precipitation of insoluble substances has been discussed by several researchers [56-59]. It is generally thought that aside geomechanical properties of sedimentary rocks, the geochemical properties of rocks and reservoir fluids can favorably or unfavorably lead to the constriction of fractures in the subsurface given the right temperature, pressure and chemical composition. This type of constrict is desired in CO<sub>2</sub> sequestration and containment. Different formation evaluation scales can be considered when describing tight shaly rocks (caprock): from the pore or grain scale in petrophysics and geochemistry, to regional scale in geology and geomechanics [60]. At small scale, the identification of geological facies and the origin of the low porosity and permeability in terms of sedimentology and diagenesis is necessary.

For clayey caprocks, the amount and type of clay is critical in characterizing its petrophysics unlike tight carbonate formation where dolomitisation is the key feature [38, 61]. Caprocks are essentially defined as low ( $<10^{-18}$  m<sup>2</sup>) or very low ( $<10^{-21}$  m<sup>2</sup>) permeability formations, and sometimes, but not necessarily, with low porosity ( $<15\%$ ) [62, 63]. They are generally viewed as hermetic layers above the storage into which no CO<sub>2</sub> should migrate. During the injection of CO<sub>2</sub>, mechanical constraints are generated in both the storage and caprock formations, and the bottom of the caprock can be affected by geochemical reactions. Geochemistry and geomechanics affect caprock effectiveness and loss of gas through caprock may take place if the integrity of the caprock is breached, although transport processes are usually not rapid and may be in the nano-darcy permeability range. In order to better understand storage integrity and the interplay between fluid-rock interactions and mechanical stability, the study of processes leading to potential leakage are indispensable. Several studies have shown that in large scale carbon sequestration, the CO<sub>2</sub> migrates a few meters during one thousand years, and that the porosity

mostly decreases by precipitation, and increases very locally at the base of the caprock when convective and hydraulic actions of CO<sub>2</sub> plume movement in the subsurface is advanced by multiple reactive and non-reactive dissolution [39, 65]. Naturally occurring fractures in shaly

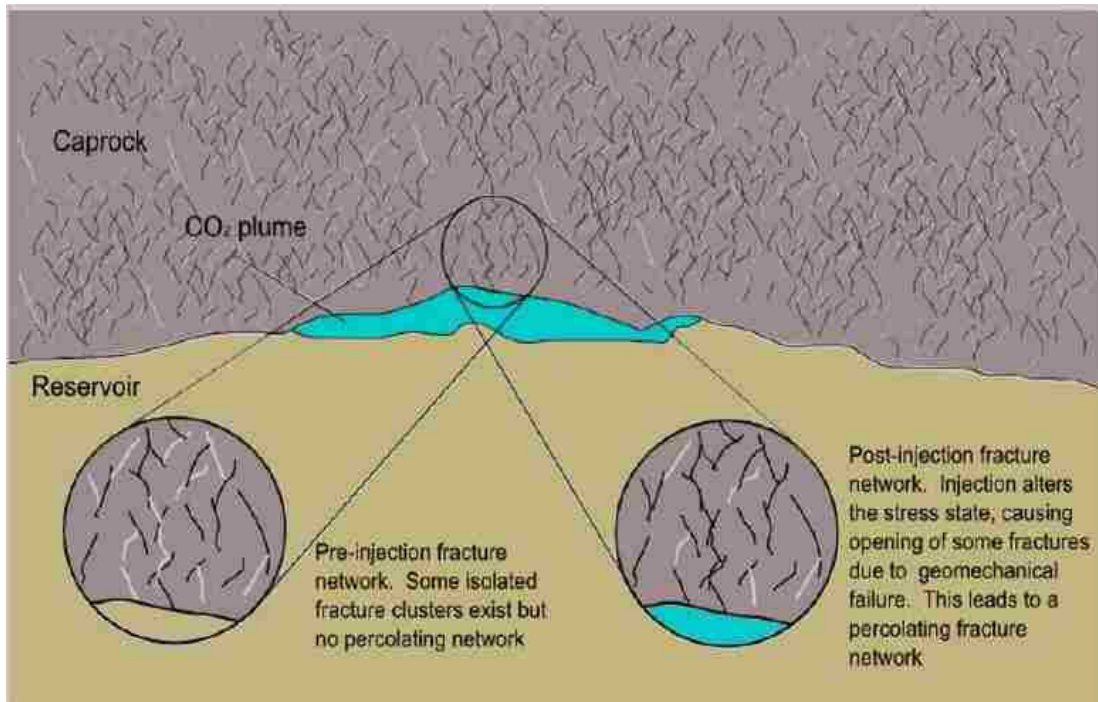


Figure 1.5: Representation of a possible CO<sub>2</sub> migration pathway from the reservoir through the caprock via fractures that have been opened during CO<sub>2</sub> injection. Black lines represent open fractures and white lines represent closed fractures [64].

caprocks under CO<sub>2</sub> sequestration and subsurface fluid extraction make significant contribution to flow and any natural or artificial geologic process that can impact them should be adequately researched [66]. Figure 1.5 shows a diagrammatic representation of natural fractures in shaly caprocks. Areal footprints of current and future hydraulically fractured oil and gas reservoirs and potential CO<sub>2</sub> repository intervals often overlap in sedimentary basins [67]. Significant vertical separations between prospective subsurface volumes, however, will limit their interaction, particularly if the carbon-storage site is deeper than the hydrocarbon resource. Environmental

risks result mostly from abandoned wells and faults, poorly characterized for carbon storage, and from defective well completions and surface spills during oil and gas production [68]. Future deployment of geologic sequestration technology on a significant scale could result in water-management challenges, ranging from increases in water demand for power plants to need of disposal space for pressure management to possible water-contamination issues. An analysis of the spatial adequacy of potential pressure-relief wells would enhance synergy between carbon sequestration and other subsurface operations.

In natural systems multiple minerals and other phases (such as organic carbon), gradients in pore size distributions and other components create potentially other complicating factors that reduce our ability to discern what is occurring in these systems[69]. Nanopores may contain the largest deviations from bulk-like reactivity, and at the same, may constitute the majority of pores in a rock. A sometimes overlooked set of effects of precipitation in pores are geomechanical [69]. That is, when rocks, cements or other porous materials have fluids circulate through them that induce crystallization, the precipitated material exerts a pressure on the rock itself and vice versa. As advances in experimental and imaging techniques allow for improved characterization of pore-scale processes, modeling approaches are being challenged to incorporate the textural and mineralogical heterogeneity of natural porous media, in particular with regard to their treatment of interfaces [69, 70]. The chemical transformation of iron-bearing minerals to form iron carbonates could impact the geochemistry of carbon sequestration and the presence of carbonate adsorbates does not impede the reduction of ferric iron to ferrous forming siderite. Through leaching, the chemical constituent of shale can cause a slight increase in porosity that may be available for sequestering CO<sub>2</sub>.

The geochemical composition of shale caprock plays a significant role in its ability to perform effectively as a regional seal. The chemical reactivity of shale has been shown by several researchers to affect its petrophysical characteristics though the multiple reaction mechanisms and kinetic rates are not clearly defined and still needs to be investigated. Different mineral compositions ranging from quartz, calcite, anorthites, and feldspar to muscovite, chlorite, illite, kaolinite and smectite have been reported for shale. Mineral dissolution, re-precipitation and redistribution could affect transport properties of shale. Post experimental fluid analysis in a shale/water/CO<sub>2</sub> batch mixing experiment showed that the aqueous concentration of major elements such as Ca, Mg, Fe, Al and K increased and that the release rate of Fe and SiO<sub>2</sub> were more pronounced in solutions reacted with CO<sub>2</sub>-brine when compared to reactions with CO<sub>2</sub>-free brine. The use of isotopic species have been suggested in tracing diagenetic changes in shale caprock due to CO<sub>2</sub> sequestration. But the cost implication of monitoring the isotope partition coefficients effectively as a control tool is yet to be determined. For example in hydraulically fractured shale for the oil and gas production purposes, tracer tests faced challenges of dissolution and loss of concentration. This was for high flow paths which are different in carbon sequestration cases of lower injectivity and with no flowback expected. Monitoring wells will be difficult to maintain.

### **1.3 Problem Definition**

Subsurface carbon dioxide leakage risk assessments to date tended to use risk scenarios, the major ones being related to wellbores, large faults and an unspecified leaking caprock. Those related to the caprock either ignore fracture networks or do not explicitly consider them in detail.

Shale caprocks are heterogeneous compaction of naturally occurring minerals and are important caprocks in oil, gas and subsurface storage (e.g CO<sub>2</sub> sequestration, nuclear waste disposal). Recently these rocks have become valuable hydrocarbon reserves. Given the fact that shale rocks are geochemically active minerals in the presence of aqueous fluids such as CO<sub>2</sub> saturated brine and high pH fracturing fluid and most shale rocks have natural fractures or are induced (hydraulic fracturing). Mineralization can affect the conductivity of fractures. Diagenetic processes involving a host of sedimentary siliciclastic minerals can play significant role in enhancing or degrading caprock integrity over the long term. Temperature and pressure play an enormous extrinsic control on these subsurface processes. The geochemical interaction of these subtle fracture networks with formation minerals has not been quantified under confining stress conditions. This is needed in long term assessment of CO<sub>2</sub> sequestration efficiency and possibly in loss of conductivity in hydraulically fractured tight reservoirs [71]. This phenomenon is a multi-faceted problem involving low pH fluid transport, geochemistry and geomechanics that needs be investigated experimentally along with analytical, theoretical and geologic simulation modelling.

#### **1.4 Objective of Research**

As most effective tight lithologies are either fine-grain siliciclastics (clay-based rocks e.g. shale) or evaporite (anhydrites, gypsum, halite), it important that they provide effective hydraulic barriers in the subsurface for underground storage. Effective tight/caprocks have capillary entry pressure or displacement pressure that exceeds the upward buoyancy pressure exerted by an underlying hydrocarbon or CO<sub>2</sub> column; assuming no inherent deformation with lithologies that are varying in mineralogy, porosity, permeability, natural fracture distribution and wettability

parameters. Shale caprocks which are preferably of low ductility, lateral geologic continuity and thick depth of burial were used in this experimental investigations. The aim of this research project is to qualify and quantify how (micro-) fracture conductivity in shaly rocks can be impacted by diagenesis, particularly with respect to CO<sub>2</sub> sequestration and containment. The objective is to investigate the impact of in-situ geochemical precipitation on conductivity of open fractures under geomechanical stress conditions using laboratory and analytical modeling tools. This will provide meaningful and predictive insight on long term storage of CO<sub>2</sub> in shale capped reservoirs with intrinsic natural fractures and or large scale injection induced fractures.

## CHAPTER 2

### LITERATURE REVIEW

#### 2.1 Diagenesis of Sedimentary Rocks

Diagenesis is the process of physical and chemical changes in sediment, after deposition that converts it to consolidated rock. Classical diagenesis is considered to be a slow process occurring over centuries, but in fact, the reactions occur fairly rapidly, requiring fractions of years at reservoir conditions [56, 57, 60]. The centuries of time normally associated with diagenesis is the time required to bury sediment deep enough to reach the pressure and temperature conditions conducive to diagenetic change. Common minerals, dissolved in or precipitated from an aqueous phase can be grouped into those that are relatively reactive or inert in that their dissolution or precipitation rates are fast or slow, respectively, relative to the flow rate of the aqueous phase [72]. Multiple investigators have outlined the consequences of variations in reaction rates relative to flow rate of the fluid in which the minerals are reacting [56, 57, 59, 60, 72]. These minerals can be further grouped according to simple and complex stoichiometry. Those minerals with complex stoichiometry are much less likely to reach the solubility equilibrium than those with simple stoichiometry. For example, it is well known that simple ionic solids with high solubilities (such as halite, mirabilite, and carnallite) will reach solubility equilibrium more quickly than complex solids with a much more covalent character and low solubility [57]. Since calcite is a reactive mineral and has simple stoichiometry, it is considered as an example of water-rock reaction problem whenever it is present in substantial amounts. Calcium carbonate minerals can become insoluble at high pH and exposure to acidic fluid can reverse it. Generally, diagenesis of carbonate rocks includes all the processes on the sediments after their initial deposition [73].

High temperatures and pressures at the subsurface create minerals and structures by metamorphism. Physical, chemical, and organic processes begin acting on carbonate sediments after their deposition, leaving an influence on the mineral composition and structure [25, 39]. Diagenesis typically changes porosity, permeability and capillary pressure characteristics of a typical rock volume [25].

## **2.2 A Brief on Properties of CO<sub>2</sub> Saturated Brine**

The distribution of CO<sub>2</sub> injected into water - rock systems is closely related to the differences in physical parameters between CO<sub>2</sub> and formation water. Carbonic acid (aqueous CO<sub>2</sub>), which is a weak acid, forms two kinds of salts, the carbonates and the bicarbonates. In geology, carbonic acid causes limestone to dissolve producing calcium bicarbonate which leads to many limestone features such as stalactites and stalagmites. Under normal atmospheric temperature and pressure conditions, carbon dioxide is in the gas phase. According to the phase diagram of CO<sub>2</sub>, solid CO<sub>2</sub> (“dry ice”) is stable under low temperatures and somewhat elevated pressures [74]. As liquid CO<sub>2</sub> forms only at pressures above 0.5 MPa, increasing the temperature at low pressures will change solid CO<sub>2</sub> directly into gaseous CO<sub>2</sub> through sublimation. It should be noted that gaseous CO<sub>2</sub> cannot be perceived by smell. This is one of the reasons why high concentration of carbon dioxide can be lethal and care should be taken when handling large quantities in the laboratory. Oxygen, carbon dioxide and carbon monoxide level detectors should always be used for precautionary purposes. Supercritical form of carbon dioxide is usually used for EOR operations where carefully conditioned and pure form of the gas is transported via pipeline. The triple point of carbon dioxide (see figure 2.1), where the solid, liquid and gaseous phases can

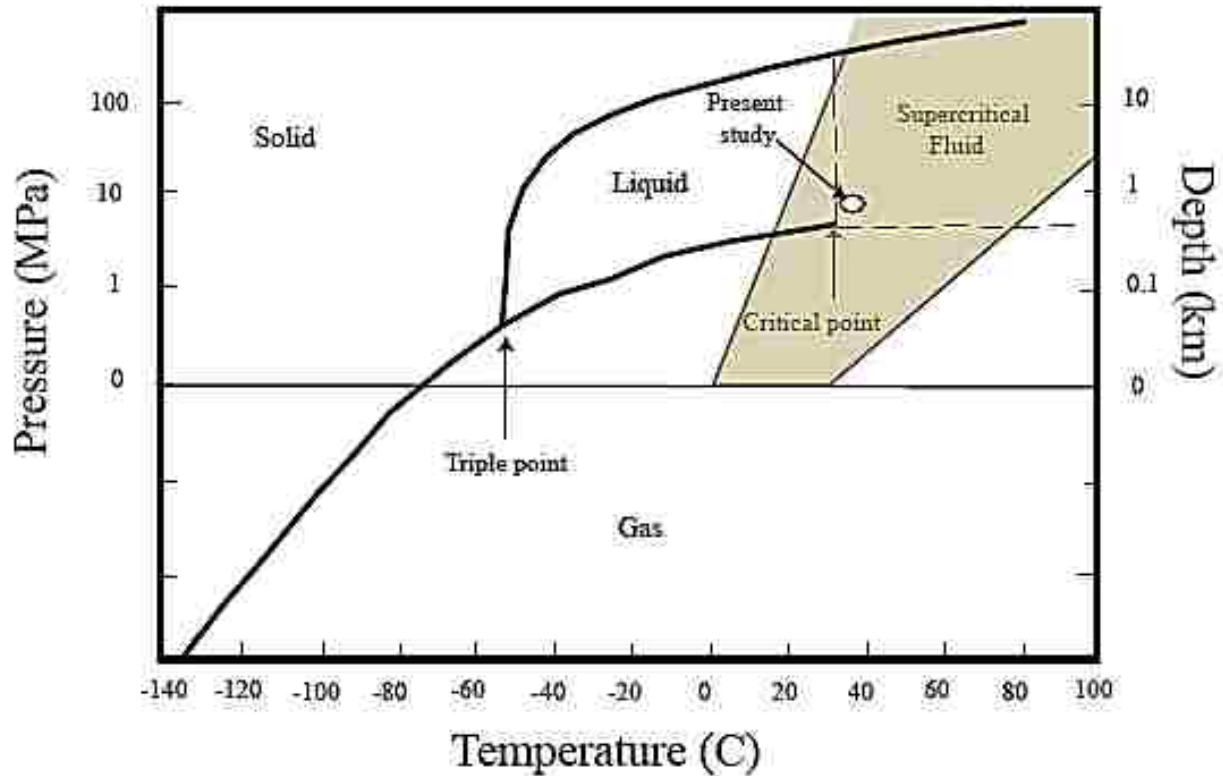


Figure 2.1: Phase diagram of CO<sub>2</sub> showing the pressure and temperature envelope for most sedimentary basins worldwide [75, 76].

coexists, is at 0.52 MPa and 56.6°C. The critical point is at 31.1°C and 7.38 MPa. Beyond this point CO<sub>2</sub> behaves in the dual way associated with supercritical fluids, namely filling all available volume like a gas, but with the density of a liquid [24, 30, 77]. Subsurface storage of carbon dioxide is usually expected to take place below depths of 800 meters, where temperature and pressure conditions are such that CO<sub>2</sub> is in the supercritical phase.

The density of CO<sub>2</sub> affects carbon dioxide storage in several ways. Higher density allows more CO<sub>2</sub> to be stored in the pore volumes available in formations. At the same time, the buoyancy forces which may threaten the safety by causing the CO<sub>2</sub> to migrate upward and up dip are reduced with increasing density. The density of CO<sub>2</sub> generally increases with pressure and

decreases with temperature. At depths considered for underground storage of CO<sub>2</sub>, the density of CO<sub>2</sub> typically varies between 0.6-0.8 g/cm<sup>3</sup>. At the pressure and temperature used in this study ( $P \sim 8.0 \text{ MPa}$  and  $T = 36^\circ\text{C}$ ) the density of CO<sub>2</sub> is close to 0.6 g/cm<sup>3</sup> (figure 2.1) [75]. The density of formation waters depends on salinity, in addition to pressure and temperature. The density ( $\rho_b$ ) of 1 M NaCl solution at 8.0 MPa and 36°C can be estimated based on an empirically derived expression by;

$$\rho_b = -3.033405 + 10.1288163x - 8.750567x^2 + 2.663107x^3 \dots\dots\dots \text{Eq. 2.1}$$

$$x = -9.9559e^{-0.004539m} + 7.0845e^{-0.0001638T} + 3.9093e^{-0.00002551P} \dots\dots\dots \text{Eq. 2.2}$$

where  $P$  is pressure in bars,  $T$  is temperature in Celsius and  $m$  is NaCl molality. The calculated density is 1.04 g/cm<sup>3</sup>, which is close to 75 % higher than the CO<sub>2</sub> density.

Viscosity describes the resistance of fluids to flow and for CO<sub>2</sub> it increases with pressure and temperature. Under the relevant conditions, CO<sub>2</sub> has a viscosity around  $3.0 \times 10^{-5}$  Pas. The viscosity of water decreases with temperature, and increases with salinity and pressure. Temperature is the main controlling factor, and under elevated pressure and temperature conditions, the viscosity of water is more than ten times that of supercritical CO<sub>2</sub> [78, 79].

The volume change of fluids in response to applied pressure is expressed as their compressibility. Compared to water, supercritical CO<sub>2</sub> has a very high compressibility, meaning that relatively small pressure and temperature changes can significantly alter its density. Actually, the compressibility of CO<sub>2</sub> close to the critical point ( $(\delta\rho/\delta P)_{T=T_c \text{ at } P \rightarrow P_c}$ ) approaches infinite values. The changes in isothermal compressibility ( $\Delta T = 0$ ) with pressure is significantly larger and more

distinct at 35°C than at 50°C (figure 2.2). For comparison, the very small compressibility of water at 8.0 MPa and 36°C is approximately  $43.4 \times 10^{-6} \text{ bar}^{-1}$  [75].

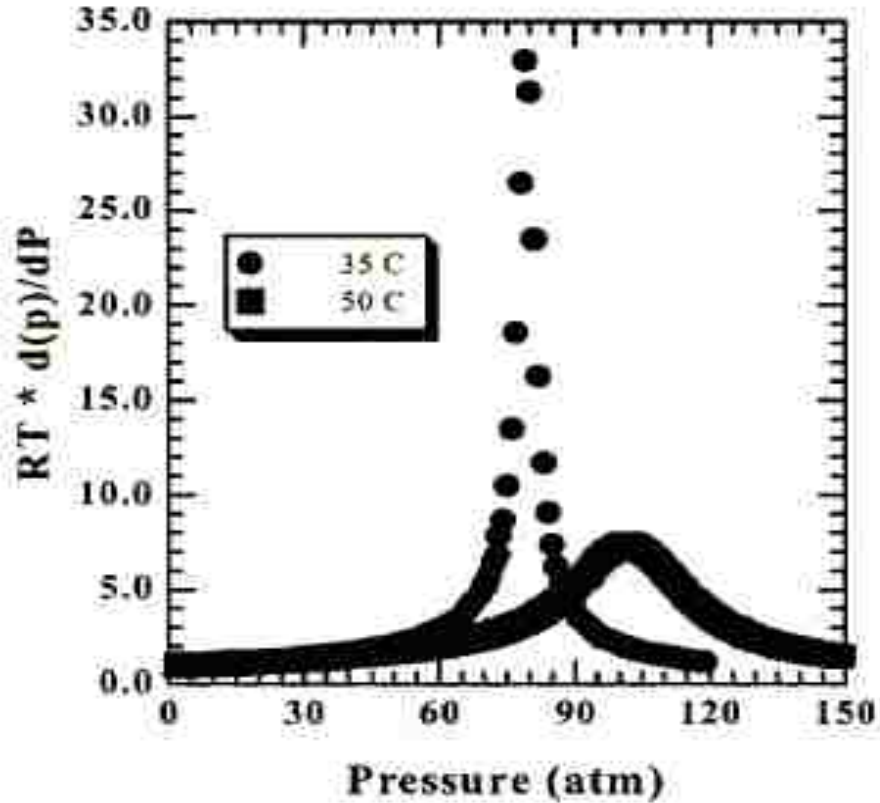


Figure 2.2: the isothermal compressibility of CO<sub>2</sub> at 35°C and 50°C [75].

In terms of displacement processes between CO<sub>2</sub> and water, the lower viscosity of CO<sub>2</sub> leads to viscous fingering, while the lower density may cause a gravitational segregation. Viscous fingering refers to the finger-shaped structures resulting from the injection of low viscosity fluids into fluids with higher viscosity. Due to viscous fingering and gravitational segregation, injected CO<sub>2</sub> will spread and accumulate above the water phase [75]. In comparison to flow in hydraulically fractured shales, flowback waters which are commonly considered to be fluids that flow out of a well within the first 2 weeks after stimulation by hydraulic fracturing, whereas production waters

are the remaining fluid that flows from the well after the initial 2-week period [80]. Flowback is driven by the release of the capped pressure and rock deformation induced by the flows from the well after the initial 2-week period post-fracturing process [81, 82].

### **2.3 Shale Caprock Geochemical Alteration and Subsurface CO<sub>2</sub> Migration**

Shale caprock constitutes more than 60% of effective seals for geologic hydrocarbon bearing formations and are therefore of considerable interest in underground CO<sub>2</sub> storage into depleted oil and gas formations [39]. Experimental studies of wettability, contact angle and interfacial tension on shale using CO<sub>2</sub>-rich fluid have not been widely reported [77, 83, 84]. Porosity, permeability, fractures and other petrophysical properties of the seal rock are of importance in seal integrity analysis and can be experimentally determined. Organic-rich shale is considered to have limited potential as membrane seals in CO<sub>2</sub> containment [85]. Shale rocks are predominantly composed of clays such as Illites, Kaolinites, Smectites and swelling Montmorillonites [33, 35, 65, 86, 87]. They might also have other silica and carbonate based minerals that contribute to their geomechanical strength. The mineralogical components of some shale samples are shown in table 2.1.

Detritus formations in the subsurface are composed of transported and deposited rock grains, minerals formed after deposition of the rock and organic material. The pore spaces between the grains and minerals are occupied by water and some oil and gas. The rocks making up the formation can be divided into cap rocks and reservoir rocks. The cap rocks are virtually impermeable rocks which form a barrier above the reservoir rocks. CO<sub>2</sub> injected into such

formations will interact with both cap rock and reservoir rock, in addition to the in situ formation water or what is generally referred to as the connate aqueous medium [20, 48].

Different mechanisms for CO<sub>2</sub> migration are possible, from small to large scales: (i) molecular diffusion of dissolved CO<sub>2</sub> in the pore water from the reservoir zone into the caprock formation, (ii) CO<sub>2</sub> diphasic flow after capillary breakthrough, (iii) CO<sub>2</sub> flow through existing open fractures.

The following mechanisms can accelerate or slow down the migration: (i) chemical alteration of the mineralogical assemblage of the caprock formation under the influence of acid water, (ii) re-opening of pre-existing fractures or micro-cracks induced by overpressure of the reservoir below, (iii) a combination of the above (including chemical alteration of the mineral filling the fractures)[48, 88, 89].

Several simulation results have predicted that influx-triggered mineral dissolution/precipitation reactions within typical shale cap rocks can continuously reduce micro-fracture apertures, while pressure and effective-stress evolution first rapidly increase then slowly constrict them. The extent of geochemical alteration is considered to be nearly independent of the injection rate while that of geomechanical deformation is thought to be more pronounced during engineered storage. The formation of wormholes in limestone or evaporate caprock core samples or dissolution of calcite and dolomite cements around quartz framework grains in siliciclastic core samples has been observed in batch or flow through reactions. Fracture evolution and permeability reduction through fines movement in fractured carbonate cap-rock has also been characterized. The potential effect on water chemistry or mineral trapping can be assessed; in addition to identifying the reaction of minor amounts of minerals not resolvable by rock characterization often necessitates identification through changes in water chemistry.

Table 2.1: Mineralogy of typical shale rock samples showing percentage composition [90].

	Pierre Shale	Arco-China Shale	C1-Shale
<b>X-Ray Diffraction</b>	%by weight	% by weight	% by weight
Quartz	19.0	51.0	14.0
Feldspar	4.0	12.0	2.0
Calcite	3.0	3.0	0.0
Dolomite	7.0	1.0	0.0
Pyrite	2.0	2.0	0.5
Siderite	1.0	0.0	0.0
*Total Clay	64.0	31.0	76.0
Chlorite	4.0	10.0	N/A
Kaolinite	11.0	14.0	39.0
Illite	19.0	44.0	N/A
Smectite	17.0	13.0	N/A
Mixed layer	49.0	20.0	N/A

*\*the percent composition of the total clay are broken down into chlorite, kaolinite, illite, smectite and mixed layer.*

There have been suggestions that ultimate restoration of pre-influx hydrodynamic seal integrity—in both EOR-EGR/storage and natural accumulation settings—hinges on ultimate geochemical counterbalancing of the resultant geomechanical effect [91, 92]. The geochemical reactivity of caprock formations should be evaluated gradually, essentially in two steps: classical batch experiments on crushed or small pieces of rock samples to evaluate reaction paths and possibly the reaction kinetics, and flow tests on plugs to evaluate, among other important quantities, the porosity and morphological variations.

In general, most researchers suggested that reaction trends are very difficult to identify at any temperature. This is not to say that no reaction occurred but the complex natural mineralogical composition envelops all reactions [65, 70]. In other experiments on the same formation and using an image analysis technique, an illitization of the illite-smectite components was identified, as well as the formation of gypsum. But similarly, these reaction paths are very difficult to identify using standard bulk measurements such as X-ray diffraction (XRD). With such difficulties in identifying reaction paths, the reaction kinetics is obviously out of reach [33, 61, 93].

Previous experimental research works have documented evidences of pore structure alteration in CO<sub>2</sub> flooded shale caprocks. The previous section (section 2.2) describes in detail some properties of the injected fluid in these experiments.

### **2.3.1 Geochemical Dissolution/Precipitation.**

The instability of clays in the presence of low-pH fluids has also been observed when using hydraulic fracturing fluid. Low-pH fluids are capable of dissolving clays and silicates. As temperature increases, the solubility of silici-clastic minerals is significantly increased especially in low-pH environment [94, 95]. These findings are often observed when immersion tests are run on cores in the laboratory. This type of fluid-mineral reactions is dynamic processes that involve many effects: complex fluid flow, pore space changes, surface chemistry, and the mineral composition. Several clays have been observed swelling rapidly in the presence of depressed pH and elevated temperature including sloughing or disappearance of swelling clays [32, 94]. After minerals are dissolved in the low-pH fluids, they can precipitate in the formation pores, restricting fluid flow and leading to scaling and progressive geochemical aggregation [57, 69]. Clay solubility

and geochemical precipitation in dry-gas, low permeability formations have a definite effect on decreasing conductivity of proppant packs and fracture walls; formation matrix and surface chemistry play a significant role in this as well as pH, ionic strength and adsorption processes. In addition, fracturing fluids can interact with formations. Water from these fluids may exhibit hydrogen bonding effects with formation clays and cause swelling and sloughing [96].

The mineral dissolution/precipitation with associated flow and reactive transport processes in porous media can be described at different scales. Reactive transport modeling represents a critical component in assessment of geochemical impact of CO<sub>2</sub> water-rock interactions. The following geochemical analytical model (equations 2.3 to 2.5) has been developed to generalize precipitation-dissolution processes [75, 97, 98]:

$$\frac{dn}{dt} = -Sk_{298.15}e^{-\frac{E}{R}\left(\frac{1}{T}-\frac{1}{298.15}\right)}\left(1-\frac{Q}{K_{eq}}\right) \dots \dots \dots Eq. 2.3$$

$$S = S_0 \left(\frac{C}{C_0}\right)^{2/3} \left(\frac{\phi}{\phi_0}\right)^{2/3} \dots \dots \dots Eq. 2.4$$

$$K = K_0 \left(\frac{\phi}{\phi_0}\right)^n \dots \dots \dots Eq. 2.5$$

Where S= specific surface area, k=permeability, Q = reaction rate, φ = porosity, Keq = equilibrium rate constant, C = spherical grain size, n = heterogeneity exponent, R = gas constant, E = activation energy. An example of temperature-quartz precipitation relationship is presented in figure 2.3 [99]. The assumptions made for generating figure 2.3 included fixing the equilibrium constants.

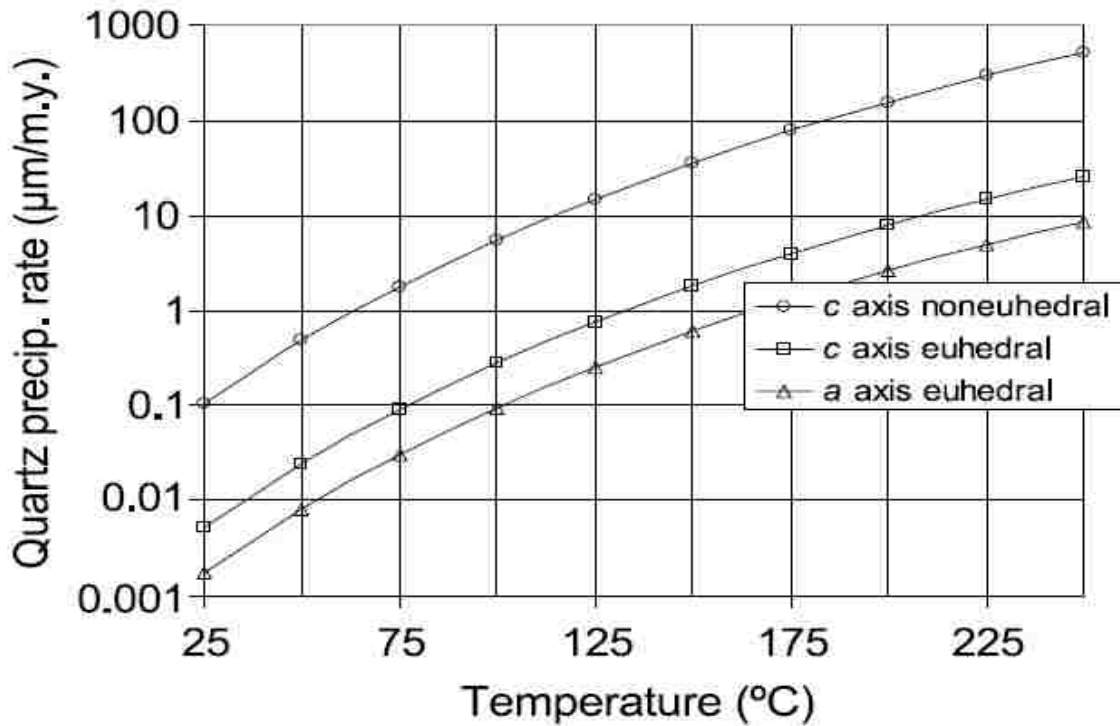


Figure 2.3: Quartz precipitation rate in micrometers per million years for a range of temperature from 25°C to 250°C. The three curves represent the range of expected growth rate in a fracture, with the greatest rate being parallel to the c crystallographic axis [99].

Measurements of the thermal gradient are crucial to decipher the thermal effects and calculate the thermodynamic and kinetic parameters of the chemical processes that occur in the reactor.

Table 2.2 presents a holistic reaction equations and chemical activity values that are representative of the interaction of various components of a sedimentary rock (highlighted in color as amorphous, carbonates, silicate and clay groups). Multiple geochemical reactions are usually occurring in the subsurface during the depositional history of sedimentary rocks. The extent of burial can determine the magnitude of the earth stress, temperature and pressure conditions that will be applicable. A predicted reaction of interest in coupled models involving exclusively clay minerals conversion is given as follows; equation 2.6 [100]:



As already mentioned, CO<sub>2</sub> will be in a supercritical phase at depths of geological formations being considered for storage of carbon dioxide. Supercritical CO<sub>2</sub> is less dense than water and will rise until it reaches the overlying cap rock. This kind of *physical trapping* beneath stratigraphic or structural barriers is the principle means to store CO<sub>2</sub> in geological formations. With time CO<sub>2</sub> will dissolve into the formation water, removing buoyancy as a reason for migration. The dissolved CO<sub>2</sub> will instead migrate according to relatively slow regional-scale groundwater flows [103]. The storing of CO<sub>2</sub> dissolved in slow moving waters is referred to as *hydrodynamic trapping*. Finally, CO<sub>2</sub> can be locked up in carbonate minerals in *mineral trapping*. Some of the most probable carbonate minerals forming are calcite (CaCO<sub>3</sub>), magnesite (MgCO<sub>3</sub>), siderite (FeCO<sub>3</sub>) and dawsonite (NaAlCO<sub>3</sub>(OH)<sub>2</sub>). The advantages of mineral trapping are apparent, as the CO<sub>2</sub> would be stored in fairly stable minerals over very long timescales [86, 104, 105].

### **2.3.2 Dissolution Kinetics in Shale Caprock Minerals**

Most of the knowledge on mineral dissolution kinetics acquired over the last fifty years comes from the ability to accurately measure the variation in aqueous chemistry as a function of time when a mineral (usually powder) and a solution are put together to react. This approach has been used to produce adequate data to formulate empirically derived dissolution rate laws that account for the effects of pH, temperature, aqueous Al, organic acids, solution saturation state, and ionic strength on clay mineral dissolution rates. In the last two decades, additional micro- and nanoscale data has come out from the improved capacity of new techniques such as atomic force microscopy (AFM), interferometry techniques (VSI (vertical scanning interferometry) and PSI (phase shifting interferometry)), and laser confocal microscopy with differential interference

contrast microscopy (LCM-DIM) to study the mineral-water interface [105]. Integration of both strategies is leading to a remarkable level of understanding of the dissolution kinetics.

Rock mineral dissolution rate can be written by considering a general law (equation 2.7), as that proposed by Lasaga in the late 90s:

$$Rate = k_0 \cdot A_{min} \cdot e^{\frac{E_a}{RT}} \cdot a_H^{n_H} \cdot \prod_i a_i^{n_i} \cdot g(I) \cdot f(\Delta G_r) \dots \dots \dots Eq. 2.7$$

Where  $k_0$  is a constant,  $A_{min}$  is the reactive surface area of the mineral,  $E_a$  is the apparent activation energy of the overall reaction,  $R$  is the gas constant,  $T$  is the temperature (K),  $a_H$  is the activity of protons in the solution,  $n_H$  is the order of the reaction with respect to  $H^+$  and the term involving the activities of other aqueous species,  $a_i$ , incorporate other possible catalytic or inhibitor effects on the overall rate [106]. The  $g(I)$  term indicates a possible dependence of the rate on the ionic strength ( $I$ ) in addition to that entering through the activities of specific ions. The  $f(\Delta G_r)$  term accounts for the variation from equilibrium ( $\Delta G_r = 0$ ;  $0 < f(\Delta G_r) < 1$ ). The formulation of the rate equation above is very useful because it relates the reaction rate to activities of ions in solution that may be obtained directly from the solution chemistry. However, silicate dissolution is a surface process and therefore, it is more appropriate to express the dependence of the rate on the concentrations (or activities) of ions adsorbed on the surface rather than on the bulk activities in solution. Hence, the equation can be written in terms of surface concentrations ( $C_{s,i}$ ) (Eq. 2.8);

$$Rate = k_0 \cdot A_{min} \cdot e^{\frac{E_a}{RT}} \cdot C_{s,H}^{n_{H,ads}} \cdot \prod_i a_i^{n_{i,ads}} \cdot g(I) \cdot f(\Delta G_r) \dots \dots \dots Eq. 2.8$$

Where the coefficients  $n_{H,ads}$  and  $n_{i,ads}$  are the reaction orders with respect to the adsorbed surface species. Given the above and based on the two rate equations, there is a diversity of rate laws that account for the dissolution kinetics of different clays [107, 108].

In the last four decades, several mechanistic models have been developed to account for the effect of deviation from equilibrium ( $f(\Delta G_r)$ ) on mineral dissolution kinetics. Among others, these mechanisms include: (1) the most widely extended one was derived from transition state theory (TST) which was developed for elementary reactions and may be applied to overall reactions governing the dissolution process and relates the variation in solution composition with mineral dissolution and precipitation rates [108, 109]. TST may be applied only in cases in which defects such as dislocations do not control the dissolution kinetics (2) at the start of the twenty-first century, a different conceptual model took off. Researchers also proposed a model of mineral dissolution that directly links the surface reactivity of minerals with their dissolution kinetics [108]; (3) in a third approach, dissolution of some alumina-silicates can be understood through the same mechanistic theory of nucleation developed for mineral growth. Another model predicts that dissolution occurs via the formation of etch pits and the generation of dissolution step-waves at the outskirts of the pit walls [110]. If the under-saturation of the solution is high enough, i.e.,  $\Delta G < \Delta G_{crit}$  (critical free energy), etch pits not only open up but they are the source for trains of steps that travel across the surface. By moving away from the defect site and lowering the silicate surface the propagation eventually controls the bulk dissolution rate. Several studies using vertical scanning interferometry (VSI) have demonstrated this mechanism and suggest that etch pits in combination with step movement control the dissolution process of several minerals independent of their degree of structural complexity [111].

It has also been showed that mineral dissolution can be understood through the same mechanistic theory of nucleation developed for mineral growth [108]. The derived dislocation model can predict variation of the normal aluminosilicate dissolution rate ( $R_n$ ) with degree of under-saturation ( $\sigma$ ). It is argued that two-dimensional nucleation dominates rates measured at higher temperatures 150°C – 200°C. In contrast, the 80°C data for kaolinite is predicted by the dislocation defect model. Nonetheless, this model has not been further developed for clay minerals other than kaolinite.

Implementation of base case dissolution model has gained terrain as real-time microscopic observations of reacted mineral surfaces offer new insights into the dissolution mechanisms [108]. Also, the validity of the TST-based rate laws to be sufficient to explain mineral dissolution kinetics as a function of distance from equilibrium has been questioned, mainly based on the fact that TST allows a relation between the forward and reverse rate constants but only of an elementary reaction [112, 113]. The adequacy of simple surface adsorption models to explain the complexity of the three-dimensional lattice and its participation in the dissolution process is also argued. Previous works showed that the use of a stochastic approach that treats crystal dissolution as a many-body problem has led to the development of the step-wave model and some in-depth exploration of the dissolution mechanism [114].

As it has been extensively discussed in the literature, most of the descriptions and interpretations of the clay dissolution kinetics are at the moment, TST-based. Therefore, TST is further discussed. The terms integrated in equation 2.8 above other than the  $f(\Delta G_r)$ , account for the effect of different environmental variables on clay dissolution rates.

In order to model the effects of pH, temperature, catalysis/inhibitors, ionic strength on clay mineral dissolution rates, it is important to separate between direct and indirect effects of the environmental variables involved. Direct effect means effect related to surface processes and therefore, one that can be used to understand the reaction mechanism. As changes in most environmental variables affect also the degree of saturation, their direct effect on the rate should be measured in experiments that are carried out under far-from-equilibrium conditions.

### 2.3.2.1 Negative Logarithm of Hydrogen Ion (pH)

The effect of pH on the dissolution rates of oxides and silicates, and hence clay minerals has been exhaustively examined in the last decade (figure 2.4). For the pH-dissolution rate dependence, in the absence of catalysts/inhibitors, the dissolution rate (equation 2.9) has been classically interpreted by three reaction mechanisms [108, 109]: proton promoted, hydroxyl-promoted and water promoted, that dominate the reaction rate under acidic, alkaline, or neutral conditions, respectively:

$$Rate = k_{H^+} \cdot a_{H^+}^{n_{H^+}} + k_W + k_{OH^-} \cdot a_{OH^-}^{n_{OH^-}} \dots \dots \dots Eq. 2.9$$

Where  $a_{H^+}$  is the proton activity;  $a_{OH^-}$  is the hydroxyl activity;  $k_H$ ,  $k_W$ , and  $k_{OH^-}$  are the rate constants under acidic, neutral, and basic conditions, respectively, and  $n_{H^+}$  and  $n_{OH^-}$  are the corresponding orders of reaction. The dissolution rates of most alumina-silicates as a function of pH exhibit a U-shape figure. In some studies the pH dependence of dissolution rate is modelled using a surface complexation model (equation 2.10) [108]:

$$Rate = k_H \cdot C_{S,H} + k_W + k_{OH^-} \cdot C_{S,OH} \dots \dots \dots Eq. 2.10$$

Where  $k_i$  is the rate coefficient of reaction mechanism  $i$ , and  $C_{S,i}$  is the mineral surface concentration of adsorbed species  $i$ .

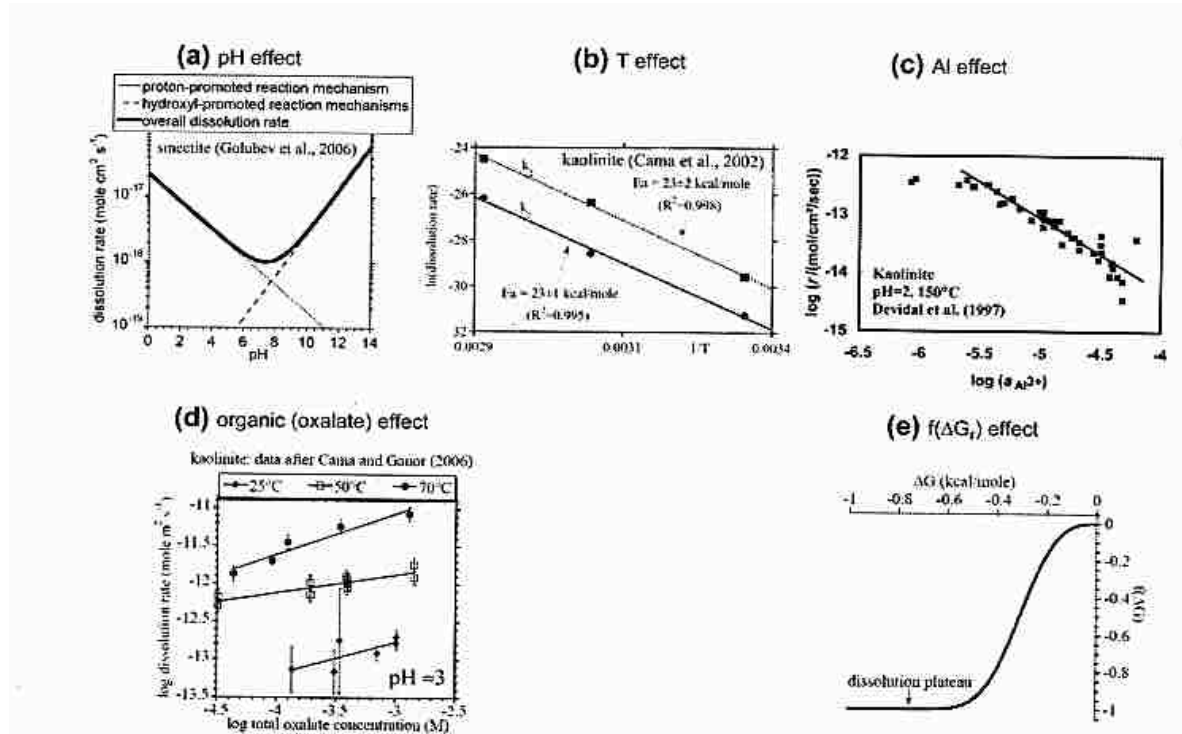


Figure 2.4: Mineral dissolution rate as a function of: (a) pH, (b)  $1/T$ , (c)  $a_{Al^{3+}}$ , (d) oxalate concentration, and (e)  $f(\Delta G_r)$  [108].

### 2.3.2.2 Temperature

The temperature dependence of the dissolution rate generally follows the Arrhenius law (equation 2.11);

$$Rate = A \cdot e^{-E_a/RT} \dots \dots \dots Eq. 2.11$$

Where  $A$  is the pre-exponential factor,  $E_a$  is the apparent activation energy of the overall reaction,  $R$  is the gas constant, and  $T$  is the temperature (K). In order to obtain the apparent

activation energy experimentally, it is common to conduct several experiments at different temperatures while all the other experimental variables (e.g., pH) are held constant. A critical assumption in calculating activation energies using this method is that the pre-exponential factor,  $A$ , is the same in all experiments. This pre-exponential factor includes other effects of the experimental variables on the rate. As mineral dissolution is a surface process, the pH effect on dissolution rate is controlled by protons adsorbed on the surface and not directly by the pH [115]. Therefore, conducting experiments under the same pH is not enough to keep the pre-exponential factor constant but the surface concentration can be held constant [108].

Under non-equilibrium conditions, and keeping all parameters except pH and temperature constant, the rate becomes (equation 2.12);

$$Rate = k \cdot e^{-E_a/RT} \cdot a_{H^+}^{n_{H^+}} \dots \dots \dots Eq. 2.12$$

Where  $k$  is a coefficient that is constant under these conditions.

**2.3.2.3 Surface Area and Reactivity**

Reactive surface area is one of the key parameters for studying the kinetics of mineral dissolution. The determination of the reactive surface area is not trivial in clay minerals as they possess both internal and external surface areas, and in which many cases the dissolution is controlled by the chemical attach on the edge surface [116, 117]. The common practice in experimental kinetics is to normalize dissolution rate to the surface area measured by the Brunauer–Emmett–Teller (BET) method. As the BET method measures the total surface area, it was suggested that it is not a valid proxy for reactive surface area of clays [108, 118, 119]. It is widely recognized that dissolution

and precipitation of clay minerals (and phyllosilicates) occur preferentially at the edge. Lack of correlation between the total and the edge surface area of smectite makes the smectite BET surface area an ineffective proxy for its reactive surface area. This conclusion may be extrapolated to all clay minerals which form layered particles. Hence, it is suggested to use AFM measurements of the specific edge surface area as an alternative proxy for the reactive surface area of smectite and other clay minerals [116, 120-122]. However, the recent VSI and AFM experiments with muscovite indicate that basal/edge surface area ratios are highly variable and change continuously over the progression of the reaction, thus obviating their utility as characteristic parameters defining mica reactivity [108].

#### **2.3.2.4 Catalysis/Inhibitors**

Aluminum (Al) and organic matter (OM) can be used as proxy for measuring catalytic and inhibiting phenomenon in clay rich shaly rocks [108, 123]. It has been showed strong Al inhibition of kaolinite dissolution reaction under very-far-from-equilibrium conditions at 150°C and pH = 2. The reaction order of this inhibition was -1. It was proposed that Al-silicate dissolution is controlled by a Si-rich precursor complex formed by the exchange of Al for protons at the surface [116, 124]. Due to differences in the surface properties of different minerals, there is a significant variability in their tendencies to adsorb organic matters. Among the naturally abundant minerals, the most effective adsorbents are clay minerals and oxides [25, 110, 125]. Although both inhibition and enhancement of clay mineral dissolution rates were observed, the latter effect is much more common. Low molar mass organic acids (e.g., oxalate, malonate, citrate, salicylate, o-phthalate, and gluconate) through ligand-promoted dissolution at mineral surfaces and



but not at 50°C ( $\approx 10^{-6} \text{ M} < [\text{Al}] < 10^{-4} \text{ M}$ ). The surface reaction mechanism consists of fast adsorption of  $\text{Al}^{3+}$  on the mineral surface (crystal edge surface sites) followed by a slow hydrolysis step [108].

#### **2.3.2.5 Ionic Strength Effect**

Transition State theory (TST) predicted that the rate constant depends on the activity coefficients of aqueous species [108]. For not too high concentrated solutions ( $< 0.1\text{M}$ ), the logarithm of the rate constant of an elementary reaction involving ions depends on the square root of the ionic strength of the solution [131, 132]. Early fast release rates of interlayer cations from clay minerals, induced by ion exchange reactions between the solution and the interlayer sites, have been observed in several studies, yielding to early non-stoichiometric dissolution of clay minerals, which is pH dependent [108]. In most cases steady-state dissolution was stoichiometric. Non-stoichiometric dissolution under steady state condition is mostly the result of precipitation of secondary phases [133]. Similarly to silicates, the dissolution rates of clay minerals slow down with increasing pH in the acidic range, become constant at an intermediate pH, and increase with increasing pH in the basic range [134, 135]. This pattern of change with pH in the dissolution rate of oxides and silicates was classically interpreted by three reaction mechanisms: proton-promoted, hydroxyl-promoted, and water-promoted, that dominate the reaction rate under acidic, basic, or near-neutral conditions, respectively [108]. The fractional reaction orders calculated from the linear regression of plot of  $\log R_{\text{Si}}$  and/or  $R_{\text{Al}}$  against pH are between 0.32 and 0.60 (Illite), 0.4 and 0.75 (Montmorillonite). The proton-dependent reaction order for trioctahedral micas (phlogopite and biotite) ranged between 0.25 and 0.61 compared to 0.14-

0.20 for dioctahedral mica (muscovite). The fractional reaction orders for pH are between 0.44 and 0.45 (vermiculite) and 0.29 and 0.49 (chlorite) [110, 136]. Experimental works to study the effect of ionic strength on kaolinite, montmorillonite, and illite show that the kaolinite dissolution rates were dependent on ionic strength. The dissolution rates of the other two clay minerals were mainly controlled by solution pH, and no effect of ionic strength was observed on the dissolution rates. In the case of illite dissolution, an increase in the release rates of  $\text{Al}^{3+}$  and  $\text{K}^+$  occurred by increasing the ionic strength from 0.01 M to 0.25 M, however, no such effect was observed on Si release rates [108].

### **2.3.3 Precipitation in Porous Media**

The interpretation of mechanisms of reactions in rocks is based on studying the microstructural development associated with the reaction [137]. The microstructure of a rock describes the relationships between the mineral grains and organic material in the rock, their size, shape, and orientation. When reactions involve fluids we look for microstructural and chemical evidence for the presence of fluid and fluid pathways [137, 138]. In that sense the porosity can be considered as an integral part of the microstructure, in that it is the space occupied by the fluid phase, and the distribution of the fluid phase is just as important to the rock properties as the distribution of the minerals. The individual mineral grains in a rock may also have a microstructure that reflects the processes taking place within the crystalline structure as a result of the geological history of the rock [20, 126, 137]. Examples would include ex-solution from an initial solid solution, or transformation twinning, or the formation of dislocation arrays during deformation [48, 139]. The rock and mineral microstructures can provide important information on how the

rock formed and its subsequent thermal and deformational history. The microstructure is thus a direct result of the mechanisms of the processes that take place when a rock or mineral reacts to lower the overall free energy of the system under the imposed physical and chemical conditions [126, 138]. The microstructure formed during any process is always a balance between the thermodynamics (reducing the free energy) and the kinetics (the time available and the rates of the processes involved). As such, a microstructure may change over time, for example by coarsening or recrystallization to reduce the surface energy [137]. When an aqueous fluid interacts with a mineral with which it is not in equilibrium (i.e., is either under-saturated or supersaturated with respect to that mineral) the mineral will either tend to dissolve or grow until equilibrium is reached, i.e., until the fluid is saturated with respect to that mineral. The solubility of a mineral can also be increased by applied stress and this leads to the phenomenon of pressure solution whereby grains in contact with one another and under compression dissolve at these pressure points (figure 2.5). The resulting fluid is then supersaturated with respect to a free mineral surface and can re-precipitate in the pore spaces [120, 137]. The newly precipitated phase may have the same major chemical composition as the dissolved phase, but can be recognized as an overgrowth both texturally and from trace element and isotope geochemistry. This mechanism of compaction reduces the porosity of a rock and leads to well-known relationships between depth of burial, porosity and rock density [69, 140]. The re-precipitated phase can also act as a cement to bind the particles during the lithification process [48, 141].

in structural geology and diagenesis, pressure solution or pressure dissolution is a deformation mechanism that involves the dissolution of minerals at grain-to-grain contacts into an aqueous pore fluid in areas of relatively high stress and either deposition in regions of relatively low stress

within the same rock or their complete removal from the rock within the fluid. It is an example of diffusive mass transfer. Figure 2.5 exemplifies the grain to grain behavior when pressure solution is considered in subsurface fluid-rock interactions.

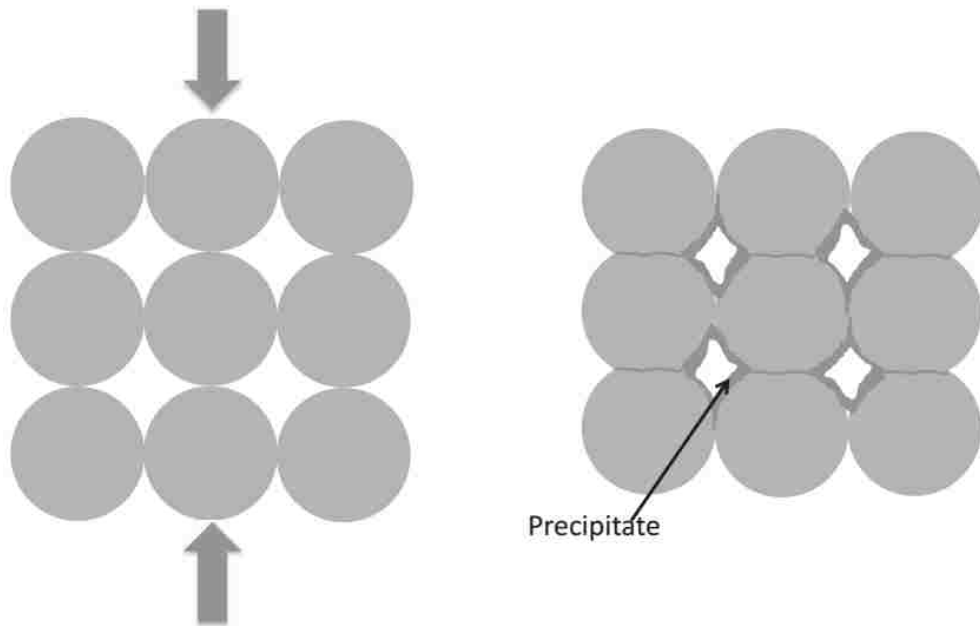


Figure 2.5: Schematic drawing of pressure solution. A material under applied stress dissolves at the stress points, where the spherical grains are in contact, and is transported through the solution to sites of lower stress where it re-precipitates. Compaction by pressure solution reduces the porosity and permeability of a rock [137].

Fluid migration through reactive rocks invariably leads to modifications of the rock porosity and pore structure [142, 143]. This, in turn, provides feedback on the fluid migration process itself. Reactions may lead to increases or decreases of the rock permeability. When the volume of solids decreases, either by an increase in the rock density or by transport of mass out of the system, the corresponding increase in porosity will enhance fluid transport and the continued propagation of the reaction front. In contrast, reactions that increase the solid volume will fill the pore space and may reduce permeability [120, 144]. In this case, the reaction will only proceed if

the stress generated by the volume increasing process is large enough to create a fracture network that will enable continued fluid flow. Reaction-induced fracturing is particularly relevant during fluid migration into high-grade metamorphic and slowly cooled magmatic rocks with very low initial porosity, but may also be important during reactive transport in more porous rocks where growth processes within the pore space exerts forces on the pore walls [20, 144] and fracture propagation. Spheroidal weathering is an example of a process where reactions produce pronounced fracturing under the low confining pressures that prevail near the Earth's surface. This kind of weathering has been described for most rock types in a wide range of climate zones. Although spheroidal weathering, per definition, involves surface-parallel fracturing and spalling of layers at the margin of rock blocks, which become progressively rounded (core stones), the progress of this mode of weathering and the fracture patterns produced are sensitive to the initial porosity of the rock type [145]. Fluid flow in fractures is assumed to be effectively instantaneous compared to the rate of other relevant processes [146, 147]. In a natural system, the progress of the fluid-driven, volume-increasing reactions, is controlled by two main parameters: rock porosity, and the shape of the initial domain undergoing volatilization [148, 149]. For circular domains, porosity variation will control both the relative rates of reaction kinetics and transport, often expressed by the dimensionless *Damkohler* or *Peclet-Damkohler* Number, and the amount of the mobile reactant that the rock can contain [70, 150]. Although reactions may produce fractures and porosity, mineral growth in pores may also lead to clogging. This may significantly decrease the permeability and therefore fluid migration through initially porous rocks, and through rocks that are initially fractured due to tectonic and thermal processes. When fluid consuming reactions occur synchronously with tectonic deformation, the externally imposed

stress may completely control the reaction rate and progress if permeability is generated at a faster rate than the infilling of pores by reaction products. On the other hand, if the precipitation rate is fast compared to the rate of fracturing and permeability generation, the progress of reaction may be modest even in extensively fractured rocks [151].

Replacement reactions mediated by a fluid phase take place through a coupled dissolution–precipitation reaction. When fluid comes into contact with the reactive mineral, dissolution takes place at the mineral surface [138]. This immediately creates a supersaturated solution with respect to the replacing mineral, which will then precipitate in the immediate vicinity of the dissolving surface. A nanometer-scale confined fluid film between the parent and daughter phases will allow the reaction to continue. If the supersaturation with respect to the precipitating phase is high, there will be enough chemical energy available for the precipitating material to exert a mechanical stress on the reacting grain, and cause fracturing, when precipitation is confined within dissolution pits and wedges [151].

A well-established example of the use of the continuum approach for interfacial reactive processes is that of reactive transport in fractures. In fractured media, there is a sharp contrast— with a clear separation of scales—between the porosity in the fracture and in the rock matrix [135]. As a result, the fracture is modeled as a fast flow path, where transport is dominated by advection, and the rock matrix, where transport is dominated by diffusion. Heterogeneous reactions take place within the porous rock matrix or the layer of precipitate that coats the surface [152]. To simulate flow in discrete fractures in Darcy-scale models, the cubic law is often used to obtain a fracture permeability under the assumption of parallel smooth walls [153]. However, this model does not typically provide an accurate estimation of fracture hydrodynamic

properties at realistic fracture roughness. Mineral rates measured in laboratory experiments are often several orders of magnitude faster than those estimated from natural systems [154]. These differences in rates have been attributed to a variety of factors including, among others, reactive surface area accessibility in natural porous media, limitations on flow and transport in heterogeneous material, or transport, rather than interface control of rates. Microfracture-scale modeling can be used to address some of these hypotheses by explicitly accounting for the rate-limiting effect of transport, and by incorporating mechanistic descriptions for the evolution of reactive surface area [155, 156].

Applications of direct numerical simulation of pore-scale processes in subsurface materials are growing in part due to the computational advantages of well-established computational fluid dynamics (CFD) methods [70, 151]. Availability of high-level, open-source libraries such as *OpenFOAM* or *Chombo* have also facilitated implementation of models into new simulation capabilities [157]. In reactive systems, the ability to calculate the heterogeneous reaction rates at the fluid–solid interfaces makes direct numerical simulation a suitable tool to mechanistically model processes that are not captured by models at larger scales, especially when well-mixed assumptions are made [158, 159]. In multiscale problems, direct numerical simulation has typically been performed using continuum methods rather than strictly using pore-scale methods. In these methods surface reactions and transport processes are not explicitly calculated at the interface and are upscaled from the pore scale [160]. Upscaling of strongly coupled non-linear processes is not straightforward and the solution of macro- and micro-scale problems is coupled. It is ultimately the combination of new microscopic characterization, experimental, and modeling approaches that presents the opportunity to provide mechanistic

explanations for many of the long-standing questions in geochemical processes in fractured porous media [97, 138, 161].

## **2.4 Geomechanical Effects**

### **2.4.1 Cap Rock Seal Integrity and Capillarity**

CO<sub>2</sub> injection may lead to pressure build up and temperature decrease, which may cause CO<sub>2</sub> leakage through the cap rock by capillary leakage or rock fracturing. CO<sub>2</sub> diffusion through the cap rock is an extremely slow process, and is only considered important over geological time. Capillary leakage occurs if the minimum pressure needed to displace the brine in the cap rock (capillary breakthrough pressure,  $P_c$ ) is exceeded [47, 162, 163].

Since cap rocks overlying gas and oil reservoirs have proven the ability to prevent upward migration of hydrocarbons through geological time, it has been argued that they will be sufficient seals also after CO<sub>2</sub> injection. Recently however, it has been pointed out that since the interfacial tension (IFT) is much lower in the CO<sub>2</sub>/water system than in the hydrocarbon/water system, the sealing capacity of the cap rock is significantly reduced after CO<sub>2</sub> injection. IFT ( $\sigma$ ) is a result of the attractive forces of molecules acting at the interface between fluids, and is closely related to capillary breakthrough pressure [83, 164]. The cohesive forces among the liquid molecules are responsible for this phenomenon of surface tension. Chiquet et al. experimentally examined the contact angle on quartz and mica under varying CO<sub>2</sub> pressures. They observed a 40°-50° increase in the contact angle of mica and 15°-25° increase for quartz over the pressure interval 0-11 MPa. This corresponds to lowering the sealing capacity by a factor of ~1.5. This wettability alteration was primarily attributed to a decrease in brine pH caused by CO<sub>2</sub> dissolution, as the electrostatic

repulsion between the negative surface charges on the mineral-brine and brine-CO<sub>2</sub> interfaces are reduced at low pH in the bulk of the liquid, each molecule is pulled equally in every direction by neighbouring liquid molecules, resulting in a net force of zero. The two are connected through the Laplace law (equation 2.14);

$$P_c = \frac{2\sigma\cos\theta}{r_p} \dots\dots\dots Eq. 2.14$$

where  $\sigma$  is the IFT between CO<sub>2</sub> and water,  $r_p$  is the largest connected pore throat radius and  $\theta$  is the contact angle between the mineral - brine - CO<sub>2</sub> - system. The general assumption has been that brine is a good wetting fluid (small contact angle). Recently however, it has been pointed out that the dense, supercritical CO<sub>2</sub> reduces the wettability of water on shale minerals (e.g. quartz, mica). It should be noted that the concept of interfacial tension in subsurface rock-fluid interactions and phase behavior has been around for several decades, with applications in water flooding operations for crude oil production.

Quantitatively, the differences in IFT between brine/CO<sub>2</sub> and brine/hydrocarbons have been addressed by several authors. Numerous other researchers have investigated IFT in (CO<sub>2</sub> + CH<sub>4</sub>) + water systems, and it was observed that the relative amounts of CO<sub>2</sub> and hydrocarbons affected the IFT [165]. Other researchers also complemented their gas breakthrough experiments with a review of existing experimental data [47, 84]. At pressures from 6 - 20 MPa and temperatures below 71°C, the IFT levels in brine-CO<sub>2</sub> are approximately half the values of water/hydrocarbon. Among pressure, temperature and salinity of the brine, pressure exerts the main control on the IFT. Combining the effects of reduced IFT and increased contact angle, the replacement of hydrocarbons by CO<sub>2</sub> can reduce the capillary breakthrough pressure by a factor of ~3.

Translating the breakthrough pressure into storage capacity for aquifers is relatively straightforward. If the reservoir in which CO<sub>2</sub> is stored has a thickness  $h$ , the buoyancy forces driving CO<sub>2</sub> upwards are the product of the gravitational constant, the thickness of the aquifer and the difference between the density of brine and CO<sub>2</sub> ( $(\rho_{water} - \rho_{CO_2}) \times g \times h$ ). If the buoyancy forces are greater than the cap rocks capillary pressure, CO<sub>2</sub> will enter the cap rock. A certain amount of work is required to move a water molecule from within the body of the liquid through the interface. This is referred to as free surface energy of liquid. The maximum height of CO<sub>2</sub> that can be stored can therefore be obtained from the simple inequality expression (equation 2.15):

$$(\rho_{water} - \rho_{CO_2}) \cdot g \cdot h \leq \frac{2\sigma \cos\theta}{r_p} \quad \text{and} \quad h \leq \frac{2\sigma \cos\theta}{r_p \cdot (\rho_{water} - \rho_{CO_2}) \cdot g} \quad \dots\dots\dots \text{Eq. 2.15}$$

It should be mentioned that the density variations of CO<sub>2</sub> and water in the reservoir is not accounted for in these equations. The low viscosity and high diffusion coefficient of supercritical CO<sub>2</sub> has made it a preferred agent in supercritical fluid extraction (SFE). The ability to extract organic matter from rocks could potentially influence the sealing performance of the organic-rich claystone from the Troll East Field. Other researchers have treated siltstone from the field injection test sites (total organic matter content 0.4 - 1.3 wt %) with supercritical CO<sub>2</sub> to identify potential cap rock alterations caused by SFE [166-168]. Even though the carbon and nitrogen levels, porosity and pore size distribution remained virtually unchanged after 150 days of treatment, significant permeability changes could not be excluded. If the minor amounts of organic matter dissolving hold grains together, the resulting pore structure alteration could drastically increase the permeability [27, 169, 170].

### 2.4.2 Fracture Conductivity and Formation Stress

A fracture has been recognized as a fluid conduit that has high permeability relative to that of the surrounding rock matrix in a fractured reservoir [171, 172]. The reservoir quality of sedimentary rocks is closely related to diagenesis, a process involving post-depositional alteration of previously deposited sediments. Rock properties such as porosity, permeability, pore-size distribution, reservoir heterogeneity and spatial correlation can be the product of diagenetic modification of original properties [173, 174]. Figures 2.6 and 2.7 illustrate hypothetical diagenetic changes in a single fracture factoring diffusion, convection and surface reaction.

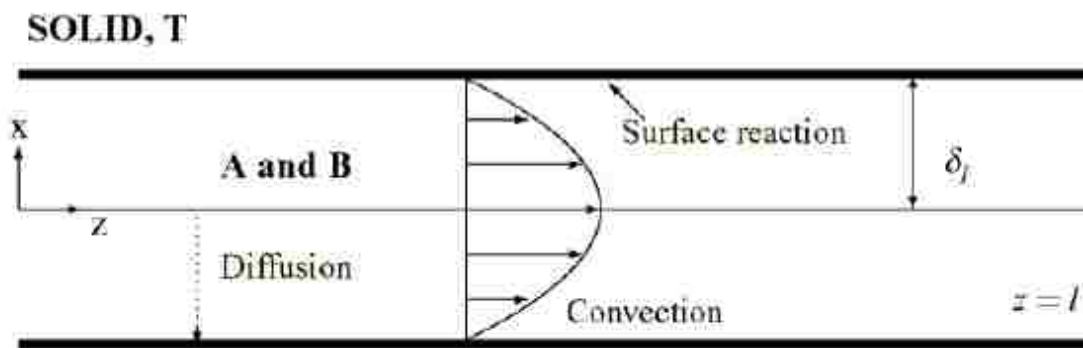


Figure 2.6: Schematic of precipitation/dissolution reaction in a finite length single fracture.

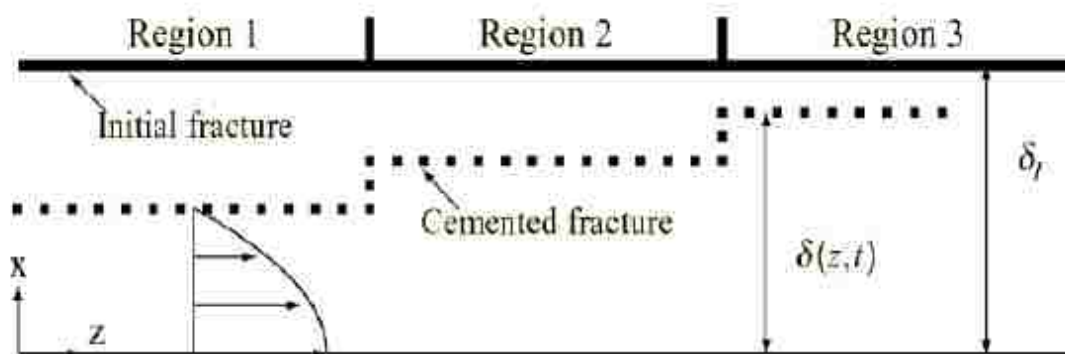


Figure 2.7: fracture shape with precipitation of cemented minerals leading to aperture loss.

One of the most important mechanisms of diagenetic processes is chemical reaction between minerals and migrating fluids. The hydraulic isolation of a porous medium by a caprock layer provides an environment amenable to several uses of the underlying porous formation. When the porous medium is under artesian pressure, it serves as a ready source of water supply. With sessile groundwater conditions, such porous formations are looked upon favorably for deep geologic disposal of contaminants and other forms of hazardous waste in liquid form. Hydrodynamic and stratigraphic trapping represents the primary phase of containment of the fluidized CO<sub>2</sub> and it is assumed that this will ensure longevity of the retention of CO<sub>2</sub> in the storage formation. This environment would enable the initiation of other time-dependent trapping mechanisms, including solution, mineral and residual phase trapping that can occur at time scales varying from the time of injection to a million years.

It can be assumed that the caprock fracture is stationary and that its dimensions are uninfluenced by the pressures of injected fluids. This is hardly the case in many oil and gas operations that are related. Fractures are nearly ubiquitous in rocks that have experienced even slight deformation and most of these are mineral filled [175]. Their presence indicates that: (1) dilation of the rock took place for fractures to be both open and provide pathways for fluid flow and (2) fluid was present and perhaps moving during and after the deformation event, and it carried sufficient mass of fracture constituents in solution to precipitate in the observed fracture void space [176, 177]. Pressure solution and compaction mechanism as a result of enormous formation stress is a driver for the diagenetic loss of fracture conductivity and adjoining formation permeability [59, 178, 179]. Pressure solution and compaction of quartz materials have been extensively studied and models have been developed that relate the rate of

porosity loss to the applied stress, temperature, and formation grain size in hydraulically fractured tight rocks (see figures 2.6, 2.7 and 2.9). These are for long term subsurface predictions.

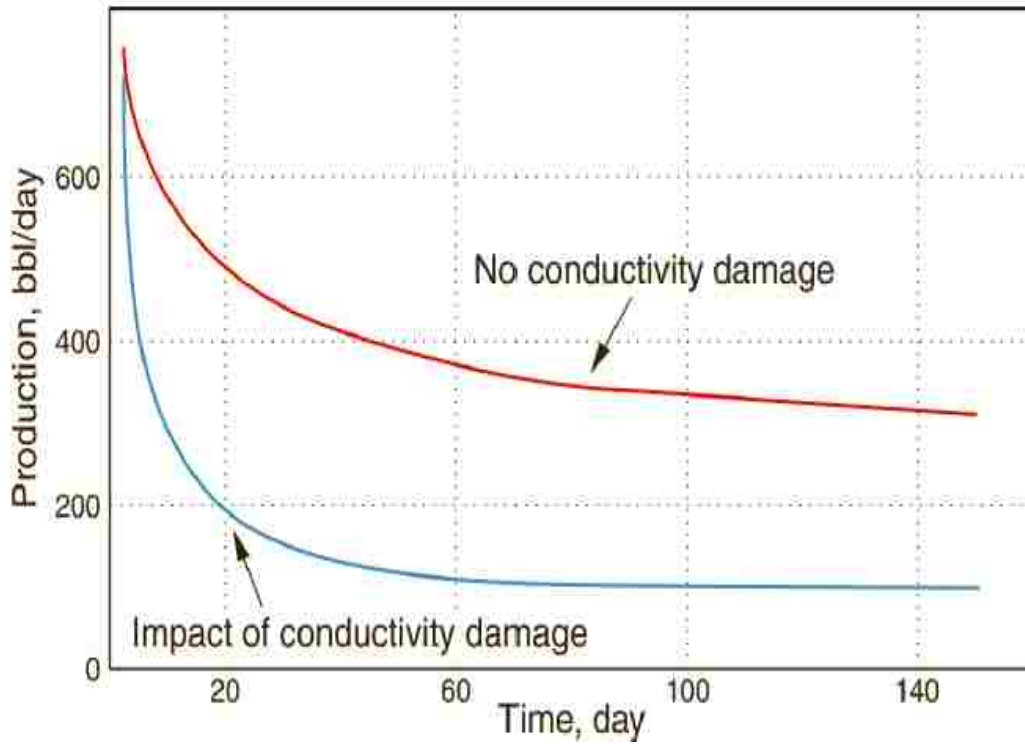


Figure 2.8: fracture production (of light oil) simulation illustrating the impact of conductivity on long-term production. Only the impact of a pressure-solution model was used as the damage mechanism under constant and elevated temperature [59].

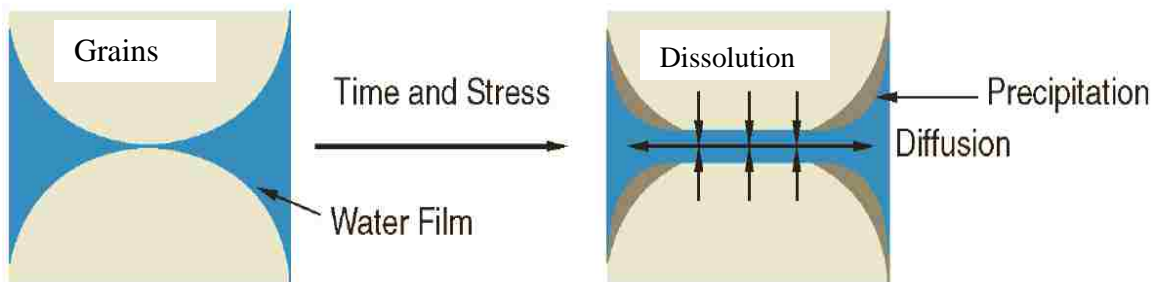


Figure 2.9: illustration of the pressure solution and compaction mechanism. High stress at the contact points increases the solubility of silica, which diffuses into the pore spaces and precipitates [59].

A crystal growing in a pore will stop growing when the stress on the crystal surface approaches the maximum crystallization pressure [137]. However, if the stress is sufficient to open a fracture, the stress on the crystal surface will decrease, thus enabling further growth. When strain rates are slow, as can be the case during precipitation in pores and cracks, fracture propagation takes place through a kinetic process known as subcritical crack growth [167, 180]. Previous works have demonstrated how to couple the rates of crystal growth and fracture propagation when a crystal grows from a supersaturated solution inside the aperture of a fracture [181]. As long as there is an unlimited supply of supersaturated solution, fracture propagation causes the stress on the crystal surface to decrease and the rate of fracture propagation will accelerate until complete failure takes place [182]. Few researchers have developed precipitation/dissolution models for the flow in finite parallel plates that represent single fractures [183]. The idea behind such models is to approximate the description of a variable fracture aperture, surface reaction, and diffusion by a set of parameters and simple rules governing the alteration of fractures [184, 185]. Fracture aperture can either grow or shrink as chemical reaction proceeds at the fracture surface. This sometimes involves mass conservation equations for the components of aqueous and solid phases simultaneously and shows the fracture aperture size distribution with time. Calcite cementation is a form of precipitation that can be modelled and incorporated. It has been shown that to replicate the lower permeability that typify tight gas shale requires the superimposition of systematic cement filling that preferentially plugs fracture tips and other narrower parts of the fracture pattern [15, 146, 186]. Additional challenge for natural fracture characterization is quantifying the effective permeability of fracture networks. A benefit of the mechanics-based analysis is that fracture aperture is an intrinsic part of the solution; a result of boundary

conditions imposed, propagation criteria, and the mechanical interaction between neighboring fractures. Four different fracture patterns in sedimentary rocks could be identified; polygonal pattern, cross-fractured pattern, and single set of nominally parallel fractures [187-189].

In subsurface fractures, crack-seal textures and other evidence suggest that cement may be deposited simultaneously with fracture opening and propagation, partially filling and propping the large aperture [173]. The highly heterogeneous quartz cement thicknesses found in partially cemented fractures in mudrocks are a function of the processes that control quartz/clay crystal growth rates. The mineral components in mudstones and shales respond to CO<sub>2</sub> in several ways. It has been reported that the interaction of water and CO<sub>2</sub> causes montmorillonites to expand, thereby increasing solid volume and leading to self-sealing of caprock fractures, which is reducing the caprock permeability. Quartz or opal crystals show substantial anisotropies in growth rate depending on the nucleation substrate [124, 190]. The fastest rates of growth occur on irregular surfaces that are perpendicular to the crystallographic axis. Geochemical precipitate growth rate is a strong function of temperature, which can be expressed using the exponential Arrhenius expression (equation 2.16);

$$q = Ae^{-\frac{Ea_{nc}}{RT}} \dots \dots \dots Eq. 2.16$$

where q is the rate of geochemical precipitation per unit area (mol/cm<sup>2</sup>s), A is a constant (mol/cm<sup>2</sup>s), E<sub>a<sub>nc</sub></sub> is the activation energy for geochemical precipitation on irregular surfaces (J/mol), R is the real gas constant (8.314 J/mol<sup>°</sup>K), and T is the temperature (K).

The result developed for the flow rate through a single fracture located in the caprock can also be used to examine the leakage through multiple vertically-aligned fractures. The global

permeability or hydraulic flow constant of diagenetic fractured grid blocks was computed as given by equations 2.17 and 2.18; where  $k_m$  is the matrix permeability and  $k_f$  is the intrinsic fracture permeability.  $\Delta c$  is the grid-block dimension and  $d$  is the fracture aperture.

$$k_{fracd} = \frac{k_f \times d + k_m \times (\Delta c - d)}{\Delta c} \dots \dots \dots Eq. 2.17$$

$$k_f = \frac{d^2}{12} \dots \dots \dots Eq. 2.18$$

the competition between diagenetic (quartz) precipitation rate and fracture opening rate determines whether a fracture is completely filled with cement (no porosity), partially filled with occasional aperture spanning bridges that prop it open, or mostly open with only a thin coating of geochemical materials [191, 192]. Emergent threshold was described in many quartz-rich mudrocks such that a kinematic aperture exists below which fractures are completely filled with cement and occluded and above which they are only partially cemented and bridged or completely open[193, 194]. The emergent threshold can be estimated by picking the slowest precipitation rate which is indicative of the formation temperature during fracturing. Figure 2.10 shows the relationship among global permeability, emergent threshold and fracture porosity. Significant changes in fracture pattern geometry and flow properties caused by minor changes in deformational or diagenetic boundary conditions highlight the challenges of accurate characterization of natural fractures caused by small strain events [51, 55, 195-197]. Only few examples of coupled chemical transport-mechanical modelling studies are available, and most of them focus on short timescales. This work by Noh and Lake are very useful in conceptual model developments of rock-fluid-fracture interactions.

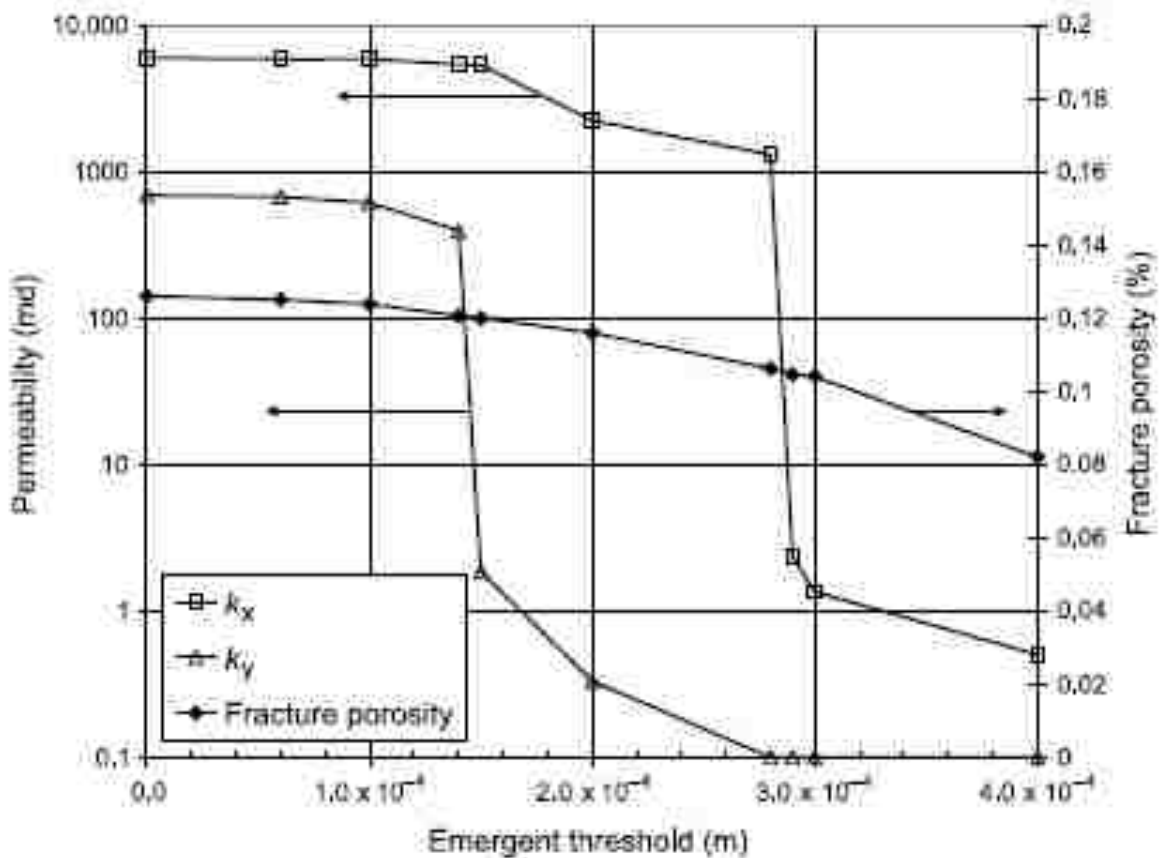


Figure 2.10: Modification of calculated steady-state effective permeability (left axis) for a generic fracture pattern showing reduction in effective permeabilities,  $k_x$  and  $k_y$ , caused by diagenetic cementation represented by the increasing emergent threshold. Fracture porosity is plotted on the right axis [173].

### 2.4.3 Mechanisms of Natural CO<sub>2</sub> Migration

There are three processes that can lead to the vertical migration of CO<sub>2</sub> from a reservoir through the caprock: *migration through unfractured caprock by capillary flow*, *migration by fracturing the caprock*, and *migration through faults*. Migration of CO<sub>2</sub> through mudrocks or shales will occur when the pressure in the reservoir exceeds that of the capillary entry pressure of fractures or pores in the seal. The small pore sizes of low permeability rocks require thousands of units of

capillary entry pressures to occur. The density and phase conditions of CO<sub>2</sub> are dependent on pressure and temperature, which is a direct function of the depth of the reservoir [143]. The density contrast between CO<sub>2</sub> and brine in the reservoir decreases with increasing depth, and hence differential buoyancy pressure on the caprock also decreases with increasing depth. For this reason shallow reservoirs (<1000 m depth) are inherently more likely to leak CO<sub>2</sub> through an unfractured caprock. Yet, there are no indications that leakage through the caprock by capillary flow is a leaking mechanism in the studied shallow reservoirs [2, 198]. For leaking CO<sub>2</sub> reservoirs in Italy, it was shown that the observed surface CO<sub>2</sub> seep rates greatly exceed the physical possibility of leakage by capillary flow through intact mudrock from the area above the site. Thus CO<sub>2</sub> migration must be via fractures not matrix flow. It has also been shown that even after an estimated 70 Ma, CO<sub>2</sub> only infiltrated 12 m of sealing mudrocks directly over a CO<sub>2</sub> rich oil field in the UK North Sea. Hence, the time-scales required for CO<sub>2</sub> migration through unfractured caprocks are orders of magnitudes longer than those necessary for CO<sub>2</sub> storage to effectively mitigate climate change [199].

As burial depth increases, it becomes more likely that fluid pressures will be over pressured, that is, pore pressures deviate from hydrostatic (or “normal”) pressures towards lithostatic pressures. If pore pressure in the reservoir exceeds both the pore pressure in the caprock and the tensile strength of the caprock (including any differences in confining stress due to different elastic properties), hydraulic fracturing and/or frictional failure along optimally oriented pre-existing fractures of the caprock occurs [30, 74, 79]. Both mechanisms can lead to migration of CO<sub>2</sub> from the reservoir through the caprock by fracture flow. This effect was induced at the CO<sub>2</sub> injection test site at in Salah. Fracturing to form dilatant joints (mode 1 fractures) induced by elevated fluid

pressure only occurs when the pressure exceeds the least principal stress of the caprock (this direction of least principal stress is typically horizontal until depths exceed 1.5–2 km) [200-202]. The pore pressure required to cause such failure is much less than the pore pressure required to overcome the capillary entry pressure of a mudstone caprock and so caprocks will transmit CO<sub>2</sub> more readily by fracture flow than by capillary flow [203, 204]. Most sedimentary rocks are fractured during burial and the fracture density depends on the geomechanical properties and thickness of the rock and thus different rock layers fracture differently in response to the same stress. Fracture density increases in the vicinity of faults and fractures provide permeability only when open or connected [205]. There is no clear evidence for leakage through dilatant joints in hydraulically fractured caprock in the examined sites [206, 207].

Strong evidence for CO<sub>2</sub> migration through fault induced fractures exists at several insecure reservoirs. CO<sub>2</sub> seeps are frequently located close to active or extinct faults, which may exist prior to CO<sub>2</sub> migration [134]. Thus fractures and flow through fractures as part of a fault zone play a significant role in permitting CO<sub>2</sub> migration. This indicates that pre-existing faults are important pathways for CO<sub>2</sub> migration, possibly due to increased fracture permeability in the fault damage zone [139, 208].

The subsurface is not a random collection of materials. Geological processes have led to structured deposits with distinct material characteristics and geometrical relationships. Processes have formed the geomechanical facies as a conceptual building block for the subsurface [143]. A geomechanical facies has specific material characteristics defined by the geology of the rocks and defined by the engineering use to which it will be put [2, 134]. Using the

geomechanical facies framework, the factors crucial to assessing the CO<sub>2</sub> storage security of a storage basin such as basin architecture, caprock architecture, reservoir quality, stress state, mechanical characteristics, fractures, burial depth, geo-thermal gradient, risk of orogenic modification, structural stability and preservation potential can all be taken into account [209, 210]. By examining the typical characteristics of the geomechanical facies within the different tectonic settings, it is possible to compare and contrast the different tectonic settings to appraise global CO<sub>2</sub> storage opportunities and predict which tectonic settings will be most suitable for CO<sub>2</sub> storage [211, 212].

It is important to note that the geomechanical facies approach for CO<sub>2</sub> site selection is the first step in what is a complex and iterative site specific assessment procedure, where uncertainty decreases as the data requirement increases. However this first appraisal step is a crucial stage in the identification and assessment of suitable CO<sub>2</sub> storage sites and underpins the later screening and ranking procedure of sedimentary basins for geological CO<sub>2</sub> storage [213, 214].

## **2.5. Previous Experimental and Modeling Works**

### **2.5.1 Similar Experimental Setups for CO<sub>2</sub> Sequestration and Containment**

Previous experimental investigations as reported in reported in unpublished thesis about a decade ago [75], examined the deformation of limestone and sandstone caused by injection of high and low P<sub>CO<sub>2</sub></sub> aqueous fluids. The experiments were performed in a triaxial cell where a vertical stress of 16 MPa was imposed by a piston directly in contact with the sample. The horizontal confining pressure was 10.2 MPa, the temperature 40°C and the salinity of the brine

0.01 M NaCl. The fluids were injected in the bottom of the sample at constant flux (0.005 ml/min) using a high pressure liquid chromatography pump. The high pressure CO<sub>2</sub>/brine mixture (8 MPa) was prepared in an autoclave. After filling the autoclave with CO<sub>2</sub> ice, they injected saline solution ([NaCl] =5.8 g/l) until the desired pressure was obtained. The mixing of CO<sub>2</sub> and water was considered satisfactory after one week as the heavier water was injected at the top and the autoclave was equipped with an impeller. Furthermore, the exchange kinetics over the interface have previously been demonstrated to rapidly equilibrate supercritical CO<sub>2</sub> and water [75].

The experimental setup used previously display some features similar to the setup used in this study. Their reacting material was placed in a 100 cm high column inside a large heated pressure vessel, with the confining pressure controlled by a syringe pump. CO<sub>2</sub> and brine were equilibrated at 70°C and 10 MPa using a second syringe pump which was also connected to the top of the column. Fluid flow was controlled by a third syringe pump connected to the bottom of the column. A 30 cm<sup>3</sup> titanium floating piston pressure sampler inserted between the outlet of the pressure vessel and the syringe pump applying the back-pressure, allowed fluid samples to be taken. Analytically the solids were examined using SEM and gas sorption on clean surfaces to determine the surface areas. In addition to pH measurements, the fluid samples were analyzed for both major and trace cations using inductively coupled plasma-optical emission spectroscopy (ICP-OES) and for anions using ion chromatography [75].

Fluids leaving triaxial from previous experiments reported were constantly collected, and analyzed by ICP-OES every second day. As the pressure was reduced in the samples upon analysis, nitric acid was added to prevent precipitation. A Triassic Arkosic sandstone was exposed to 70

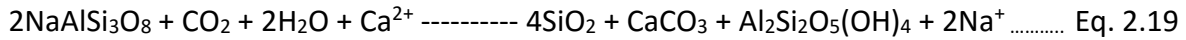
days of high  $P_{\text{CO}_2}$  (8.3 MPa) injection, followed by 50 days of no-flow. During fluid injection, the aqueous concentrations of Ca, Si and Sr decreased, while Mg increased. After the 50 days without flow, a second injection period was started with an injection rate 10 times the original one. This rate was later lowered to 2 times the original rate, thereby completing an increase-decrease sequence simulating uplift followed by burial. All the steady state concentrations decreased after the injection rate was increased, whereas decreasing the injection rate again led to increasing concentrations in a step-like manner. The overall higher concentrations of Mg and Ca compared to Si were attributed to a well-known decrease in reactivity from dolomite and calcite to quartz [65].

Furthermore, injected  $\text{CO}_2$  at 200°C and 20 MPa into an aquifer-aquitard system composed of Arkosic sandstone and shale, respectively. The injection period lasted for 80 days, and the purpose was to examine fluid-rock interactions with focus on carbonate mineral precipitation [43, 149]. This was done by investigating reaction textures on aquifer and aquitard minerals, carbonate minerals precipitated and changes in brine chemistry. In addition to precipitated magnesite, amalcine mica and clay minerals, their results showed textures on silicate minerals which indicated significant reactions. The arkosic sandstone serving as the aquifer was composed of equal amounts of quartz, oligoclase and microcline. On the edges of pits and open fractures of the quartz grains, abundant clay minerals were observed using SEM. Smectites not present on the initial oligoclase were present in abundance on the surfaces and cleavages of the  $\text{CO}_2$  exposed oligoclase grains. While it was observed that there were differential etching on the microcline surfaces, the same phenomenon was not observed for the oligoclase. For the shale (mostly composed of quartz and clay minerals), they saw clay coatings draping across surfaces and small

cavities. Halite crystals had accumulated on the shale surfaces, something which may have resulted from brine trapping during quenching. The levels of major ions in the brine stabilized within the first 670 hours after start of injection. Whereas the Na- and B-concentrations stayed close to the initial concentrations, K-, Mg- and Cl-levels decreased by 15-20%. Ca increased by approximately 30%, while Si increased from zero to a level just below what was calculated based on quartz solubility. The concentrations of Sulphate and Iron did not stabilize and continued to change throughout the duration of the experiment [75].

Previous works examined the cap rock effects of CO<sub>2</sub> injection at Sleipner by reactive transport modeling of dissolved CO<sub>2</sub> in the cap rock [38]. As it is considered unlikely that capillary leakage will occur through the Nordland Group shales overlying the Utsira sand at Sleipner, only reaction kinetics and diffusive transport was included in the model [37, 215]. The Oseberg formation water was equilibrated with the cap rock mineralogy by geochemical modeling as a starting point. Under 37°C and approximately 10 MPa, two types of batch models were done; one assuming instantaneous thermodynamic equilibrium and one incorporating the kinetics over 15,000 years [6]. There are multiple complex reactions that are taking place during rock-fluid interactions and only very few have been extensively described. In the experiments carried out by the authors of the previously described procedure, it was shown that the latter far-from equilibrium geo-reactions showed a fairly fast dissolution of calcite after the initial pH drop from 7.7 to 3.0. In the thermodynamic batch model an unrealistically high reactivity was revealed by a significant reduction in pure H<sub>2</sub>O levels. Overall smectites and illite dissolved, while chalcedony, kaolinite and large amounts of carbonates (magnesite, dolomite, dawsonite and siderite) precipitated. Relatively small amounts of calcite were needed to stabilize the pH at 4.5. In the long run,

kaolinite and calcite formed from the dissolution of albite combined with  $\text{Ca}^{2+}$  ions from the initial dissolution of carbonates according to equation 2.19;



As the  $\text{Ca}^{2+}$  concentration decreased with time, the model predicted a shift from calcite to dawsonite formation. However, the total amounts of carbonate minerals formed over the 15,000 years were minor, and the porosity of the cap rock remained virtually unaffected by the dissolution/precipitation reactions. Replacing albite with the more reactive anorthite retarded the  $\text{CO}_2$  migration as the  $\text{CO}_2$  rapidly reacted with the anorthite in the lower part of the cap rock [216].

The main lesson learned from the diffusive transport model was that the process is very slow particularly in tight caprocks, even when the effective diffusion coefficients were in the high end of their calculated range [75].

### **2.5.2 Geomechanical Experiments**

The axial displacement sensors in previous rock-fluid interaction experiments indicated that the compaction response of the sandstone after injection start, was very rapid. After 1 day the deformation rate was already at the limit of what could be measured. The rapid compaction was believed to be caused by a sudden increase in pore fluid pressure. This pressure increase initiated grain-grain rearrangement and grain-grain sliding, which led to the compaction. A porosity increase in the sandstone of 1.7 % was estimated based on the amount of carbonates such as dolomite and calcite cement dissolved in aqueous medium [75].

Capillary breakthrough pressure tests for supercritical CO<sub>2</sub> have been performed with somewhat different approaches. Researchers experimentally investigated the breakthrough pressure of supercritical CO<sub>2</sub> for Midale evaporites (Weyburn cap rock) [40, 215]. These rocks have very low porosity and permeability. Using a constant backpressure of 7.3 MPa and the in-situ temperature of 59°C, they increased the injection pressure in steps of 0.5 – 1.0 MPa. For samples with porosities ranging from 0.3-0.7 %, they got breakthrough at differential pressures from 11.2-5.0 MPa. It was determined that capillary entry and breakthrough pressure of the Nordland shale cap rock under reservoir conditions can be estimated. With a confining pressure of 15.3 MPa, they started with equal pore pressure in the top and bottom of their samples (10.3 MPa). Next, the downstream pressure was decreased in steps of approximately 0.3 MPa until upstream CO<sub>2</sub> moved into the sample. This occurred after the downstream pressure had been reduced to 8.6 MPa, resulting in a breakthrough pressure of 1.7 MPa.

The laboratory tests on  $V_p$  and  $V_s$  performed two decades ago were motivated by the discrepancies between theoretically derived and observed seismic velocities after CO<sub>2</sub> injection at the McElroy field, Texas. The higher velocities observed compared to the ones predicted using the special theory of Gassmann, were attributed to a more significant pore pressure increase following the CO<sub>2</sub> injection than what was initially assumed. Therefore, they flooded eight dolostone cores with CO<sub>2</sub> under higher pressure and temperature conditions and examined the velocities as functions of CO<sub>2</sub> saturation and pore pressure. Their experimental data suggested 3.0 – 10.9 % decrease in  $V_p$  and 3.3 – 9.5 % decrease in  $V_s$ . The results obtained from the two decades experiments indicated that while  $V_p$  is sensitive to changes in both CO<sub>2</sub> saturation and pore pressure,  $V_s$  is only sensitive to pore pressure changes. Based on this, they suggested that

S-wave velocities can be used to separate the effect of pore pressure increase from the combined effect of pore pressure build up and increasing CO<sub>2</sub> saturation. This can possibly be used to separate between reservoir zones with CO<sub>2</sub> and high pressure zones without CO<sub>2</sub> [75].

## CHAPTER 3

### EXPERIMENTAL SETUP AND PROCEDURE

#### 3.1 Experimental Methods and Sample Preparation

The approach to investigating the problem of the effects of diagenetic alterations in fracture conductivity entails experimental and simulation design using artificially prepared composite rocks with capillary tubing embedded to mimic fractures. The experimental and simulation methods are described below in details. The experimental design entails flooding crushed samples of four different shaly rocks with CO<sub>2</sub>-brine fluid and/or hydraulic fracturing fluid. Temperature and pressure will be elevated throughout the system with adequate regulation of flow rate at sub-unity level. The dissolved/precipitated minerals from this flooding process are transported through the artificial composite rocks with real time monitoring of pressure drop overtime across the composite core using the Core Flooding System (CFS 200) data acquisition unit with advanced differential pressure transducers for real time analysis of responses. Detailed effluent and crushed rock analysis will be carried out using various analytical techniques and tools as indicated below. The proposed composite core will be made of kaolinite, cement and non-corrosive PEEK polymer microtubings. Figures 3.1 to 3.4 show the schematics of the experimental setup and the composite core respectively.

The equipment used in the flow-through experiments part of this research work are unique due to highly scientific and precision driven instrumentation that were included. The overall experimental work applied specific analytical techniques in investigating changes in surface/near-surface properties of the shale rock after exposure (by flooding) to CO<sub>2</sub>-brine,

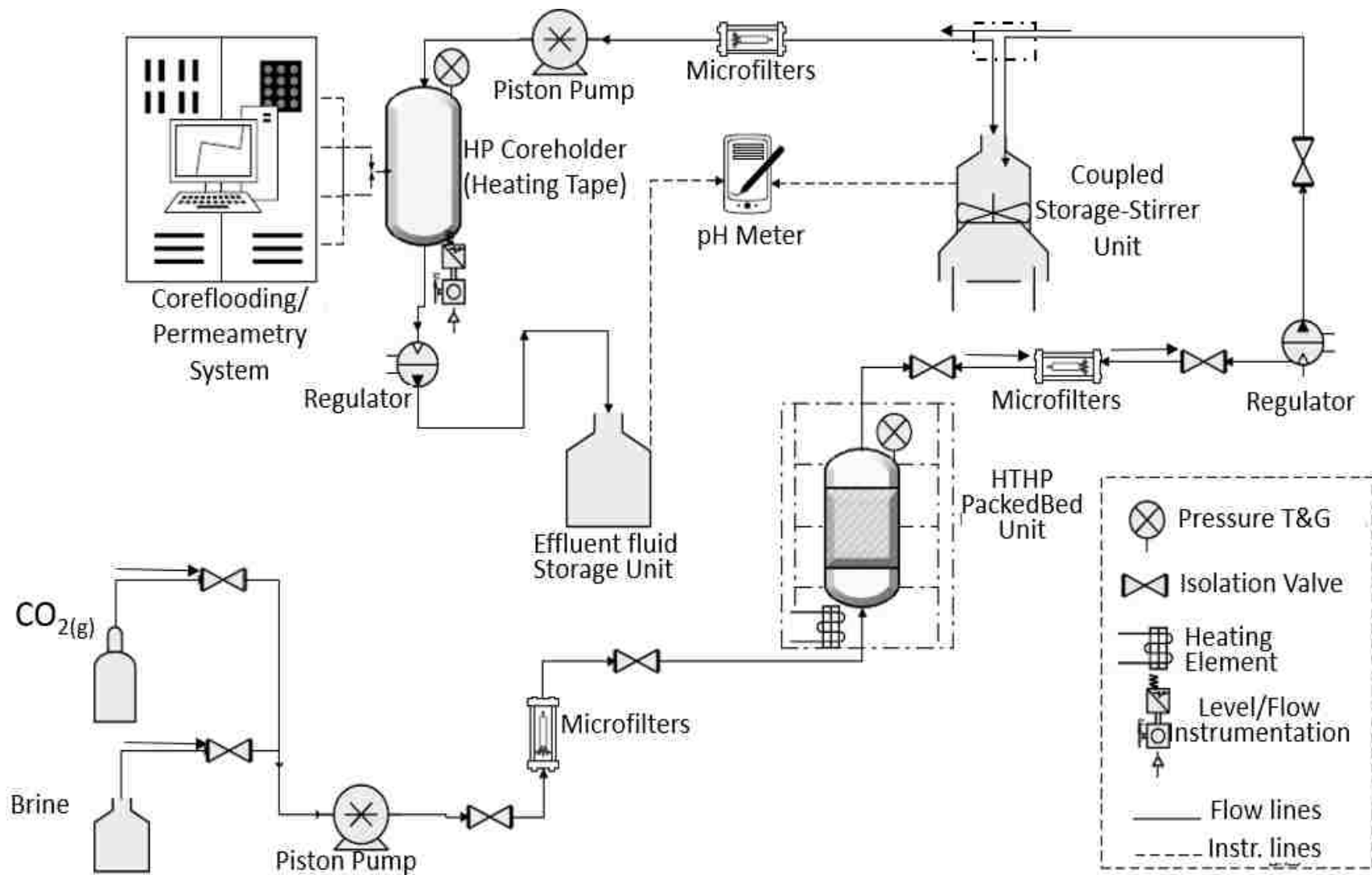


Figure 3.1: Detailed process flow diagram of the experimental setup showing critical devices and equipment for CO<sub>2</sub>-brine flooding and composite core conductivity measurement.

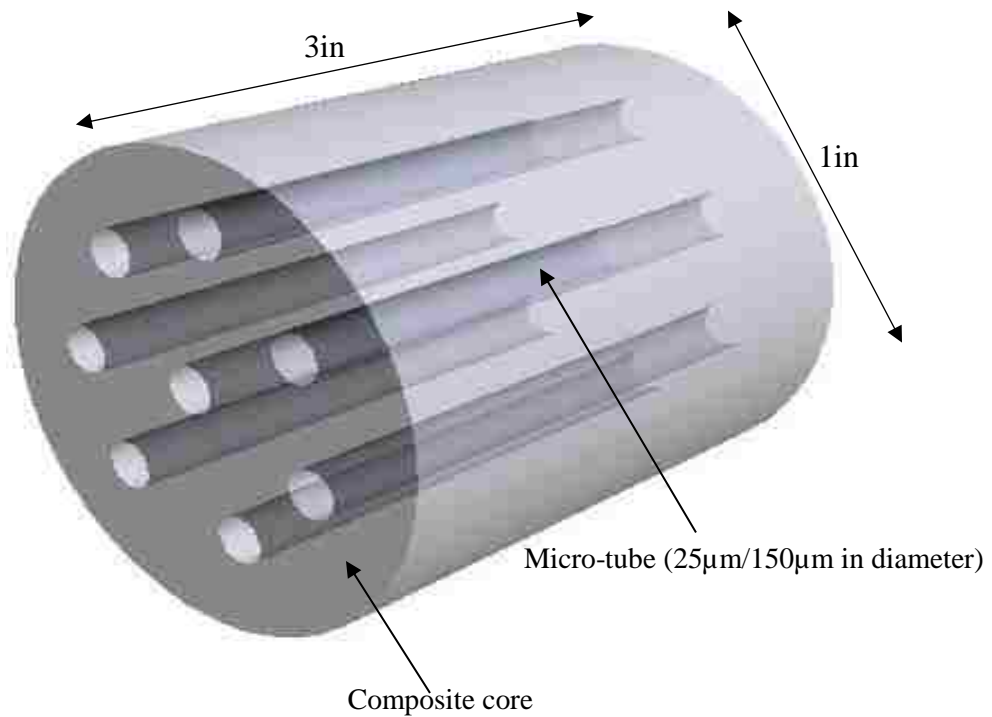


Figure 3.2: Visual design of composite core made of kaolinite, cement and micro-tubes (magnified) using SolidWorks©.



Figure 3.3: Visual sample design of composite core made of kaolinite, cement and polymer PEEK micro-tubes which are not evenly distributed as envisage through SolidWorks©.



Figure 3.4: Multiple samples of composite core made of kaolinite, cement and polymer PEEK micro-tubes to mimic fractures.

for a time frame of 5 days per run. The shale rock was comminuted (crushed) to predetermined dimensions that are suitable for use in analytical instrument. See figures in appendix A. Particle sizes in the packed-beds were of the order of 1mm - 2mm in dimension. A single flow cell was used with designs similar to a packed-bed. This exposed as much surface area of the crushed shale as possible to CO<sub>2</sub>-brine. Each experimental run holds an average of 350g of shale caprock samples with different mineralogy which are dependent on basins and formations type. Multiple representative samples were analyzed and compared to corresponding control samples. All instrument and process devices are of stainless steel and PEEK (Polyether Ether Ketone) material. This ensured that metallic corrosion processes do not interfere with critical measurements during the experiment. PEEK and stainless steel materials are generally resistant to CO<sub>2</sub>-brine induced corrosion. Ceramic/stainless steel micro-filters (50µm limit) and circularly-cut filter papers (5µm limit) were used to prevent fines migration within tubings and packed-bed respectively.

### **3.2 Experimental Setup**

The experimental set-up consisted of a core flooding unit (CFS-200), an automated Oven, a heating tape, a stainless steel pressure cell, a syringe pump (and a piston pump for backup), a back pressure regulator (BPR), accumulators (glass beaker), multiple transducers, three pressure gauges, PEEK and stainless steel tubings, National Instruments data acquisition device, two ceramic filter to prevent fines carry over (larger than 50  $\mu\text{m}$ ) and a computer system. PEEK polymers were used because it has high resistance to corrosion as a result of low pH or high temperature and pressure conditions. Schematics of the CO<sub>2</sub>-brine flooding of shale caprock and composite fractured core injection are shown in Figures 3.1 and 3.2. The packed-bed was mounted vertically in the oven for temperature control with aqueous CO<sub>2</sub> flowing from the top to the bottom of the experimental fixture. This is to prevent particulate fluidization were it to be the other way round i.e. bottom to top. Also the effect of gravity is assumed to be negligible. A schematic of the experimental setup is shown in figure 3.3. Figure A.1 in Appendix A has pictures of the physical components of the experimental setup among other equipment and consumable.

### **3.3 Experimental Shale Rocks Geology**

The approach used in the design of experiments required multiple shale rock samples to be used such that geographical and mineralogical variations are factored into the experimental matrix configuration. Table 3.1 below shows the geological properties of the shale samples that were used in the flooding experiment. This consist of Mancos, Marcellus, Pottsville and Wilcox shales. These shales are found in different geographic regions of the United States with potentials for energy fluid extraction or storage of carbon dioxide.

Table 3.1. Geological properties of shale rock samples used in the experiment.

Shale Properties	Sample A (Mancos)	Sample B (Marcellus)	Sample C (Pottsville)	Sample D (Wilcox)
Age	Upper (Late) Cretaceous	Lower Devonian	Upper Pennsylvanian	Upper Cretaceous
Depth	~2,500ft	~6,500ft	>4,000ft	>10,000ft
Location	Colorado/Utah	Pennsylvania	Alabama	Louisiana
Ductility	Low	Medium	Low	High
Fractability	High	Medium	High	Low
Permeability	1 to 5nD	100-450nD	>100nD	~140nD
Porosity	~7%	~10%	1-9%	2.5 -15%
Bulk Density	2.52 - 2.58 g/cm <sup>3</sup>	2.2 - 2.6g/cm <sup>3</sup>	-----	-----
Compressive Strength	6300 to 8900psi	3000 – 8,800psi	-----	<2000psi
Lithology	calcareous silty shale	calcerous clay- rich fossiliferous mudstone	quartz rich silty shale	swelling clay rich mudstone
Poisson's Ratio	0.36 - 0.39	0.12 - 0.25	-----	-----

### 3.4 Mineralogical Composition of Shale Rock Samples

The ternary diagram in figure 3.5 shows the compositional distribution of the major minerals in the shale rock samples as determined from X-ray Diffraction (XRD) analysis. X-ray diffraction is a technique used for determining the atomic and molecular structure of a crystal, in which the crystalline atoms cause a beam of incident X-rays to diffract into many specific directions. By

measuring the angles and intensities of these diffracted beams, an XRD equipment can produce quality geochemical data. Figure 3.6 compared the composition to other CO<sub>2</sub> sequestration shale caprock sites and hydraulically fractured shale for oil and gas production as provided by Bourg [217]. Table 3.2 contains the details of the percentage composition of each mineral. The samples consist on a broad scale quartz, feldspar, pyrite, calcite, dolomite, chlorite, illite, kaolinite and montmorillonite. The relative abundance of these components in each shale rock type showed the preponderance of quartz, carbonates and clay in general terms. The compositions presented in this report have similar characteristics to data available in the literature. It affirms the fact that shale rocks are heterogeneous compactions of multiple sedimentary minerals.

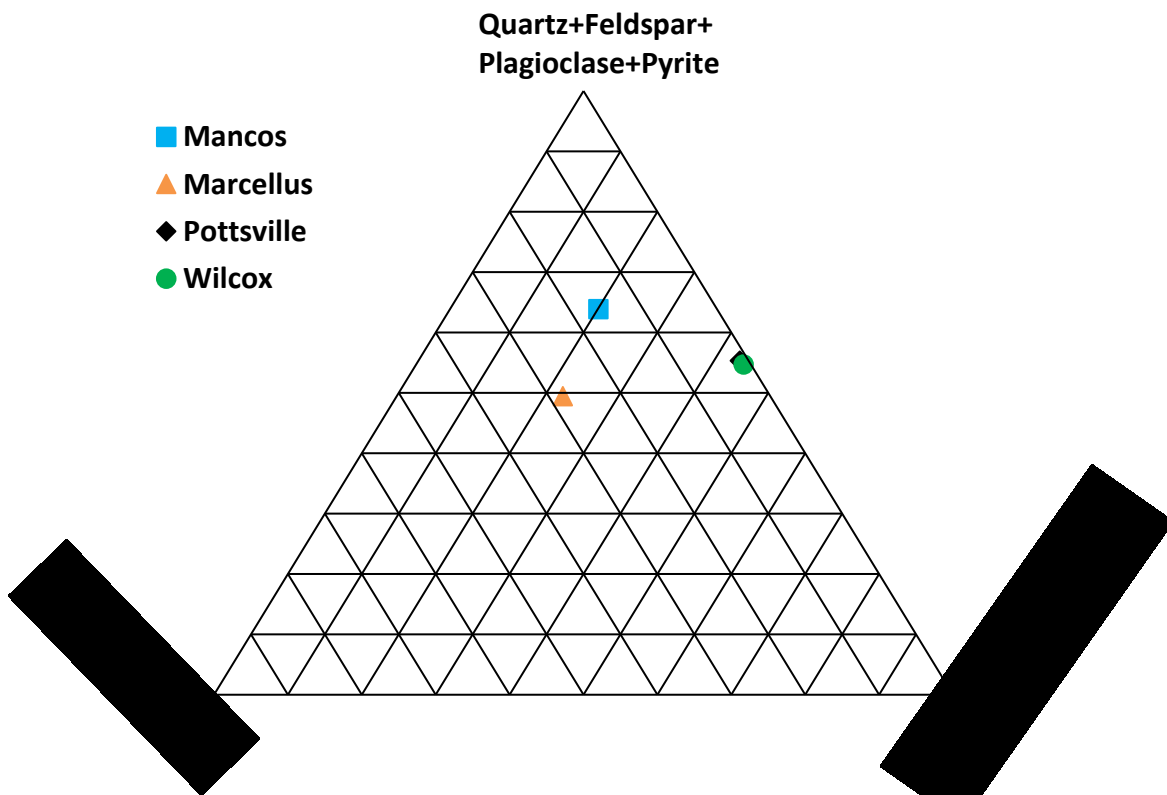


Figure 3.5: Initial mineralogical composition of four shale rock samples (from XRD Analysis) used in rock-fluid interaction experiment. The ternary diagram shows carbonates, quartz, feldspar, pyrite and clay as main components of the shale rocks used for the experiment.

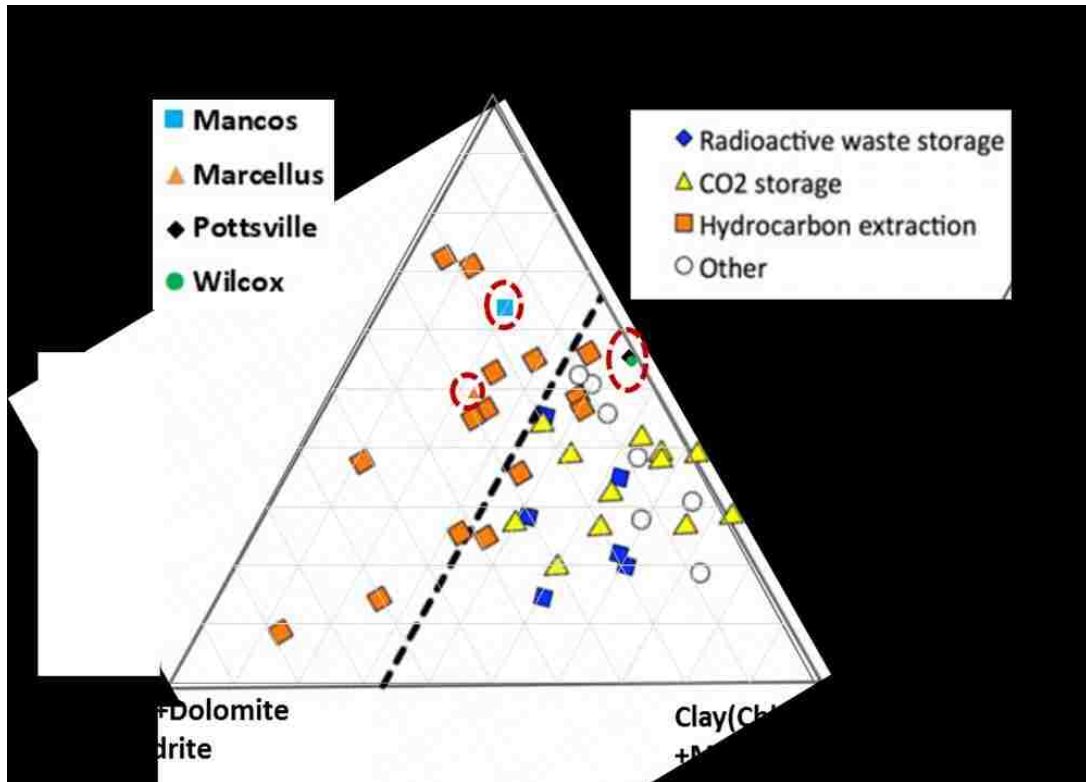


Figure 3.6: Initial mineralogical composition of four shale rock samples (from XRD Analysis) used in rock-fluid interaction experiment when compared to other shale plays [217]. The ternary diagram shows carbonates, quartz, feldspar, pyrite and clay as main components of the shale rocks used for the experiment. The samples used for experimental investigations fall between CO<sub>2</sub> storage and hydrocarbon shales [20].

Experimental results on the mineralogy of well-characterized shale and mudstone formations. The superimposed ternary diagram shows the three main types of minerals present in the studied shales: phyllosilicates (clay minerals), tectosilicates (quartz and feldspar), and other minerals (primarily carbonates). Plot of total organic carbon (TOC) content as a function of phyllosilicate content (referred to as X<sub>clay</sub>) was excluded. Colors indicate the current uses or proposed uses of each shale formation: orange, hydrocarbon extraction; yellow, CCS; blue, radioactive waste storage; white, other. The dashed line in the panel indicates rocks with X<sub>clay</sub> = 1/3.

Table 3.2: Mineralogical composition of the four shale samples in percentages as captured by the ternary diagram of figure 3.5.

Components		Mancos(%)	Marcellus(%)	Pottsville(%)	Wilcox(%)
Quartz		60.47	43.43	49.77	46.09
K-Feldspar		0.88	0.8	0	1.43
Plagioclase		1.35	1.21	5.58	3.83
Calcite		7.92	25.25	0	0
Dolomite		8.14	2.44	0	0
Anhydrite		0	0.41	1.2	1.02
Pyrite		1.18	4.01	0	3.35
Clay		20.06	22.46	43.45	44.28
	Chlorite	3.5	0	10.37	10.31
	Illite	11.46	20.61	25.15	12.69
	Kaolinite	5.1	1.85	7.93	14.24
	Montmorillonite	0	0	0	7.04

### 3.5 Experimental CO<sub>2</sub>-brine Fluid

Carbon dioxide saturated brine solution was used for all experiments. Brine was prepared with distilled water to ensure that unknown species were not present in the solution. The brine composition was designed to simulate typical shale formation brine as observed in hydraulic stimulation flowback water [218]. This brine contained Mg and CaCO<sub>3</sub> in minor amounts. The composition was then simplified to include only NaCl which contains trace amount of KCl (<0.05%). As seen in the Table 3.3, the brine solution contained ~ 2% dissolved solids. After mixing water and salts, the brine was filtered using filter paper to eliminate undissolved solid particles

that can plug the flow lines in the experimental set-up. A filter was also installed upstream of injection to reduce the risk of plugging the flow lines. An accumulator (volume ~25 liters) was used to hold the brine solution as CO<sub>2</sub> was bubbled through at 40 psi for approximately 80 mins resulting in average pH value of 3.7 over the course of the experiment. This method was selected because of ease of preparation. A digital pH meter was used to record pH measurements every morning and calibration was done with standard buffer solutions (pH= 4, 7, 10) each week. Figure A.6 in Appendix A shows the setup for CO<sub>2</sub>-brine preparation.

Table 3.3. Experimental brine composition for Shale/CO<sub>2</sub>-brine flooding experiment based on flowback fluid composition from stimulated shale. NaCl is the principal component [80, 218].

Salts	Amount added to 1 L of De-ionized Water
Sodium Chloride (NaCl)	22.6g

### 3.6 Techniques in Rock and Fluid Analyses

Prior to and after the experiments, various material characterization techniques were employed to assess the internal and external mineralogical and petrophysical alterations of the shale caprock. The following discusses the specific analytical tools used for fluid and shale caprock analysis. The analytical techniques that were used include:

- 1) **XRD Analysis:** X-Ray Diffraction (XRD) was used in the mineralogical analysis of the shale caprock- the inorganic mineral composition. XRD is a bulk analysis technique, used to determine the mineralogical content of a core sample, in which the section of interest is powdered and placed inside the X-Ray diffractometer. X-rays are emitted and rotated from 2 to 70 degrees at a step of 0.02 degree increments with Cu K $\alpha$ 1 (copper) radiation.

The X-ray source sends the signal and receives a response. Each mineral has a characteristic response. Computer software determines the type of mineral and outputs peak versus intensity plots for the minerals present in the core sample. Since XRD can only determine crystalline substances, amorphous materials present cannot be identified by XRD. XRD analyses were conducted on the control sample and the CO<sub>2</sub>-brine contacted samples at the LSU's Shared Instrumentation Facility (SIF) using a Siemens Kristalloflex D5000 X-Ray Diffractometer. This technique was used in the mineralogical analysis of the shale caprock- inorganic mineral composition.

- 2) **SEM-FIB Imaging with EMPA:** Scanning Electron Microscopy with Focused Ion Beam (SEM-FIB) is a technique that was used to examine physical changes on the surface of the shale particles providing useful information at high magnification and resolution. Portions of CO<sub>2</sub>-brine contacted and uncontacted crushed shale caprock samples were imaged using SEM for microstructural characterization. SEM was deployed to further investigate the nature of altered surfaces at a much finer scale and under low vacuum conditions in order to obtain clearer images during the analysis. Micro-porous spaces can be identified from the captured images. The SEM images were obtained using an EDAX model electron microscope at the Center for Material Characterization, in the LSU Mechanical Engineering Department. Light microscopy images were obtained using a Leica microscope at the LSU Sustainable Energy and Environmental Laboratory. These techniques were used to examine physical changes on the surface of the shale particles providing useful information on structural morphology at high magnification and resolution. Thin sections slides are the appropriate samples to use.

- 3) **Micro-indentation:** This was a complimentary analysis that can provide useful information on chemo-geomechanical changes in the flooded shaly rocks. The material hardness characterization technique was used to analyze polished customized samples. The micro-hardness test uses an established method where a diamond indenter tip with a known geometry is driven into a specific site of the sample by applying an increasing normal load. Nanovea® MicroHardness Tester, which was used, is based on the standards for instrumented indentation, ASTM E2546 and ISO 14577. The indenter tip with a known geometry (Vickers' Diamond) is driven into the shale sample to be tested, by applying an increasing normal load. When reaching a pre-set maximum value, the normal load is reduced until partial or complete unloading of the sample occurs. For each loading/unloading cycle, the applied load value is plotted with respect to the corresponding position of the indenter. Six-spot indentation was done in a form of a 3-line profile, on every sample ranging from outer pipe position to the inner region of the shale specimen, covering its entire cross-section (more than 20 indentation points in total). The following set of conditions was used in all the indentation experiments: the maximum force used was 20 N; the loading and unloading rates were kept the same at 20 N/min; the pause at maximum load as 30 seconds; the contact load was 30 mN. The hardness was obtained with computation method from Oliver and Pharr [219]. The indenter type was Vickers diamond with the Poisson coefficient of 0.07.
- 4) **ICP-OES Analysis of influent/effluent:** Analysis of influent/effluent fluid included metallic mineral evaluation of the influent and the effluent which established the expected geochemical alterations in the rock with CO<sub>2</sub>-brine depletion. Inductively Coupled Plasma-

Optical Emission Spectroscopy (ICP-OES) is a method which was conducted to determine metallic cation contents in the fluid. The fundamental characteristic of this process is that each element emits energy at specific wavelengths peculiar to its atomic character. By determining which wavelengths are emitted by a sample and their intensities, the analyst can determine the elements from the given sample relative to a reference standard qualitatively and quantitatively. The samples were analyzed in the LSU's School of Plant, Environmental and Soil Sciences. During the experiments, effluent brine samples were monitored for pH and collected daily while samples were selected for ICP-OES analysis depending on pH values. Metallic mineral analysis of the influent and the effluent were used to correlate the expected geochemical alterations in the rock with CO<sub>2</sub>-brine pH change and fracture conductivity loss.

### **3.7 Experimental Parameters**

The following geochemical, geomechanical, and flow parameters were experimentally determined using crushed shaly rocks samples and composite rock respectively. The reactive fluid of interest is the CO<sub>2</sub> saturated brine.

#### **3.7.1 Geochemical Properties**

1. Cationic assay of effluent (ICP-OES)
2. pH of effluent
3. Mineralogy of flooded crushed shale rocks (XRD, EDS, EMPA, XPS)
4. Morphology of crushed shale rocks (FIB-SEM)
5. Total organic carbon content of crushed shale rock

### 3.7.2 Geomechanical/Flow Properties

1. Composite fracture conductivity (PDLP/CFS)
2. Fracture porosity of composite rock (Helium porosimeter)
3. Hardness of crushed rocks (Nano-indentation)

Initial fracture conductivity was qualitatively estimated using equations 3.1 to 3.12 as an approximation of capillary tubing bundles of fractures; tubing dimensions are assumed to be fracture properties.  $R$ = micro-tubing radius,  $n$ = number of tubings,  $\Delta p$  = differential pressure drop,  $k$ = permeability,  $\phi$  = tubing porosity. The assumption here is that the matrix contribution to flow is negligible. These equations were only used for qualitative purposes.

$$\frac{\pi R^4 \Delta p}{8 \mu L} = \frac{k(\pi R^2) \Delta p}{\mu L} \quad Eq. 3.1$$

$$k = \frac{R^2}{8} \quad Eq. 3.2$$

$$k_{total} = k_1 + k_2 = \frac{R_1^2 + R_2^2}{8} \quad Eq. 3.3$$

$$k_{total} = \sum k_n = \frac{1}{8} \sum R_n^2 \quad Eq. 3.4$$

$$k'_{eff} = \phi k_{total} = \phi \sum k_n = \frac{\phi}{8} \sum R_n^2 \quad Eq. 3.5$$

$$w_f k'_{eff} = \pi C_r k L_f \quad Eq. 3.6$$

### 3.8 Experimental Matrix

The following experimental program is used in the investigation of the impact of geochemical changes on fracture conductivity of artificially fractured composite core under axial and radial stress conditions. This will be a flow-through mode involving two-staged vessels one with packed crushed shale rocks and the other holding the artificially fractured core. These was used for two major “extreme” conditions of fracture aperture obtained by varying tubing sizes inserted in composite cores. It should be noted that the results presented in Chapter 4 are from the experimental runs under the first and second sets of laboratory temperature, pressure and flow conditions i.e. (A) and (B). The experimental matrices, pre-flow through and post-flow through analyses are outlined and summarized in tables 3.4 and 3.5 as follows:

(A) Flow through experiments involving **25µm artificially fractured cores** and four different (crushed) shale rocks at conditions of;

- 1400psi (Overburden pressure; axial and radial stress)
- 1000psi flow through/injection pressure
- 50°C operating temperature

Table 3.4: Experimental Matrix for CO<sub>2</sub>-brine/shale interaction at conditions of 50°C temperature and 1000 psi pressure stated in (A) above.

	Run 1 (days)	Run 2 (days)	Run 3 (days)
<b>Sample A (Mancos)</b>	5	5	5
<b>Sample B (Marcellus)</b>	✓	✓	✓
<b>Sample C (Pottsville)</b>	✓	✓	✓
<b>Sample D (Wilcox)</b>	✓	✓	✓

(B) Flow through experiments involving **150 $\mu$ m artificially fractured cores** and four different (crushed) shale rocks at conditions of;

- 1400psi (Overburden pressure; axial and radial stress)
- 1000psi flow through/injection pressure
- 50°C operating temperature

Table 3.5: Experimental Matrix for CO<sub>2</sub>-brine/shale interaction at conditions of 50°C temperature and 1000 psi pressure stated in (B) above.

Samples	Run 1 (days)	Run 2 (days)	Run 3 (days)
Sample A (Mancos)	5	5	5
Sample B(Marcellus)	✓	✓	✓
Sample C (Pottsville)	✓	✓	✓
Sample D (Wilcox)	✓	✓	✓

### 3.8.1 Geochemical Analysis

- i. Pre- and Post-flow through experiment (crushed rocks)
  - a. X-Ray Diffraction (XRD) Analysis
  - b. Total Organic Carbon Content (TOC) Analysis
  - c. Scanning Electron Microscopy/Energy Dispersive Spectroscopy (SEM/EDS)
  - d. Electron Micro-Probe (EMPA) Analysis
  - e. Micro-indentation
- ii. Pre-flow through experiment (fluid)
  - a. pH
  - b. Inductively Coupled Plasma-Optical Emission Spectroscopy (ICP-OES)

### 3.8.2 Measurement of Hardness and Conductivity; Artificially fractured composite cores

This is done at 1000psi and 50°C operating conditions as outlined in table 3.6. The units of measurements are conductivity (mdft; from differential pressure drop permeability) vs time (days). Individual plots in mdft versus days for each rock formation sample was analyzed and a combined plot generated to compare responses of the two micro-tubing sizes. Dimensionless fracture conductivity was used for estimating the impact of geochemistry on flow characteristics. *Dimensionless fracture conductivity* ( $C_r$ ) is defined as fracture conductivity,  $k_{fw}$  (md-ft), divided by reservoir permeability ( $k$ ) multiplied by the fracture half-length,  $x_f$  (ft). It provides a means of optimizing the amount of conductivity in a fracture for varying permeability and fracture length. In the case of tight rocks, matrix permeability is assumed to be zero.

Each run of the flow through experiment as stated below will undergo rock and fluid analyses pre-injection and post-injection of CO<sub>2</sub>-brine. The steps involved are presented in table 3.7.

Table 3.6: Micro/Nano-indentation; Hardness and Young Modulus at different temperature and pressure conditions of the rock-fluid interactions experiment.

	No. of samples at 1000psi and 50°C (25µm cores)				No. of samples at 1000psi and 50°C (150µm cores)			
	Run 1	Run 2	Run 3	Total	Run 1	Run 2	Run 3	Total
<b>Pottsville</b>	1	1	1	3	1	1	1	3
<b>Marcellus</b>	1	1	1	3	1	1	1	3
<b>Mancos</b>	1	1	1	3	1	1	1	3
<b>Wilcox</b>	1	1	1	3	1	1	1	3

Table 3.7: Pre-injection and Post-injection analyses for each CO<sub>2</sub>-brine flooding experimental run including rock and fluid sampling procedure.

Run No.	Type of Analysis
<b>Step 1</b>	Flood crushed shale rock with CO <sub>2</sub> -brine and transport effluent to composite core under varying axial and radial stress.
<b>Step 2</b>	Take real time measurement of differential pressure drop for changes in conductivity. This will be automatically acquired during injection and transport of CO <sub>2</sub> -brine.
<b>Step 3</b>	Analyze final effluent composition (pH, ICP-OES). Analyze crushed shale rock for morphology, mineral composition, total organic carbon composition and hardness characteristics (SEM, EDS, XRD, TOC, Micro-indentation).
<b>Step 4</b>	Calculate effective fracture aperture and fracture conductivity.
<b>Step 5</b>	Use geochemical results to bound overall chemo-flow modelling in aqueous CO <sub>2</sub> -shale interaction under constant geomechanical conditions

### 3.8.3 Critical Experimental Conditions and Materials

-Artificial Cores Solids Fraction: made from cement (~97%), kaolinite (~3%) and PEEK polymer micro-tubing (resistant to chemical corrosion)

-Crushed Shale Rocks: sizes <2mm (lots of fines)

-CO<sub>2</sub>-Brine Composition: 22.6g/l (22600 ppm) of NaCl solution

-Pressure Vessels and Flowlines: high temperature and pressure rated (max. of 350°F, 4000psi)

### **3.8.4 Experimental Process Parameters for Conditions A and B as Reported in Chapter 4**

The following experimental conditions were used during the shale/CO<sub>2</sub>-brine flooding

- a. Global flow rate: 0.5ml/min
- b. Flow cell(s) back pressure: 1000psi
- c. Flow cell(s) axial and radial pressure:1400psi
- d. Operating temperature: 50°C
- e. pH of CO<sub>2</sub> – brine: 3.7 – 3.8

**The raw data of most of the experimental results presented in Chapter 4 are included in the Appendix section of this report.**

## CHAPTER 4

### RESULTS FROM SHALE ROCK/FLUID INTERACTIONS EXPERIMENTS

#### 4.1 pH Measurement

Measurements of the pH of the effluent for all the 24 experiments were taken and the averages reported in figure 4.1. The pH values for each sample type were used for the computation of the standard error (standard deviation). It can be observed from the pH profile that the alkaline buffer strength of the shale rocks through reactive interaction with the CO<sub>2</sub>-brine fluid at the experimental pressure and temperature conditions is significantly pronounced for the Mancos, Marcellus and Pottsville shale rocks while that of the Wilcox shale is markedly lower.

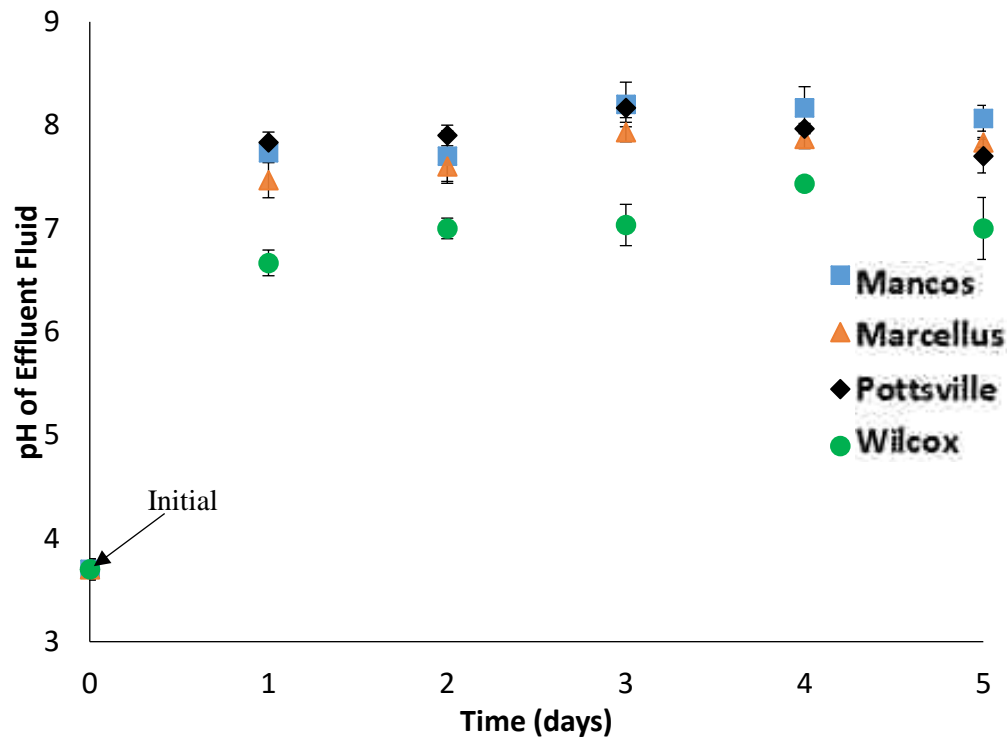


Figure 4.1: pH measurement of effluent for the four different shale rock samples used for the rock-fluid interaction experiment. It shows consistent increase in the pH values indicating significant alkalinity buffer strength of the shale rocks in the presence of acid CO<sub>2</sub> -brine fluid that was injected. This buffer strength is expected to reduce over time under dynamic condition.

The profile showed a trend pointing towards a waning of the buffer strength by the 5<sup>th</sup> day. The error bars are standard deviation values based on 3 measurements of pH values. These observations are in agreement with previous experiments conducted in the laboratory and reported by other researchers. This changes in pH is expected to control, to some degree, the ability of the various rock minerals to exchange ions with one another.

## **4.2 Inductively Coupled Plasma-Optical Emission Spectroscopy (ICP-OES) Analysis**

The inductively coupled plasma optical emission spectroscopy analysis of the effluent from moderate temperature- moderate pressure runs using the four shale rock samples are shown in figures 4.2 to 4.15. The dimensionless concentration of both the major and trace elements in the effluent solution at the end of the experiments were analyzed using the initial composition of the influent CO<sub>2</sub> saturated brine as the normalizing quantity. The elemental concentration of the influent is 1 on each of the graph. Sections 4.2.1 and 4.2.2 discusses the major and trace elements present in the fluid in details and relating them to the mineralogical composition of the bulk rock samples. Geochemical reactions of interest are also further discussed in Chapter 5.

### **4.2.1 Major Elemental Concentration in Effluent**

Elemental Calcium concentration in the effluent collected at the outlet of the artificially fractured cores are presented in figure 4.2. The ratios of  $C_{a_n}/C_{a_0}$  are presented as data points on the chart.  $C_{a_n}$  represent the concentration of Calcium in part per million (ppm) for each day ( $n$ = time in days).  $C_{a_0}$  is the original elemental concentration in the influent CO<sub>2</sub> saturated brine. This dimensionless entity represents the fractional increase or decrease in the elemental composition

of Calcium and other major alkaline earth metals discussed in this section (Magnesium (Mg), Potassium (K), Selenium (Se), Sulphur (S) and Silicon (S)). The error bars are standard deviation values based on 3 measurements of elemental composition.

The concentration profile for Calcium shows that the Marcellus samples had the highest fraction in solution which rapidly decreased over the five day period of continuously flooding the samples with CO<sub>2</sub> saturated brine. The initial pH of the influent fluid is approximately 3.7. The Mancos, Marcellus and Wilcox shale rocks exhibited similarly trend of a gradual exponential decline over the five day period. The Pottsville shales reflected a gradual increase that appears to continue over the experimental period.

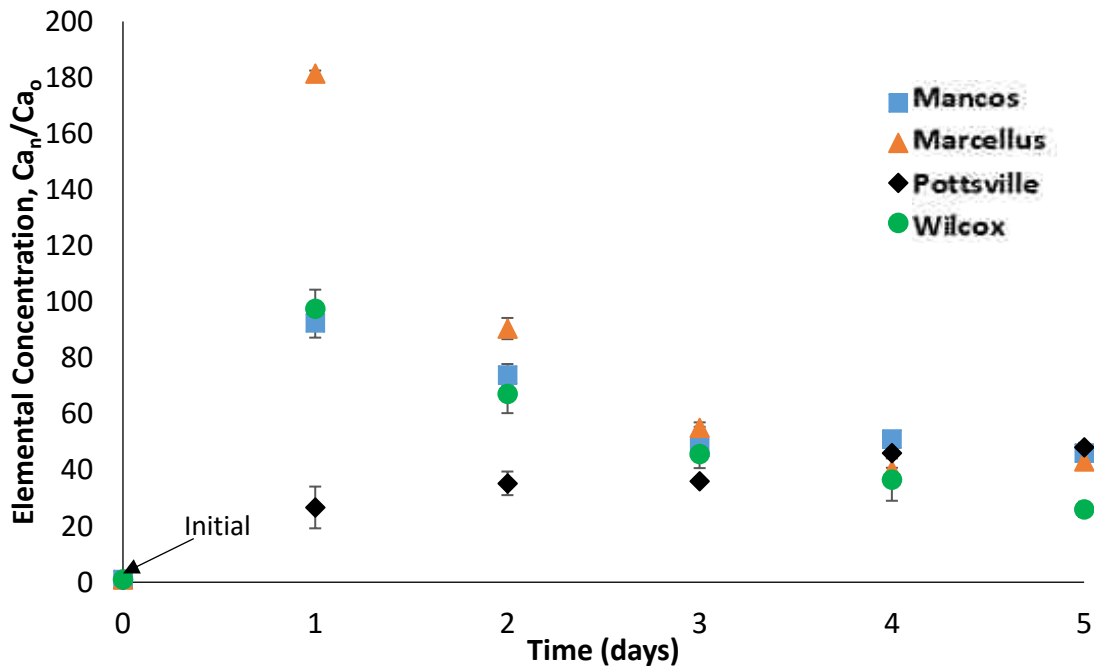


Figure 4.2: Dimensionless elemental concentration of the effluent fluids showing the fraction of Calcium (Ca) that were leached out from the shale rock samples. The Mancos, Marcellus and Wilcox shale rocks had significantly higher fraction of Ca within the first two days of the experiment compared to the Pottsville, indicating greater dissolution of calcium based minerals.

While the elemental concentration of Calcium in the Mancos, Marcellus and Wilcox shales peaks on the first day of the experiment, that of the Pottsville shale continued to increase over the five day period but it also expected to peak and gradually decline with similar trend to the Mancos, Marcellus and Wilcox shales. This resilient behavior of the Pottsville shale might suggest a slower dissolution reaction of its calcium based minerals constituent compared to the Mancos, Marcellus and Wilcox shales. The bulk rock XRD analysis indicated calcite and dolomite as the main calcium bearing minerals in the Mancos, Marcellus and Wilcox shales while anhydrites are the main calcium bearing minerals in the Pottsville.

Figure 4.3 presents the five day elemental concentration trend in the effluent for Magnesium. The profile for the four samples are similar to that of calcium. It can be observed that the fractional composition of magnesium in the effluent are about half of elemental calcium presented in figure 4.2. The Mancos, Pottsville and Wilcox shale rocks appear to be plateauing out after the five-day experimental period, while the Marcellus shale samples is rapidly approaching zero concentration during the same period. The similarity of concentration profile suggests that plausible geochemical dissolution reactions are occurring along with magnesium based minerals in the shale rocks. This type of reactions are mostly associated with calcite, dolomite and illitic (illite containing) clay minerals.

Elemental Potassium in solution (figure 4.4) exhibited a trend that showed a reduction in the free potassium available in the influent fluid for the Marcellus and Wilcox shale rocks before stabilizing after the five-day experimental period. This indicated a consumption of the potassium element in the injected fluid via reactive rock-fluid interaction for the two samples. The Mancos and Pottsville shale samples exhibited the general trend of initial increases in elemental

(potassium) concentration, in the effluent fluid, followed by a decreasing profile as the experiment progresses. This is most-likely due to limited rock volume.

Concentrations of Selenium (figure 4.5) are most significant for the Mancos and Pottsville shale rocks while the Marcellus and Wilcox shales had little to no selenium ions leached into the effluent fluid. The presence of selenium in the effluent solution showed the extent of shale rock samples' heterogeneity as no known selenium bearing mineral was identified in the rocks by XRD analysis. This suggests that these selenium bearing minerals only exist in trace amounts within these sedimentary rocks matrix. The presence of free selenium in solution could act as catalysts for faster reactive flow. Furthermore, Sulphur content (figure 4.6) was highest in the Wilcox shale followed by the Mancos and Marcellus shale. This confirms that CO<sub>2</sub> saturated-brine can effectively dissolve stable minerals like pyrites and other sulphur bearing minerals. The Marcellus and Wilcox shale samples had the highest content of pyrite mineral as identified by XRD analysis. It appears that there is a preferential dissolution of pyrite in the Wilcox shale compared to the Marcellus, even though it has a higher content of pyrite. It can be assumed that relative abundance of these soluble minerals in the rock matrix would have influence on geochemical speciation in the effluent. The convective transport of these geochemical species are important in balancing the equilibrium conditions of the subsurface. The introduction of fluids such as dissolved CO<sub>2</sub> in brine can significantly alter the equilibrium landscape that can affect the natural in-take or release of chemical species. The trend noticeable in these results suggest that massive dissolution of calcites and dolomites might pose significant challenges in cases where there are significant ingress of carbon dioxide in aqueous form into the shale caprock. This can lead to increased percentage of flow paths within the rock.

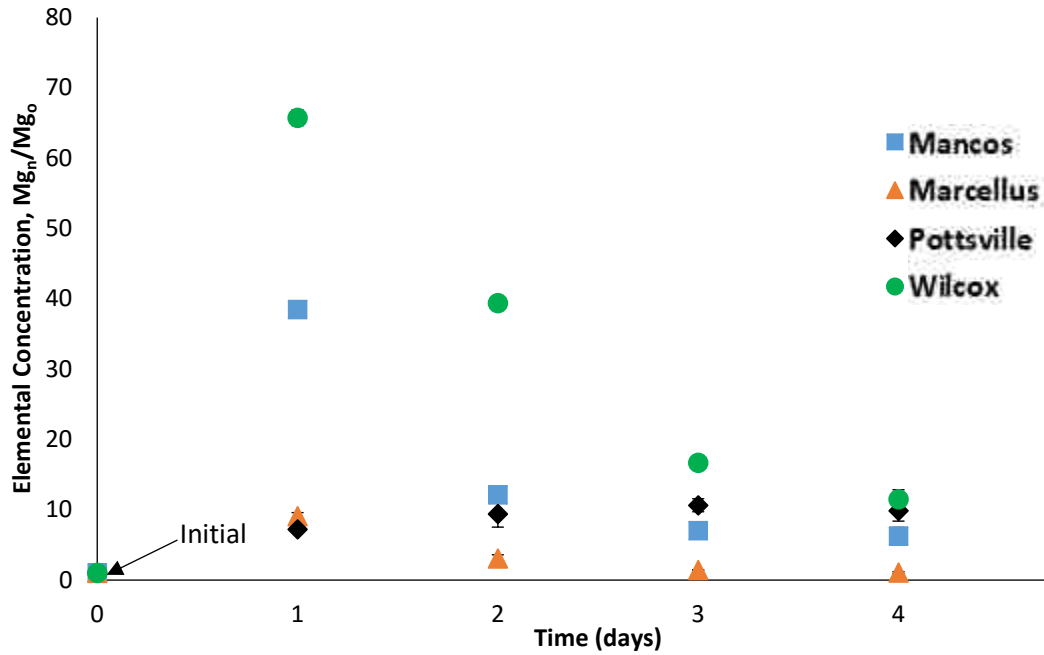


Figure 4.3: Dimensionless cationic concentration of the effluent fluids showing the fraction of Magnesium (Mg) that were leached out from the shale rock samples. The trend of the Mg concentration is similar to that of Ca indicating concurrent geochemical reactions.

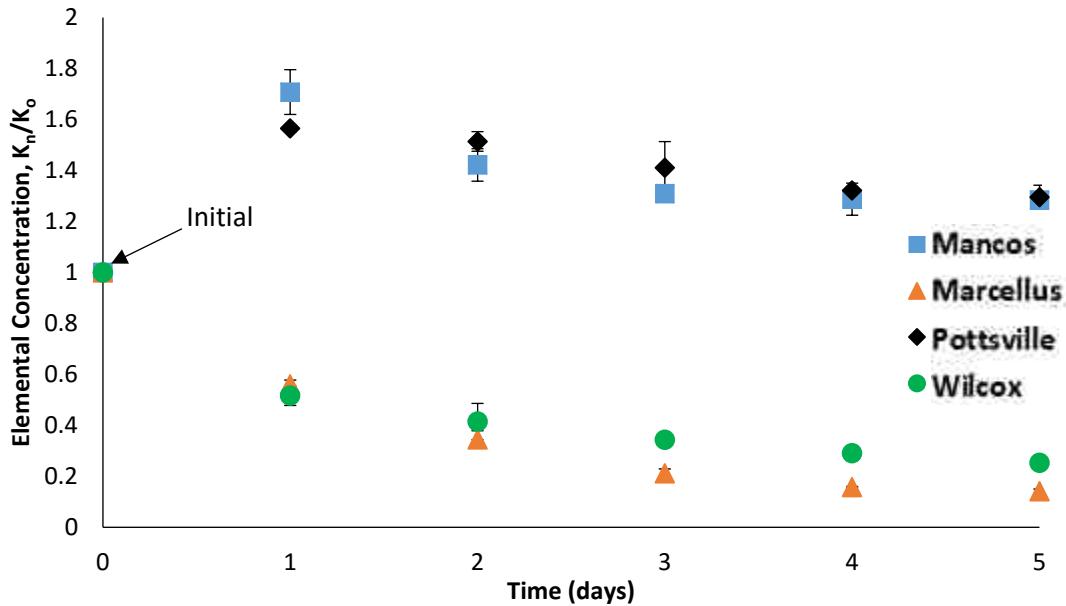


Figure 4.4: Dimensionless cationic concentration of the effluent fluids showing the fraction of Potassium (K) that were leached out from the shale rock samples. The profile for the Marcellus and Wilcox shale rocks indicated a marked reduction in potassium concentration beginning from the start of the experiment. This suggests that trace amount of K in the brine were absorbed.

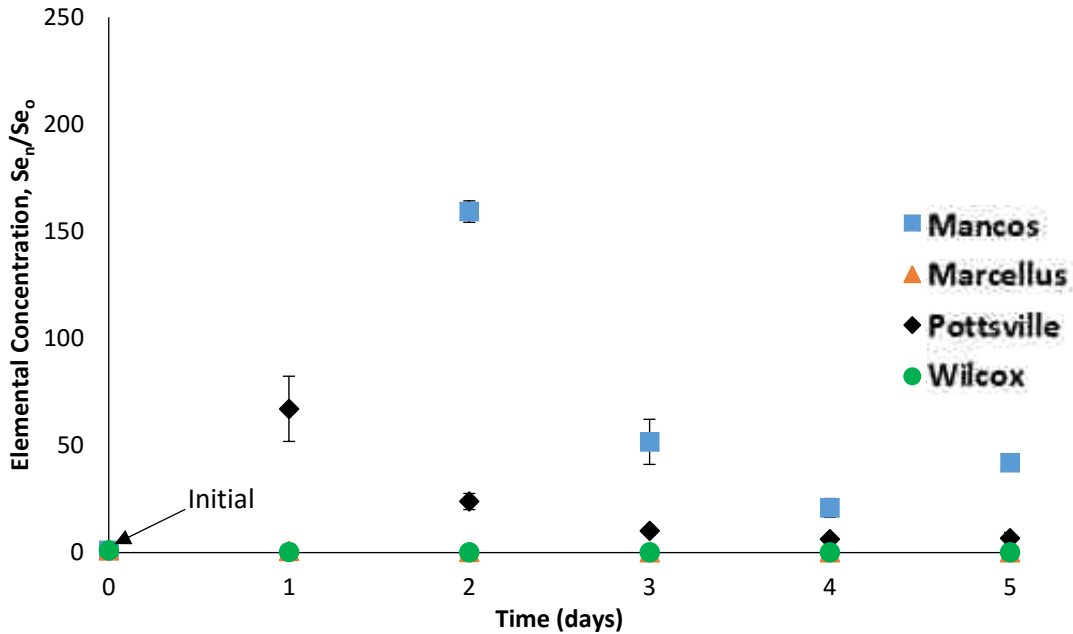


Figure 4.5: Dimensionless cationic concentration of the effluent fluids showing the fraction of Selenium (Se) that were leached out from the shale rock samples. The profile showed that selenium is present in significant quantity within the shale rock of Mancos and Pottsville with only trace amounts in the Marcellus and Wilcox shale rocks.

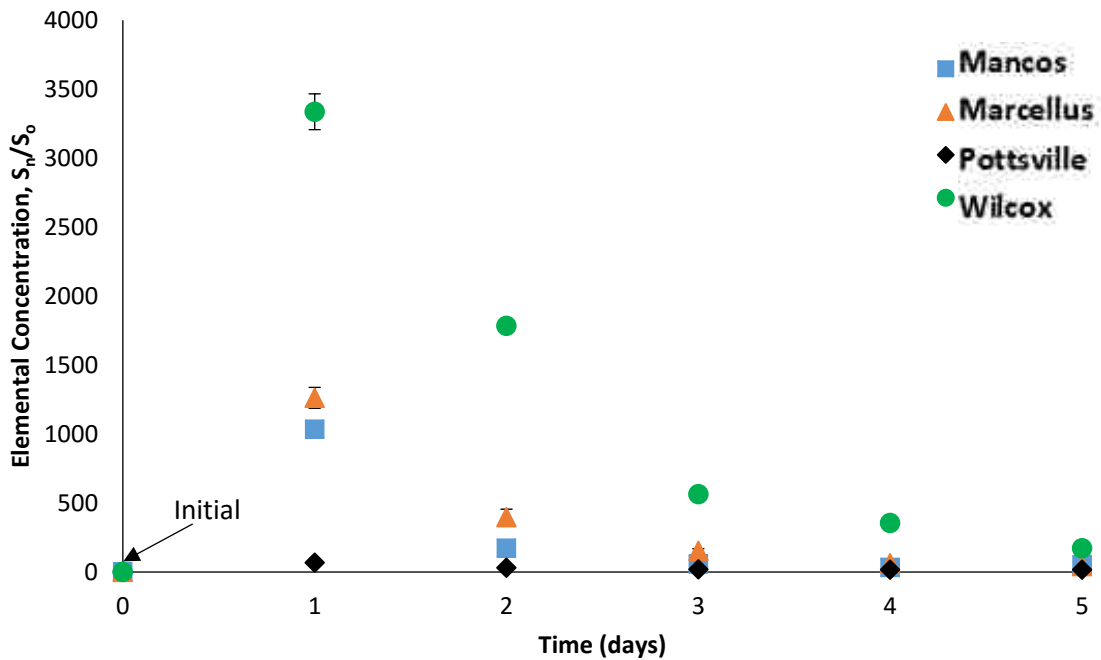


Figure 4.6: Dimensionless cationic concentration of the effluent fluids showing the fraction of Sulphur (S) that were leached out from the shale rock samples. The concentration of Sulphur was highest in the Wilcox shale with fractional values peaking with the first day of the experiment. Pottsville shale appears lean in Sulphur content all through experiment.

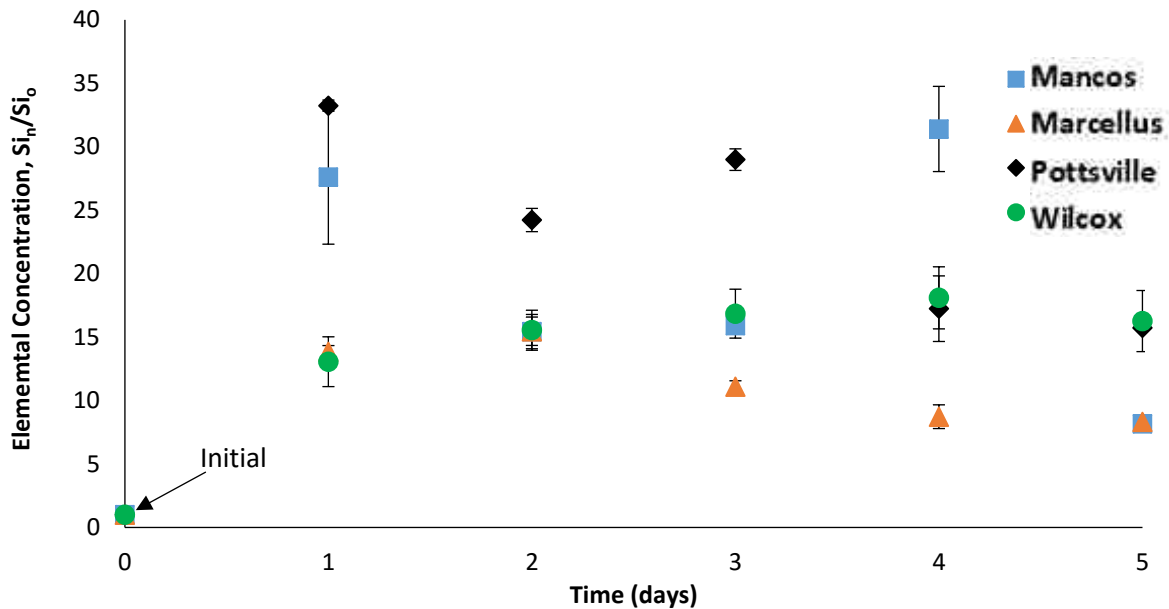


Figure 4.7: Dimensionless cationic concentration of the effluent fluids showing the fraction of Silicon (Si) that were leached out from the shale rock samples. The fractional profile of silicon indicated dissolution of silicon bearing minerals. It is possible that of early precipitation in form of diagenetic quartz occurred as the concentration of Si remained fairly constant.

Elemental silicon concentration in the effluent analyzed showed that they are present in solution in significant quantity compared to the initial CO<sub>2</sub>-brine fluid that was injected. Figure 4.7 documents these Si concentrations for all the shale samples. The presence of diagenetic quartz in the precipitates recovered, indicated that most of the silicon in solution had crystallized out of the solution to form a variant of opal mineral that is amorphous in shape.

#### 4.2.2 Minor Elemental Concentration in Effluent

Trace concentration of certain elements in the effluent solution is discussed. These include Aluminum (Al), Arsenic (As), Boron (B), Iron (Fe), Manganese (Mn), Nickel (Ni), Phosphorus (P) and Zinc (Zn). They are described as occurring in trace amounts because the actual part per million (ppm) concentrations are in the range 0.1 mg/l to 10mg/l which are significantly lower

compared to the concentration of the major elemental compositions described above. Previous researchers have attempted to model trace metals mechanism of release and evolution in carbonates reservoirs that are capped by shale rocks [43].

Figure 4.8 shows the concentration of Al in the effluent solution for all the four samples used in the five day experiment at moderate temperature and pressure conditions. The concentration for the Marcellus and Wilcox followed the trend observed in potassium concentration profile indicating a consumption of the element during possible reactive rock-fluid interaction. It is safe to assume that Aluminum did not participate significantly in these reactions given its low concentration in the effluent, though dissolved aluminum bearing minerals in solution could have precipitated out of the solution in form of clay, therefore the low concentration. The Mancos and Pottsville shale rocks showed little to no change in Al concentration indicating passive interaction of aluminum bearing minerals in these samples with CO<sub>2</sub>-brine influent fluid. Arsenic and Boron elemental compositions (Figures 4.9 and 4.10) showed a similar trend to that of Aluminum for all the samples analyzed.

Elemental concentration of Iron is quite significant in the Wilcox as shown in figure 4.11. The chart presents a confirmation that the pyrite (FeS<sub>2</sub>) content in the Wilcox reactively interacted more with the influent fluid leading to high concentrations of Iron (Fe) and Sulphur (S) in the effluent. Other samples (Mancos, Marcellus and Pottsville shales) have iron concentration in trace amounts. Manganese (Mn) concentration followed the trend observed in Iron with the Wilcox shale having a disproportionate concentration of Mn in the solution compared to the other three samples. This can be seen in figure 4.12 with the concentration declining exponentially during the five-day experiment. The concentration of Mn in the effluent recovered

for the Mancos, Marcellus and Pottsville shales were in trace amounts though the Wilcox's fifth day concentration rapidly approached the range for these other samples. The concentration of Mn in the Wilcox indicate a rapid reactive interaction of the manganese bearing minerals in the shale rock with CO<sub>2</sub> saturated brine leading to free manganese cations in solution. The elemental concentration of Nickel (Ni) and Phosphorus (P) showed a trend of trace element consumption similar to K, Al, B and As for the Marcellus and Wilcox shales while the Ni and P concentrations of A and C appeared unchanged in the effluent when compared to the influent CO<sub>2</sub>-brine fluid. Figures 4.13 and 4.14 showed the trace concentrations of Ni and P. These trace metals may be able to act as catalysts for surface and internal reactions in the sample rock pore spaces.

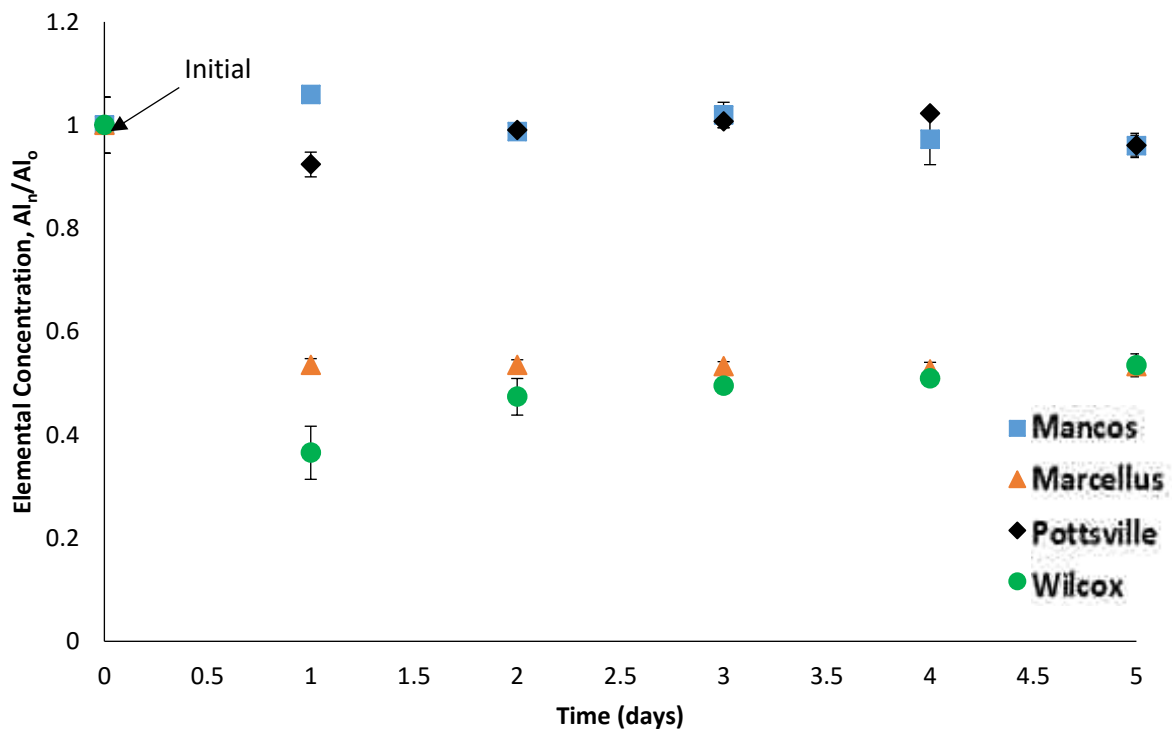


Figure 4.8: Dimensionless cationic concentration of the effluent fluids showing the fraction of Aluminum (Al) that were leached out from the shale rock samples. The trace concentrations of Al remained constant for the Mancos and Pottsville shale rocks. The Al profile for the Marcellus and Wilcox shale rocks were initially mildly reduced but later held constant during the last three days of the experiment.

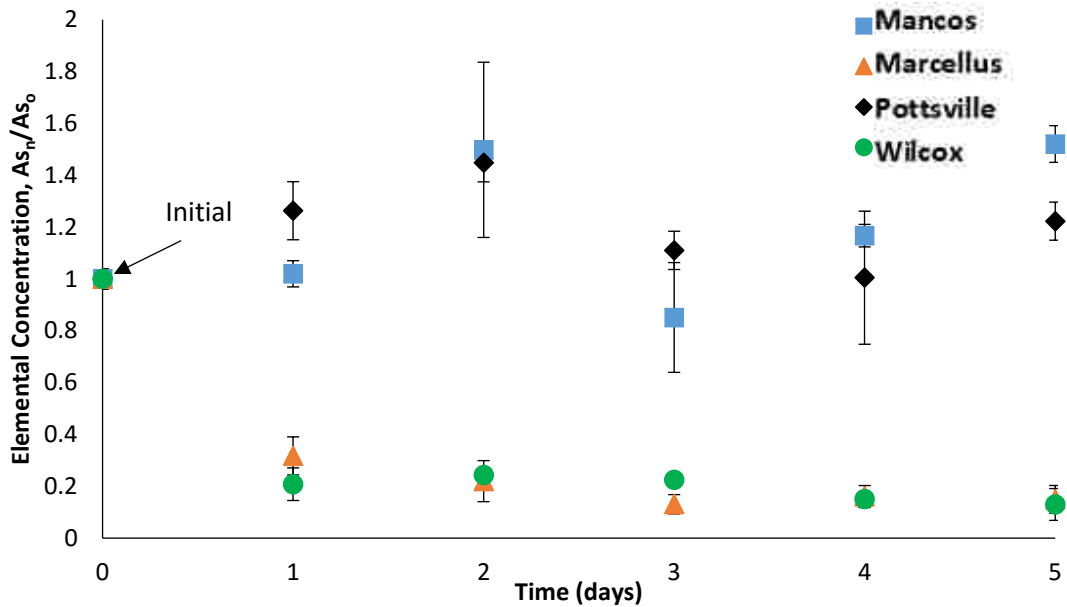


Figure 4.9: Dimensionless cationic concentration of the effluent fluids showing the fraction of Arsenic (As) that were leached out from the shale rock samples. The trace concentrations of As in the effluent fluid from the Mancos and Pottsville shale rocks significantly diverged from the Marcellus and Wilcox over the 5 day experiment plateauing out for all samples at end of the experiment.

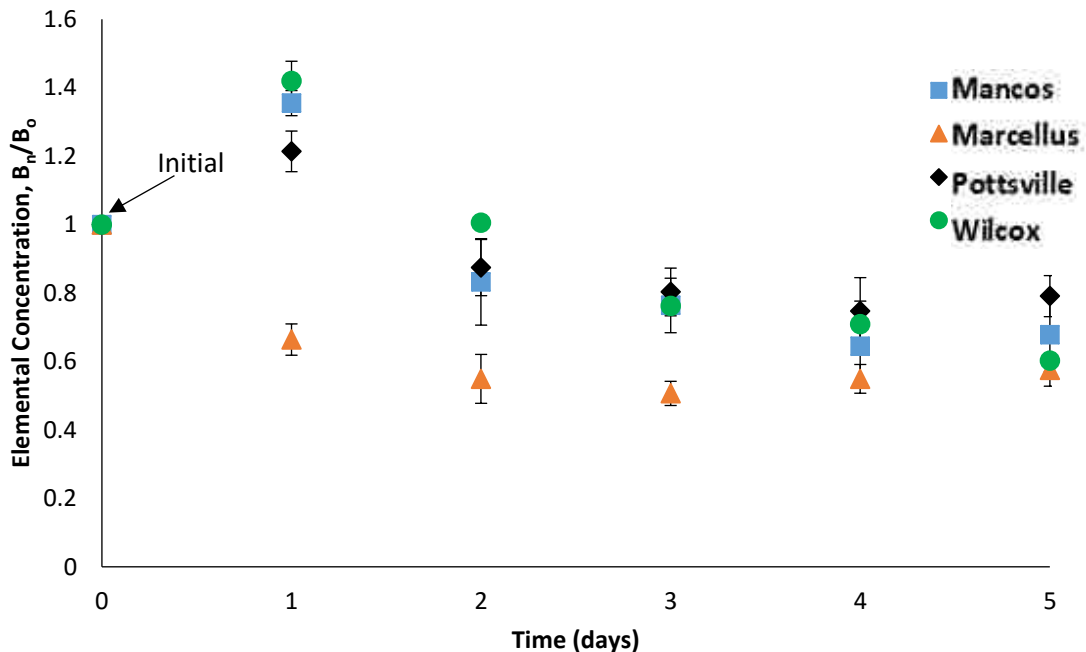


Figure 4.10: Dimensionless cationic concentration of the effluent fluids showing the fraction of Boron (B) that were leached out from the shale rock samples. The minor concentrations of Boron showed a common decreasing pattern for all the samples, stabilizing towards the end of the experiment at values that are lower than the initial.

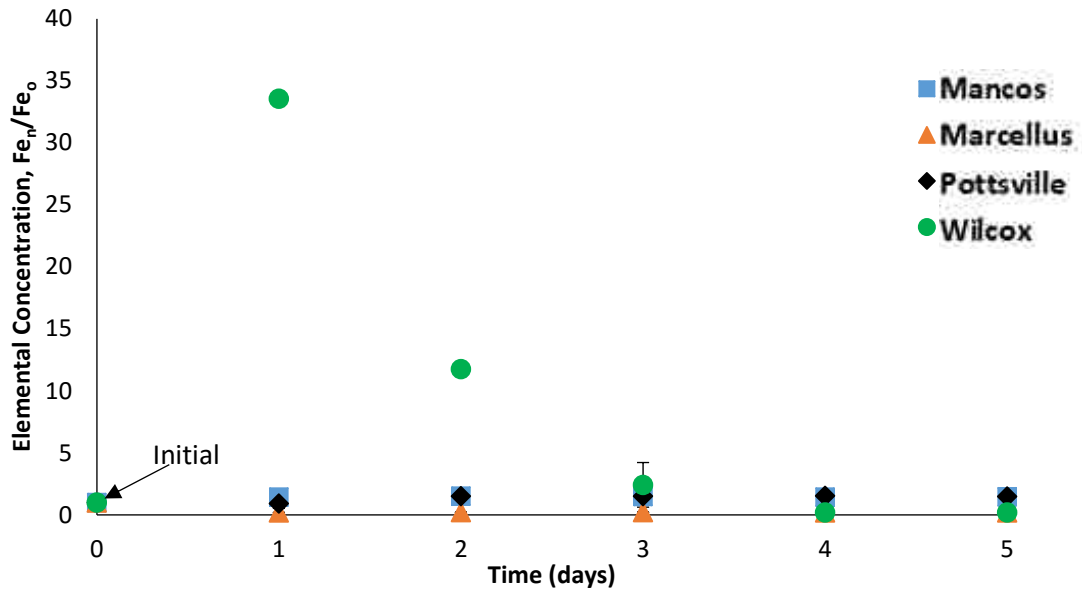


Figure 4.11: Dimensionless cationic concentration of the effluent fluids showing the fraction of Iron (Fe) that were leached out from the shale rock samples. The trace Fe content profile showed that the Wilcox shale had a much higher fraction of Fe in solution compared to the other three samples. This Fe concentration rapidly reduced over time during the experiment.

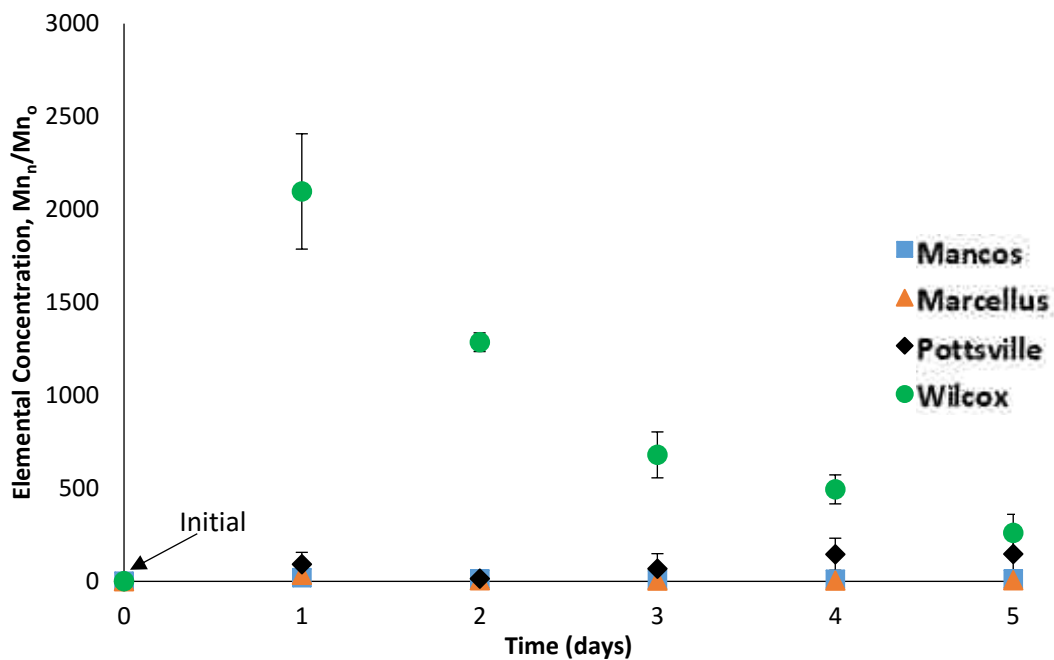


Figure 4.12: Dimensionless cationic concentration of the effluent fluids showing the fraction of Manganese (Mn) that were leached out from the shale rock samples. The Mn profile showed a much higher concentration of Mn in the effluent associated with the Wilcox shale rocks compared to the other three samples. This Mn concentration rapidly reduced over time during the experiment.

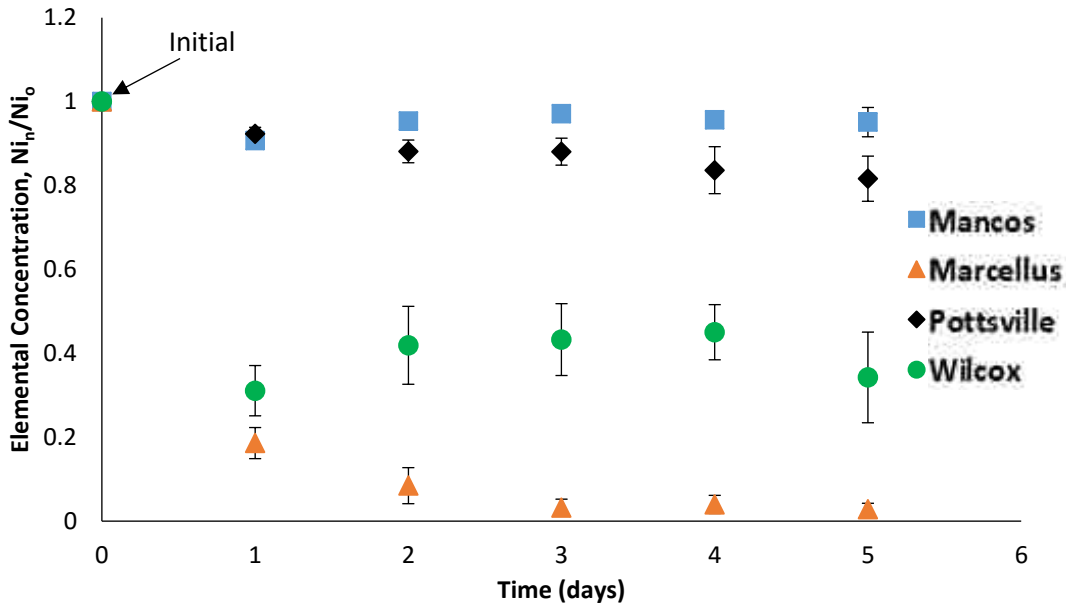


Figure 4.13: Dimensionless cationic concentration of the effluent fluids showing the fraction of Nickel (Ni) that were leached out from the shale rock samples. The trace profile for Ni indicated that the Marcellus and the Wilco shales had a mild decrease in the associated effluent compared to the initial CO<sub>2</sub>-brine fluid. Nickel concentration remained constant for the Mancos and Pottsville shale rocks.

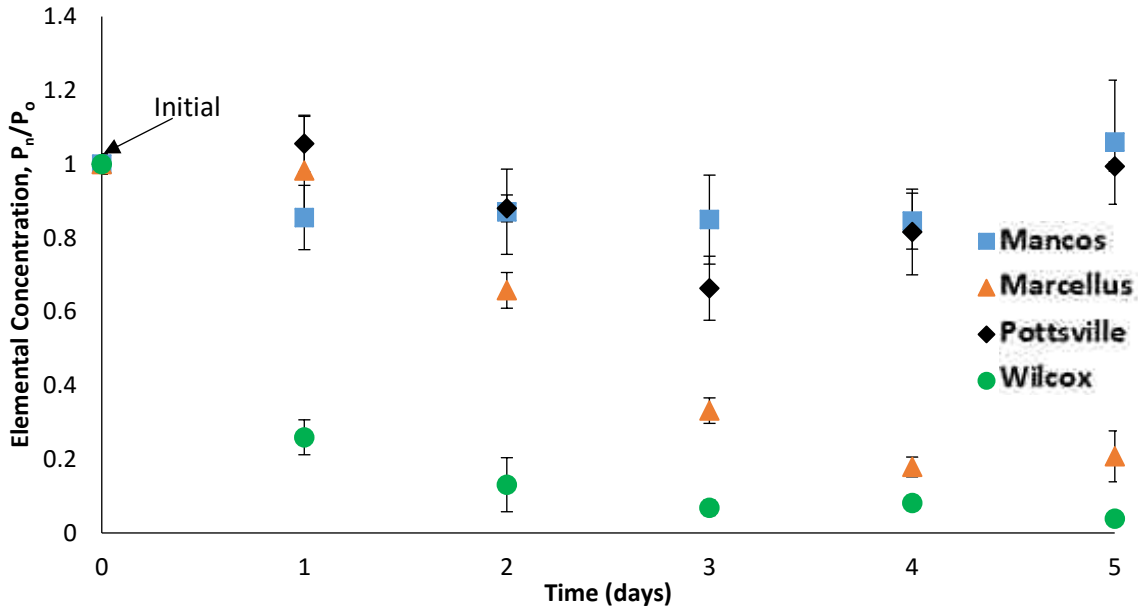


Figure 4.14: Dimensionless cationic concentration of the effluent fluids showing the fraction of Phosphorus (P) that were leached out from the shale rock samples. The trace profile for P indicated that the Marcellus and Wilcox shale rocks had a mild decrease in the associated effluent compared to the initial CO<sub>2</sub>-brine fluid. Phosphorus concentration remained fairly constant for the Mancos and Pottsville shale rocks.

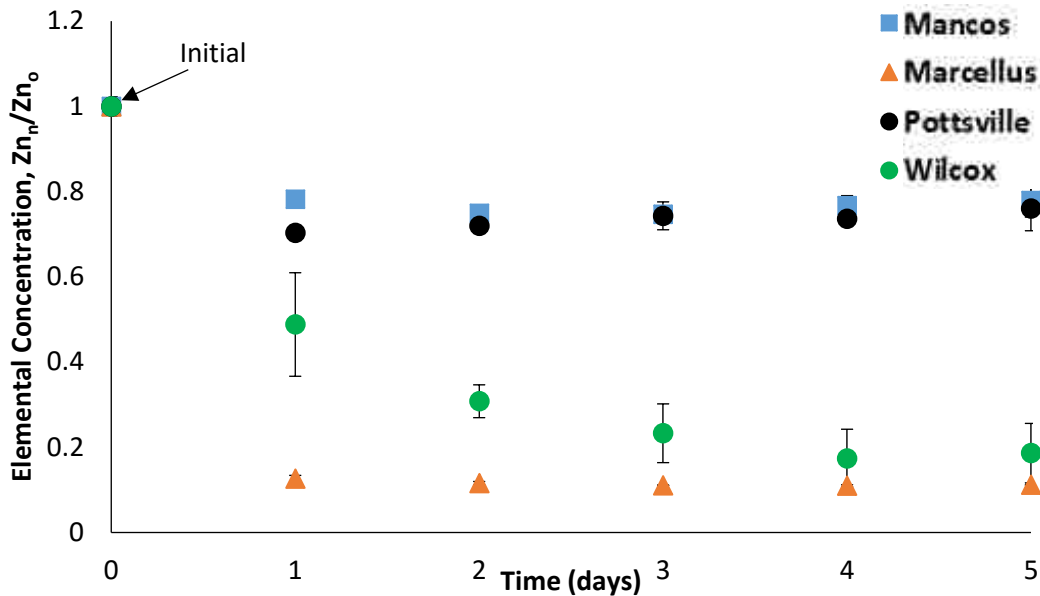


Figure 4.15: Dimensionless cationic concentration of the effluent fluids showing the fraction of Zinc (Zn) that were leached out from the shale rock samples. The concentration of Zn in the effluent fluid associated with all the shale samples decreased compared to the initial CO<sub>2</sub>-brine fluid. This decrease is most pronounced in the Marcellus and Wilcox shale rocks.

Figure 4.15 shows the concentration profile for Zinc (Zn) that not only has a trend similar to that of Ni and P described above, it was also a trend of persistent concentration reduction for all the four samples analyzed. This indicates that Zn is most-likely participating in geochemical reactions as a facilitating components given its trace concentration.

### 4.3 Total Carbon Analysis

The total carbon contents of all the four samples were analyzed for the three runs per sample experiment at moderate temperature and pressure conditions. Figure 4.16 shows the Marcellus shale as having the highest percentage of carbon compared to other samples as expected for a highly fossiliferous shale rock. The percentage carbon content were in the order Marcellus >

Wilcox > Mancos > Pottsville. This order of magnitude still holds after the CO<sub>2</sub>-brine flooding experiment. It can be observed for the figure that there were significant increases in the percentage content of carbon in all the samples which can be indicative of both adhered carbon and mineralized carbon in these shale samples. This might be good for carbon sequestration.

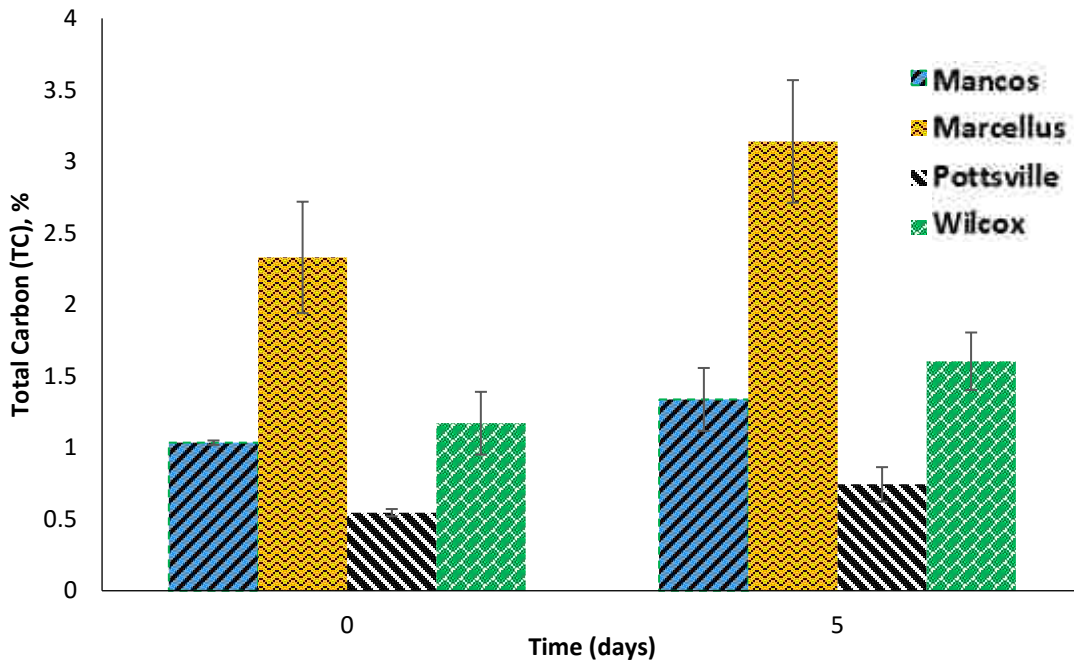


Figure 4.16: Total Carbon measurement of bulk rock for the four different samples analyzed. It shows major increase in carbon content for the Marcellus shale compared to the other three samples. This increase can be associated with surface CO<sub>2</sub> adsorption or carbon mineralization.

It suggests that shale caprock can act like repositories for CO<sub>2</sub> when sufficient surface area are available for rock fluid interaction. The surface area of the shale caprock exposed in these experiments are equivalent of several thousand meter square. Subsurface CO<sub>2</sub> plume movement will be contact seal rocks in this manner and scope. Distinguishing between adhered carbon and mineralized carbon content might shed more light on which process- adsorption or mineralization- will be most significant for CO<sub>2</sub> sequestration in shaly rocks over the long term.

The error bars are standard deviation (SD) values for the three runs per sample experiments. The total carbon analysis is more qualitative than quantitative for conclusive interpretations.

#### **4.4 X-Ray Diffraction (XRD) Analysis**

X-ray diffraction (XRD) analysis were carried on the bulk rock and the precipitates that were recovered from the effluent fluid. Both bulk and clay XRD analysis were performed in order to decipher the minerals that are most active in rock-fluid interaction and their implication on precipitates generation which can be transported in solution. These precipitates are of interest as hydraulic paths (micro-fractures, worm holes etc.) may be possibly plugged if the right quantity are generated from the bulk rock as dissolved substances. These dissolved minerals can then precipitate given the right pH, pressure, temperature, compositional and other conditions. The following sections (4.4.1 and 4.4.2) discuss the XRD analyses in details.

##### **4.4.1 Bulk XRD Analysis**

After the five days of flooding the shale rock samples continuously with CO<sub>2</sub> saturated brine at moderate temperature and pressure conditions, XRD analyses were carried out on the bulk experimental shale rock samples and the precipitates that were recovered from the effluent fluid with the aim of qualifying and quantifying geochemical changes that could have taken place as a result of reactive rock-fluid interaction. These geochemical changes are expected to affect the mineralogical composition and structure of the shale rocks. The results were compared to the initial shale rock samples that were not flooded with CO<sub>2</sub>-brine. Figures 4.17 to 4.20 show the profiles of the main mineralogical components in the shale rocks (pre- and post-flooding with CO<sub>2</sub>-brine) and the recovered precipitates as identified by bulk XRD analysis for the Mancos, Marcellus, Pottsville and Wilcox shale rocks respectively. The bulk shale rocks show little to no

change in mineralogical content pre- and post-flooding with CO<sub>2</sub>-brine within the limit of XRD resolution. This was the observed trend in all the four samples. It can however be observed that the mineralogy identification peaks were better resolved in the post-flooding samples. It suggests that the amorphous content of the shale rocks have been largely removed by the acidic fluid. In the data reported by expert researchers in the field of carbon sequestration, defects or inherent errors in measuring equipment can affect the accuracy of XRD readings.

Amorphous content of rocks are usually responsible for suppressed peaks in XRD qualitative analysis. The bulk XRD analysis of precipitates showed the appearance of diagenetic minerals that were formed from the major mineralogical components of the shale rocks.

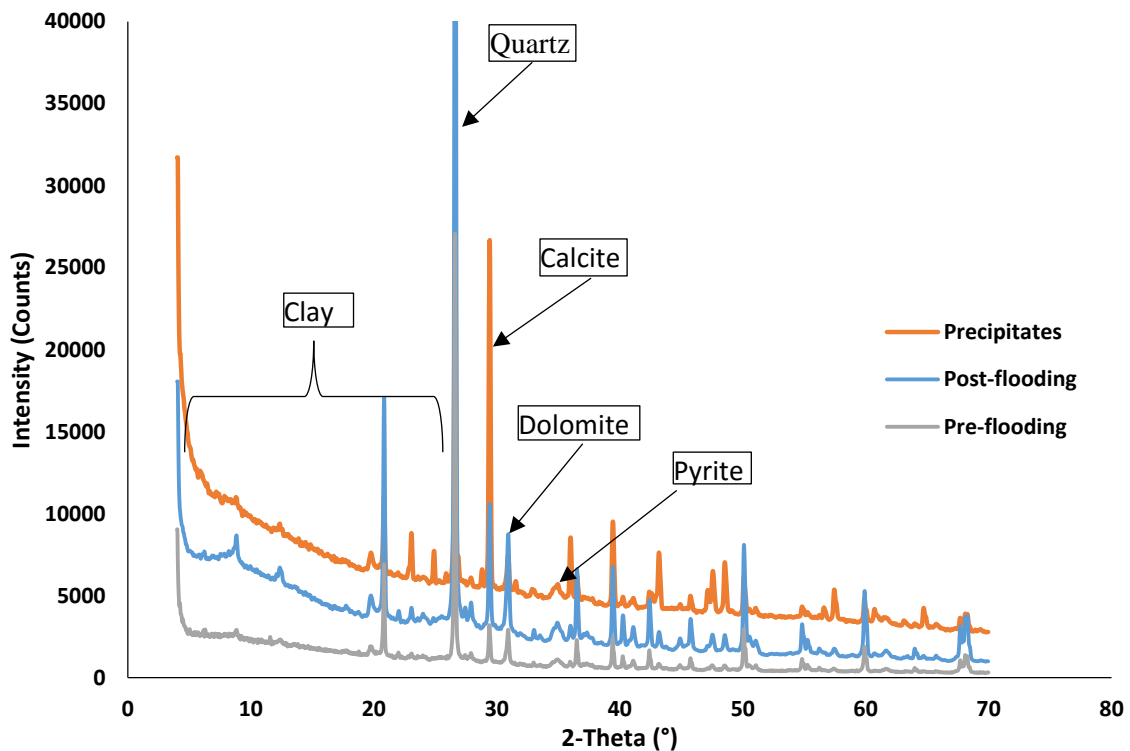


Figure 4.17: XRD Analysis of bulk rock (**Mancos**) before and after CO<sub>2</sub>-brine flooding at moderate temperature and pressure conditions along with the mineralogical composition of the associated precipitates recovered from the effluent. It showed higher amount of diagenetic carbonates in the precipitates compared to the pre- and post-flooding samples.

Precipitate recovered from the effluent of flooding the Mancos shale with CO<sub>2</sub> saturated brine showed quartz, plagioclase, calcite, dolomite and pyrite as main constituent. This is excluding the clay fraction. Precipitates associated with the Marcellus shale included quartz aragonite and calcite only with no clay detected using XRD analysis. Precipitates associated with the Pottsville shale included quartz, albite and calcite while precipitates associated with the Wilcox shale included quartz, plagioclase and pyrite, excluding clay fractions from both samples. It can be seen from the bulk XRD output that mineral constituents of the original shale rocks are largely responsible for the diagenetic constituents of the associated precipitates which are dominated by quartz, calcites and clays.

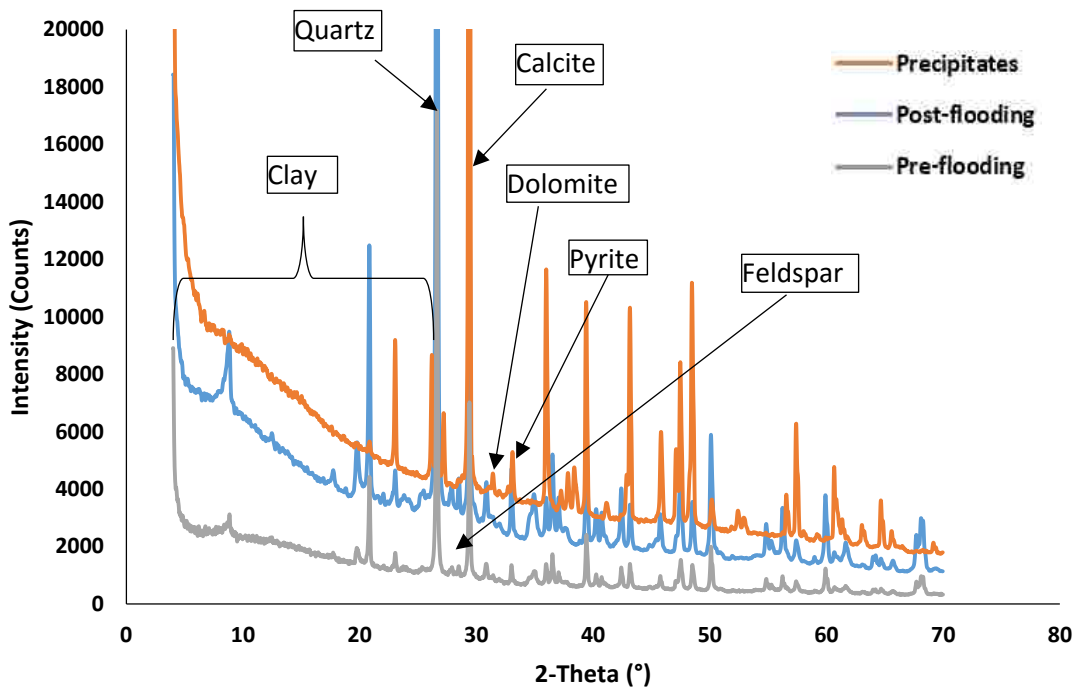


Figure 4.18: XRD Analysis of bulk rock (**Marcellus**) before and after CO<sub>2</sub>-brine flooding at moderate temperature and pressure conditions along with the mineralogical composition of the associated precipitates recovered from the effluent. It showed higher amount of diagenetic carbonates in the precipitates compared to the pre- and post-flooding samples

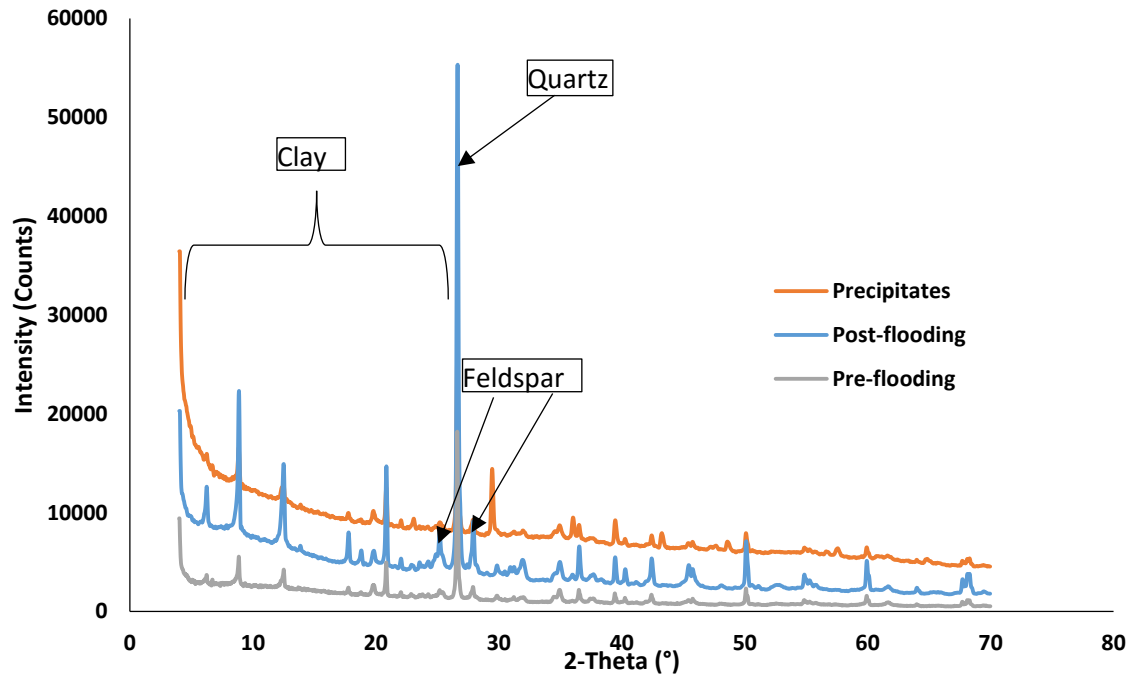


Figure 4.19: XRD Analysis of bulk rock (**Pottsville**) before and after CO<sub>2</sub>-brine flooding at moderate temperature and pressure conditions along with the mineralogical composition of the associated precipitates recovered from the effluent. It showed higher amount of diagenetic quartz and clays in the precipitates versus the pre- and post-flooding samples.

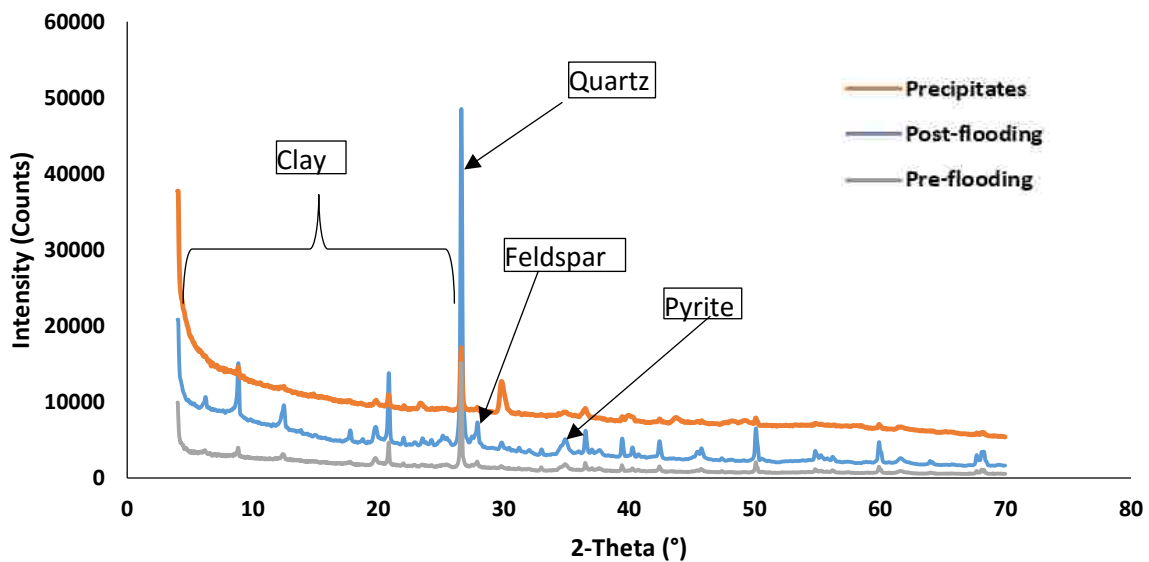


Figure 4.20: XRD Analysis of bulk rock (**Wilcox**) before and after CO<sub>2</sub>-brine flooding at moderate temperature and pressure conditions along with the mineralogical composition of the associated precipitates recovered from the effluent. It showed higher amount of diagenetic quartz and clays in the precipitates versus the pre- and post-flooding samples.

The quantitative assessment of the mineralogical changes in the both the bulk shale rock and the precipitates are presented in section 4.4.3. The analysis of clay constituents in both the bulk rock and precipitates are presented in section 4.4.2.

#### **4.4.2 Clay XRD Analysis**

Clay XRD analysis is performed by first removing all other non-clay mineralogical contents in the shale rock. This is then followed by four stages of XRD analysis: a) Air dried analysis b) Glycolated analysis c) 300 Celsius analysis d) 550 Celsius analysis. These staged analysis are specifically important in quantitative clay content evaluation. The results of Ethylene glycolated samples are discussed in this section as it is representative of all the other stages in clay mineral identification. Figures 4.21 to 4.24 show the clay XRD analyses of the pre- and post-flooding samples as well as the recovered precipitates for all the four samples used during the experiment. The results showed sharper identification peaks for the clay minerals similar to the trend observed in bulk XRD analysis in the precipitates. An indication of non-interference of amorphous substances in mineral identification using XRD analysis.

The clay composition of the Mancos shale showed illite, chlorite and kaolinite as the main component (figure 4.21). The precipitates has mainly chlorite and kaolinite with traces of illite. Figure 4.22 indicated the presence of only Illitic clay and kaolinite in the bulk shale rock of the Marcellus shale with no identifiable clay peak in the precipitates associated with it. Clay fraction in Pottsville shale and the associated precipitates are presented in figure 4.23 showing the multiple identification peaks of illites, chlorite and kaolinite in the shale bulk rock and the associated precipitates recovered after the CO<sub>2</sub> brine flooding experiment. The Wilcox shale rock

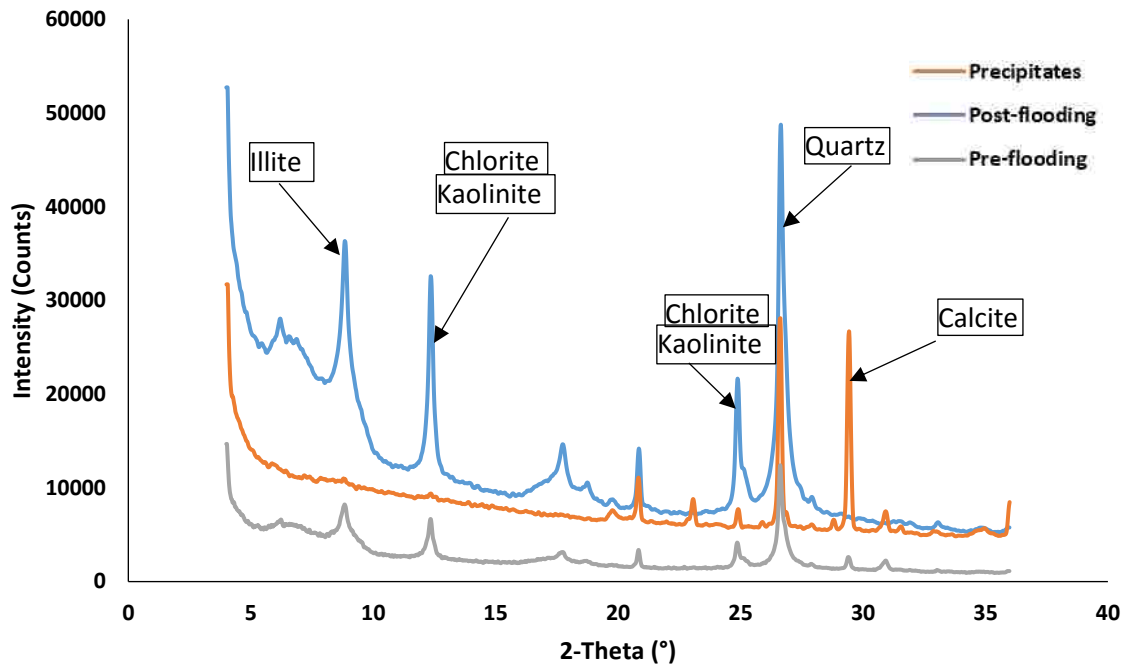


Figure 4.21: XRD Analysis of clay components (**Mancos**) before and after CO<sub>2</sub>-brine flooding at moderate temperature and pressure conditions along with the mineralogical composition of the associated precipitates recovered from the effluent. It showed sharper clay peaks in post-flooding data and higher carbonate content in the precipitates.

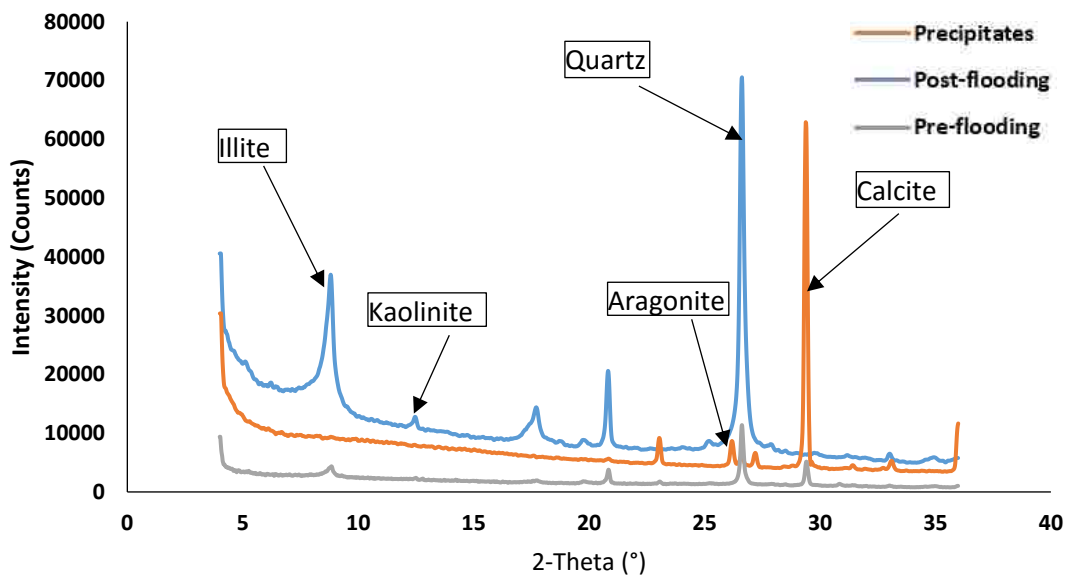


Figure 4.22: XRD Analysis of clay components (**Marcellus**) before and after CO<sub>2</sub>-brine flooding at moderate temperature and pressure conditions along with the mineralogical composition of the associated precipitates recovered from the effluent. It showed sharper clay peaks in post-flooding data and higher diagenetic carbonate content in the precipitates.

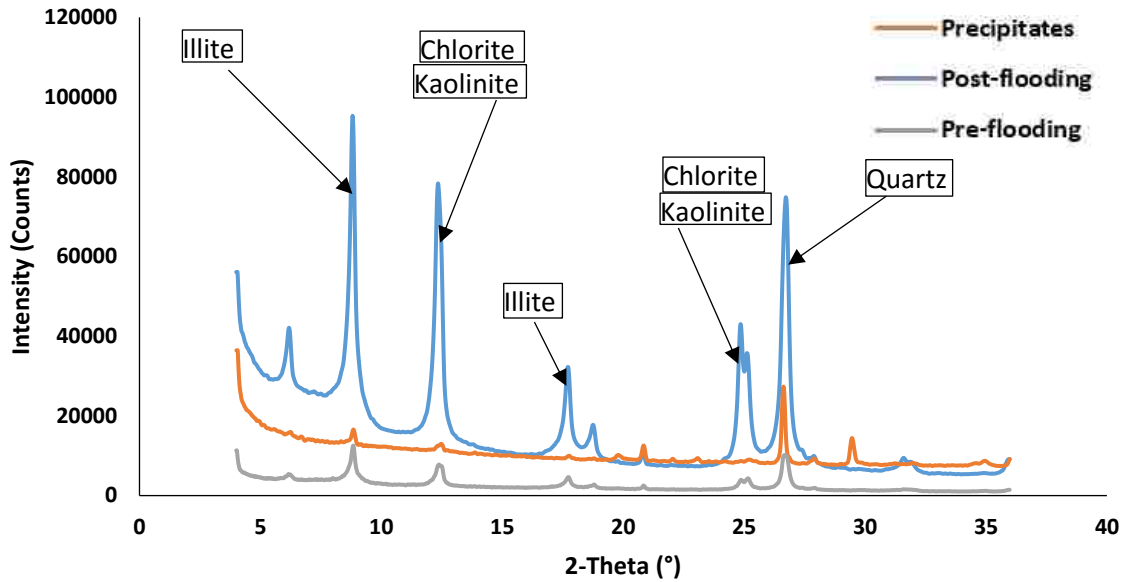


Figure 4.23: XRD Analysis of clay components (**Pottsville**) before and after CO<sub>2</sub>-brine flooding at moderate temperature and pressure conditions along with the mineralogical composition of the associated precipitates recovered from the effluent. Significantly higher clay content is present in precipitates compared to previous samples.

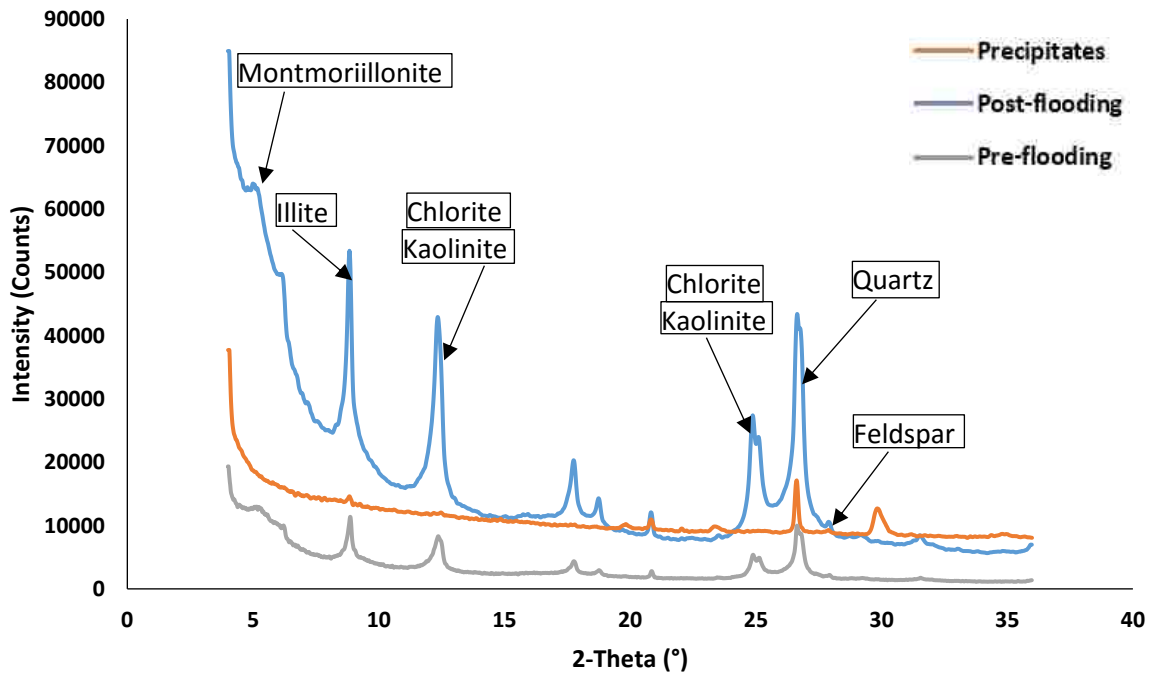


Figure 4.24: XRD Analysis of clay components (**Wilcox**) before and after CO<sub>2</sub>-brine flooding at moderate temperature and pressure conditions along with the mineralogical composition of the associated precipitates recovered from the effluent. Significantly higher clay content is present in precipitates compared to previous samples combined with pyrite.

as shown in figure 4.24 indicated the presence of four distinct clay fractions which are montmorillonite (a characteristic swelling clay), illite, chlorite and kaolinite. The dissolution and re-precipitation of siliciclastic minerals such as illitic clays and quartz show that acidified aqueous media such as CO<sub>2</sub>-brine can effect disequilibrium conditions. The qualitative results from the clay analysis of the shale bulk rock and the associated precipitates recovered from effluent fluid after CO<sub>2</sub>-brine flooding indicated that the clay composition of the shale rocks are not significantly diagenetically modified at the operating laboratory conditions of the moderately high temperature and injection pressure (50 Celsius and 1000 psi).

#### **4.4.3 Quantitative XRD Mineralogical Analysis**

Quantitative evaluation of the changes in mineralogical content of the shale rocks are presented in table 4.1. It can be seen that non-clay minerals that are compounds of alkaline earth metals (Ca, Mg, Fe) such as calcite, dolomite, pyrite and feldspar are significantly altered, mostly a reduction in percentage within the accuracy of quantitative XRD analysis.

Mancos shale had reductions in feldspar, dolomite, pyrite and total clay (particularly illite and kaolinite). There was a slight increase in quartz, plagioclase, calcite, and chlorite in the Mancos shale. The Marcellus shale had reductions in feldspar, plagioclase, calcite, dolomite, anhydrite and kaolinite, while its quartz, chlorite and illite content increased. Furthermore, bulk shale rock of Pottsville shale had reductions in anhydrite, chlorite and illite with associated increases in quartz, feldspar, plagioclase and kaolinite. The Wilcox shale had mineralogical reductions in feldspar, anhydrite, pyrite, chlorite and kaolinite with associated increases in quartz, plagioclase, illites and swelling clay montmorillonite. It can be observed that significant reduction in total clay component in most of the samples analyzed was accompanied with significant increases in quartz

fraction of the mineralogy. This was a strong indication of diagenetic alteration of shale rock minerals due to aqueous CO<sub>2</sub>-shale rock interaction under laboratory temperature and pressure conditions. The flow rate was set to a value that would replicate convective fluid transport in the subsurface. This type of flow characteristics represent long term scenarios.

Table 4.1: Bulk rock compositional change (in percentages) for the shale rock samples. These values were computed from the pre- and post-XRD quantitative analysis using the bulk and clay XRD methods. There were slight changes in quartz, carbonates and clay contents.

<b>Component</b>		<b>Mancos(%)</b>	<b>Marcellus(%)</b>	<b>Pottsville(%)</b>	<b>Wilcox(%)</b>
<b>Quartz</b>		1.25	0.61	11.19	5.57
<b>K-Feldspar</b>		-0.07	-0.8	0.86	-0.12
<b>Plagioclase</b>		0.18	-0.15	3.3	1.13
<b>Calcite</b>		1.04	-8.29	0	0
<b>Dolomite</b>		-0.65	-0.57	0	0
<b>Anhydrite</b>		0	-0.41	-1.2	-1.02
<b>Pyrite</b>		-0.74	0.56	0	-1.79
<b>Clay(total)</b>		-1.01	9.04	-14.15	-3.77
	Chlorite	0.4	0.18	-4.64	-0.88
	Illite	-1.17	10.12	-9.83	1.82
	Kaolinite	-0.24	-1.26	0.32	-5.44
	Montmorillonite	0	0	0	0.73

The mineralogical constituents of the precipitates that were recovered from the effluent during the shale/CO<sub>2</sub>-brine flooding experiment are presented in table 4.2. The minerals were definitely derived from the bulk shale rocks showed diagenetic components that have elemental

compositions that indicated reactive dissolution-precipitation process occurred during the experiment. Precipitates from CO<sub>2</sub>-brine flooding of the Mancos shale showed quartz, calcite and fine clays in nearly equal proportion. Precipitates from the Marcellus shale showed aragonite and calcite (both carbonates of calcium) as the sole component, indicating pronounced preferential dissolution of carbonates in this organics rich shale rock. Precipitates associated with the Pottsville and Wilcox shale rocks showed mainly clays and quartz with traces of calcite in that were probably formed from the dissolution of minor amount anhydrite present in the rocks by the CO<sub>2</sub>-brine. Further clay analyses confirmed this compositions.

Table 4.2: Percentage composition of the mineralogical components of precipitates that were recovered from the effluent during the shale/CO<sub>2</sub>-brine flooding experiment. The analysis indicated diagenetic quartz and carbonates as new minerals that were formed.

<b>Minerals</b>	<b>Mancos(%)</b>	<b>Marcellus(%)</b>	<b>Pottsville(%)</b>	<b>Wilcox(%)</b>
<b>Quartz</b>	30.15	1.8	43.56	39.39
<b>K-Feldspar</b>	-	-	-	-
<b>Plagioclase</b>	0.99	-	-	2.36
<b>Albite</b>	-	-	3.73	-
<b>Aragonite</b>	-	19.28	-	-
<b>Calcite</b>	38.06	78.92	3.07	1.22
<b>Dolomite</b>	4.1	-	-	-
<b>Anhydrite</b>	-	-	-	-
<b>Pyrite</b>	1.42	-	-	2.37
<b>Clays (total)</b>	25.28	-	49.64	54.66

#### **4.5 Electron Micro-Probe Analysis (EMPA) of Bulk Rock**

The geochemical surface imaging of the shale rocks using Electron Microprobe Analyzer (EMPA) technique revealed the nature of the changes to surface chemistry at micron scale and the possible transport and re-crystallization of secondary mineralogical textures. Polished thin sections of pre- and post- CO<sub>2</sub> flooding samples of the shale rocks were studied in order to map all the identifiable elemental component of the constituent minerals as applicable in sedimentary petrology. Figures 4.25 to 4.36 present the unique elemental maps for each of the shale caprock sample types.

Major element and select trace element compositions were determined by Electron Microprobe Analysis (EMPA). EMPA is one of several particle-beam techniques. A beam of accelerated electrons is focused on the surface of a specimen using a series of electromagnetic lenses, and these energetic electrons produce characteristic X-rays within a small volume (typically 1 to 9 cubic microns) of the specimen. Two dimensional maps were obtained for multiple elements that constitute the shale rocks, under operating conditions of accelerating voltage of 15 kV and beam current of 200 nA. The electron microprobe was run in mapping mode allowing automated analysis overnight. A total of four thin sections were mapped over a period of 4-5 hours each. Maps depict relative abundances of elements of interest, allowing the determination of compositional zones. The results showed the presence of Iron (Fe), Sodium (Na), Potassium (K), Silicon (Si), Carbon (C), Oxygen (O), Chlorine (Cl), Manganese (Mn), Calcium (Ca), Magnesium (Mg) and Aluminum (Al). They are present in rock minerals capable of exchanging ions with carbonic acid or aqueous CO<sub>2</sub>. The elemental distribution of Ca and Mg in the reacted Mancos and Marcellus shales were lower within grain facies as shown in figures 4.25 to 4.27 and figures

4.28 to 4.30 (top row) respectively when compared to the corresponding control samples (bottom row). These were the surface maps for elemental spread involving CO<sub>2</sub>-brine flooded samples. It has been noted that in addition to common alkali earth metals such as Na and K that

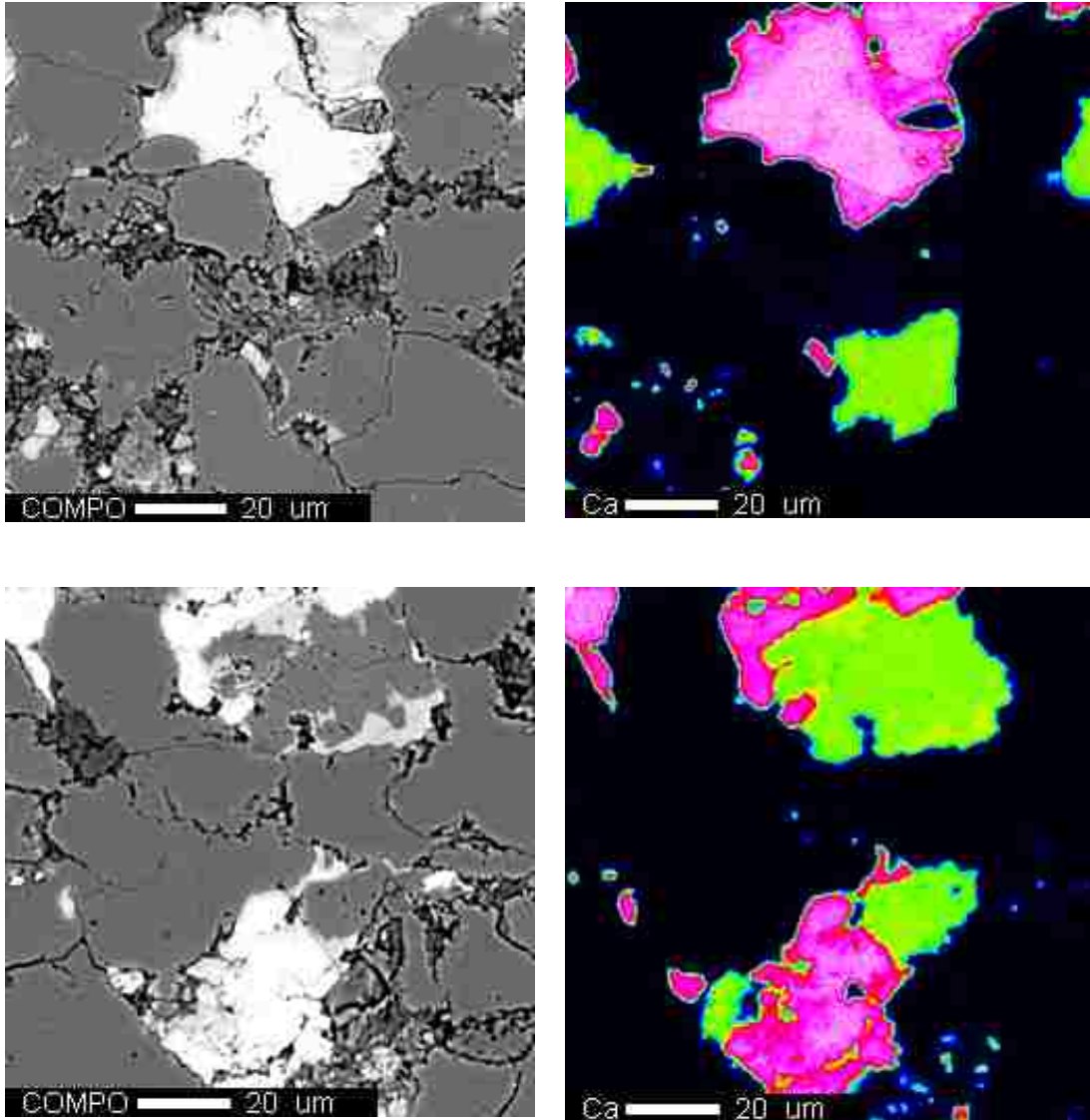


Figure 4.25: 20µm Electron Micro-Probe maps for **the Mancos shale** showing the Calcium (Ca) surface geochemical profile of the CO<sub>2</sub>-reacted sample (top row) compared to control specimen (bottom row). Note the general depletion of elemental components that are associated with minerals that are susceptible to dissolution. These trends are only detected at the lower micron resolution presented above.

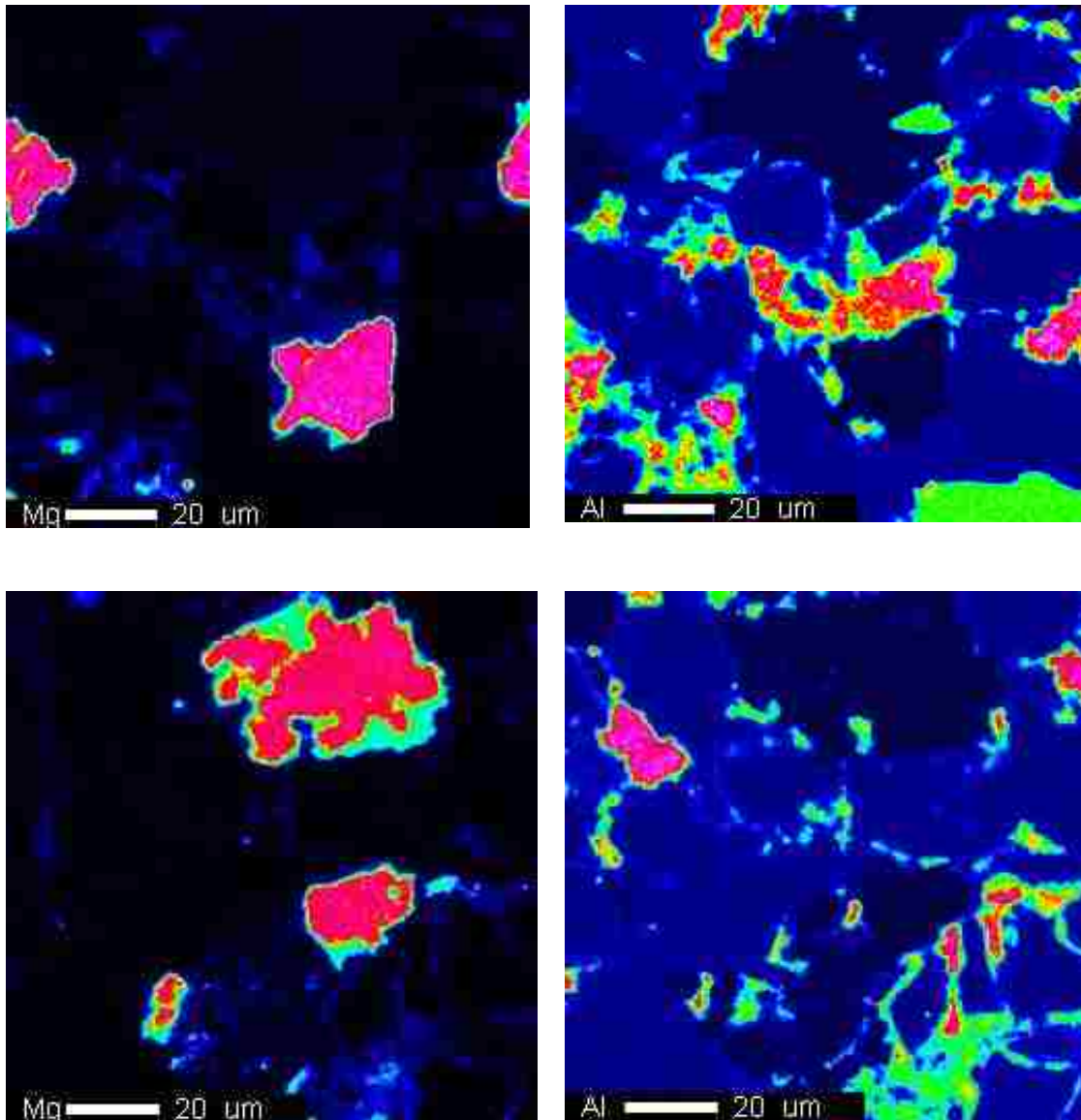


Figure 4.26: 20 $\mu$ m Electron Micro-Probe Analysis for **the Mancos shale** showing Magnesium (Mg) and Aluminum (Al) surface geochemical profile of the CO<sub>2</sub>-reacted sample (top row) compared to control specimen (bottom row). Note the general depletion of elemental components that are associated with minerals that are susceptible to dissolution. These trends are only detected at the lower micron resolution presented above.

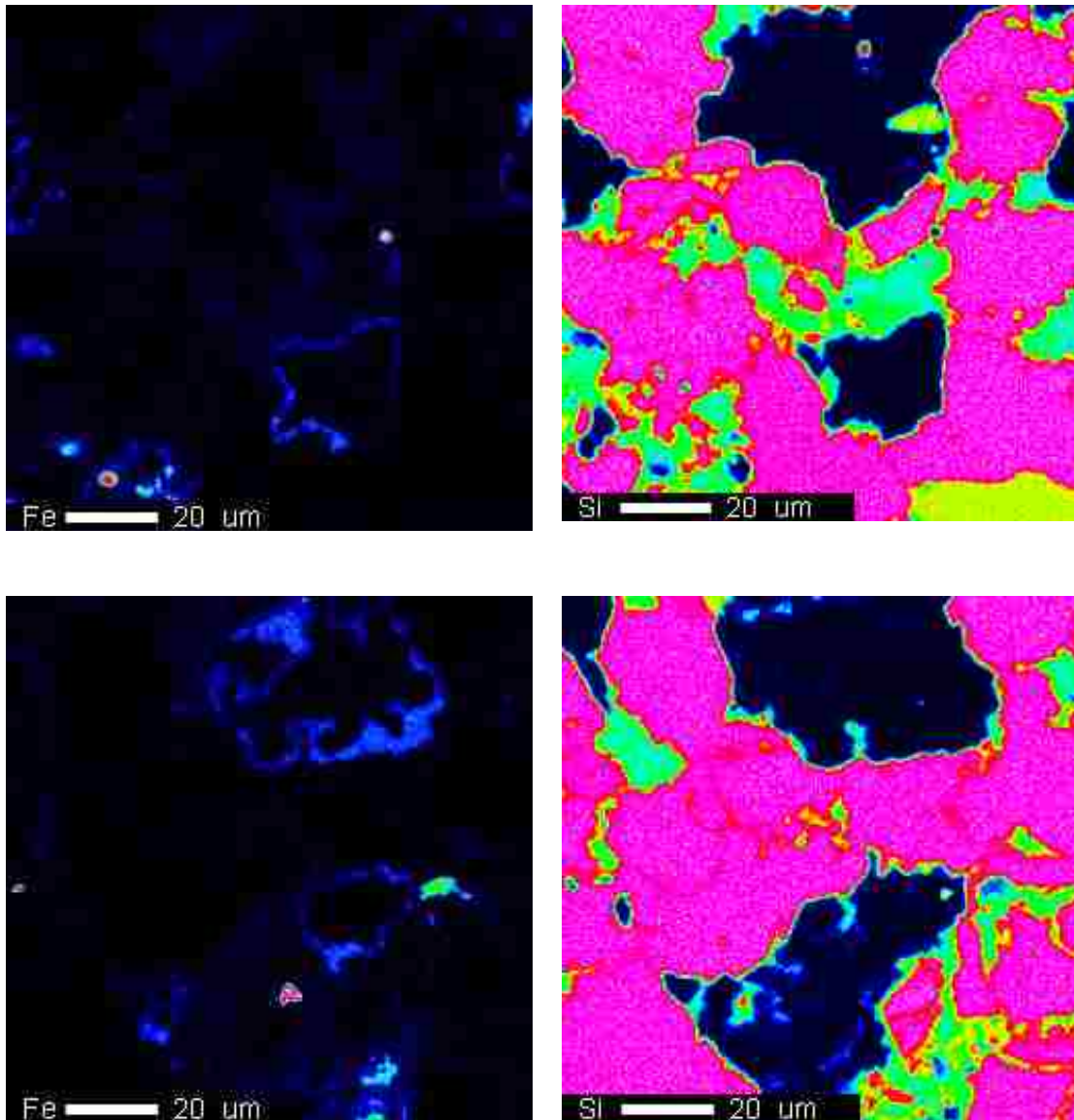


Figure 4.27: 20µm Electron Micro-Probe Analysis for **the Mancos shale** showing Iron (Fe) and silicon (Si) surface geochemical profile of the CO<sub>2</sub>-reacted sample (top row) compared to control specimen (bottom row). Note the general depletion of elemental components that are associated with minerals that are susceptible to dissolution. These trends are only detected at the lower micron resolution presented above.

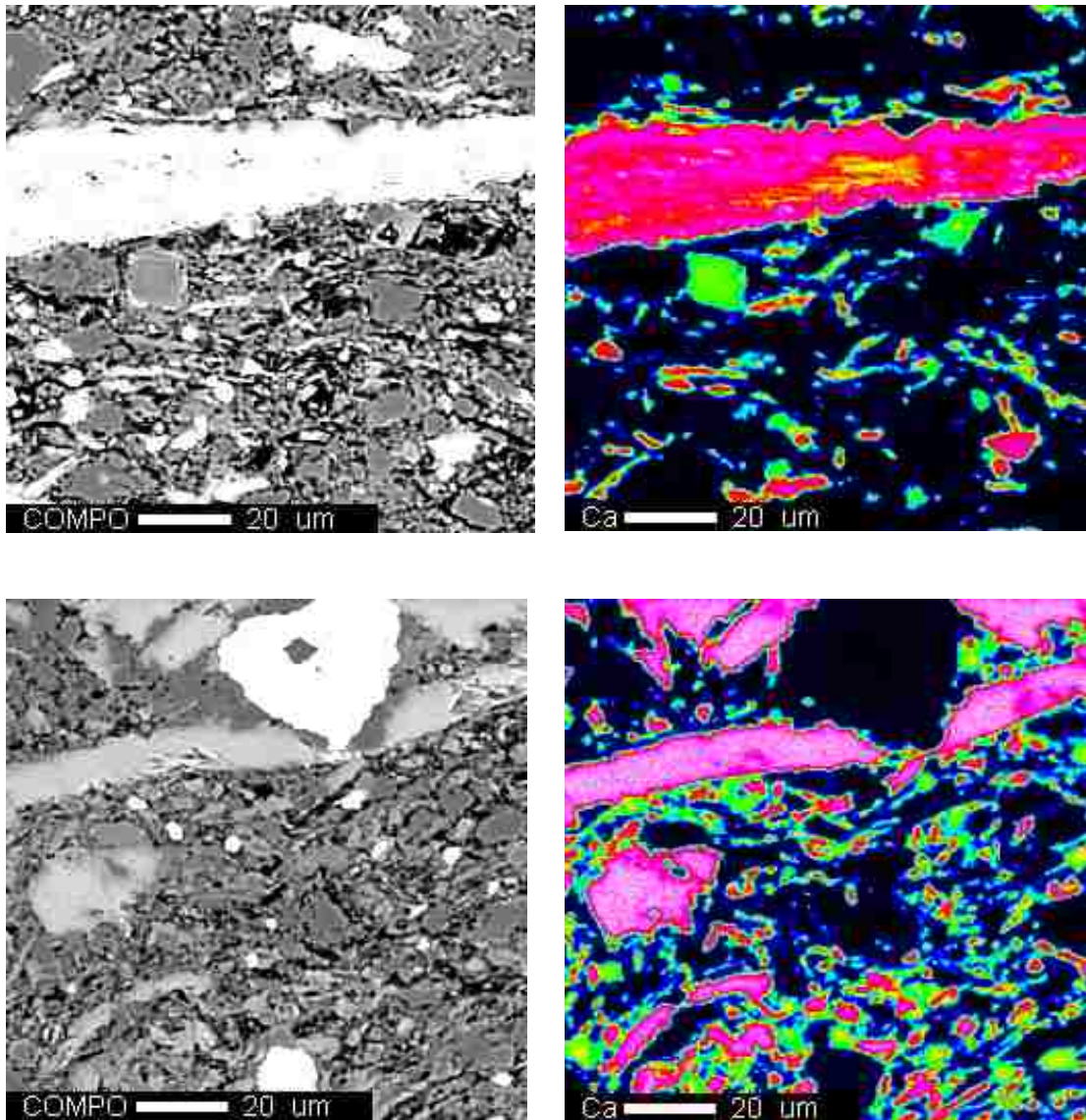


Figure 4.28: 20μm Electron Micro-Probe Analysis for **the Marcellus shale** showing the Calcium (Ca) surface geochemical profile of the CO<sub>2</sub>-reacted sample (top row) compared to control specimen (bottom row). Note the general depletion of elemental components that are associated with minerals that are susceptible to dissolution. These trends are only detected at the lower micron resolution presented above.

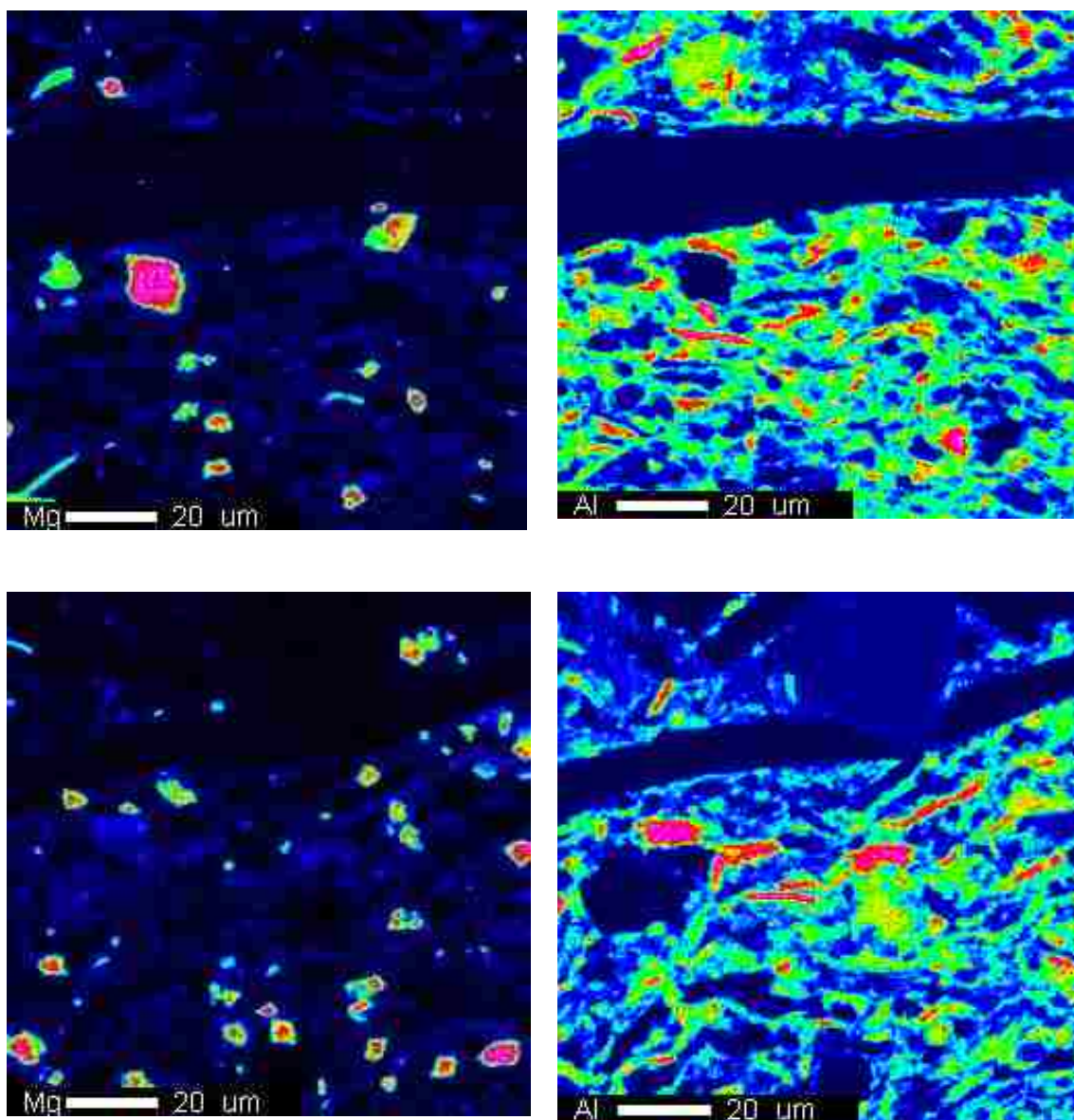


Figure 4.29: 20μm Electron Micro-Probe Analysis for **the Marcellus shale** showing Magnesium (Mg) and Aluminum (Al) surface geochemical profile of the CO<sub>2</sub>-reacted sample (top row) compared to control specimen (bottom row). Note the general depletion of elemental components that are associated with minerals that are susceptible to dissolution. These trends are only detected at the lower micron resolution presented above.

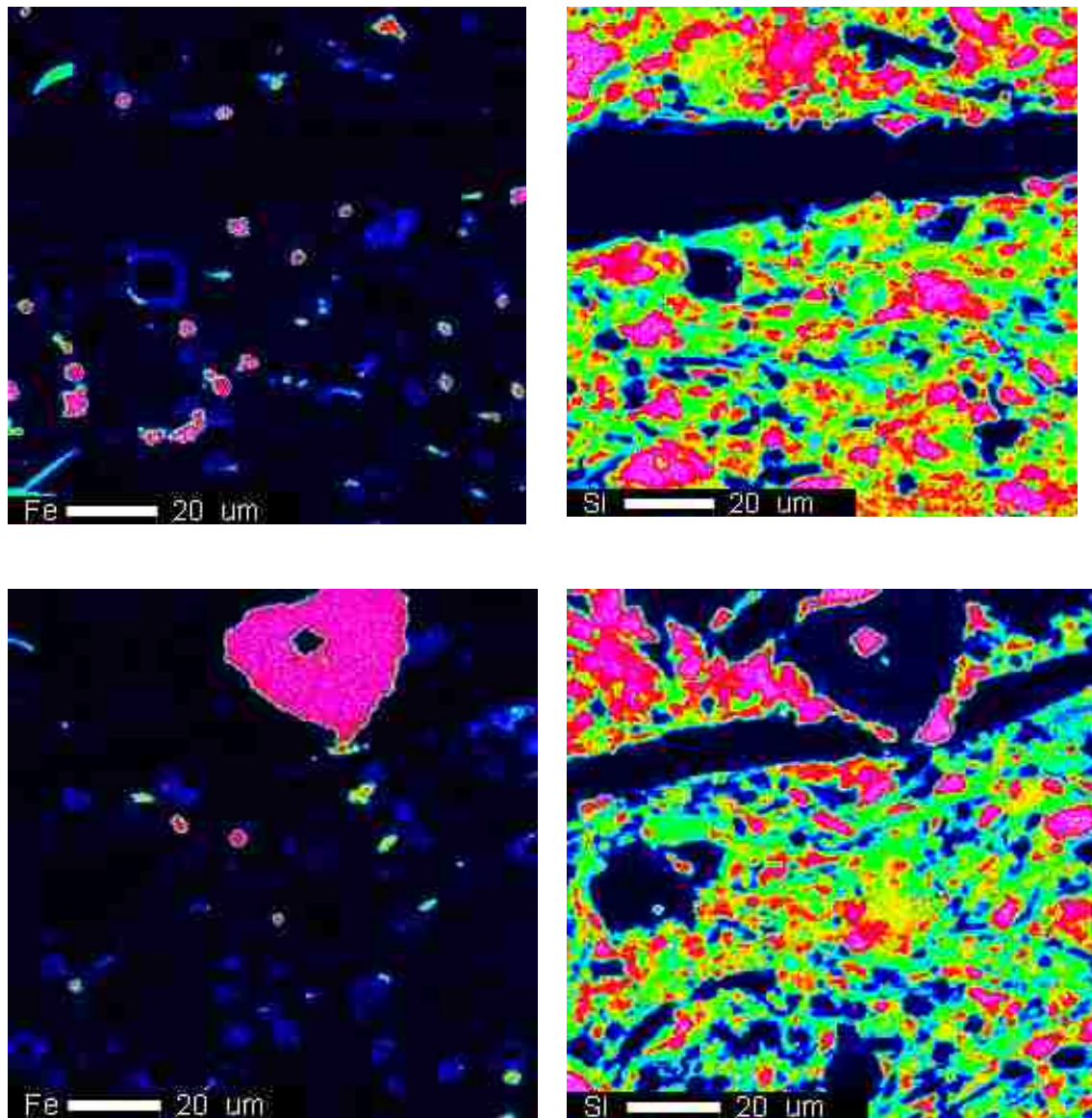


Figure 4.30: 20 $\mu$ m Electron Micro-Probe Analysis for **the Marcellus shale** showing Iron (Fe) and silicon (Si) surface geochemical profile of the CO<sub>2</sub>-reacted sample (top row) compared to control specimen (bottom row). Note the general depletion of elemental components that are associated with minerals that are susceptible to dissolution. These trends are only detected at the lower micron resolution presented above.

form compounds which are generally soluble in acidic or alkaline fluids, Ca and Mg solutes have significant ion-exchange capacity as well. The surface depletion within grains show the extent of the reach of aqueous CO<sub>2</sub> in supporting dissolutive rock-fluid interaction in the subsurface. Pottsville and Wilcox shales are lean in Ca and Mg based minerals which informed the limited traces of these elements on the surface of the thin section samples. The distribution of Al and Fe as shown in figures 4.26/27 and figures 4.29/30 for Mancos and Marcellus shales respectively indicated low activity in the reacted samples while figures 4.31 to 4.33 and figures 4.34 to 4.36 for Pottsville and Wilcox shales respectively reflected significant concentration of Al and Fe which have smaller percentages in the minerals bearing them. These imply that compounds of Ca, Mg, Al, and Fe which were identified in the shale caprock samples, either as major or trace minerals, would be reactively soluble with faster kinetics in aqueous CO<sub>2</sub> with the possibility of re-precipitation to form new minerals at subsurface pressure and temperature. The formation of Aragonite in experiments involving Marcellus shale exemplify the dissolution-precipitation processes that impact long term caprock integrity. The ratio of the elements identified at the surface of the samples over the 5 days of CO<sub>2</sub>-brine flooding showed mixed variations which could be partially attributed to mineral dissolution/precipitation and sample heterogeneity. Though the EMPA images were not shot on exactly the same rock piece thin section, the compared images in most of the specimen analyzed pointed to surface alterations as a result of reactive rock-fluid interaction in the shale rock samples. Additional data on these EMPA results are available in the appendix. Furthermore, the electron microprobe can function like a scanning electron microscope (SEM) and obtain highly magnified secondary- and backscattered-electron images of a sample under vacuum conditions.

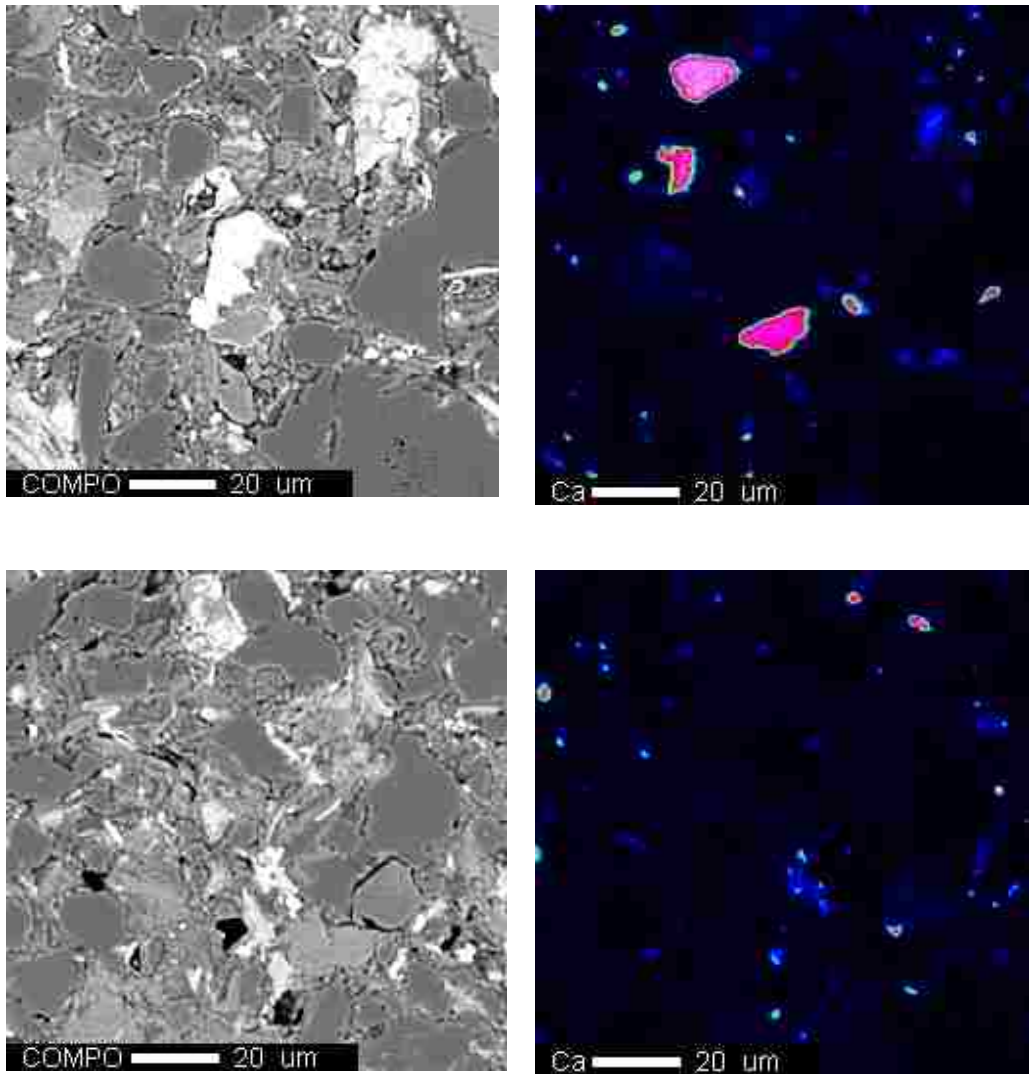


Figure 4.31: 20 $\mu$ m Electron Micro-Probe Analysis for **the Pottsville shale** showing the Calcium (Ca) surface geochemical profile of the CO<sub>2</sub>-reacted sample (top row) compared to control specimen (bottom row). Note the general depletion of elemental components that are associated with minerals that are susceptible to dissolution. These trends are only detected at the lower micron resolution presented above.

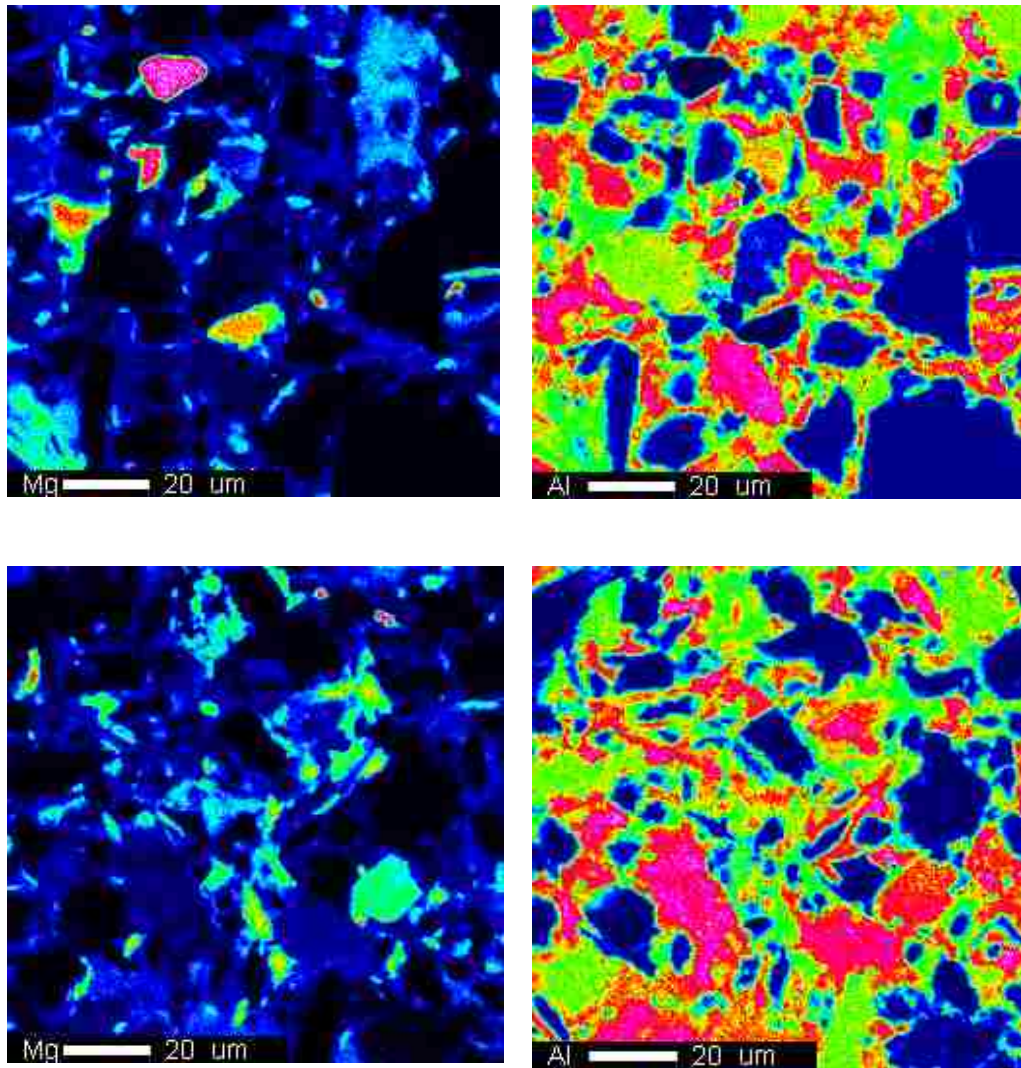


Figure 4.32: 20 $\mu$ m Electron Micro-Probe Analysis for **the Pottsville shale** showing Magnesium (Mg) and Aluminum (Al) surface geochemical profile of the CO<sub>2</sub>-reacted sample (top row) compared to control specimen (bottom row). Note the general depletion of elemental components that are associated with minerals that are susceptible to dissolution. These trends are only detected at the lower micron resolution presented above.

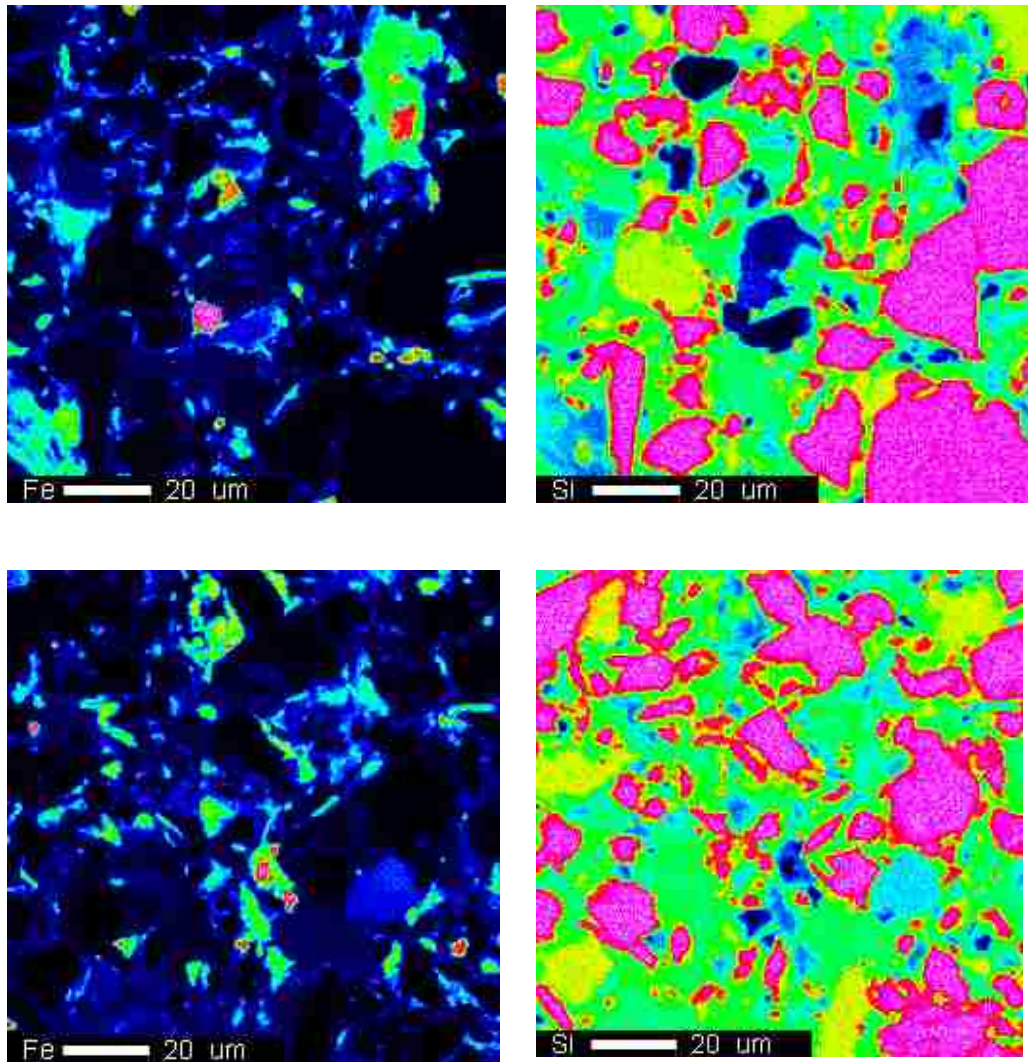


Figure 4.33: 20 $\mu$ m Electron Micro-Probe Analysis for **the Pottsville shale** showing Iron (Fe) and silicon (Si) surface geochemical profile of the CO<sub>2</sub>-reacted sample (top row) compared to control specimen (bottom row). Note the general depletion of elemental components that are associated with minerals that are susceptible to dissolution. These trends are only detected at the lower micron resolution presented above.

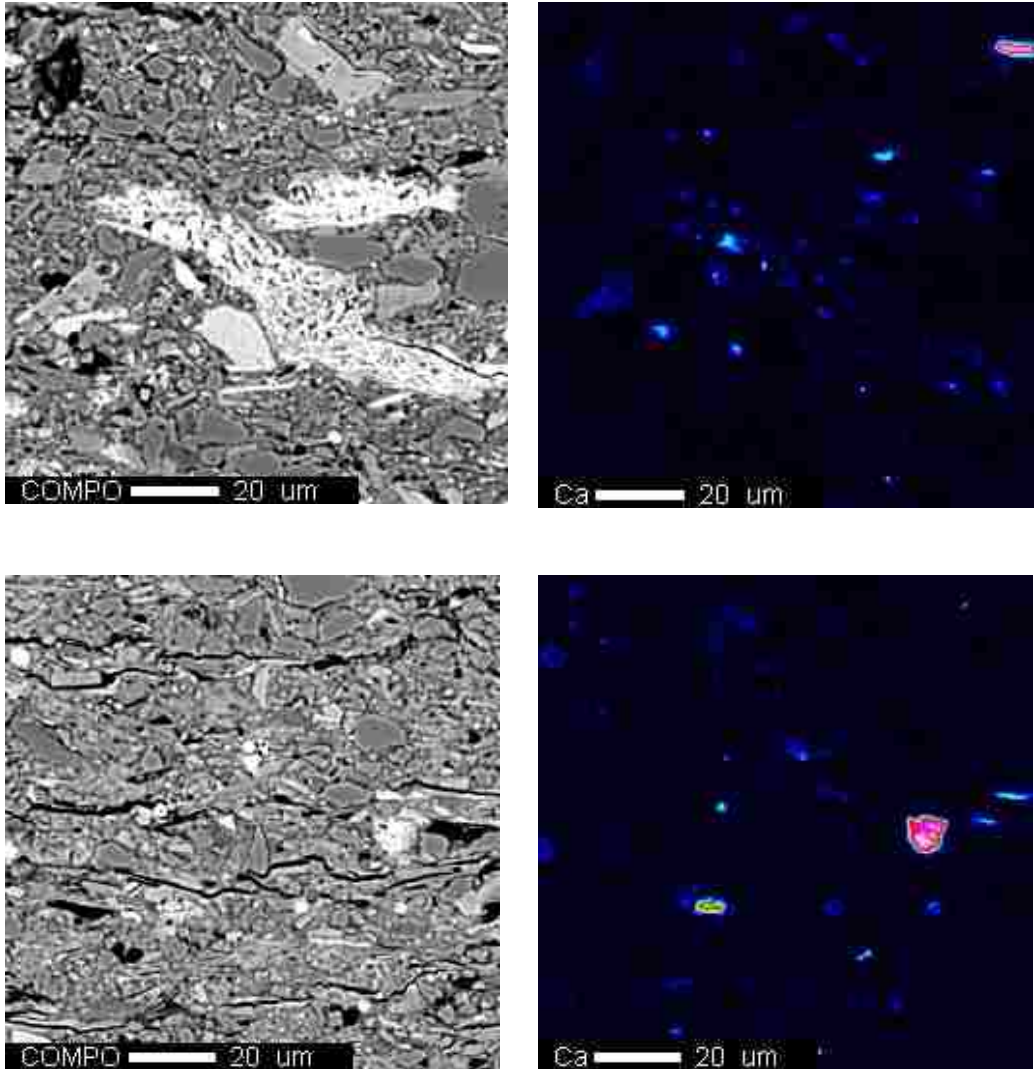


Figure 4.34: 20 $\mu$ m Electron Micro-Probe Analysis for **the Wilcox shale** showing the Calcium (Ca) surface geochemical profile of the CO<sub>2</sub>-reacted sample (top row) compared to control specimen (bottom row). Note the general depletion of elemental components that are associated with minerals that are susceptible to dissolution. These trends are only detected at the lower micron resolution presented above.

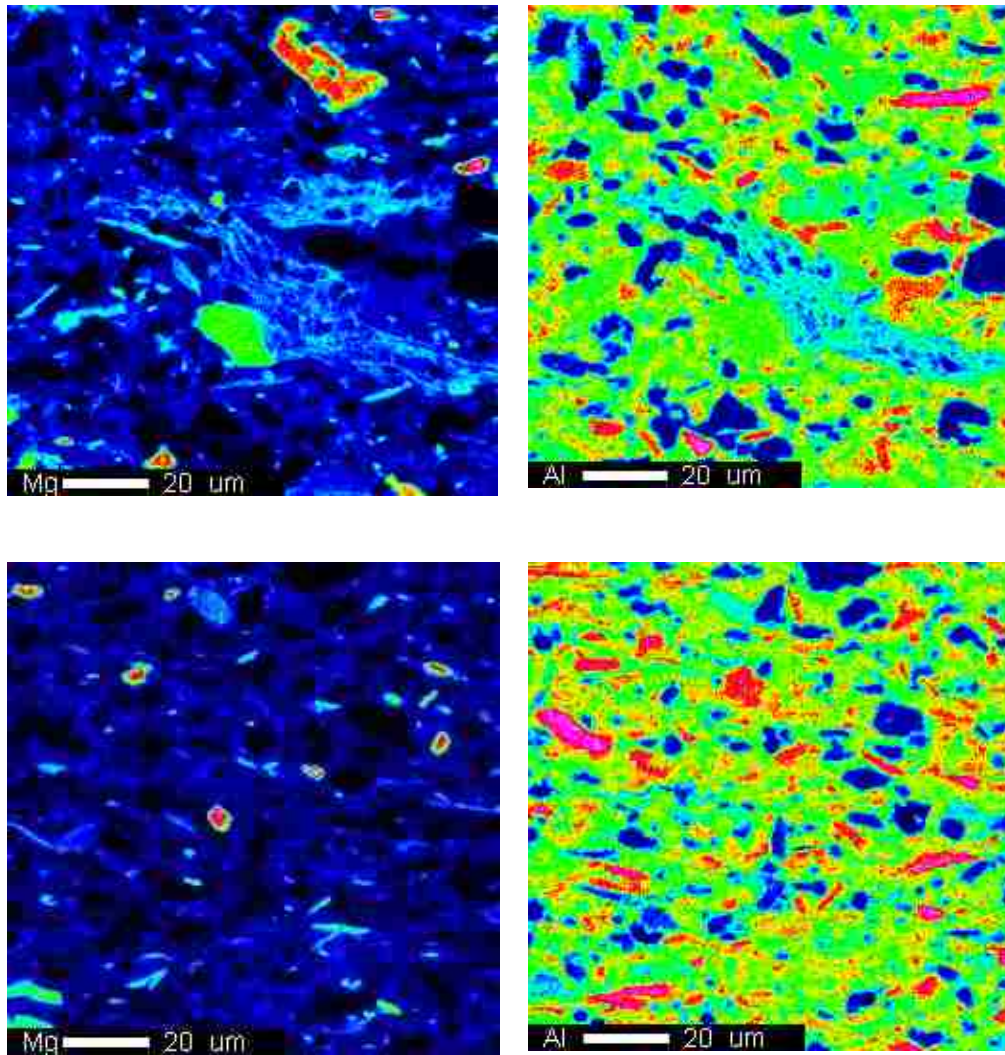


Figure 4.35: 20 $\mu$ m Electron Micro-Probe Analysis for **the Wilcox shale** showing Magnesium (Mg) and Aluminum (Al) surface geochemical profile of the CO<sub>2</sub>-reacted sample (top row) compared to control specimen (bottom row). Note the general depletion of elemental components that are associated with minerals that are susceptible to dissolution. These trends are only detected at the lower micron resolution presented above.

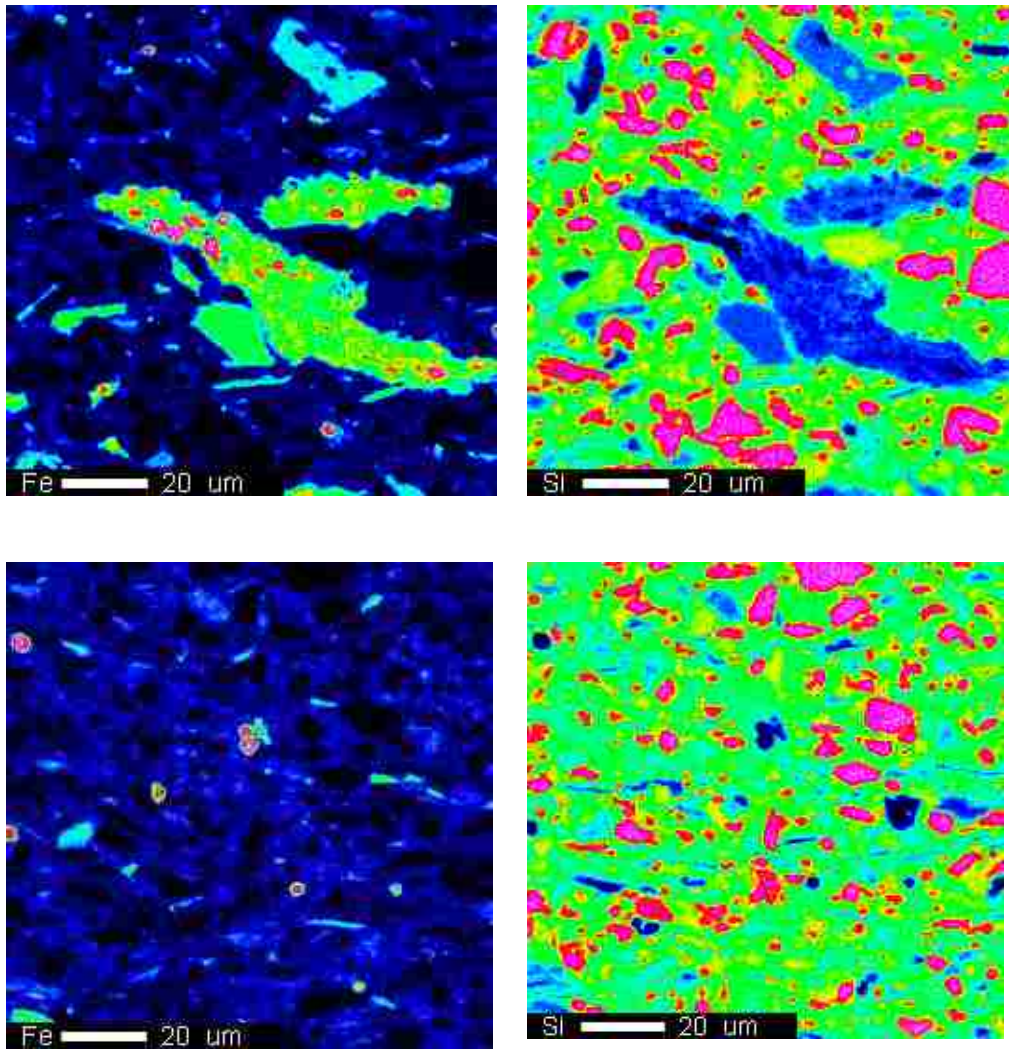


Figure 4.36: 20 $\mu$ m Electron Micro-Probe Analysis for **the Wilcox shale** showing Iron (Fe) and silicon (Si) surface geochemical profile of the CO<sub>2</sub>-reacted sample (top row) compared to control specimen (bottom row). Note the general depletion of elemental components that are associated with minerals that are susceptible to dissolution. These trends are only detected at the lower micron resolution presented above.

#### 4.6 Micro-Indentation of Rock Samples

Micro-indentation analyses were performed on polished samples of the shale rocks with the aim of determining the extent of possible changes in hardness level of the rocks after the CO<sub>2</sub>-brine flooding experiment. The following set of conditions were used in all the indentation experiments: the maximum force used was 10 N; the loading and unloading rates were kept the same at 10 N/min; the pause at maximum load was 30 seconds; the contact load was 30 mN. The hardness was obtained with computational method from Oliver and Pharr [219]. The indenter type was Vickers' diamond with the Poisson coefficient of 0.07. There are scientific documentation of using this method for nano-indentation of pure clay minerals [220].

Figure 4.37 shows the Vickers' micro-hardness measurements acquired on the samples with the error bar equivalent of standard deviation (SD) from three experimental runs per sample. There was noticeable decrease in the hardness of the Mancos, Marcellus and Wilcox shale rocks in that order with the Pottsville shale showing little to no change at the moderate temperature and pressure conditions in which the experiments were performed.

This might indicate a weakening of the shale rocks under carbon sequestration conditions in the case of pervasive CO<sub>2</sub> intrusion into the overlaying caprock or most importantly at the seal rock-reservoir rock interphase where the impact of the injected CO<sub>2</sub> plume will be most significant. The impact of higher temperature and pressure conditions is recommended to be investigated in subsequent experimental research involving shale-aqueous CO<sub>2</sub> interactions. Experimental set up for the indentation is annotatively explained in the appendix A. Figures 4.38 shows the Young's Modulus equivalent of the Vickers' hardness and figure 4.39 attempted to combine the two parameters. YM and HV refers to Young's Modulus and Vickers' Hardness respectively. The

results show loss of geomechanical hardness particularly for the samples that are most susceptible to dissolution i.e. The Mancos and Marcellus shale rocks. The significant difference between the profiles of the Young Modulus and Vickers' Hardness is explained in the computation properties of the rock used. Vickers' Hardness captured more variations in the properties of the reacted samples when compared with the controls after the five days of the experiment. These two properties have been shown in other data acquired on engineered materials not to have any correlation. They were independently analyzed in this section for the impact of geochemical changes at the surface. Heterogeneity in material composition is believed to have significant effect on the trends that can be obtained for geomechanical properties.

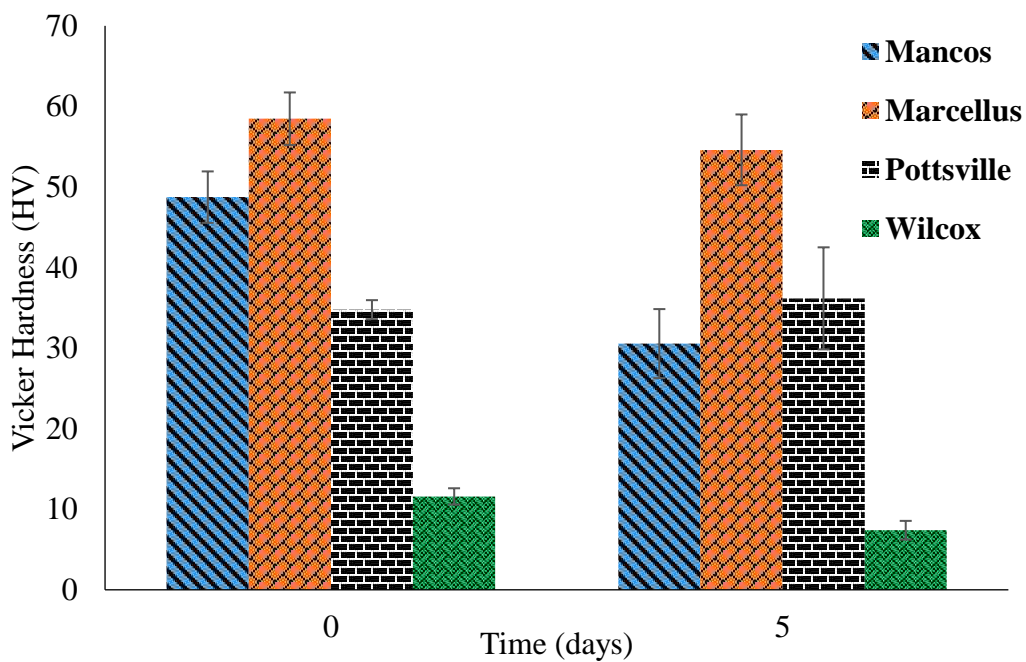


Figure 4.37: **the Vickers' micro-hardness** measurement taken on multiple samples of the experimental shale rocks. The results indicated a mild reduction in geomechanical hardness of the rock samples which are most significant in the Mancos, Marcellus and Wilcox shale rocks with lower quartz contents. This implies that initial quartz composition of shaly caprocks might be important in maintaining geomechanical integrity in long term CO<sub>2</sub> sequestration.

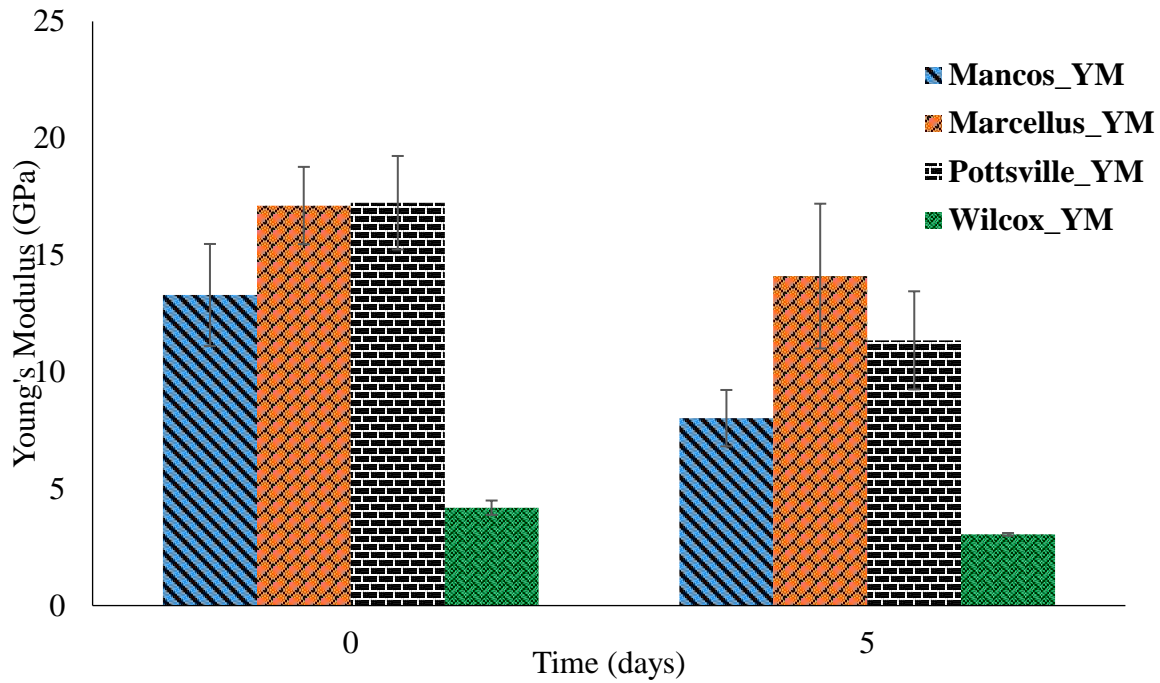


Figure 4.38: **Young's Modulus (GPa)** plots showing across the board decreases in measured values for the shale caprocks after flooding with CO<sub>2</sub>-brine at 50°C and 1000psi.

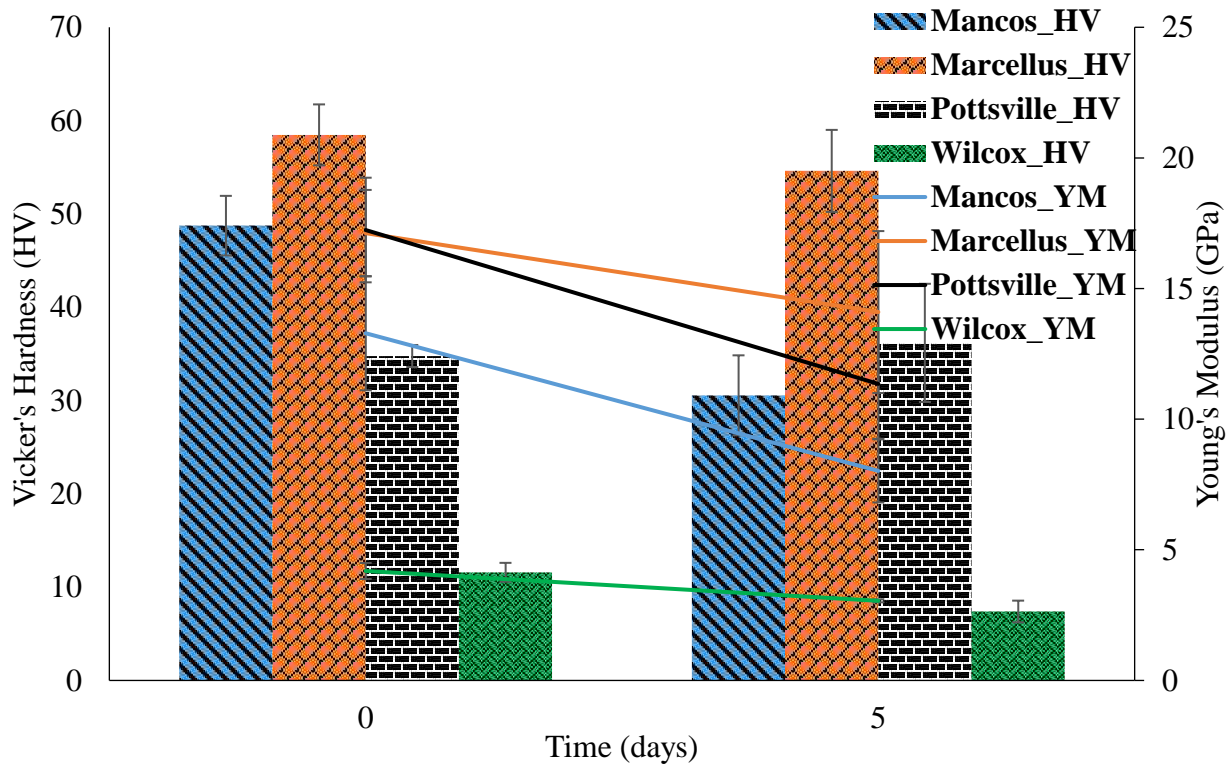


Figure 4.39: **Combined Hardness and Young's Modulus** plots showing across the board decreases in measured values for the shale caprocks after flooding with CO<sub>2</sub>-brine at 50°C and 1000psi.

Figure 4.40 shows a plot of magnitude change in Vickers' hardness versus changes in the mineralogical composition of the shale rocks with respect to quartz, clay and carbonates. It can be suggested that formation of diagenetic quartz could improve the hardness of the shale rock as observed in the Pottsville shale where the percentage change in quartz content exceeded 10% which likely resulted from the clay fractions that were reduced by almost 15%. Significant reduction in clay and carbonates fraction of the shale rock which did not necessarily transformed to diagenetic quartz, as observed in the Mancos, Marcellus and Wilcox shale rocks, could shrink the geomechanical hardness of the rock. Higher temperature and pressure experiment could be used to confirm this observation.

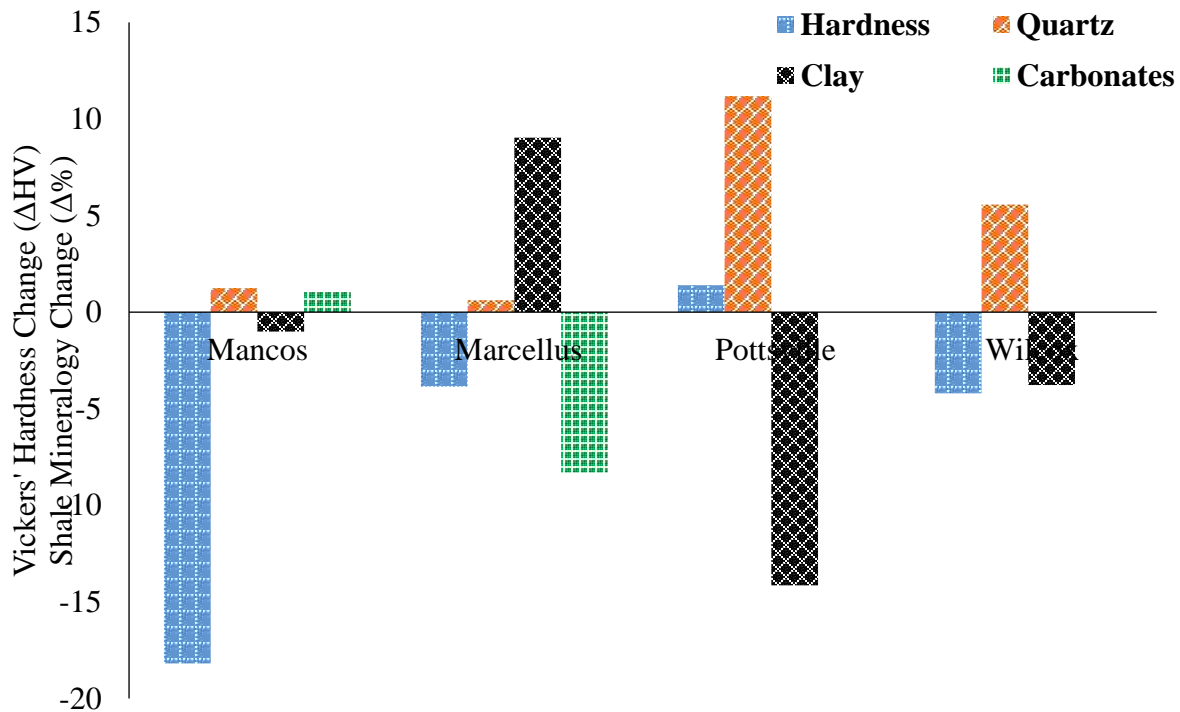


Figure 4.40: A correlation between the hardness of the shale rock and quantifiable mineralogical change in percentages. The graph shows that formation of diagenetic quartz can improve the hardness of the shale rock as observed in **Pottsville shale**. Significant reduction in clay and carbonates fraction of the shale rock, as observed in the **Mancos, Marcellus and Wilcox shale rocks**, can shrink the geomechanical hardness of the rock.

#### 4.7 Differential Pressure Analysis

Differential pressure drop data acquired during the experimental runs were analyzed for flow inferences and diagnostics. Each shale caprock type had associated experimental runs that acquired multiple differential pressure data over a 5-day period. For example, three experimental runs were performed on the Mancos shale using composite fractured cores (**25 $\mu$ m and 150 $\mu$ m micro-tubing embedded**) with reaction effluent flowing through. This yielded thousands of differential pressure data points at 20 secs interval that were averaged for diagnostic and flow characteristic trends. These experimental runs were the same for other shale caprock types. These flow experiments were repeated for composite fractured cores with 150 $\mu$ m micro-tubing embedded for all the shale caprock types. The results of the averaged differential pressure data (dP), the 1<sup>st</sup> derivative of the differential pressure (dP/dt) and the estimated fracture conductivity are presented in figures 4.41 to 4.46. A comparison of the two fracture conductivity profiles are presented in figure 4.47. The effective fracture width was first estimated which formed a major input for the calculation of dimensionless fracture conductivity. The differential pressure drop, dP, data acquired during the experiment are presented in figures 4.41 (**for 25 $\mu$ m micro-tubing embedded cores**) and 4.42 (**for 150 $\mu$ m micro-tubing embedded cores**).these are averaged data points of pressure measurement acquired per every 20 seconds.

Figures 4.43 and 4.44 show the 1<sup>st</sup> order derivative of the differential pressure data for all the samples used in the experiment involving 25 $\mu$ m and 150 $\mu$ m micro-tubing embedded cores respectively. The results showed a gradual increase in the differential pressure (dP) drop across the composite core as dissolved precipitates laden fluid in flowed through it under equivalent temperature and pressure conditions prevailing in the whole closed system. These dP

measurements were acquired to tract the possibility of micro-fracture occlusion as a result of intra-fracture path precipitation. The differential pressure drop profiles (figures 4.41 and 4.42) showed significant increases within the initial two days of the experiment which gradually stabilized in the last three days. It will be noted that the stabilized value (or peak) of the pressure drops for the 150 $\mu$ m fractured cores profile (figure 4.42) is about half of the stabilized peak for 25 $\mu$ m composite fractured cores (figure 4.41). These profiles are indicative of possible particulate build up along conductive flow paths in the fractured composite cores.

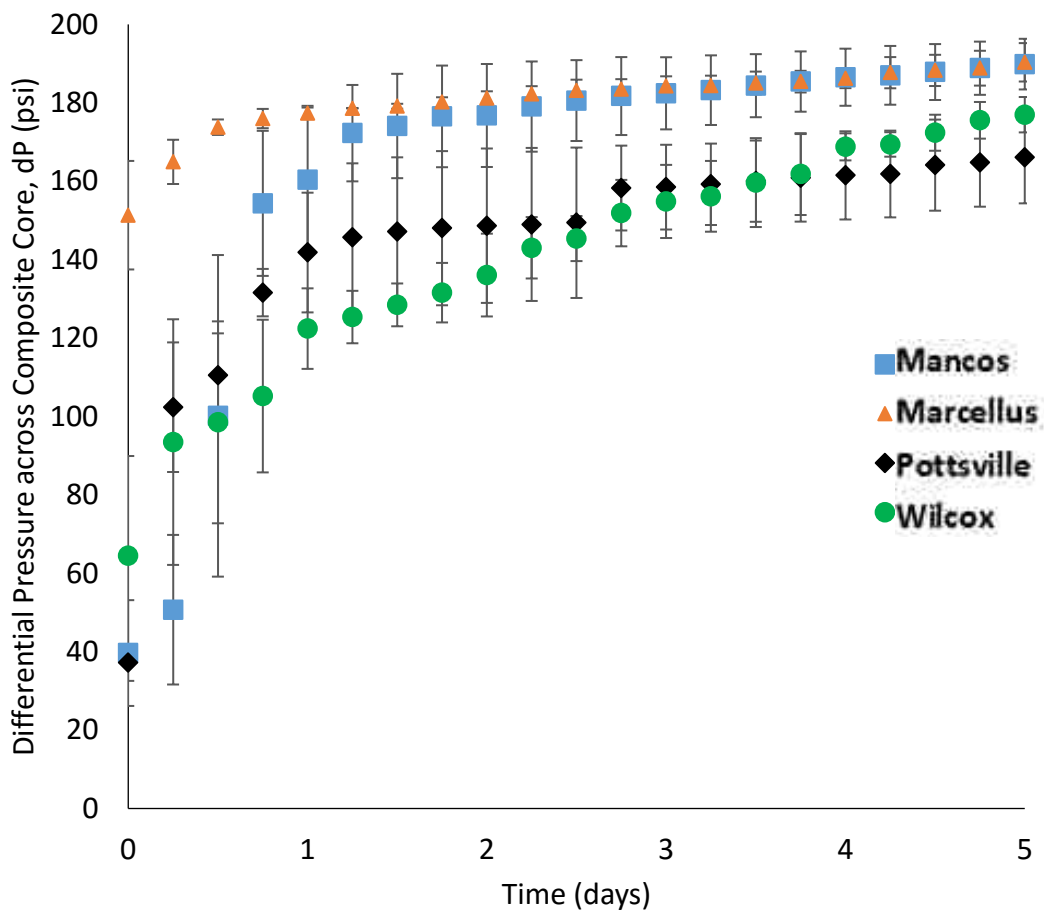


Figure 4.41: Average differential pressure profile across the **25 $\mu$ m composite core**, with embedded micro-tubings to mimic fractures. The injected fluid was directly from the outlet of the packed bed of crushed shale rock samples. Each data point represented a moving average from the three experimental runs per shale rock samples.

The first derivative of dP data as shown in figure 4.43 reveals that the most significant change to pressurized flow occurred in the first two days of starting the experiment for all the shale rock samples considered. The large fracture cores have similar behavior as expected (figure 4.44). It can be inferred that the impact of reactive flow on micro-fracture conductivity under carbon sequestration conditions will be most significant in the short term with the effect tapering off over the long term. The impact of high temperature and pressure conditions need to be investigated in subsequent experiments. The pressure profiles and their 1st derivatives are important in capturing the onset of changes in fracture flow and behavior. The estimation of fracture conductivity provides a quantitative view of these changes.

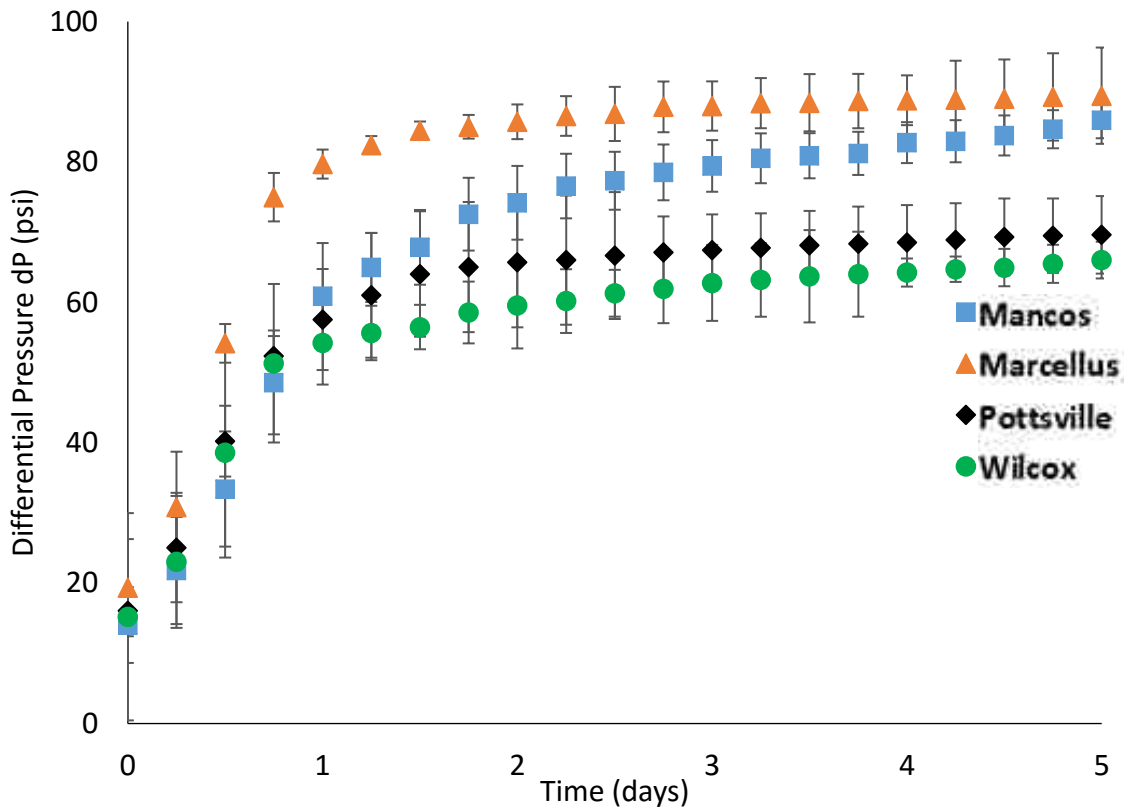


Figure 4.42: Average differential pressure profile across **150µm composite core**, with embedded micro-tubings to mimic fractures. The injected fluid was directly from the outlet of the packed bed of crushed shale rock samples. Each data point represented a moving average from the three experimental runs per shale rock samples.

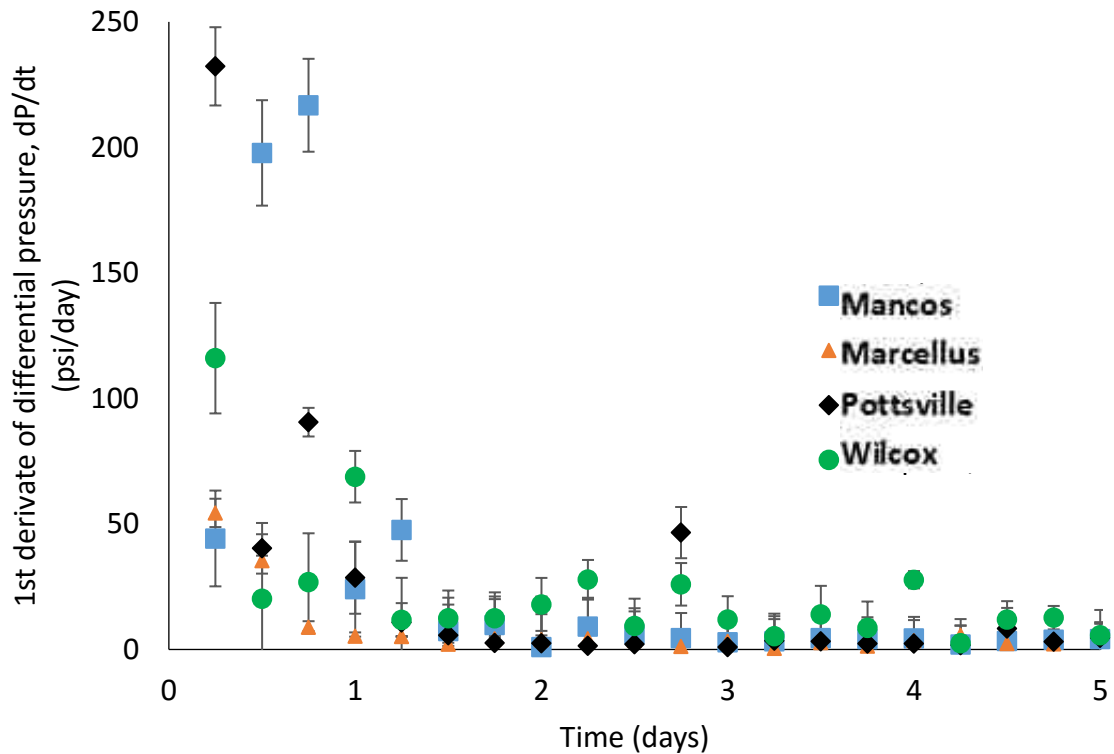


Figure 4.43: Average first derivative of differential pressure drop across the **25 $\mu$ m composite core**, with embedded micro-tubings to mimic fractures. The injected fluid was from directly from the outlet of the packed bed of crushed shale rock samples. The profile showed that most significant changes to pressurized flow behavior occurred within the first two days of the experiment. This probably due to flow path occlusion.

The use of pressure derivative is to help identify possible inflection points that could be diagnostic of the pressure responses. The acquisition of thousands of differential pressure data is useful in this regard. Laboratory transient pressure analysis provides a description of the fracture flow behavior though the length and geometry of the effect fracture in these experiments are several order of magnitude shorter than that obtained in the field. The observations from the pressure derivative presented in this report showed conclusively that day 2 of the experiments was the most significant for flow properties change.

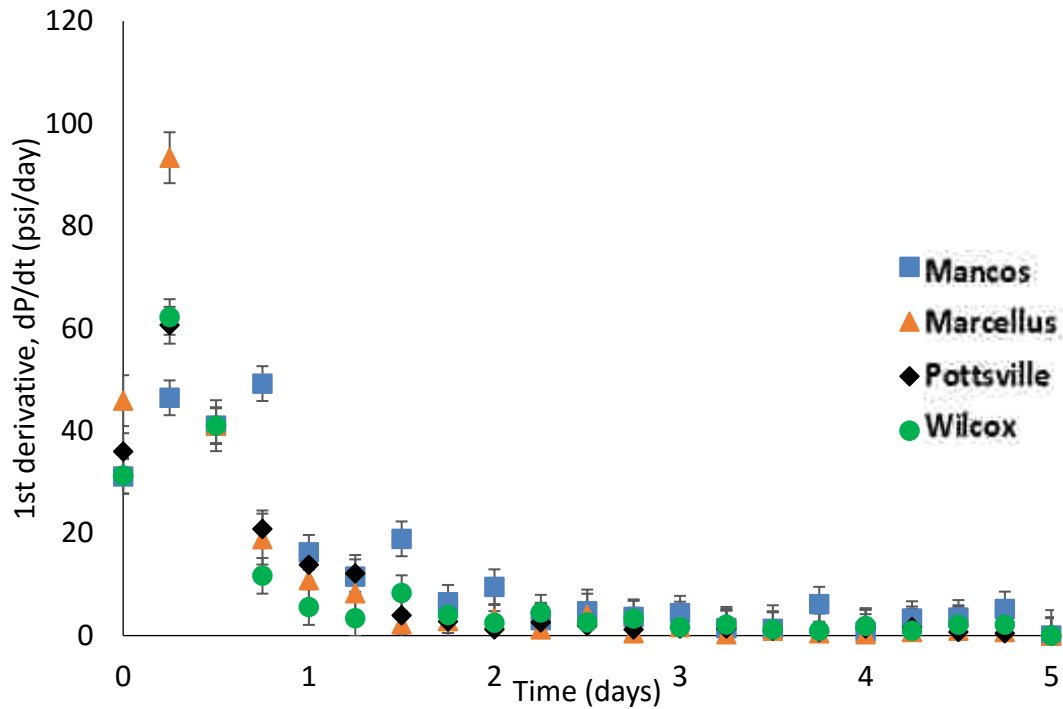


Figure 4.44: Average first derivative of differential pressure drop across the **150 $\mu$ m composite core**, with embedded micro-tubings to mimic fractures. The injected fluid was from directly from the outlet of the packed bed of crushed shale rock samples. The profile showed that most significant changes to pressurized flow behavior occurred within the first two days of the experiment. This probably due to flow path occlusion.

#### 4.8 Fracture Conductivity Estimation

The fracture conductivity of the multiple composite fractured cores were estimated using the equations proposed by Dicman et al., [193, 221], and Warren and Root [222] for flow in fractures. Each shale caprock type had associated experimental runs that acquired multiple differential pressure data over a 5-day period. For example, three experimental runs were performed on the Mancos shale using composite fractured cores (25 $\mu$ m micro-tubing embedded) with reaction effluent flowing through. This yielded differential pressure data points at 20 secs interval that were averaged for diagnostic and flow characteristic trends. These experimental runs were the

same for other shale caprock types. These flow experiments were repeated for composite fractured cores with 150 $\mu$ m micro-tubing embedded for all the shale caprock types. The results of the estimated fracture conductivity are presented in figures 4.45 to 4.47. The effective fracture width was first estimated which formed a major input for the calculation of dimensionless fracture conductivity. The critical assumptions were i.) flow was primarily through fractures ii.) bulk fracture flow properties are captured in the experimental differential pressure measurements ii.) CO<sub>2</sub>-brine viscosity was constant throughout the experiment iii.) the length of the core approximates the fracture length. Using equations 4.1 to 4.8;

$$k_f = 8.45 \times 10^9 w_f^2 \quad \text{Eq. 4.1}$$

$$k_f = \frac{k_{av}A - k_m(A - w_f l)}{w_f l} \quad \text{Eq. 4.2}$$

$$8.45 \times 10^9 w_f^3 l - k_{av}A + k_m(A - w_f l) = 0 \quad \text{Eq. 4.3}$$

$$q_m = \frac{k_m A \Delta P}{\mu L} \quad \text{Eq. 4.4}$$

$$q_f = 9.86 \times 10^9 \frac{w_f^3 l \Delta P}{12 \mu L_f} \quad \text{Eq. 4.5}$$

$$w_f k_f = \pi C_r k L_f \quad \text{Eq. 4.6}$$

$$w_f = \sqrt[3]{\frac{q_f \times 12 \mu}{9.86 \times 10^9 \Delta P}} \quad \text{Eq. 4.7}$$

$$C_r = \frac{w_f k_f}{\pi K_{av} L_f} \approx \frac{w_f}{\pi L_f} \quad \text{Eq. 4.8}$$

Where  $\Delta P$ ,  $w_f$ ,  $l$ ,  $L_f$ ,  $k_m$ ,  $k_f$ ,  $k_{av}$ ,  $A$ ,  $q_m$ ,  $q_f$ ,  $\mu$ , and  $C_r$  represent differential pressure (atm), fracture width (cm), core diameter (cm), fracture length (cm), matrix permeability (darcy), fracture permeability (darcy), average permeability (darcy), cross sectional area (cm<sup>2</sup>), flow rate through matrix (cm<sup>3</sup>/sec), flow rate through fracture (cm<sup>3</sup>/sec), viscosity (cp) and dimensionless fracture conductivity respectively.

Figure 4.45 shows the dimensionless fracture conductivity for flow through the artificially fractured composite cores (with 25 $\mu$ m micro-tubings embedded), calculated using equation 4.8. The profile suggests that the conductivity of the fractures degenerated rapidly within the first day of the experiment, tapering off at a constant rate towards the end of the experiment. The data presented in figure 4.45 were based on three experimental runs per shale rock sample with the error bar representing the standard deviation values. The fracture conductivity profile for the experiments that were conducted using fractured composite cores with 150 $\mu$ m micro-tubing embedded showed similar trend in rapid conductivity loss within the initial two days of the experiments (figure 4.46). With the recovery of significant amount of precipitates from effluent fluid, it can be inferred that in-situ geochemical precipitation was responsible for the loss of fractured conductivity as differential pressure drop across the cores built up and later stabilized during the experiments. It is estimated that only few micron size particulates are required to completely occlude fracture flow paths. It also appears there is no direct linear correlations between the fracture conductivity trends and the micro-tubings sizes that were used during the experiment. Chapters 5 and 6 explored the attempts at fitting the experimental data of the calculated fractured conductivity and reaction kinetics for some form of generalization.

Figure 4.47 compared the trends of the fracture conductivity of the 25 $\mu$ m cores with the 150 $\mu$ m cores. The extent of conductivity reduction is about 30% lower for the bigger micro-fractures (150 $\mu$ m). This indicates that there is a significant limit to fracture aperture closure due to geochemical effects. The data presented in figure 4.47 can be used for modelling the impact of diagenetic alterations within subsets of naturally fractured shale caprocks. The availability of more geochemical data and their impacts on flow properties in micro-fractures will help build more robust numerical approximations that can be applied field-wide. The number of shale rock samples used in these experimental reports fall within and outside those that have been reported in the literature. The fact that the larger the potential micro-fracture defects in an intact rock the less likely short-term diagenesis can seal them, implies that we can only depend to a limited extent on the ability of rock-aqueous CO<sub>2</sub> interactions to heal inherent anomalies in caprocks. The field-wide effects of this can be investigated with discrete fracture network studies. In many instances, modeling flow characteristics in fractured media can be through the use of the dual-continuum algorithm whereby fractures and matrix are modeled as two separate kinds of continua. These facsimile type of models usually do not replicate many commonly observed types of fractured tight rock characteristics as they do not explicitly model the shape of discrete fractures, geological inclusion features, and characteristic beddings that govern flow direction in the subsurface. One of the perceived issues with using DFN models to address this short coming is that the fractures in the model tend to be too uniform in length, area and spatial distribution but these features describe the interpretative assumptions made in this experimental report.

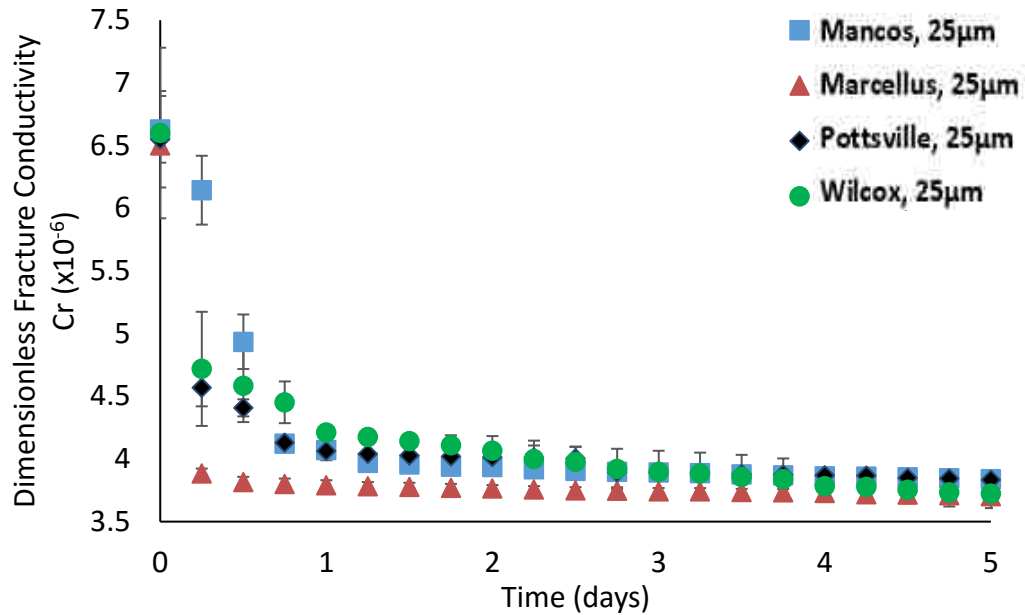


Figure 4.45: Calculated dimensionless fracture conductivity profile from experimental differential pressure (dP) data using fractured core parameters with **25 $\mu\text{m}$  micro-tubings embedded**. The profile indicated a rapid reduction in the conductivity of the artificial fractured core within the first two days of the experiment. This reduction can only be attributed to in-situ geochemical precipitation.

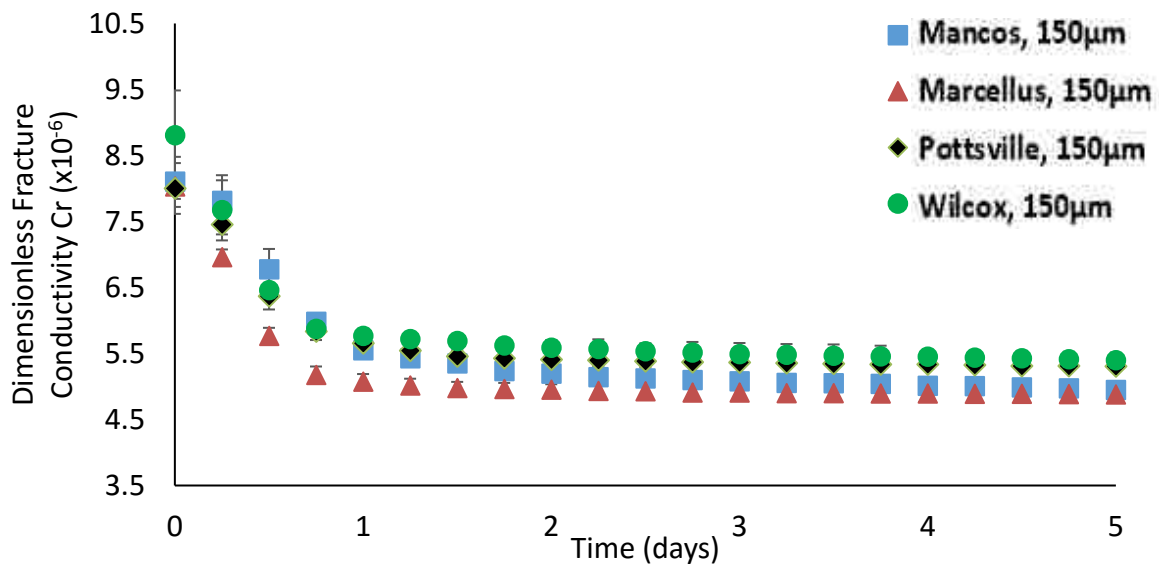


Figure 4.46: Calculated dimensionless fracture conductivity profile from experimental differential pressure (dP) data using fractured core parameters with **150 $\mu\text{m}$  micro-tubings embedded**. The profile indicated a rapid reduction in the conductivity of the artificial fractured core within the first two days of the experiment. This reduction can only be attributed to in-situ geochemical precipitation.

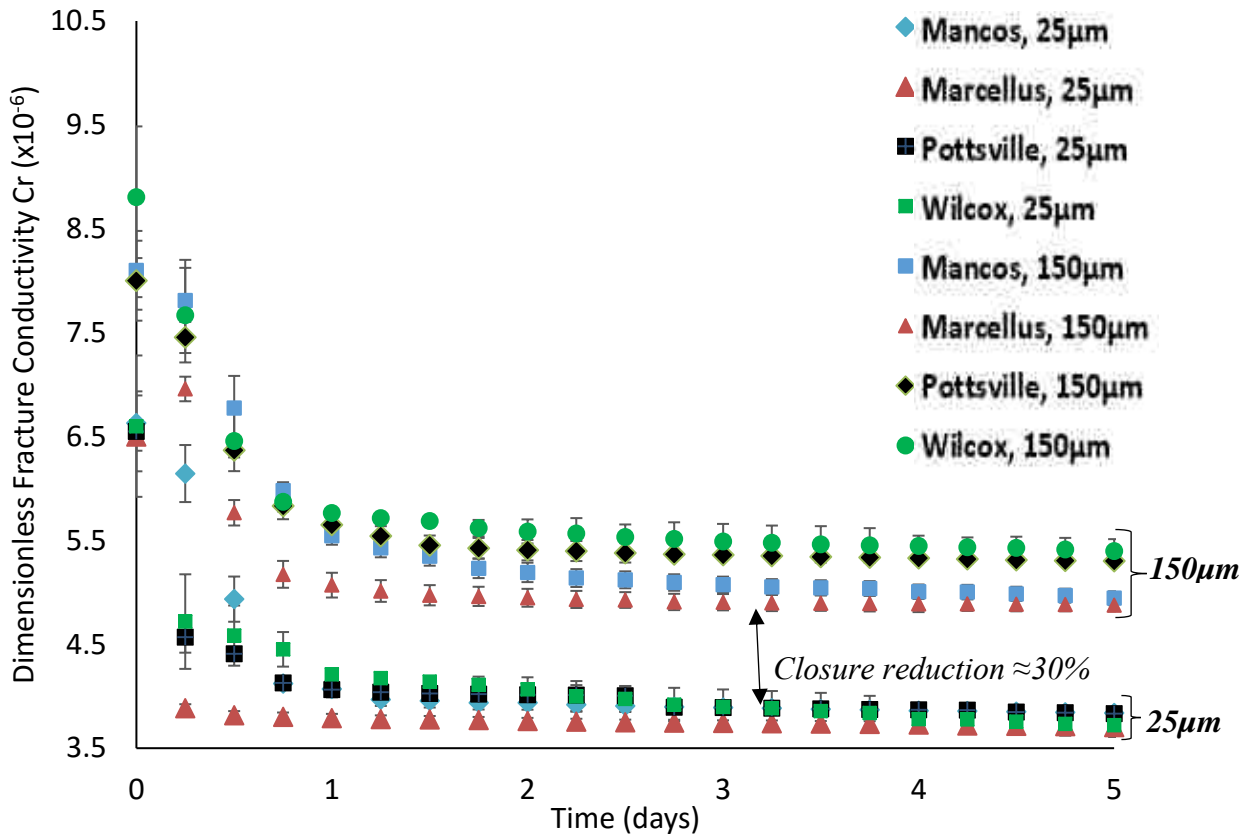


Figure 4.47: **Comparison** of calculated dimensionless fracture conductivity profile from experimental differential pressure (dP) data using fractured core parameters with **25µm and 150µm embedded micro-tubings**. The profile indicated a rapid reduction in the conductivity of the artificial fractured core within the first two days of the experiment. The extent of conductivity reduction is about 30% lower for the bigger micro-fractures (150µm). This indicates that there is significant limit to fracture aperture closure due to geochemical effects.

## CHAPTER 5

### DISCUSSION OF RESULTS OF SHALE ROCK/FLUID INTERACTIONS EXPERIMENTS

#### 5.1 General Discussion of Experimental Results

The detailed discussion of experimental results is presented in this chapter. The discussion is done under three sub-headings; (1) geochemical speciation in effluent fluid, (2) bulk rock/precipitates analysis, (3) fracture flow characterization. The discussion covers in detail the aqueous geochemistry of the resulting dissolved-mineral-saturated fluid (after rock-fluid interactions experiments) and the impact of rock-fluid interactions on surface and bulk rock geochemistry, including the precipitates that were recovered from the effluent. The effect of the convective transport of the geochemically active effluent through fractured media is also discussed; primarily differential pressure drop and micro-fracture conductivity. The impact of these phenomena are captured by the various analytical methods and techniques that were used for fluid, rock and fractured media characterization.

##### 5.1.1 Geochemical Speciation in Experimental Effluent Fluid

The geochemical characterization of the effluent fluid showed the most pronounced documentation of reactive rock-fluid interactions. The pH of the effluent fluid showed initial resilience to acidic fluid medium. The shaly rocks acted as alkaline buffering media where by the final effluent indicated geochemical reactions that brought acidity conditions up to and above neutral scale. It can be observed from the pH profile (figure 4.1) that the alkaline buffer strength of the shale rocks through reactive interaction with the CO<sub>2</sub>-brine fluid at the experimental pressure and temperature conditions is significantly pronounced for the Mancos, Marcellus and Pottsville shale rocks while that of the Wilcox shale is markedly lower. Many geochemical

reactions are dependent on the pH of the medium. It is expected that forward dissolution reactions will be encouraged under acidic pH conditions of CO<sub>2</sub> geo-sequestration. These observations are in agreement with previous experiments conducted in the laboratory and reported by other researchers. The changes in pH is expected to control, to some degree, the ability of the various rock minerals to exchange ions with one another. The diffusion and subsequent dissolution of free CO<sub>2</sub> molecules in the connate water of the caprock is expected to lead to localized ultra-low pH ranges that will catalyze pore and micro-fracture surface dissolution. The idea that supercritical CO<sub>2</sub> would sink to the deep bottom part of the reservoir brings the idea of convective transport of super-saturated acidic fluid into the overlaying seal rocks. This will have the same effect as gaseous CO<sub>2</sub> diffusion in the tight hydraulically connected spaces within the rock. The pH data reported suggest varying degrees of alkaline buffering strength of the rocks; the higher the fraction of calcium based minerals, the higher the alkaline buffering strength. This is consistent with literature reports.

The ICP-OES concentrations of both major and trace metals such as Ca<sup>2+</sup>, Mg<sup>2+</sup>, Se<sup>2+</sup>, Al<sup>3+</sup> Si<sup>2+</sup>, and Zn<sup>2+</sup> indicated rapid dissolution of rock minerals that have alkaline earth metals in their crystalline or amorphous matrices (figures 4.2 to 4.15). The concentration profile for Calcium shows that the Marcellus samples had the highest fraction in solution which rapidly decreased over the five day period of continuously flooding the samples with CO<sub>2</sub> saturated brine. The initial pH of the influent fluid is approximately 3.7. The Mancos, Marcellus and Wilcox shale rocks exhibited similarly trend of a gradual exponential decline over the five day period. The Pottsville shales reflected a gradual increase that appears to continue over the experimental period. While the elemental concentration of Calcium in the Mancos, Marcellus and Wilcox shales peaks on the

first day of the experiment, that of the Pottsville shale continued to increase over the five day period but it also expected to peak and gradually decline with similar trend to the Mancos, Marcellus and Wilcox shales. This resilient behavior of the Pottsville shale might suggest a slower dissolution reaction of its calcium based minerals constituent compared to the Mancos, Marcellus and Wilcox shales. The bulk rock XRD analysis indicated calcite and dolomite as the main calcium bearing minerals in the Mancos, Marcellus and Wilcox shales while anhydrites are the main calcium bearing minerals in the Pottsville. These observations in the effluent are significant as the cationic content of any fluid determines the extent to which sizeable amount of dissolved solutes precipitates out of solution. This is evident in the Marcellus and Mancos samples where large amount of carbonate precipitates were recovered. The precipitation of dissolved minerals at normal temperature and pressure conditions shows that in the subsurface, changes in geochemical and thermodynamic conditions can affect the speed at which aqueous precipitation processes take place.

### **5.1.2 Bulk Rock/Precipitates Analysis**

The XRD analysis of the bulk rocks yielded useful information about the possible changes in the mineralogy of the shales. Figures 4.17 to 4.20 show the profiles of the main mineralogical components in the shale rocks (pre- and post-flooding with CO<sub>2</sub>-brine) and the recovered precipitates as identified by bulk XRD analysis for the Mancos, Marcellus, Pottsville and Wilcox shale rocks respectively. Bulk XRD analysis reflected changes that are not significant enough in their percentages in order to make affirmative conclusions. The clay XRD analysis also showed that there are only subtle changes in the clay component of all the rock samples. But the

Marcellus shale showed far greater heterogeneity in both mineralogy and morphology. These heterogeneities does not make the Marcellus shale a good candidate for seal rocks of CO<sub>2</sub> sequestration sites. The Pottsville shale shows platy grain structures that are tightly packed and efficient for preventing fluid movement. In terms of pre- and post-flooding minerology, it appears the Pottsville shale is most stable followed by the Wilcox which is not tight in pore structure. Furthermore, the recovery of amorphous precipitates in all of the associated effluent samples showed the role that temperature plays in the ability of dissolved minerals to remain in solution for an extended period. More than ninety percent of the precipitates were recovered within a month after the experiments. These precipitates are of varying coloration; dark brown to light pink (see Appendix A). While the bulk shale rock samples showed little changes at the surface, the mineralogical analysis carried out on them revealed the removal of amorphous contents from the rocks in significant amounts. These amorphous contents form the bulk of the precipitates were recovered from the effluent. Amorphous content of rocks are usually responsible for suppressed peaks in XRD qualitative analysis. The bulk XRD analysis of precipitates showed the appearance of diagenetic minerals that were formed from the major mineralogical components of the shale rocks. The quantitative XRD analysis performed on samples are largely qualitative with minor evidence of changes in the mineralogy of the rock samples after the experiment. But for the margin of changes reported in tables 4.1 and 4.2, it best to assume that the contents of the precipitates are largely amorphous and crystalline forms of carbonates as seen in XRD.

The total carbon content of the shale rocks (figure 4.16) indicated that the higher the organic content of the seal rock, the higher the potential for carbon absorption to the surface of the rock. The Marcellus shale exemplified this behavior well when compared to other shale samples. The

percentage carbon content were in the order Marcellus > Wilcox > Mancos > Pottsville. This order of magnitude still holds after the CO<sub>2</sub>-brine flooding experiment. It can be observed for the figure that there were significant increases in the percentage content of carbon in all the samples which can be indicative of both adhered carbon and mineralized carbon in these shale samples.

The electron microprobe analysis (EMPA) showed the presence of Iron (Fe), Sodium (Na), Potassium (K), Silicon (Si), Carbon (C), Oxygen (O), Chlorine (Cl), Manganese (Mn), Calcium (Ca), Magnesium (Mg) and Aluminum (Al). They are present in rock minerals capable of exchanging ions with carbonic acid or aqueous CO<sub>2</sub>. The elemental distribution of Ca and Mg in the reacted Mancos and Marcellus shales were lower within grain facies as shown in figures 4.25 to 4.27 and figures 4.28 to 4.30 (top row) respectively when compared to the corresponding control samples (bottom row). These were the surface maps for elemental spread involving CO<sub>2</sub>-brine flooded samples. It has been noted that in addition to common alkali earth metals such as Na and K that form compounds which are generally soluble in acidic or alkaline fluids, Ca and Mg solutes have significant ion-exchange capacity as well. The surface depletion within grains shows the extent of the reach of aqueous CO<sub>2</sub> in supporting dissolutive rock-fluid interaction in the subsurface. Pottsville and Wilcox shales are lean in Ca and Mg based minerals which informed the limited traces of these elements on the surface of the thin section samples. The distribution of Al and Fe as shown in figures 4.26/27 and figures 4.29/30 for Mancos and Marcellus shales respectively indicated low activity in the reacted samples while figures 4.31 to 4.33 and figures 4.34 to 4.36 for Pottsville and Wilcox shales respectively reflected significant concentration of Al and Fe which have smaller percentages in the minerals bearing them. These imply that compounds of Ca, Mg, Al, and Fe which were identified in the shale caprock samples, either as major or trace minerals,

would be reactively soluble with faster kinetics in aqueous CO<sub>2</sub> with the possibility of re-precipitation to form new minerals at subsurface pressure and temperature. The formation of Aragonite in experiments involving Marcellus shale exemplify the dissolution-precipitation processes that impact long term caprock integrity.

The magnitude of the mechanical strength of the bulk shale rocks was reduced for most of the samples analyzed (figures 4.37 and 4.38). This was measured in terms of Vickers' Hardness. The most impacted was the Wilcox shale which has the highest percentage of swelling clay (Montmorillonite). The tablet of shale rocks used were polished using laboratory grinder which could have altered some mechanical properties. These polishers are graded from fine to coarse applications. The finest grade of polisher is used at the final stage of rock preparation for micro-indentation. This is expected to have some effects on near-wellbore stability of shale caprock sections for CO<sub>2</sub> sequestration sites. Also, the correlation of changes in mineralogy to hardness and Young's Modulus (figures 4.39 and 4.40) suggested that the higher the diagenetic quartz formed, the higher the mechanical properties. It implies that rock-fluid geochemical interactions that can continuously convert clays and other minerals into opal will provide higher geomechanical stability and tighter hydraulic barrier on the longer term.

### **5.1.3 Fracture Flow Characterization**

The characterization of fracture flow properties showed that the formation of precipitates in the super-saturated fluid can occlude hydraulic conductivity. This phenomenon is supported by the experimental data presented in figures 4.41 to 4.47. These are in specific cases when soluble alkaline earth metal minerals are present in large amount with the host rock as seen with

carbonates rich shale rocks. The next chapter attempts to integrate the geochemical and fracture flow experimental data obtained and provide models to represent them. The applications of such integrated models will be in numerical reservoir simulations where discrete fracture network models can be used to describe and visualize long term behavior of sedimentary tight rocks under carbon sequestration conditions. It is expected that deep fractured shale will exhibit greater diagenesis when in contact with aqueous carbon dioxide. The experimental data reported showed that 25 $\mu$ m sized fractures can be closed more rapidly with 150 $\mu$ m sized ones taking longer time to close and are 30% less in fracture sizes. The first derivatives of the differential pressures showed that most of the changes occurred during the first two days of the experiment with the Marcellus sample reflecting the most changes in the rapid exponential decline. The use of pressure derivative is to help identify possible inflection points that could be diagnostic of the pressure responses. The acquisition of thousands of differential pressure data is useful in this regard. Laboratory transient pressure analysis provides a description of the fracture flow behavior though the length and geometry of the effect fracture in these experiments are several order of magnitude shorter than that obtained in the field the Mancos and the Wilcox also indicated a rapid loss of fracture conductivity. These losses are attributable to the generation of significant amount of precipitates from the effluent fluid of shale rock-aqueous CO<sub>2</sub> interactions. These precipitates were crystalized at varying rates and this was thought to have been responsible for the different initial gradients. The rapid precipitation of aragonites from the effluent samples of the CO<sub>2</sub>-brine flooding Marcellus shales showed that the convective transport of precipitate laden fluid at 50°C and 1000psi pressure, can lead to fast fracture conductivity closure.

## 5.2 Integrated Experimental Observations

The integration of the sections described above leads to the flow diagram shown in figure 5.1. The geochemical footprint in the effluent and the mineralogical/morphological characteristics of the shale rocks is shown to have impacted the conductivity of micro-fractures. This is through the formation of precipitates. The physics of geochemical-fracture flow in shale caprock can be described analytically. The upper decline curve represents lower impact of the effects of geochemical interactions under constant geomechanical conditions. The upper decline curve represent higher impact of the effects of geochemical interactions. These effects can be mathematically/analytically modelled as an exponential-natural logarithmic function. This function can be used in used in complex discrete fracture networks representing natural flow path deformities in shale caprock. This function is exclusively for corrections to flow characteristics over time in re-activated or open micro-fracture networks inherent in shale caprocks. The monitoring of leakages via caprock should account for geochemical changes and not just geomechanical alterations which tend to first worsen seal integrity during the initial phase of injection. The independent modelling of coupled geochemical effects and micro-fracture conductivity can be described by the exponential-natural logarithm relationship, leaving out complex reactions which are difficult to account for simultaneously. In the literature, the effect of capillarity is highly emphasized as a determining factor for seal integrity but the presence of scattered, randomly distributed micro-fractures lead to low or non-accounting of carbon molecules that could be involved in rock-fluid interactions under CO<sub>2</sub> sequestration and containment conditions.

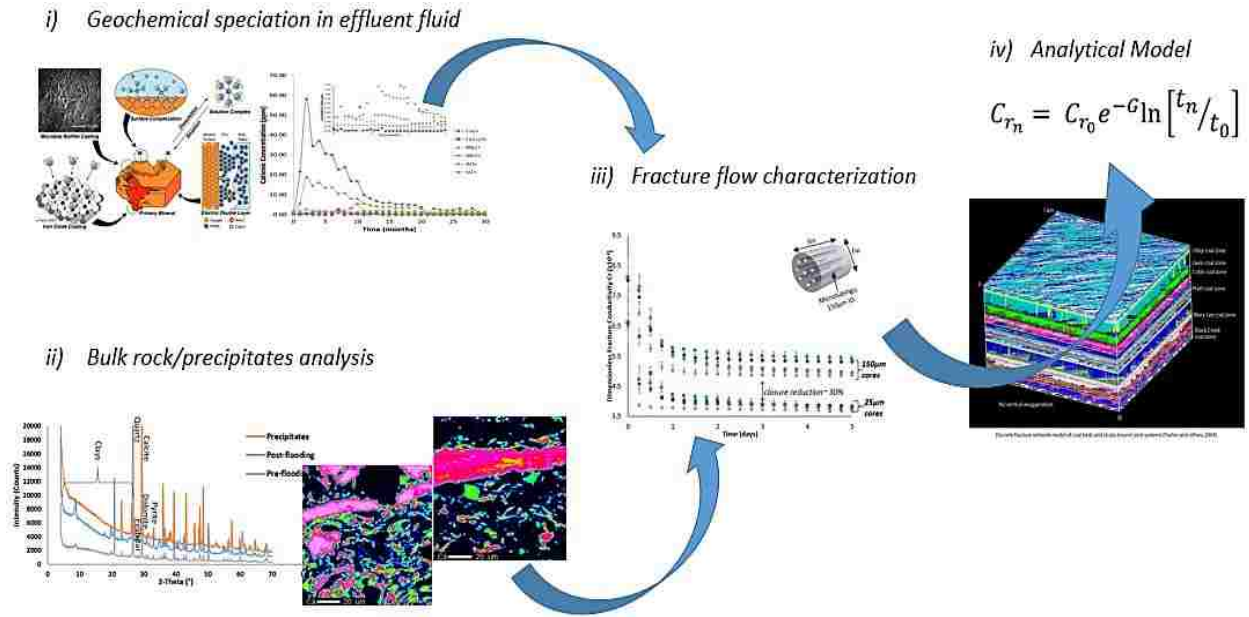


Figure 5.1. The integration of the geochemical, geomechanical and micro-fracture conductivity in shale rock-aqueous CO<sub>2</sub> interactions. The schematics showed how convective fluid transport will provide the necessary flow-path bridging materials after repetitive dissolution-precipitation reactions. These reactions provide significant quantities of precipitates for flow occlusion.

The use of analytical solutions in discrete fracture network models will improve the process of carbon account in CO<sub>2</sub> sequestration projects by ensuring that mineralized carbon molecules are accounted for in flow-path closure. Multiple layers of unevenly distributed tight rocks can reveal heterogeneous behavior via pressure and saturation field monitoring. Comparison with field data/simulation will be tremendously useful for carbon sequestration site characterization.

## CHAPTER 6

### CONCLUSIONS AND RECOMMENDATIONS

#### 6.1 Conclusions

The interaction of aqueous CO<sub>2</sub> and shale caprocks that are representative of the geological seals suitable for CO<sub>2</sub> sequestration and containment projects have been experimentally studied under laboratory conditions of stress (1400psi axial and radial stress), temperature (50°C) and injection pressures (1000 psi). Four shale caprock samples from different geologic formations within the United States were used. The effluent emanating from these closed system diagenetic rock-fluid interactions were flowed through an artificially fractured media made of cylindrical cement cores with PEEK polymer micro-tubings embedded. This was intended to mimic micro-fractures, which are sometimes present in intact caprocks. Several experimental runs using the unique setup described in Chapter 3 were carried out with two different sets of micro-tubing diameters (25µm and 150 µm ID). Effluent fluid analysis were carried out using pH meters and ICP-OES techniques for acidity/alkalinity measurements and ionic content analysis. Bulk shale rocks were analyzed with XRD, SEM, EMPA, TOC and Micro-indentation techniques for changes in rock mineralogy, morphology, elemental composition, inorganic carbon and geomechanical properties. The measurement of differential pressure drop across the artificially fractured cores yielded information on the impact of geochemical changes in the experimental fluid on effective micro-fracture apertures and corresponding fracture conductivity.

The following major conclusions can be inferred from the laboratory experiment involving shale rock interactions with CO<sub>2</sub> saturated brine under dynamic flow conditions:

1. Moderately high temperature (50°C) and injection pressure (1000psi) in the core scale experiment indicate rapid dissolution of shale rock minerals as shown by the analyses of effluent fluid, bulk rock and precipitate analyses.
2. The effluent fluid indicated that alkaline earth metal based minerals particularly Calcium and Magnesium in shale caprocks are the most susceptible to reactive dissolution at these experimental conditions.
3. Reactive dissolution leads to the formation of new diagenetic minerals, notably in carbonates-rich shale caprocks, which precipitated out of the effluent fluid in significant quantity. These precipitates are capable of aggregating in saturated solutions.
4. The distribution of major elements on the surface of the bulk shale caprocks showed minute morphological changes at the edges of distinct grains and the association of minor elements with major minerals. This shows that significant heterogeneity within the tight rocks are responsible for the release of environmentally unfriendly trace elements that can compromise groundwater quality.
5. Reaction kinetic models indicated that there is significant increase in rates of diagenetic rock fluid interactions as temperature is additively doubled. This implied that deep hot shale rocks will experience higher rates of diagenetic rock-fluid interactions that could possibly impact hydraulic fractures. This is applicable to large scale CO<sub>2</sub> sequestration into stimulated shale reservoirs with hydraulic fracture networks.
6. Micro-hardness property of the bulk rock showed significant reduction in geomechanical strength for three samples; Mancos, Marcellus and Wilcox. Micro-hardness property of

the bulk rock is not significantly affected as observed in this 5-day experiment for Pottsville shale samples with non-swelling clay and no carbonates.

7. The gradual rise of differential pressure drop across the fractured composite core is an indication of loss of flow characteristics. Dimensionless fracture conductivity indicated that the loss of flow characteristics was most pronounced within the first two days of the experiment leading to aperture closure over time.
8. There is significant limit to the size of effective fracture apertures that can be closed by diagenetic rock-fluid interactions. Experimental data showed approximately 30% reduction in end-of-experiment conductivity loss when micro-tubings sizes were changed from 25 $\mu\text{m}$  to 150 $\mu\text{m}$ .
9. The loss of fracture conductivity can be analytically modelled as an exponential-natural logarithm function for two profiles of fracture conductivity that represent the extremes.
10. The modelling of discrete fracture networks in shale caprocks can be the key to the accuracy of carbon accounting. It can be opined that given the potential of rock-fluid interactions in generating significant amount of precipitates, the exact amount of carbon from molecules of carbon dioxide injected and minerally sequestered can be estimated.
11. The data presented in this report can be used in incorporating the effect of short term diagenesis on fracture flow characteristics by assigning physics based models (exponential-natural logarithm function is developed) to discrete fracture network cases. The integration of various models of geochemistry, geomechanics and micro-fracture conductivity can provide a single model representation of caprock behavior/integrity under carbon sequestration conditions.

## 6.2 Recommendations

The understanding of diagenetic rock-fluid interactions in tight shale caprocks require detailed experimental data for successful theoretical and numerical modelling. Base on the additions to the body of knowledge through this research works, the following recommendations are proposed:

1. Experimental runs at higher temperature and pressure conditions could be carried out to investigate rock-fluid interactions effect in the case of injection of CO<sub>2</sub> into deep fractured shale formations. For example the experimental conditions could be: Overburden stress = 4000psi, Backpressure = 3600psi; Injection pressure = 3600 psi, Operating temperature = 150°C. Temperature and pressure control will present the biggest challenge and more sophisticated instrumentation can be deployed to achieve the desired conditions.
2. Acquire geochemical, geomechanical and flow parameters as were in the moderate temperature and pressure experiments described in this report. Imaging analyses of relevant samples will also be carried out to identify morphological changes.
3. Model the reaction rate and flow characteristics at multiple experimental conditions of pressure and temperature at the core scale for possible scale up to numerical simulation.
4. Predict subsurface implication of the impact of diagenesis and stress on fracture conductivity from core scale experiment and the associated models.
5. Additional shale rock samples could be explored to create a more robust statistically useful data base for geostatistical and discrete fracture network predictions of long term rock-fluid interaction effects on other geological basins of interests to CO<sub>2</sub> sequestration project managers.

## REFERENCES

1. Shukla, R., et al., A Review of Studies on CO<sub>2</sub> Sequestration and Caprock Integrity. *Fuel*, 2010. 89(10): p. 2651-2664.
2. Stevens, S.H., Natural CO<sub>2</sub> Fields as Analogs for Geologic CO<sub>2</sub> Storage. 2005. Volume 2(Carbon Dioxide Capture for Storage in Deep Geologic Formations – Results from the CO<sub>2</sub> Capture Project Geologic Storage of Carbon Dioxide with Monitoring and Verification, Sally M. Benson, Lawrence Berkeley Laboratory, Berkeley, CA, USA): p. Pages 687-697.
3. Wollenweber, J., et al., Experimental Investigation of the CO<sub>2</sub> Sealing Efficiency of Caprocks. *International Journal of Greenhouse Gas Control*, 2010. 4(2): p. 231-241.
4. Bicocchi, G., et al., Chemical Alteration and Mineral Growth under High Pco<sub>2</sub> Conditions: Insights from the Mineral Chemistry of Carbonate Phases in the Caprese Reservoir (Northern Apennines, central Italy). *Chemical Geology*, 2017. 450: p. 81-95.
5. Arts, R.C., O. Eiken, and N. Scott- Sylvain, Ten Years' Experience of Monitoring CO<sub>2</sub> Injection in the Utsira Sand at Sleipner, Offshore Norway. *First Break*, 2008. 26: p. 65-72.
6. Akervoll, I., E. Lindeberg, and A. Lackner, Feasibility of Reproduction of Stored CO<sub>2</sub> from the Utsira Formation at the Sleipner Gas Field. *Energy Procedia*, 2009. 1(1): p. 2557-2564.
7. Buttinelli, M., et al., the Geo-database of Caprock Quality and Deep Saline Aquifers Distribution for Geological Storage of CO<sub>2</sub> in Italy. *Energy*, 2011. 36(5): p. 2968-2983.
8. Chadwick, R.A., et al., Geological Characterization of CO<sub>2</sub> Storage Sites: Lessons from Sleipner, Northern North Sea, in *Greenhouse Gas Control Technologies - 6th International Conference*, J. Gale and Y. Kaya, Editors. 2003, Pergamon: Oxford. p. 321-326.
9. Davis, E.J. and S.D. Marsic, Interpretation of CO<sub>2</sub>-Sequestration-Induced Surface Deformation at Krechba, Algeria, in *SPE International Conference on CO<sub>2</sub> Capture, Storage, and Utilization*. 2010: New Orleans, Louisiana, USA. doi:10.2118/147444-MS.
10. Farokhpoor, R., et al., Experimental and Numerical Simulation of CO<sub>2</sub> Injection Into Upper-Triassic Sandstones in Svalbard, Norway, in *SPE International Conference on CO<sub>2</sub> Capture, Storage, and Utilization*. 2010: New Orleans, Louisiana, USA.

11. Giday-WoldeGabriel, M.F., et al., Textural and Geochemical Features along a Reservoir-Cap Rock Contact in the Sacroc Unit of West Texas, L.A.N.L. Earth and Environmental Sciences Division, Editor. 2007: Los Alamos, NM, 87545 USA.
12. Xu, T., et al., Reactive Transport Modeling to Study Changes in Water Chemistry Induced By CO<sub>2</sub> Injection at the Frio-I Brine Pilot. *Chemical Geology*, 2010. 271(3-4): p. 153-164.
13. Zhang, W., et al., Long-Term Variations of CO<sub>2</sub> Trapped in different Mechanisms in Deep Saline Formations: A Case Study of the Songliao Basin, China. *International Journal of Greenhouse Gas Control*, 2009. 3(2): p. 161-180.
14. Carbon Sequestration Atlas of the United States and Canada. National Energy Technology Laboratory, Department of Energy 2010. Vol. 3: p. 162.
15. Ellis, B., et al. Alteration of Caprock Fracture Geometries During Flow of CO<sub>2</sub>-acidified Brine: Informing Basin-scale Leakage Models From Pore-scale modeling and Core-scale Experiments. in AGU Fall Meeting Abstracts. 2011.
16. Javadpour, F., CO<sub>2</sub> Injection in Geological Formations: Determining Macroscale Coefficients From Pore Scale Processes. *Transport in Porous Media*, 2009. 79(1): p. 87-105.
17. Renard, S., et al., Geochemical Study of the Reactivity of a Carbonate r=Rock in a Geological Storage of CO<sub>2</sub>: Implications of co-injected Gases. *Energy Procedia*, 2011. 4: p. 5364-5369.
18. Salem, A.M. and S.A. Shedid, Variation of Petrophysical Properties due to Carbon Dioxide (CO<sub>2</sub>) Storage in Carbonate Reservoirs. *Journal of Petroleum and Gas*, 2013. 4(4): p. 91-102.
19. Wei, N., et al., Geochemical Impact of Aquifer Storage for Impure CO<sub>2</sub> containing O<sub>2</sub> and N<sub>2</sub>: Tongliao field experiment. *Applied Energy*, 2015. 145: p. 198-210.
20. Bourg, I.C., L.E. Beckingham, and D.J. DePaolo, the Nanoscale Basis of CO<sub>2</sub> Trapping for Geologic Storage. *Environmental science & technology*, 2015.
21. Hong, K.C. and J.W. Ault, Effects of Noncondensable Gas Injection on Oil Recovery by Steamflooding. *SPE Journal of Petroleum Technology*, 1984. 36(12): p. 2160-2170.
22. Bagci, A.S. and F. Gumrah, Effects of CO<sub>2</sub> and CH<sub>4</sub> Addition to Steam on Recovery of West Kozluca Heavy Oil, in SPE International thermal Operations and Heavy Oil Symposium and Western Regional Meeting. 2004, Society of Petroleum Engineers: Bakersfield, California.

23. Smith, S.A., et al., Geomechanical Testing and Modeling of Reservoir and Cap Rock Integrity in an Acid Gas EOR/Sequestration Project, Zama, Alberta, Canada. *Energy Procedia*, 2009. 1(1): p. 2169-2176.
24. Mohammad, S., R.L. Robinson, and K. Gasem, Multiphase Analysis for CO<sub>2</sub>: Water/Mixed-Gas Adsorption on Coals, in SPE International Conference on CO<sub>2</sub> Capture, Storage, and Utilization. 2010: New Orleans, Louisiana, USA.
25. Pitman, J.K., et al., Origin of Minerals in Joint and Cleat Systems of the Pottsville Formation, Black Warrior Basin, Alabama: Implications for Coalbed Methane Generation and Production. *AAPG Bulletin*, 2003. 87(5): p. 713-731.
26. Pashin, J.C., et al., Carbon Sequestration and Enhanced Recovery Potential of Mature Coalbed Methane Reservoirs in the Black Warrior Basin. *AAPG Special Volume*, 2009.
27. Goodman, A., et al., Methodology for Assessing CO<sub>2</sub> Storage Potential of Organic-Rich Shale Formations. *Energy Procedia*, 2014. 63: p. 5178-5184.
28. Murphy, R., et al., Ferrihydrite Phase Transformation in the Presence of Aqueous Sulfide and Supercritical CO<sub>2</sub>. *Chemical Geology*, 2010. 271(1-2): p. 26-30.
29. Alemu, B.L., et al., Caprock Interaction with CO<sub>2</sub>: A Laboratory Study of reactivity of shale with supercritical CO<sub>2</sub> and brine. *Applied Geochemistry*, 2011. 26(12): p. 1975-1989.
30. Pentland, C.H., et al., Measurement of Supercritical Carbon Dioxide Capillary Trapping in Core Analysis, in SPE International Conference on CO<sub>2</sub> Capture, Storage, and Utilization. 2010: New Orleans, Louisiana, USA. doi:10.2118/138476-MS.
31. Hemme, C. and W. van Berk, Change in Cap Rock Porosity triggered by Pressure and Temperature Dependent CO<sub>2</sub>–Water–Rock Interactions in CO<sub>2</sub> Storage Systems. *Petroleum*, 2017. 3(1): p. 96-108.
32. Michels, L., et al., Intercalation and Retention of Carbon Dioxide in a Smectite Clay promoted by Interlayer Cations. *Scientific reports*, 2015. 5: p. 8775.
33. Busch, A., et al., Effects of Physical Sorption and Chemical Reactions of CO<sub>2</sub> in Shaly Caprocks. *Energy Procedia*, 2009. 1(1): p. 3229-3235.
34. Wollenweber, J., et al., Caprock and Overburden Processes in Geological CO<sub>2</sub> Storage: an Experimental Study on Sealing Efficiency and Mineral Alterations. *Energy Procedia*, 2009. 1(1): p. 3469-3476.

35. Busch, A., et al., Carbon Dioxide Storage Potential of Shales. *International Journal of Greenhouse Gas Control*, 2008. 2(3): p. 297-308.
36. Audigane, P., et al., Reactive Transport Modeling Using TOUGHREACT for the Long Term CO<sub>2</sub> Storage at Sleipner, North Sea. *Carbon Capture and Sequestration*, 2005. 2.
37. Eiken, O., et al., Lessons Learned From 14 Years of CCS Operations: Sleipner, In Salah and Snøhvit. *Energy Procedia*, 2011. 4: p. 5541-5548.
38. Gaus, I., M. Azaroual, and I. Czernichowski-Lauriol, Reactive Transport Modelling of the Impact of CO<sub>2</sub> Injection on the Clayey Cap Rock at Sleipner (North Sea). *Chemical Geology*, 2005. 217(3): p. 319-337.
39. Allen, P.A. and J.R. Allen, *Basin Analysis - Principles and Applications (2nd Edition)*. John Wiley & Sons.
40. Li, Z., et al., CO<sub>2</sub> Sequestration in Depleted Oil and Gas Reservoirs--Caprock Characterization and Storage Capacity. *Energy Conversion and Management*, 2006. 47(11-12): p. 1372-1382.
41. Bryant, S. and L.W. Lake, Effect of Impurities on Subsurface CO<sub>2</sub> Storage Processes, in *Carbon Dioxide Capture for Storage in Deep Geologic Formations*. 2005, Elsevier Science: Amsterdam. p. 983-996.
42. Wang, J., et al., Effects of Impurities on CO<sub>2</sub> Transport, Injection and Storage. *Energy Procedia*, 2011. 4: p. 3071-3078.
43. Marcon, V. and J.P. Kaszuba, Carbon Dioxide–Brine–Rock Interactions in a Carbonate Reservoir Capped By Shale: Experimental Insights Regarding the Evolution of Trace Metals. *Geochimica Et Cosmochimica Acta*, 2015. 168: p. 22-42.
44. Busch, A., et al., Investigation of High-Pressure Selective Adsorption/Desorption Behaviour of CO<sub>2</sub> and CH<sub>4</sub> on Coals: An Experimental Study. *International Journal of Coal Geology*, 2006. 66(1-2): p. 53-68.
45. Busch, A. and A. Amann-Hildenbrand, Predicting Capillarity of Mudrocks. *Marine and Petroleum Geology*, 2013. 45: p. 208-223.
46. Bennett, R.H., W.R. Bryant, and M.H. Hulbert, *the Microstructure of Fine-Grained Sediments, From Mud to Shale*. 1991, New York: Springer-Verlag.
47. Hildenbrand, A., S. Schlömer, and B.M. Krooss, Gas Breakthrough Experiments on Fine-Grained Sedimentary Rocks. *Geofluids*, 2002. 2(1): p. 3-23.

48. Emmanuel, S., L.M. Anovitz, and R.J. Day-Stirrat, Effects of Coupled Chemo-Mechanical Processes on the Evolution of Pore-Size Distributions in Geological Media. *Rev Mineral Geochem*, 2015. 80: p. 45-60.
49. Mouzakis, K.M., et al., Experimental Study of Porosity Changes in Shale Caprocks Exposed to CO<sub>2</sub>-Saturated Brines I: Evolution of Mineralogy, Pore Connectivity, Pore Size Distribution, and Surface Area. *Environmental Engineering Science*.
50. Miller, Q.R., et al., Experimental Study of Porosity Changes in Shale Caprocks Exposed to Carbon Dioxide-Saturated Brine II: Insights From Aqueous Geochemistry. *Environmental Engineering Science*. 33.10 (2016): p. 736-744.
51. Khan, S., et al., An Integrated Geomechanics Workflow for Caprock-Integrity Analysis of a Potential Carbon Storage, in *SPE International Conference on CO<sub>2</sub> Capture, Storage, and Utilization*. 2010: New Orleans, Louisiana, USA. doi:10.2118/139477-MS.
52. Vilarrasa, V., S. Olivella, and J. Carrera, Geomechanical Stability of the Caprock During CO<sub>2</sub> Sequestration in Deep Saline Aquifers. *Energy Procedia*, 2011. 4: p. 5306-5313.
53. Busch, A., et al., The Significance of Caprock Sealing Integrity for CO<sub>2</sub> Storage, in *SPE International Conference on CO<sub>2</sub> Capture, Storage, and Utilization*. 2010: New Orleans, Louisiana, USA. doi:10.2118/139588-MS.
54. Ellis, B.R., et al., Changes in Caprock Integrity Due to Vertical Migration of CO<sub>2</sub>-Enriched Brine. *Energy Procedia*, 2011. 4: p. 5327-5334.
55. Mcpherson, B., Modeling Caprock Integrity: Assessment Objectives. *IEA-GHG CO<sub>2</sub> Geological Storage Modelling Workshop Orleans, France*, 2009.
56. Armitage, P.J., et al., Diagenetic and Sedimentary Controls on Porosity in Lower Carboniferous Fine-Grained Lithologies, Krechba Field, Algeria: a Petrological Study of a Caprock to a Carbon Capture Site. *Marine and Petroleum Geology*, 2010. 27(7): p. 1395-1410.
57. Ali, S.A., et al., Diagenesis and Reservoir Quality. *Oilfield Review*, 2010. 22(2): p. 14-27.
58. Duenckel, R., et al., Proppant Diagenesis--Integrated Analyses Provide New Insights Into Origin Occurrence and Implications for Proppant Performance. *SPE Production & Operations*, 2012. 27(02): p. 131-144.
59. Weaver, J.D., et al., Fracture-Related Diagenesis may Impact Conductivity. *SPE Journal*, 2007. 12(03): p. 272-281.

60. Katsube, T.J. and M.A. Williamson, Effects of Diagenesis on Shale Nano-Pore Structure and Implications for Sealing Capacity. *Clay Minerals*, 1994. 29(4): p. 451-472.
61. Kohler, E., T. Parra, and O. Vidal, Clayey Cap-Rock Behavior in H<sub>2</sub>O-CO<sub>2</sub> Media at Low Pressure and Temperature Conditions: An Experimental Approach. *Clays and Clay Minerals*, 2009. 57(5): p. 616-637.
62. Nogues, J.P., et al., Permeability Evolution Due to Dissolution and Precipitation of Carbonates Using Reactive Transport Modeling in Pore Networks. *Water Resources Research*, 2013. 49(9): p. 6006-6021.
63. Armitage, P., et al., Permeability of the Mercia Mudstone: Suitability As Caprock to Carbon Capture and Storage Sites. *Geofluids* 16.1 (2016): p. 26-42.
64. Edlmann, K., S. Haszeldine, and C. Mcdermott, Experimental Investigation Into the Sealing Capability of Naturally Fractured Shale Caprocks to Supercritical Carbon Dioxide Flow. *Environmental Earth Sciences*, 2013. 70(7): p. 3393-3409.
65. Liu, F., et al., CO<sub>2</sub>-Brine-Caprock Interaction: Reactivity Experiments on Eau Claire Shale and a Review of Relevant Literature. *International Journal of Greenhouse Gas Control*, 2012. 7: p. 153-167.
66. Elsworth, D. and H. Yasuhara, Mechanical and Transport Constitutive Models for Fractures Subject to Dissolution and Precipitation. *International Journal for Numerical and Analytical Methods in Geomechanics*, 2010. 34(5): p. 533-549.
67. Reynolds, M. and J. Buendia. Permanently Sequester Anthropogenic Carbon Dioxide-Through Hydraulic Fracturing. in *SPE Unconventional Resources Conference*. 2017. Society of Petroleum Engineers. doi:10.2118/185033-MS.
68. Nicot, J.p. and I.J. Duncan, Common attributes of Hydraulically Fractured Oil and Gas Production and CO<sub>2</sub> Geological Sequestration. *Greenhouse Gases: Science and Technology*, 2012. 2(5): p. 352-368.
69. Stack, A.G., Precipitation in Pores: A Geochemical Frontier. *Rev Mineral Geochem*, 2015. 80: p. 165-190.
70. Molins, S., Reactive Interfaces in Direct Numerical Simulation of Pore Scale Processes. *Rev Mineral Geochem*, 2015. 80: p. 461-481.
71. Vidic, R.D., et al., Impact of Shale Gas Development on Regional Water Quality. *Science*, 2013. 340(6134).

72. Amthor, J.E. and J. Okkerman, Influence of Early Diagenesis on Reservoir Quality of Rotliegende Sandstones, Northern Netherlands. AAPG Bulletin, 1998. 82(12): p. 2246-2265.
73. Wendler, J., et al., Carbonate Diagenesis and Feldspar Alteration in Fracture-Related Bleaching Zones (Buntsandstein, Central Germany): Possible Link to CO<sub>2</sub>-Influenced Fluid–Mineral Reactions. International Journal of Earth Sciences, 2012. 101(1): p. 159-176.
74. Altundas, B., et al., Retardation of CO<sub>2</sub> Migration Due to Capillary Pressure Hysteresis: a New CO<sub>2</sub> Trapping Mechanism, in SPE International Conference on CO<sub>2</sub> Capture, Storage, and Utilization. 2010: New Orleans, Louisiana, USA. doi:10.2118/139641-MS.
75. Soldal, M., Caprock Interaction with CO<sub>2</sub>: Geomechanical and Geochemical Effects, in Department of Geosciences. 2008, University of Oslo: Oslo. p. 106.
76. Pashin, J.C. and M.R. McIntyre, Temperature–Pressure Conditions in Coalbed Methane Reservoirs of the Black Warrior Basin: Implications for Carbon Sequestration and Enhanced Coalbed Methane Recovery. International Journal of Coal Geology, 2003. 54(3): p. 167-183.
77. Espinoza, D.N. and J.C. Santamarina, Water-CO<sub>2</sub>-Mineral Systems: Interfacial Tension, Contact Angle, and Diffusion; Implications to CO<sub>2</sub> Geological Storage. Water Resour. Res., 2010. 46(7): p. W07537.
78. Moulton, O.A., et al., Self-Diffusion Coefficients of the Binary H<sub>2</sub>O–CO<sub>2</sub> Mixture at High Temperatures and Pressures. the Journal of Chemical thermodynamics 93 (2016): p. 424-429.
79. Busch, A. and N. Müller, Determining CO<sub>2</sub>/Brine Relative Permeability and Capillary Threshold Pressures for Reservoir Rocks and Caprocks: Recommendations for Development of Standard Laboratory Protocols. Energy Procedia, 2011. 4: p. 6053-6060.
80. Blauch, M.E. Developing Effective and Environmentally Suitable Fracturing Fluids Using Hydraulic Fracturing Flowback Waters. in SPE Unconventional Gas Conference. 2010. Society of Petroleum Engineers. doi:10.2118/131784-MS
81. EPA, Characteristics of Coalbed Methane Production and Associated Hydraulic Fracturing Practices. Evaluation of Impacts to Underground Sources of Drinking Water by Hydraulic Fracturing of Coalbed Methane Reservoirs, 2004: p. 32.
82. USGS, Summary of Studies Related to Hydraulic Fracturing Conducted by USGS Water Science Centers. USGS, 2012. 5: p. 1 - 8.

83. Chalbaud, C., et al., Interfacial Tension Measurements and Wettability Evaluation for Geological CO<sub>2</sub> Storage. *Advances in Water Resources*, 2009. 32(1): p. 98-109.
84. Hildenbrand, A., et al., Gas Breakthrough Experiments on Pelitic Rocks: Comparative Study with N<sub>2</sub>, CO<sub>2</sub> and CH<sub>4</sub>. *Geofluids*, 2004. 4(1): p. 61-80.
85. Bacon, D.H., et al., CO<sub>2</sub> Storage by Sorption on Organic Matter and Clay in Gas Shale. *Journal of Unconventional Oil and Gas Resources*, 2015. 12: p. 123-133.
86. Xu, T., J.A. Apps, and K. Pruess, Mineral Sequestration of Carbon Dioxide in a Sandstone–Shale System. *Chemical Geology*, 2005. 217(3): p. 295-318.
87. Schieber, J., Reverse Engineering Mother Nature—Shale Sedimentology From An Experimental Perspective. *Sedimentary Geology*, 2011. 238(1): p. 1-22.
88. Anovitz, L.M. and D.R. Cole, Characterization and Analysis of Porosity and Pore Structures. *Rev Mineral Geochem*, 2015. 80: p. 61-164.
89. Bennion, D.B. and S. Bachu, Permeability and Relative Permeability Measurements at Reservoir Conditions for CO<sub>2</sub>-Water Systems in Ultra Low Permeability Confining Caprocks, in EUROPEC/EAGE Conference and Exhibition. 2007: London, U.K.
90. Al-Bazali, T.M., et al., Measurement of the Sealing Capacity of Shale Caprocks, in SPE Annual Technical Conference and Exhibition. 2005: Dallas, Texas. doi:10.2118/96100-MS.
91. Johnson, J. W., J.J. Nitao and J.P. Morris, Environmental Sciences Division, Lawrence Livermore National Laboratory, Livermore, CA, USA, Reactive Transport Modeling of Cap-Rock Integrity During Natural and Engineered CO<sub>2</sub> Storage. *Carbon Dioxide Capture for Storage in Deep Geologic Formations*, 2005. Vol. 2.
92. Morris, J., S. Johnson, and S.J. Friedmann, Geomechanical Simulations of Caprock Integrity Using the Livermore Distinct Element Method. 2008. Medium: ED; Size: PDF-File: 10 Pages; Size: 1 Mbytes.
93. Amann-Hildenbrand, A., et al., Experimental Investigation of the Sealing Capacity of Generic Clay-Rich Caprocks. *International Journal of Greenhouse Gas Control*, 2013. 19: p. 620-641.
94. Hensen, E.J.M. and B. Smit, Why Clays Swell. *the Journal of Physical Chemistry B*, 2002. 106(49): p. 12664-12667.
95. Eke, P.E., A. Curtis, and S. Haszeldine, CO<sub>2</sub>-Brine Surface Dissolution and Injection: CO<sub>2</sub> Storage Enhancement, in *Offshore Europe*. 2009: Aberdeen, UK.

96. Kampman, N., et al., Drilling and Sampling a Natural CO<sub>2</sub> Reservoir: Implications for Fluid Flow and CO<sub>2</sub>-Fluid–Rock Reactions During CO<sub>2</sub> Migration Through the Overburden. *Chemical Geology*, 2013.
97. Ruiz-Agudo, E., C. Putnis, and A. Putnis, Coupled Dissolution and Precipitation at Mineral–Fluid Interfaces. *Chemical Geology*, 2014. 383: p. 132-146.
98. Rimmelé, G., V. Barlet-Gouédard, and F. Renard, Evolution of the Petrophysical and Mineralogical Properties of Two Reservoir Rocks Under thermodynamic Conditions Relevant for CO<sub>2</sub> Geological Storage at 3 Km Depth. *Oil & Gas Science and Technology–Revue De l’Institut Français Du Pétrole*, 2010. 65(4): p. 565-580.
99. Olson, J.E., S.E. Laubach, and R.H. Lander, Natural Fracture Characterization in Tight Gas Sandstones: Integrating Mechanics and Diagenesis. *AAPG Bulletin*, 2009. 93(11): p. 1535-1549.
100. Johnson, J.W., J.J. Nitao, and C. I. Steefel, Fundamental Elements of Geologic CO<sub>2</sub> Sequestration in Saline Aquifers, G.A.E.T. Division and L.L.N. Laboratory, Editors. 2006: Livermore, CA 94550.
101. Carroll, S.A., W.W. McNab, and S.C. Torres, Experimental Study of Cement-Sandstone/Shale-Brine-CO<sub>2</sub> Interactions. *Geochemical Transactions*, 2011. 12(1): p. 9.
102. Carroll, S., et al., Wellbore Integrity in Carbon Sequestration Environments: 1. Experimental Study of Cement-Sandstone/Shale-Brine-CO<sub>2</sub>. *Energy Procedia*, 2011. 4: p. 5186-5194.
103. De Lucia, M., et al., Modelling CO<sub>2</sub>-Induced Fluid–Rock Interactions in the Altensalzwedel Gas Reservoir. Part I: From Experimental Data to a Reference Geochemical Model. *Environmental Earth Sciences*, 2012. 67(2): p. 563-572.
104. Peters, C., et al., Basin-Scale Leakage Risks From Geologic Carbon Sequestration: Impact on Carbon Capture and Storage Energy Market Competitiveness. 2013, the Trustees of Princeton University DOE Award DE-FE0000749, Final Technical Report Number DOE/FE0000749-41.
105. Giammar, D.E., R.G. Bruant Jr, and C.A. Peters, Forsterite Dissolution and Magnesite Precipitation at Conditions Relevant for Deep Saline Aquifer Storage and Sequestration of Carbon Dioxide. *Chemical Geology*, 2005. 217(3): p. 257-276.
106. Bergaya, F. and G. Lagaly, Chapter 1 General Introduction: Clays, Clay Minerals, and Clay Science, in *Developments in Clay Science*, B.K.G.T. Faïza Bergaya and L. Gerhard, Editors. 2006, Elsevier. p. 1-18.

107. Lagaly, G., Chapter 5 Colloid Clay Science, in *Developments in Clay Science*, B.K.G.T. Faïza Bergaya and L. Gerhard, Editors. 2006, Elsevier. p. 141-245.
108. Tournassat, C., et al., *Natural and Engineered Clay Barriers*. Vol. 6. 2015: Elsevier.
109. Landais, p. and J.-F. Aranyosy, *Clays in Natural and Engineered Barriers for Radioactive Waste Confinement*. *Physics and Chemistry of the Earth, Parts A/B/C*, 2011. 36(17): p. 1437.
110. Bildstein, O. and F. Claret, Chapter 5 - Stability of Clay Barriers Under Chemical Perturbations, in *Developments in Clay Science*, C.I.S.I.C.B. Christophe Tournassat and B. Façza, Editors. 2015, Elsevier. p. 155-188.
111. Lagaly, G., M. Ogawa, and I. Dékány, Chapter 7.3 Clay Mineral Organic Interactions, in *Developments in Clay Science*, B.K.G.T. Faïza Bergaya and L. Gerhard, Editors. 2006, Elsevier. p. 309-377.
112. Sterpenich, J., et al., Experimental Simulation of the Impact of a thermal Gradient on a Clayey Caprock Submitted to the Combined Action of Water and CO<sub>2</sub>.
113. Steefel, C.I., L.E. Beckingham, and G. Landrot, Micro-Continuum Approaches for Modeling Pore-Scale Geochemical Processes. *Rev Mineral Geochem*, 2015. 80: p. 217-246.
114. Xu, T., et al., TOUGHREACT--A Simulation Program for Non-Isothermal Multiphase Reactive Geochemical Transport in Variably Saturated Geologic Media: Applications to Geothermal Injectivity and CO<sub>2</sub> Geological Sequestration. *Computers & Geosciences*, 2006. 32(2): p. 145-165.
115. Credoç, A., et al., Mixed-Layer Illite–Smectite Reactivity in Acidified Solutions: Implications for Clayey Caprock Stability in CO<sub>2</sub> Geological Storage. *Applied Clay Science*, 2011. 53(3): p. 402-408.
116. Beckingham, L.E., et al., Evaluation of Mineral Reactive Surface Area Estimates for Prediction of Reactivity of a Multi-Mineral Sediment. *Geochimica Et Cosmochimica Acta*, 2016. 188: p. 310-329.
117. Schoonheydt, R.A. and C.T. Johnston, Chapter 3 Surface and Interface Chemistry of Clay Minerals, in *Developments in Clay Science*, B.K.G.T. Faïza Bergaya and L. Gerhard, Editors. 2006, Elsevier. p. 87-113.

118. Olabode, A. and M. Radonjic, Characterization of Shale Cap-Rock Nano-Pores in Geologic CO<sub>2</sub> Containment. *Environmental & Engineering Geoscience*, 2014. 20(4): p. 361-370.
119. Bertier, P., et al., on the Use and Abuse of N<sub>2</sub> Physisorption for the Characterization of the Pore Structure of Shales. *Clay Clay Miner*, 2016.
120. Liu, C., et al., Pore-Scale Process Coupling and Effective Surface Reaction Rates in Heterogeneous Subsurface Materials. *Rev Mineral Geochem*, 2015. 80: p. 191-216.
121. Hong, M. and H.H. Teng, Implications of Solution Chemistry Effects: Direction-Specific Restraints on the Step Kinetics of Calcite Growth. *Geochimica Et Cosmochimica Acta*, 2014. 141: p. 228-239.
122. Golubev, S.V., O.S. Pokrovsky, and J. Schott, Experimental Determination of the Effect of Dissolved CO<sub>2</sub> on the Dissolution Kinetics of Mg and Ca Silicates at 25°C. *Chemical Geology*, 2005. 217(3): p. 227-238.
123. Min, Y. and Y.-S. Jun, Anorthite Dissolution Under Conditions Relevant to Subsurface CO<sub>2</sub> Injection: Effects of Na<sup>+</sup>, Ca<sup>2+</sup>, and Al<sup>3+</sup>. *Environmental Science & Technology*, 2016.
124. Yang, L., et al., CO<sub>2</sub>-Induced Geochemical Reactions in Heterogeneous Sandstone and Potential Conditions Causing the Tight Cementation. *Applied Geochemistry*, 2017.
125. Brigatti, M.F., E. Galan, and B.K.G. theng, Chapter 2 Structures and Mineralogy of Clay Minerals, in *Developments in Clay Science*, B.K.G.T. Faïza Bergaya and L. Gerhard, Editors. 2006, Elsevier. p. 19-86.
126. Tournassat, C. and C.I. Steefel, Ionic Transport in Nano-Porous Clays with Consideration of Electrostatic Effects. *Rev Mineral Geochem*, 2015. 80: p. 287-329.
127. Giesting, P., et al., Interaction of Carbon Dioxide with Na-Exchanged Montmorillonite at Pressures to 640bars: Implications for CO<sub>2</sub> Sequestration. *International Journal of Greenhouse Gas Control*, 2012. 8: p. 73-81.
128. Petro, M. Experimental Study of Rock-Fluid Interaction Using Automated Multichannel System Operated Under Conditions of CO<sub>2</sub>-Based Geothermal Systems. in *38th Annual Workshop on Geothermal Reservoir Engineering*, Stanford, CA, Feb. 11-13, 2013. 2014.
129. Wan, Y., et al., Experimental and Numerical Simulation Study of the Mineral Sequestration Mechanism of the Shiqianfeng Saline Aquifers in the Ordos Basin, Northwest China. *Environmental Earth Sciences*, 2017. 76(1): p. 43.

130. Labus, K., et al., Preliminary Geochemical Modeling of Water–Rock–Gas Interactions Controlling CO<sub>2</sub> Storage in the Badenian Aquifer within Czech Part of Vienna Basin. *Environmental Earth Sciences*, 2016. 75(14): p. 1-13.
131. Wigand, M., et al., Geochemical Effects of CO<sub>2</sub> Sequestration on Fractured Wellbore Cement at the Cement/Caprock Interface. *Chemical Geology*, 2009. 265(1-2): p. 122-133.
132. Lima, V.D., et al., CO<sub>2</sub> Geological Storage in Saline Aquifers: Paraná Basin Caprock and Reservoir Chemical Reactivity. *Energy Procedia*, 2011. 4: p. 5377-5384.
133. Rosenbauer, R.J., T. Koksalan, and J.L. Palandri, Experimental Investigation of CO<sub>2</sub>-Brine-Rock Interactions at Elevated Temperature and Pressure: Implications for CO<sub>2</sub> Sequestration in Deep-Saline Aquifers. *Fuel Processing Technology*, 2005. 86(14-15): p. 1581-1597.
134. Shipton, Z.K., et al., Natural Leaking CO<sub>2</sub>-Charged Systems As Analogs for Failed Geologic Storage Reservoirs, in *Carbon Dioxide Capture for Storage in Deep Geologic Formations*. 2005, Elsevier Science: Amsterdam. p. 699-712.
135. Sathaye, K.J., et al., Constraints on the Magnitude and Rate of CO<sub>2</sub> Dissolution at Bravo Dome Natural Gas Field. *Proceedings of the National Academy of Sciences*, 2014. 111(43): p. 15332-15337.
136. Cantucci, B., et al., Geochemical Barriers in CO<sub>2</sub> Capture and Storage Feasibility Studies. *Transport in Porous Media*, 2015. 106(1): p. 107-143.
137. Putnis, A., Transient Porosity Resulting From Fluid–Mineral Interaction and Its Consequences. *Rev Mineral Geochem*, 2015. 80: p. 1-23.
138. Røyne, A. and B. Jamtveit, Pore-Scale Controls on Reaction-Driven Fracturing. *Reviews in Mineralogy and Geochemistry*, 2015. 80(1): p. 25-44.
139. Zoback, M.D. and S.M. Gorelick, to Prevent Earthquake Triggering, Pressure Changes Due to CO<sub>2</sub> Injection Need to Be Limited. *Proceedings of the National Academy of Sciences*, 2015. 112(33): p. E4510-E4510.
140. Navarre-Sitchler, A., S.L. Brantley, and G. Rother, How Porosity Increases during Incipient Weathering of Crystalline Silicate Rocks. *Rev Mineral Geochem*, 2015. 80: p. 331-354.
141. Druhan, J.L., S.T. Brown, and C. Huber, Isotopic Gradients Across Fluid–Mineral Boundaries. *Reviews in Mineralogy and Geochemistry*, 2015. 80(1): p. 355-391.

142. Frery, E., et al., Geochemical Transect through a Travertine Mount: A Detailed Record of CO<sub>2</sub>-Enriched Fluid Leakage from Late Pleistocene to Present-Day–Little Grand Wash Fault (Utah, USA). *Quaternary International*, 2016.
143. Mcdermott, C.I., et al., Natural Analogue Studies, in *Geological Storage of CO<sub>2</sub> in Deep Saline Formations*. 2017, Springer. p. 473-520.
144. Mehmani, Y. and M.T. Balhoff, Mesoscale and Hybrid Models of Fluid Flow and Solute Transport. *Rev Mineral Geochem*, 2015. 80: p. 433-459.
145. Johnson, J.W., J.J. Nitao, and K.G. Knauss, Reactive Transport Modeling of CO<sub>2</sub> Storage in Saline Aquifers to Elucidate Fundamental Processes, Trapping Mechanisms and Sequestration Partitioning. *Geological Storage of Carbon Dioxide*, 2004. 233: p. 107-128.
146. Ellis, B.R., et al., Dissolution-Driven Permeability Reduction of a Fractured Carbonate Caprock. *Environmental Engineering Science*, 2013. 30(4): p. 187-193.
147. Keller, A.A., *Single and Multiphase Flow and Transport in Fractured Porous Media*. 1996, Stanford University.
148. Park, Y., et al., Sequestering Carbon Dioxide Into Complex Structures of Naturally Occurring Gas Hydrates. *Proceedings of the National Academy of Sciences*, 2006. 103(34): p. 12690-12694.
149. Lo Ré, C., et al., Fluid–Rock Interactions in CO<sub>2</sub>-Saturated, Granite-Hosted Geothermal Systems: Implications for Natural and Engineered Systems From Geochemical Experiments and Models. *Geochimica et Cosmochimica Acta*, 2014. 141: p. 160-178.
150. Noiriél, C., Resolving Time-Dependent Evolution of Pore-Scale Structure, Permeability and Reactivity Using X-Ray Microtomography. *Rev Mineral Geochem*, 2015. 80: p. 247-285.
151. Yoon, H., Q. Kang, and A. Valocchi, Lattice Boltzmann-Based Approaches for Pore-Scale Reactive Transport. *Rev Mineral Geochem*, 2015. 80: p. 393-431.
152. Kampman, N., et al., Observational Evidence Confirms Modelling of the Long-Term Integrity of CO<sub>2</sub>-Reservoir Caprocks. *Nature Communications*, 2016. 7.
153. Kim, T.H., J. Cho, and K.S. Lee, Evaluation of CO<sub>2</sub> Injection in Shale Gas Reservoirs with Multi-Component Transport and Geomechanical Effects. *Applied Energy*, 2017. 190: p. 1195-1206.

154. Pawar, R.J., et al., Recent Advances in Risk Assessment and Risk Management of Geologic CO<sub>2</sub> Storage. *International Journal of Greenhouse Gas Control*, 2015. 40: p. 292-311.
155. Goldberg, D.S., T. Takahashi, and A.L. Slagle, Carbon Dioxide Sequestration in Deep-Sea Basalt. *Proceedings of the National Academy of Sciences*, 2008. 105(29): p. 9920-9925.
156. Jenkins, C.R., et al., Safe Storage and Effective Monitoring of CO<sub>2</sub> in Depleted Gas Fields. *Proceedings of the National Academy of Sciences*, 2012. 109(2): p. E35-E41.
157. Sadhukhan, S., P. Gouze, and T. Dutta, A Simulation Study of Reactive Flow in 2-D Involving Dissolution and Precipitation in Sedimentary Rocks. *Journal of Hydrology*, 2014.
158. Ahmad, N., et al., Reactive Transport Modeling of Leaking CO<sub>2</sub>-Saturated Brine Along a Fractured Pathway. *International Journal of Greenhouse Gas Control*, 2015. 42: p. 672-689.
159. Algive, L., Et Al. Reactive Transport: Experiments and Pore Network Modelling. in Paper SCA2007-10 Presented at the International Symposium of the Society of Core Analysts, Calgary, Canada. 2007.
160. Neunhauserer, L., et al., Flow and Transport Processes in Fractured Porous Media. *Computational Methods in Water Resources XII. Volume 2*, 1998: p. 101-108.
161. Sarkar, S., M.N. Toksoz, and D.R. Burns, Fluid Flow Simulation in Fractured Reservoirs. 2002, Massachusetts Institute of Technology. Earth Resources Laboratory.
162. Rezaeyan, A., et al., A Laboratory Study on Capillary Sealing Efficiency of Iranian Shale and Anhydrite Caprocks. *Marine and Petroleum Geology*, 2015.
163. Shah, V., D.F. Broseta, and G. Mouronval. Capillary Alteration of Caprocks by Acid Gases. in SPE Symposium on Improved Oil Recovery. 2008. Society of Petroleum Engineers.
164. Farokhpoor, R., Akervol I., Torsater O., Bjorkvik B.J.A. CO<sub>2</sub> Capillary Entry Pressure Into Flow Barrier and Caprock. in SCA Symposium. 2013. California.
165. Aggelopoulos, C.A., M. Robin, and O. Vizika, Interfacial Tension Between CO<sub>2</sub> and Brine (NaCl + CaCl<sub>2</sub>) at Elevated Pressures and Temperatures: the Additive Effect of Different Salts. *Advances in Water Resources*, 2011. 34(4): p. 505-511.

166. Zhu, H.-Y., et Al. Multiscale Change Characteristics of Chinese Wufeng Shale Under Supercritical Carbon Dioxide. in SPE Annual Technical Conference and Exhibition. 2016. Society of Petroleum Engineers. doi:10.2118/181369-MS.
167. Dávila, G., et al., Interaction Between a Fractured Marl Caprock and CO<sub>2</sub>-Rich Sulfate Solution Under Supercritical CO<sub>2</sub> Conditions. *International Journal of Greenhouse Gas Control* 48 (2016): p. 105-119.
168. Schütt, H., M. Wigand, and E. Spangenberg, Geophysical and Geochemical Effects of Supercritical CO<sub>2</sub> on Sandstones, in *Carbon Dioxide Capture for Storage in Deep Geologic Formations*. 2005, Elsevier Science: Amsterdam. p. 767-786.
169. Sidiq, H.H. and R. Amin, Supercritical CO<sub>2</sub>/Methane Relative Permeability Investigation, in *SPE International Conference on CO<sub>2</sub> Capture, Storage, and Utilization*. 2010: New Orleans, Louisiana, USA. doi:10.2118/137884-MS.
170. Ishiwatari, H.Y.A.R., Characterization of Organic Matter Generated From Green River Shale by Infrared Laser Pyrolysis. *Geochemical Journal*, 2002. 36: p. 73-82.
171. Selvadurai, A.P.S., Fluid Leakage Through Fractures in An Impervious Caprock Embedded Between Two Geologic Aquifers. *Advances in Water Resources*, 2012. 41: p. 76-83.
172. Jung, H.B., et al., Wellbore Cement Fracture Evolution at the Cement–Basalt Caprock Interface During Geologic Carbon Sequestration. *Applied Geochemistry*, 2014. 47: p. 1-16.
173. Noh, M.H. and L.W. Lake. Geochemical Modeling of Fracture Filling. in *SPE/DOE Improved Oil Recovery Symposium*. 2002. Society of Petroleum Engineers.
174. Yu, D. and A. Ladd, A Numerical Simulation Method for Dissolution in Porous and Fractured Media. *Journal of Computational Physics*, 2010. 229(18): p. 6450-6465.
175. Chappell, B.A., Deformational Response of Differently Shaped and Sized Test Pieces of Shale Rock. *International Journal of Rock Mechanics and Mining Sciences & Geomechanics Abstracts*, 1974. 11(1): p. 21-25.
176. Yasuhara, H., et al., Evolution of Fracture Permeability Through Reactive Flow at Elevated Temperature. *Trans. Geotherm. Res. Council*, 2005. 29: p. 437-441.
177. Yasuhara, H. and D. Elsworth, A Numerical Model Simulating Reactive Transport and Evolution of Fracture Permeability. *International Journal for Numerical and Analytical Methods in Geomechanics*, 2006. 30(10): p. 1039-1062.

178. Weaver, J.D. and R.D. Rickman. Productivity Impact from Geochemical Degradation of Hydraulic Fractures. in SPE Deep Gas Conference and Exhibition. 2010. Society of Petroleum Engineers. doi:10.2118/130641-MS.
179. Weaver, J.D., R.D. Rickman, and H. Luo, Fracture-Conductivity Loss Caused by Geochemical Interactions Between Man-Made Proppants and Formations. SPE Journal, 2010. 15(01): p. 116-124.
180. De Borst, R., J. Réthoré, and M.-A. Abellan, Two-Scale Approaches for Fracture in Fluid-Saturated Porous Media. Interaction and Multiscale Mechanics: An International Journal, 2007. 1: p. 83-101.
181. De Borst, R., J. Rethore, and M.-A. Abellan, A Precis of Two-Scale Approaches for Fracture in Porous Media, in Lecture Notes on Composite Materials. 2009, Springer. p. 149-171.
182. Edlmann, K., et al., Appraisal of Global CO<sub>2</sub> Storage Opportunities Using the Geomechanical Facies Approach. Environmental Earth Sciences: p. 1-22.
183. Kang, Q., D. Zhang, and S. Chen, Simulation of Dissolution and Precipitation in Porous Media. J. Geophys. Res., 2003. 108(B10): p. 2505.
184. Wilson-Lopez, R. and F. Rodriguez. A Network Model for Two-Phase Flow in Microfractured Porous Media. in SPE International Petroleum Conference in Mexico. 2004. Society of Petroleum Engineers. doi:10.2118/92056-MS.
185. Rosen, B. and C. König, Calculation and Interpretation of Interaction Between Fluid Flow and Deformation in Fractured Rock. [http://www.delta-h.de/DELTAH/referenzen/ck\\_veroeffentlichungen/veroeff\\_fluid.pdf](http://www.delta-h.de/DELTAH/referenzen/ck_veroeffentlichungen/veroeff_fluid.pdf).
186. Yalcinkaya, T., Experimental Study on Single Cement Fracture Exposed to CO<sub>2</sub> Saturated Brine Under Dynamic Conditions, in Petroleum Engineering. 2010, Unpublished Thesis, Louisiana State University: Baton Rouge. p. 105.
187. White, J.A., et al., Geomechanical Behavior of the Reservoir and Caprock System at the in Salah CO<sub>2</sub> Storage Project. Proceedings of the National Academy of Sciences, 2014. 111(24): p. 8747-8752.
188. Ferronato, M., et al., Geomechanical Issues of Anthropogenic CO<sub>2</sub> Sequestration in Exploited Gas Fields. Energy Conversion and Management, 2010. 51(10): p. 1918-1928.

189. David, C. and M. Le Ravalec-Dupin, Rock Physics and Geomechanics in the Study of Reservoirs and Repositories. Geological Society, London, Special Publications, 2007. 284(1): p. 1-14.
190. Kjølner, C., et al., Novel Experimental/Numerical Approach to Evaluate the Permeability of Cement-Caprock Systems. International Journal of Greenhouse Gas Control, 2016. 45: p. 86-93.
191. Bastian, P., et al., Numerical Simulation of Multiphase Flow in Fractured Porous Media, in Numerical Treatment of Multiphase Flows in Porous Media. 2000, Springer. p. 50-68.
192. Bagherieh, A., et al., Drying Response and Effective Stress in a Double Porosity Aggregated Soil. Engineering Geology, 2009. 105(1): p. 44-50.
193. Alfred, D., Modeling Fluid Flow Through Single Fracture Using Experimental, Stochastic, and Simulation Approaches. 2004, Unpublished Thesis, Texas A&M University.
194. Veer, E., S. Van Der Waldmann, and P. Fokker. A Coupled Geochemical-Transport-Geomechanical Model to Address Caprock Integrity During Long-Term CO<sub>2</sub> Storage. in 49th US Rock Mechanics/Geomechanics Symposium. 2015. American Rock Mechanics Association.
195. Smith, J., et al., Carbon Dioxide Storage Risk Assessment: Analysis of Caprock Fracture Network Connectivity. International Journal of Greenhouse Gas Control, 2011. 5(2): p. 226-240.
196. Streit, J.E., A.F. Siggins, and B.J. Evans, Predicting and Monitoring Geomechanical Effects of CO<sub>2</sub> Injection, in Carbon Dioxide Capture for Storage in Deep Geologic Formations. 2005, Elsevier Science: Amsterdam. p. 751-766.
197. Moreno, F.J., R. Chalaturnyk, and J. Jimenez, Methodology for Assessing Integrity of Bounding Seals (Wells and Caprock) for Geological Storage of CO<sub>2</sub>, in Greenhouse Gas Control Technologies 7, E.S. Rubin, et al., Editors. 2005, Elsevier Science Ltd: Oxford. p. 731-739.
198. Zhou, X., Z. Zeng, and H. Liu, Laboratory Testing on Pierre Shale for CO<sub>2</sub> Sequestration Under Clayey Caprock, in 44th U.S. Rock Mechanics Symposium and 5th U.S.-Canada Rock Mechanics Symposium. 2010, American Rock Mechanics Association: Salt Lake City, Utah.

199. Heath, J.E., et al., Pore-Lining Phases and Capillary Breakthrough Pressure of Mudstone Caprocks: Sealing Efficiency of Geologic CO<sub>2</sub> Storage Sites. *International Journal of Greenhouse Gas Control*, 2012. 11: p. 204-220.
200. Wu, Y.-S., Numerical Simulation of Single-Phase and Multiphase Non-Darcy Flow in Porous and Fractured Reservoirs. *Transport in Porous Media*, 2002. 49(2): p. 209-240.
201. Hangx, S.J.T., C.J. Spiers, and C.J. Peach, the Effect of Deformation on Permeability Development in Anhydrite and Implications for Caprock Integrity During Geological Storage of CO<sub>2</sub>. *Geofluids*, 2010. 10(3): p. 369-387.
202. Hangx, S., C. Spiers, and C. Peach, the Mechanical Behavior of Anhydrite and the Effect of CO<sub>2</sub> Injection. *Energy Procedia*, 2009. 1(1): p. 3485-3492.
203. Vernescu, B., Convergence Results for the Homogenization of Flow in Fractured Porous Media. Unpublished Thesis, University of Minnesota, 1990.
204. Diomampo, G.P., Relative Permeability Through Fractures, Technical Report, Department of Energy and Department of Petroleum Engineering, Editor. 2001: Stanford, California.
205. Macquarrie, K.T.B. and K.U. Mayer, Reactive Transport Modeling in Fractured Rock: A State-Of-the-Science Review. *Earth-Science Reviews*, 2005. 72(3-4): p. 189-227.
206. Chen, Z.M., et al., Appraising Carbon Geological Storage Potential in Unconventional Reservoirs Using Well-Testing Method: Engineering Parameters Analysis. *Society of Petroleum Engineers*. doi:NA
207. Li, P., et al., Assessment of the Effective CO<sub>2</sub> Storage Capacity in the Beibuwan Basin, Offshore of Southwestern P. R. China. *International Journal of Greenhouse Gas Control*, 2015. 37: p. 325-339.
208. Szulczewski, M.L., et al., Lifetime of Carbon Capture and Storage As a Climate-Change Mitigation Technology. *Proceedings of the National Academy of Sciences*, 2012. 109(14): p. 5185-5189.
209. Zhang, R., et al., A Novel Computational Framework for thermal-Hydrological-Mechanical-Chemical Processes of CO<sub>2</sub> Geological Sequestration Into a Layered Saline Aquifer and a Naturally Fractured Enhanced Geothermal System. *Greenhouse Gases: Science and Technology*, 2015.
210. Randolph, J.B. and M.O. Saar, Coupling Carbon Dioxide Sequestration with Geothermal Energy Capture in Naturally Permeable, Porous Geologic Formations: Implications for CO<sub>2</sub> Sequestration. *Energy Procedia*, 2011. 4: p. 2206-2213.

211. Sasaki, S., Characteristics of Microseismic Events Induced During Hydraulic Fracturing Experiments at the Hijiori Hot Dry Rock Geothermal Energy Site, Yamagata, Japan. *Tectonophysics*, 1998. 289(1): p. 171-188.
212. Lyon, T.A., et al., Integrated Study of a Faulted and Fractured Reservoir, in Abu Dhabi International Petroleum Exhibition and Conference. 1998, Society of Petroleum Engineers: Abu Dhabi, United Arab Emirates. doi:10.2118/49453-MS
213. Goodarzi, S., et al., Thermal Aspects of Geomechanics and Induced Fracturing in CO<sub>2</sub> Injection with Application to CO<sub>2</sub> Sequestration in Ohio River Valley, in SPE International Conference on CO<sub>2</sub> Capture, Storage, and Utilization. 2010: New Orleans, Louisiana, USA. doi:10.2118/139706-MS.
214. Mutschler, T., T. Triantafyllidis, and K. Balthasar, Geotechnical Investigations of Cap Rocks above CO<sub>2</sub>-Reservoirs. *Energy Procedia*, 2009. 1(1): p. 3375-3382.
215. Verdon, J.P., et al., Comparison of Geomechanical Deformation Induced by Megatonne-Scale CO<sub>2</sub> Storage at Sleipner, Weyburn, and in Salah. *Proceedings of the National Academy of Sciences*, 2013. 110(30): p. E2762-E2771.
216. Gaus, I., Role and Impact of CO<sub>2</sub>-Rock Interactions During CO<sub>2</sub> Storage in Sedimentary Rocks. *International Journal of Greenhouse Gas Control*, 2010. 4(1): p. 73-89.
217. Bourg, I.C., Sealing Shales Versus Brittle Shales: A Sharp Threshold in the Material Properties and Energy Technology Uses of Fine-Grained Sedimentary Rocks. *Environmental Science & Technology Letters*, 2015. 2(10): p. 255-259.
218. Haluszczak, L.O., A.W. Rose, and L.R. Kump, Geochemical Evaluation of Flowback Brine from Marcellus Gas Wells in Pennsylvania, USA. *Applied Geochemistry*, 2013. 28: p. 55-61.
219. Oliver, W.C. and G.M. Pharr, Measurement of Hardness and Elastic Modulus by Instrumented Indentation: Advances in Understanding and Refinements to Methodology. *Journal of Materials Research*, 2004. 19(01): p. 3-20.
220. Zhang, G., Z. Wei, and R.E. Ferrell, Elastic Modulus and Hardness of Muscovite and Rectorite Determined by Nanoindentation. *Applied Clay Science*, 2009. 43(2): p. 271-281.
221. Dicman, A., E. Putra, and D.S. Schechter, Modeling Fluid Flow through Single Fractures Using Experimental, Stochastic and Simulation Approaches. 2004, Society of Petroleum Engineers. doi:10.2118/89442-MS.
222. Lee, J. and R.A. Wattenbarger, *Gas Reservoir Engineering*. 1996.

## APPENDIX A

### EQUIPMENT AND MATERIALS USED FOR SHALE ROCK/CO<sub>2</sub> BRINE EXPERIMENTS



Figure A.1: Core flooding setup showing core holder and instrumentation



Figure A.2: Helium porosimetry unit for estimation of porosity of fractured cores



Figure A.3: Core flooding control unit



Figure A.4: Automated oven for temperature control



Figure A.5: Piston pump



Figure A.6: PEEK micro-tubing used in composite

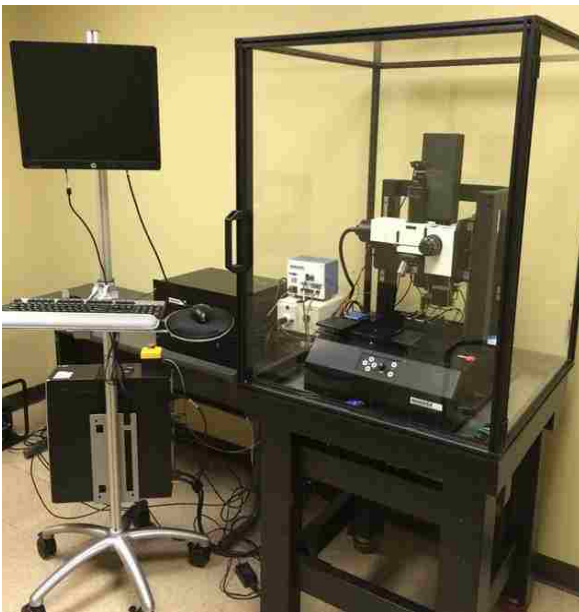


Figure A.7: Micro-indentation Fixture



Figure A.8: Example of shale fragment and the indentation points

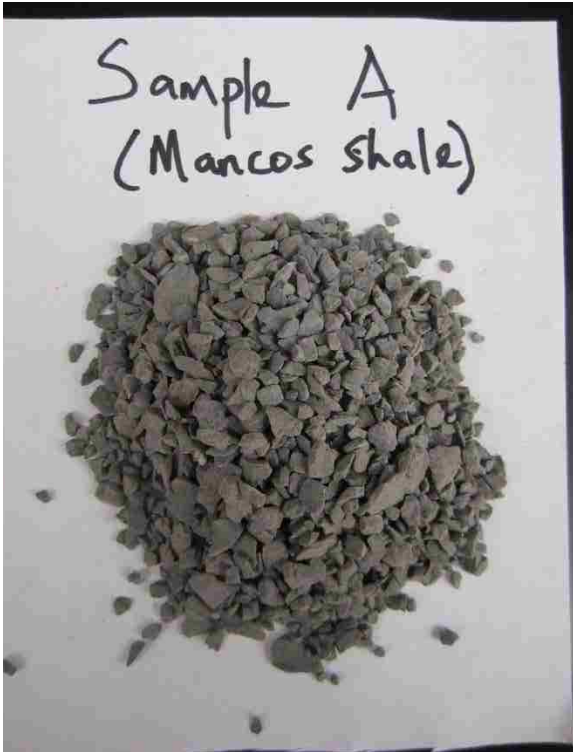


Figure A.9: Crushed shale samples, **pre-flooding** with CO<sub>2</sub>-brine; Mancos



Figure A.10: Crushed shale samples, **pre-flooding** with CO<sub>2</sub>-brine; Marcellus



Figure A.11: Crushed shale samples, **pre-flooding** with CO<sub>2</sub>-brine; Pottsville

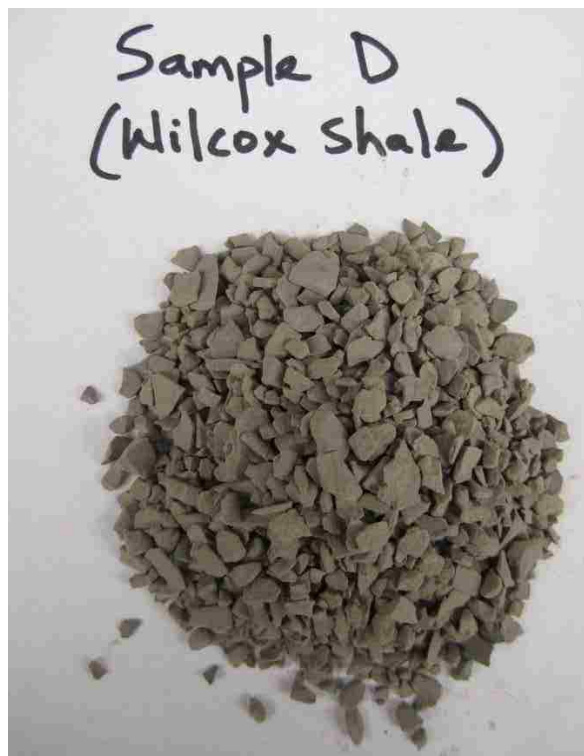


Figure A.12: Crushed shale samples, **pre-flooding** with CO<sub>2</sub>-brine; Wilcox

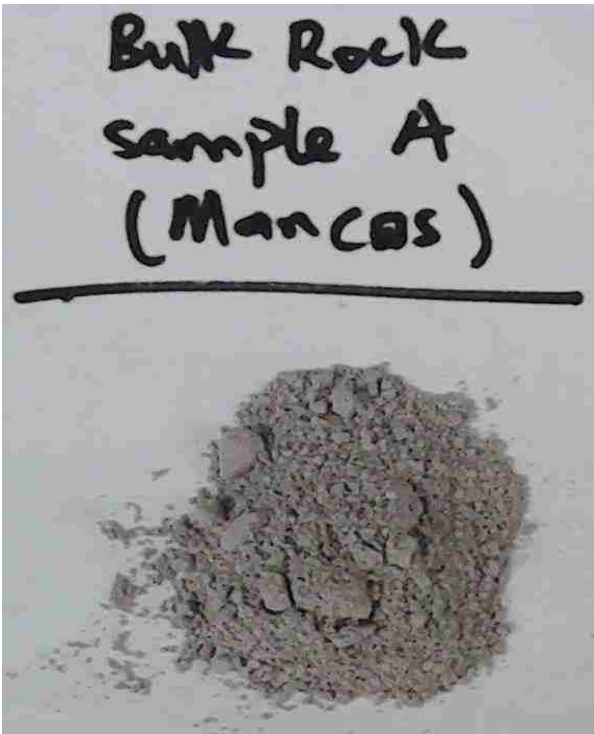


Figure A.13: Crushed shale samples, **post-flooding** with CO<sub>2</sub>-brine; Mancos

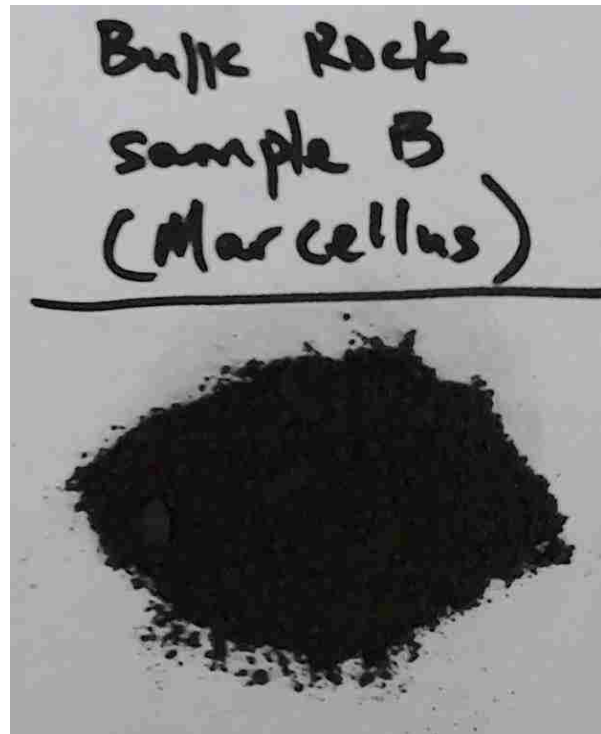


Figure A.14: Crushed shale samples, **post-flooding** with CO<sub>2</sub>-brine; Marcellus



Figure A.15: Crushed shale samples, **post-flooding** with CO<sub>2</sub>-brine; Pottsville

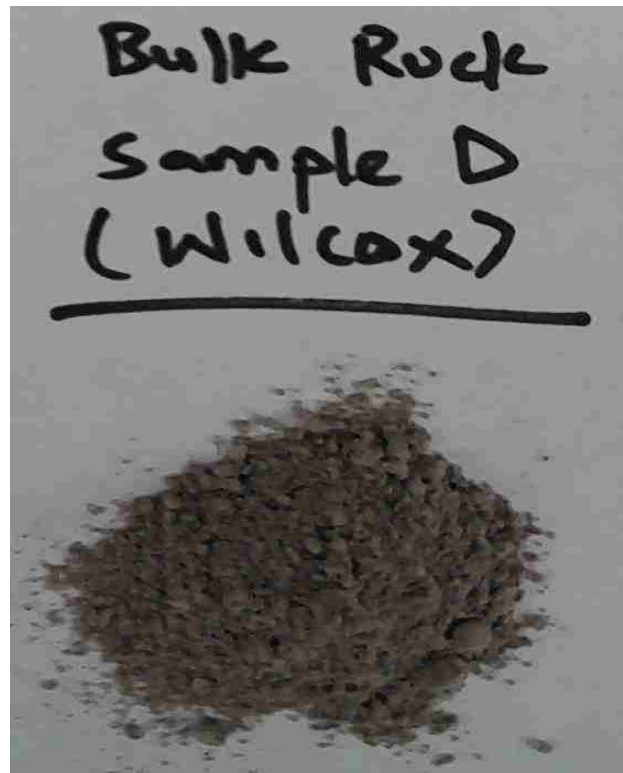


Figure A.16: Crushed shale samples, **post-flooding** with CO<sub>2</sub>-brine; Wilcox

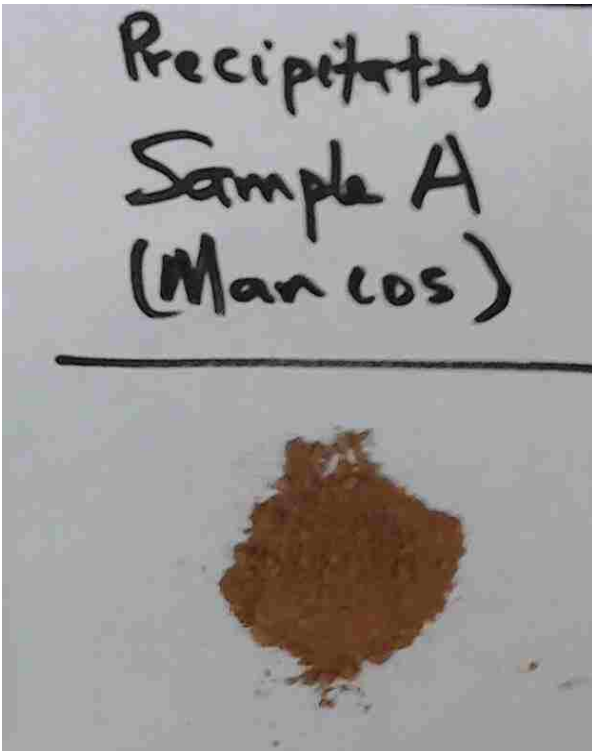


Figure A.17: Recovered effluent **precipitates**, post-flooding with CO<sub>2</sub>-brine; Mancos

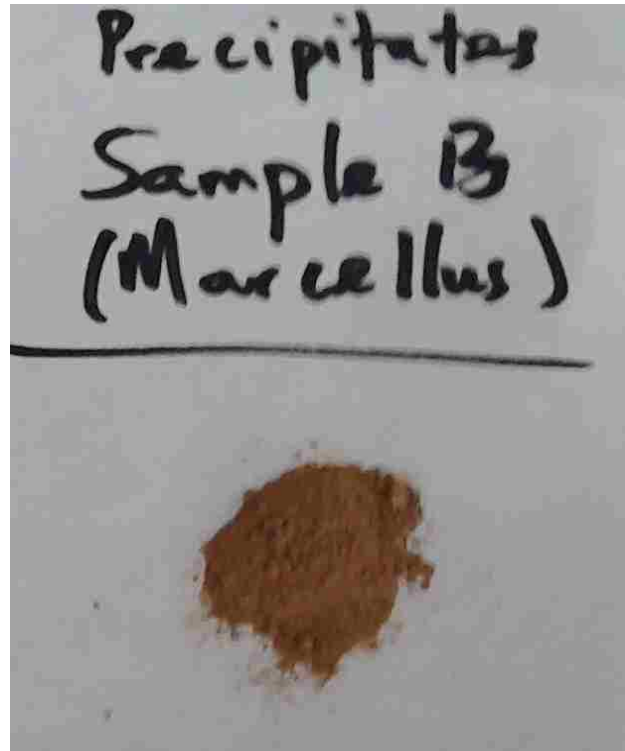


Figure A.18: Recovered effluent **precipitates**, post-flooding with CO<sub>2</sub>-brine; Marcellus

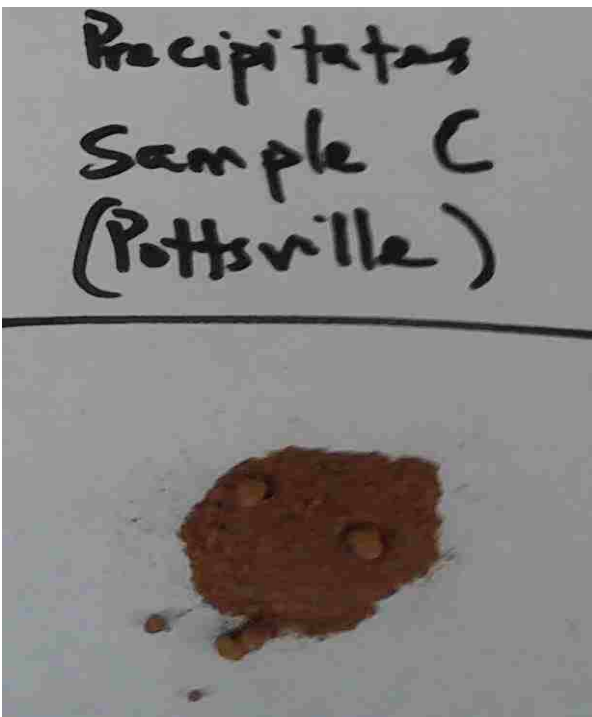


Figure A.19: Recovered effluent **precipitates**, post-flooding with CO<sub>2</sub>-brine; Pottsville

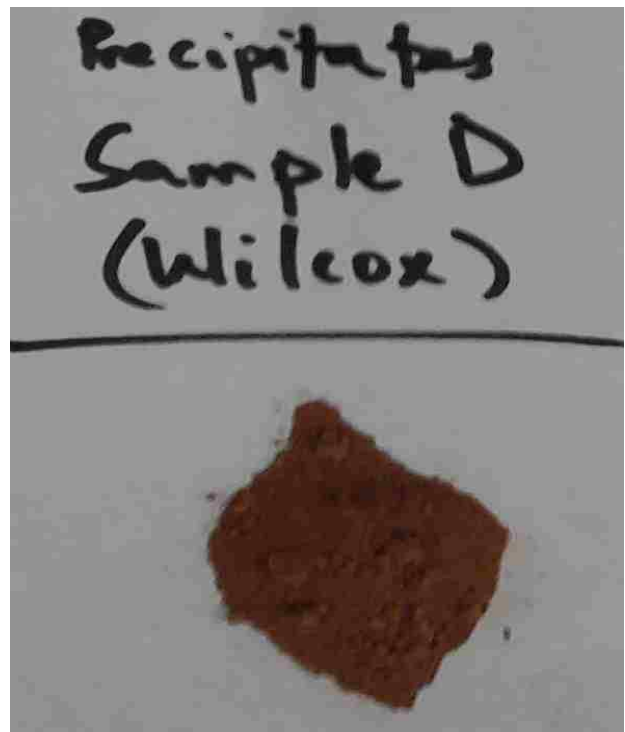


Figure A.20: Recovered effluent **precipitates**, post-flooding with CO<sub>2</sub>-brine; Wilcox

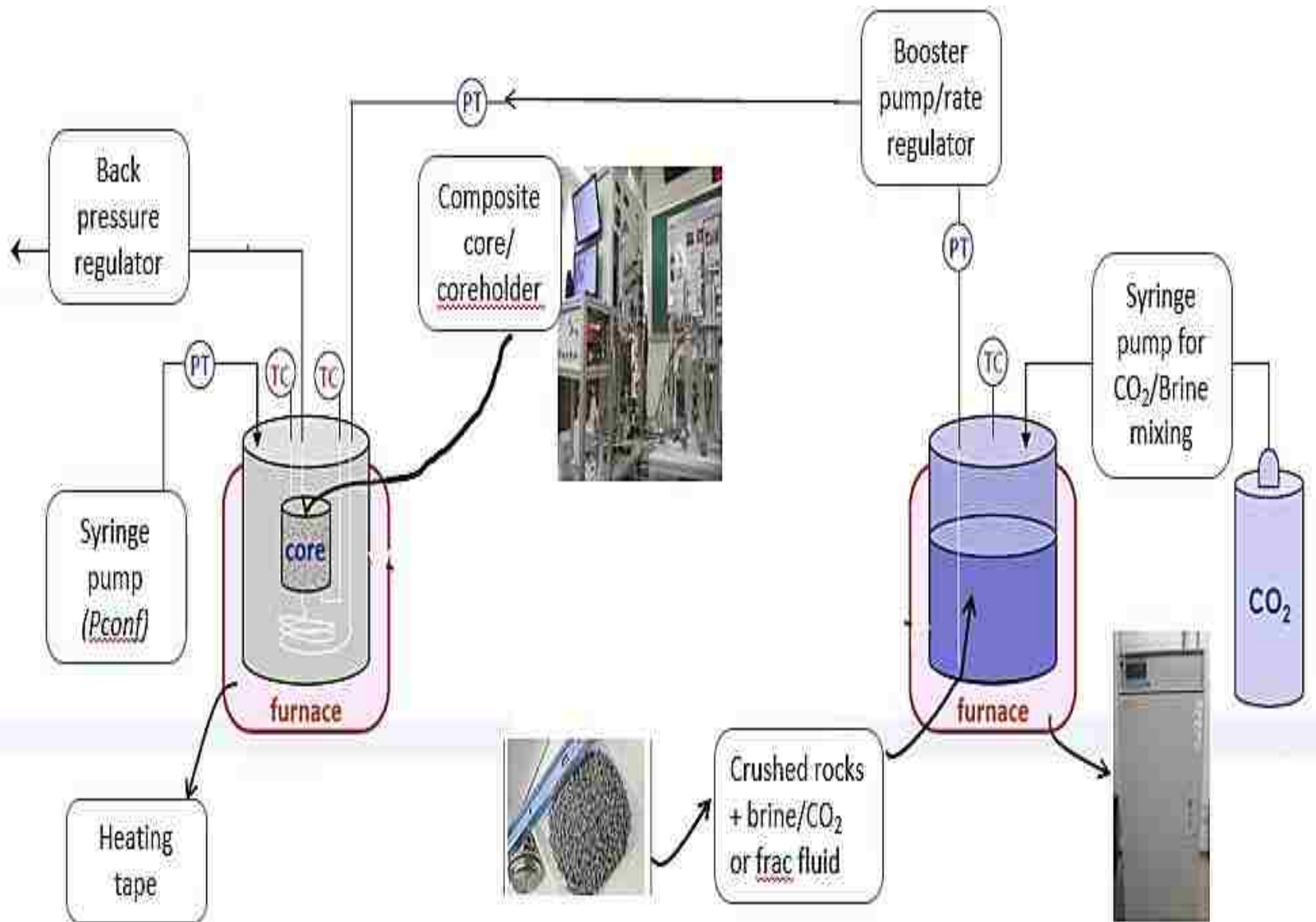


Figure A.21: Process schematics of experimental setup showing materials and equipment used for CO<sub>2</sub>-brine flooding and composite core conductivity measurement.

## APPENDIX B

### EXPERIMENTAL PROCEDURE FOR ROCK-FLUID INTERACTION EXPERIMENTS

The following table and detailed description of steps summarizes the procedures used in conducting the shale rock – aqueous CO<sub>2</sub> interactions:

Table B.1: Pre-injection and Post-injection analysis for each CO<sub>2</sub>-brine flooding run

Run X	Type of Analysis
Step 1	Flood crushed shale rock with CO <sub>2</sub> -brine and transport effluent to composite core under varying axial and radial stress.
Step 2	Take real time measurement of differential pressure drop for changes in conductivity. This will be automatically acquired during injection and transport of CO <sub>2</sub> -brine.
Step 3	Analyze final and intermediate effluent composition (pH, ICP-OES). Analyze crushed shale rock for morphology, mineral composition, total organic carbon composition and hardness (SEM, EDS, XRD, TOC, Micro-indentation).
Step 4	Measure effective fracture aperture and conductivity.
Step 5	Use geochemical results to bound overall chemo-fracture flow modelling in aqueous CO <sub>2</sub> -shale interactions.

#### Description of a Single Experimental Run and the Associated Analyses

For a typical single run of the experiment, the two units of the experimental setup- the packed bed vessel and high pressure coreholder are opened up. The packed bed vessel is filled with sieved crushed shale rock samples up to 350g per experiment. The dimensions of the crushed

rock were about 2mm in diameter. The fractured core samples are placed in the high pressure coreholder and the two vessels capped afterwards. The high pressure coreholder has a heating tape around it for the maintenance of temperature and the packed bed vessel is placed in the oven with regulated temperature. The experiments were run at constant temperature of 50°C. The CO<sub>2</sub>-brine reservoir is then connected to the pump for steady injection at 0.5ml/min. The injection pressure is gradually ramped up at 100psi/hr at the start. Minor trouble shootings such as trapped air bleeding and leakage points tightening are done. pH measurements are taken three times a day for each run. The stability of temperature is very important. Sometimes adjustments are made to the heating tape temperature which sometimes shoots above or below the set value. This is due to the analogue nature of the device. The differential pressure measurement is acquired at 15 to 20 sec rate. This yielded a wealth of differential pressure data points that can be averaged over the five day experimental period. These averaged data points are reported in the results and discussion sections for fracture flow characterization. All the effluent fluid is collected and stored for further analyses. Verification runs involving using only brine and/or unfractured cores were carried out to know the source of geochemical species. These runs confirmed that the unique geochemical responses are attributable to the shale rocks.

During the five days experimental run per shale type, one sample per day of the effluent fluid is taken and sent for ICP-OES analysis. This is to be able to obtain geochemical species within the fluid. The precipitates recovered from the effluents as well as the bulk rock were subjected to XRD analysis. The precipitates were fully recovered via concentrated sedimentation and room temperature dried. This is to ensure that no material damage was done to chemical components of the precipitates. About 10g of the post-flooding bulk rock are analysed with bulk and clay XRD

techniques. For total carbon content, about 5g of the rock samples are analysed. Special samples (1 inch cylindrical cuts of about 5mm thickness) which have been placed in the packed bed vessels for indentation analyses are recovered. This special tablets (1 inch diameter) are polished to reduce the impact of surface roughness on measured indentation values. Some of the cylindrical samples are used for thin section slides. These slides were used in data acquisition of surface morphology coupled with geochemical spread or maps (using EMPA technique).

## APPENDIX C

### pH DATA

Average= Average of six data points, SD= Standard Deviation

Time (days)	Mancos_Average pH	Mancos_SD
0	3.70	0.10
1	7.73	0.047
2	7.70	0.24
3	8.20	0.22
4	8.17	0.21
5	8.07	0.12
Time (days)	Marcellus_Average pH	Marcellus_SD
0	3.70	0.10
1	7.47	0.17
2	7.60	0.16
3	7.93	0.09
4	7.87	0.09
5	7.83	0.05
Time (days)	Pottsville_Average pH	Pottsville_SD
0	3.70	0.10
1	7.83	0.10
2	7.90	0.10
3	8.17	0.09
4	7.97	0.05
5	7.70	0.16
Time (days)	Wilcox_Average pH	Wilcox_SD
0	3.70	0.10
1	6.67	0.12
2	7.00	0.10
3	7.03	0.20
4	7.43	0.05
5	7.00	0.30

**APPENDIX D**

**INDUCTIVELY COUPLED PLASMA EMISSION SPECTROSCOPY (ICP-OES) DATA**

<b>Samples No.</b>	<b>Al, ppm</b>	<b>As, ppm</b>	<b>B, ppm</b>	<b>Ca, ppm</b>	<b>Fe, ppm</b>	<b>Mg, ppm</b>	<b>Mn, ppm</b>	<b>Ni, ppm</b>	<b>P, ppm</b>	<b>K, ppm</b>	<b>Se, ppm</b>	<b>S, ppm</b>	<b>Zn, ppm</b>
<b>1(initial)</b>	0.938	0.133	1.018	3.891	0.152	3.890	0.019	2.119	0.189	91.369	0.230	0.224	0.227
<b>Samples No.</b>	<b>Al, ppm</b>	<b>As, ppm</b>	<b>B, ppm</b>	<b>Ca, ppm</b>	<b>Fe, ppm</b>	<b>Mg, ppm</b>	<b>Mn, ppm</b>	<b>Ni, ppm</b>	<b>P, ppm</b>	<b>K, ppm</b>	<b>Se, ppm</b>	<b>S, ppm</b>	<b>Zn, ppm</b>
<b>2</b>	0.758	0.182	1.523	41.434	0.145	34.312	0.012	1.985	0.218	159.566	19.718	18.401	0.156
<b>3</b>	0.836	0.211	0.824	158.029	0.225	54.701	0.017	1.638	0.166	139.844	4.888	6.680	0.163
<b>4</b>	0.931	0.172	0.901	151.769	0.224	63.216	0.020	1.902	0.139	129.423	2.373	4.352	0.161
<b>5</b>	0.963	0.204	0.851	280.687	0.236	61.940	3.527	1.677	0.139	131.376	1.535	5.538	0.165
<b>6</b>	0.937	0.222	0.737	287.855	0.232	58.276	3.674	1.647	0.185	107.804	2.391	6.422	0.163
<b>Samples No.</b>	<b>Al, ppm</b>	<b>As, ppm</b>	<b>B, ppm</b>	<b>Ca, ppm</b>	<b>Fe, ppm</b>	<b>Mg, ppm</b>	<b>Mn, ppm</b>	<b>Ni, ppm</b>	<b>P, ppm</b>	<b>K, ppm</b>	<b>Se, ppm</b>	<b>S, ppm</b>	<b>Zn, ppm</b>
<b>7</b>	0.898	0.111	1.402	99.404	0.212	33.274	2.837	1.974	0.183	133.381	15.503	14.766	0.159
<b>8</b>	0.982	0.231	1.008	62.982	0.235	40.383	0.117	2.040	0.175	128.279	4.871	5.275	0.159
<b>9</b>	0.958	0.153	0.825	158.254	0.237	56.015	3.489	1.771	0.102	146.651	2.105	4.329	0.166
<b>10</b>	0.959	0.135	0.809	135.917	0.244	50.535	4.333	1.701	0.185	100.017	1.165	3.165	0.164
<b>11</b>	0.981	0.066	0.794	137.811	0.224	53.508	4.304	1.651	0.191	116.427	0.918	2.823	0.166
	<b>Al, ppm</b>	<b>As, ppm</b>	<b>B, ppm</b>	<b>Ca, ppm</b>	<b>Fe, ppm</b>	<b>Mg, ppm</b>	<b>Mn, ppm</b>	<b>Ni, ppm</b>	<b>P, ppm</b>	<b>K, ppm</b>	<b>Se, ppm</b>	<b>S, ppm</b>	<b>Zn, ppm</b>

Table Cont'd

<b>12</b>	0.943	0.212	0.783	170.567	0.064	16.609	2.381	1.911	0.197	136.113	11.133	12.307	0.165
<b>13</b>	0.969	0.138	0.838	190.773	0.231	14.309	0.721	1.925	0.158	146.863	6.718	9.065	0.169
<b>14</b>	0.943	0.120	0.727	110.283	0.228	4.929	0.331	1.926	0.134	110.789	2.503	4.009	0.179
<b>15</b>	0.955	0.063	0.622	121.485	0.218	2.533	0.506	1.940	0.138	131.005	1.592	3.148	0.173
<b>16</b>	0.784	0.202	0.885	136.905	0.226	1.423	0.488	1.891	0.187	130.773	1.307	3.024	0.189
<b>Samples No.</b>	Al, ppm	As, ppm	B, ppm	Ca, ppm	Fe, ppm	Mg, ppm	Mn, ppm	Ni, ppm	P, ppm	K, ppm	Se, ppm	S, ppm	Zn, ppm
<b>17</b>	0.992	0.131	1.385	299.766	0.209	155.486	0.026	1.913	0.214	149.931	264.710	252.782	0.180
<b>18</b>	0.850	0.299	0.965	250.543	0.226	43.309	0.154	2.021	0.192	131.438	42.562	43.913	0.170
<b>19</b>	0.925	0.078	0.891	181.867	0.215	19.395	0.179	2.045	0.177	133.871	14.157	15.090	0.170
<b>20</b>	0.861	0.171	0.507	139.011	0.212	11.346	0.130	2.062	0.139	122.004	4.360	5.965	0.182
<b>21</b>	0.936	0.204	0.834	142.500	0.215	7.519	0.179	2.089	0.191	114.017	2.688	4.499	0.183
<b>Samples No.</b>	Al, ppm	As, ppm	B, ppm	Ca, ppm	Fe, ppm	Mg, ppm	Mn, ppm	Ni, ppm	P, ppm	K, ppm	Se, ppm	S, ppm	Zn, ppm
<b>22</b>	0.982	0.117	1.331	341.123	0.216	129.537	0.569	1.964	0.152	133.875	214.068	204.079	0.180
<b>23</b>	0.971	0.105	0.669	280.464	0.241	54.869	0.276	2.021	0.139	143.070	44.862	46.500	0.174
<b>24</b>	0.963	0.160	0.709	124.545	0.234	29.227	0.026	2.076	0.176	113.514	8.541	9.695	0.170
<b>25</b>	0.903	0.113	0.760	231.745	0.222	26.108	0.239	1.966	0.170	133.517	3.840	7.110	0.170
<b>26</b>	0.974	0.223	0.672	224.777	0.230	25.617	0.222	2.043	0.128	127.760	2.930	5.811	0.165
<b>Samples No.</b>	Al, ppm	As, ppm	B, ppm	Ca, ppm	Fe, ppm	Mg, ppm	Mn, ppm	Ni, ppm	P, ppm	K, ppm	Se, ppm	S, ppm	Zn, ppm

Table Cont'd

<b>27</b>	1.005	0.160	1.422	439.562	0.228	163.691	0.544	1.892	0.119	184.273	249.904	238.647	0.173
<b>28</b>	0.955	0.196	0.909	332.542	0.219	43.471	0.321	2.021	0.162	115.198	22.512	25.968	0.167
<b>29</b>	0.980	0.103	0.732	254.728	0.230	33.583	0.299	2.053	0.128	111.499	13.009	15.231	0.169
<b>30</b>	0.972	0.183	0.700	225.436	0.225	35.698	0.235	2.056	0.169	97.375	6.199	9.094	0.171
<b>31</b>	0.792	0.182	0.565	170.797	0.218	29.904	0.372	1.914	0.281	110.092	23.395	24.581	0.184

**APPENDIX E**

**MICRO-INDENTATION OF SHALE ROCKS DATA**

<b>Properties</b>	<b>Time(days)</b>	<b>Mancos</b>	<b>Marcellus</b>	<b>Pottsville</b>	<b>Wilcox</b>
<b>Vicker's Hardness</b>	0	48.74	58.47	34.77	11.59
	5	30.56	54.61	36.18	7.39
<b>Young's Modulus</b>	0	13.29	17.12	17.24	4.19
	5	8.02	14.1	11.35	3.05

<b>Rock Type</b>	<b>Original</b>	<b>SD_Original</b>	<b>Runs_AV</b>	<b>SD_Runs_AV</b>
<b>Mancos</b>	48.74	3.19	30.56	4.28
<b>Marcellus</b>	58.47	3.27	54.61	4.39
<b>Pottsville</b>	34.77	1.18	36.18	6.33
<b>Wilcox</b>	11.59	1.01	7.39	1.16

## APPENDIX F

### ADDITIONAL DATA FOR ELECTRON MICROPROBE ANALYSIS (EMPA)

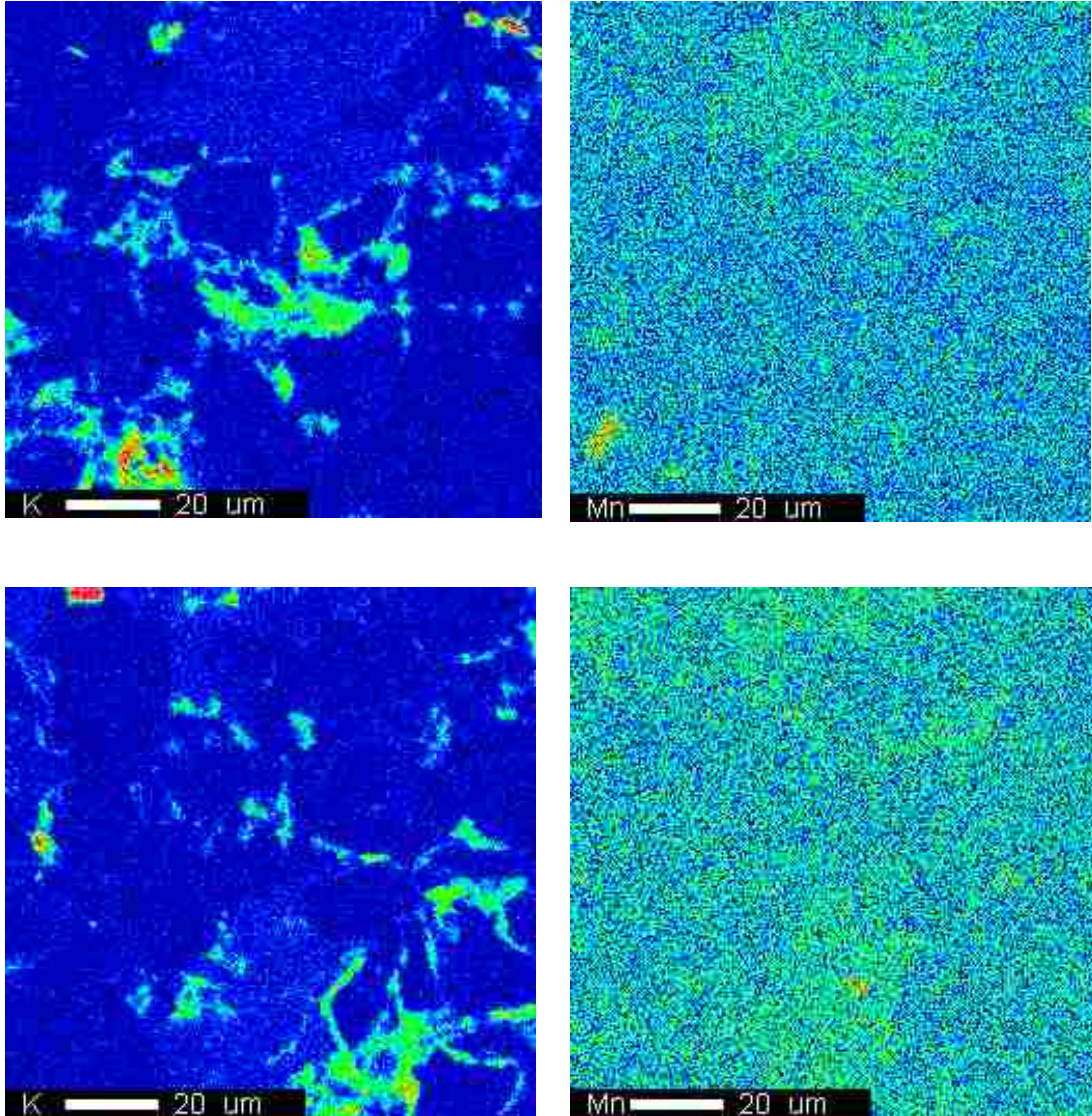


Figure G1: 20μm Electron Micro-Probe Analysis for **Mancos shale** showing **Potassium (K)** and **Manganese (Mn)** surface geochemical profile of the CO<sub>2</sub>-reacted sample (top row) compared to control specimen (bottom row). Note the general depletion of elemental components that are associated with minerals that are susceptible to dissolution. These trends are only detected at the lower micron resolution presented above. The Scanning Electron Microscopy (SEM) back scatter image for these profiles is in **figure 4.25**.

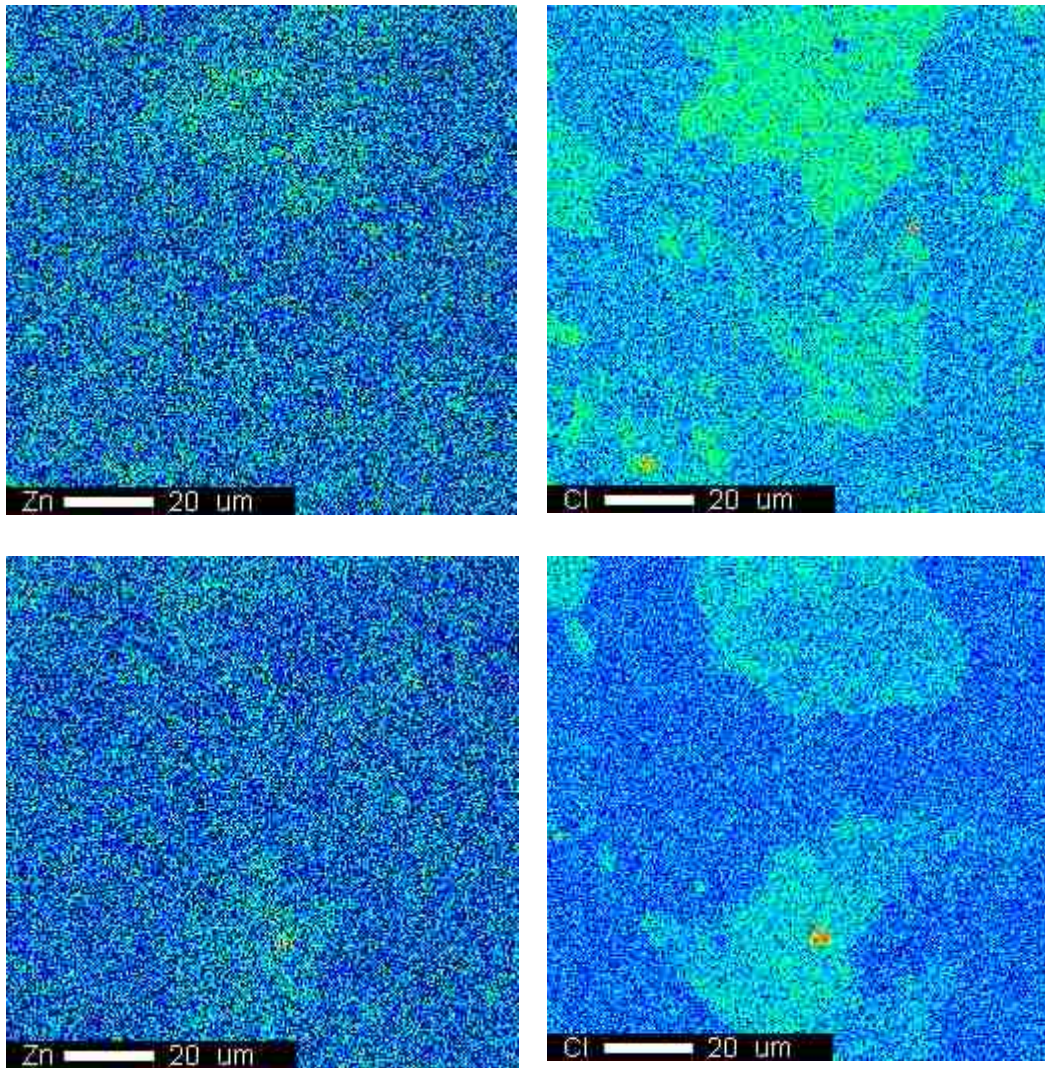


Figure G2: 20 $\mu$ m Electron Micro-Probe Analysis for **Mancos shale** showing **Zinc (Zn)** and **Chlorine (Cl)** surface geochemical profile of the CO<sub>2</sub>-reacted sample (top row) compared to control specimen (bottom row). Note the general depletion of elemental components that are associated with minerals that are susceptible to dissolution. These trends are only detected at the lower micron resolution presented above. The Scanning Electron Microscopy (SEM) back scatter image for these profiles is in **figure 4.25**.

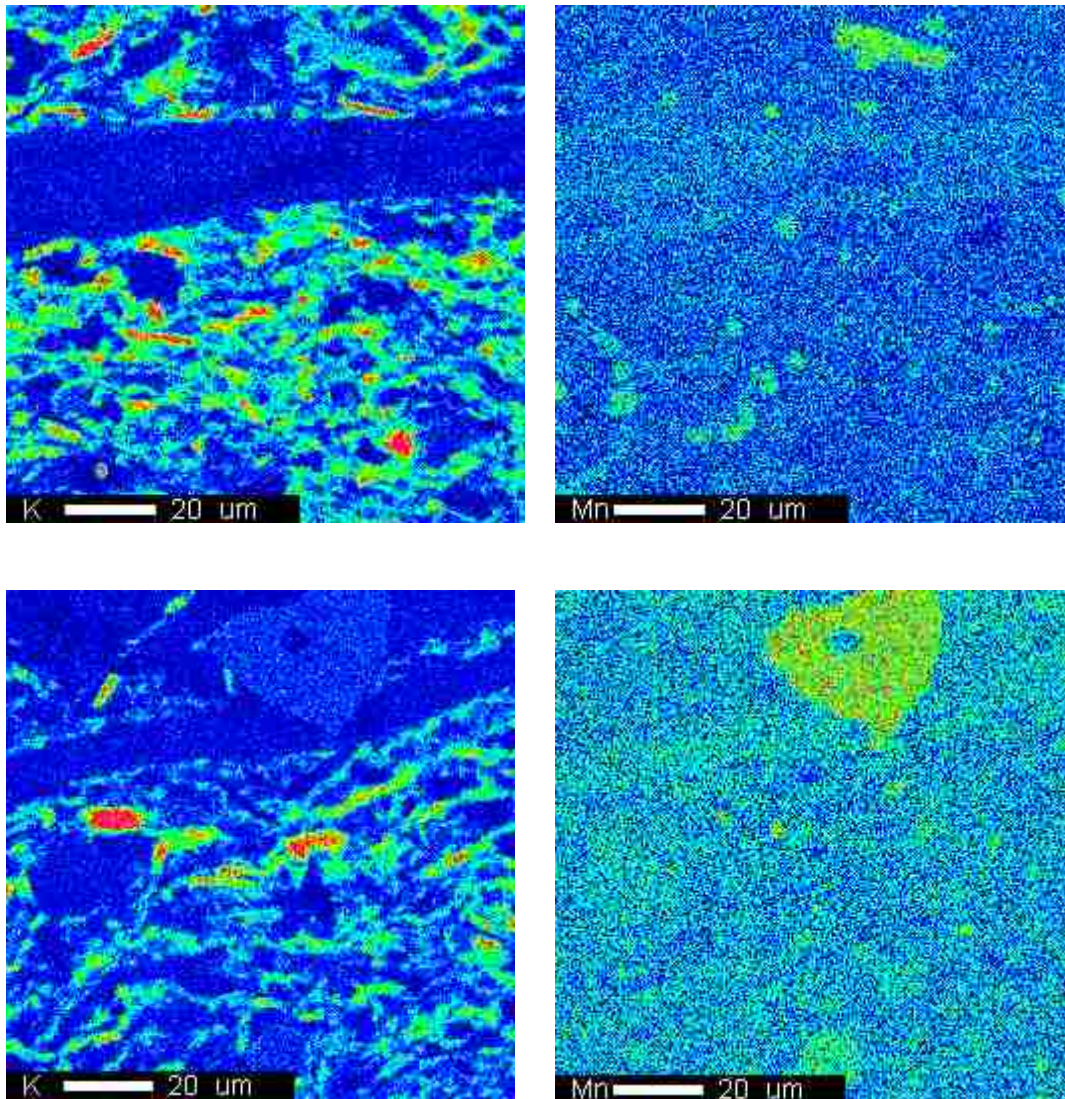


Figure G3: 20µm Electron Micro-Probe Analysis for **Marcellus shale** showing **Potassium (K)** and **Manganese (Mn)** surface geochemical profile of the CO<sub>2</sub>-reacted sample (top row) compared to control specimen (bottom row). Note the general depletion of elemental components that are associated with minerals that are susceptible to dissolution. These trends are only detected at the lower micron resolution presented above. The Scanning Electron Microscopy (SEM) back scatter image for these profiles is in **figure 4.28**.

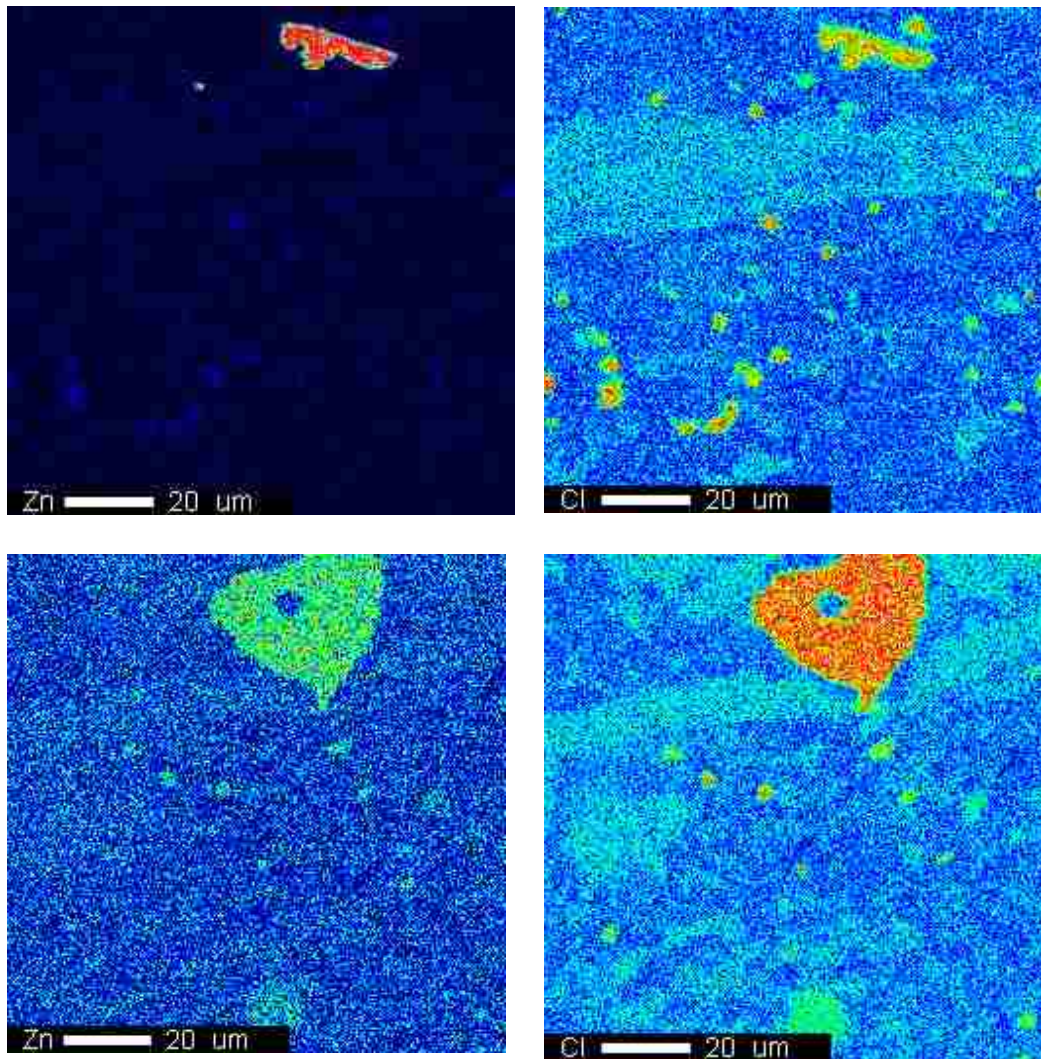


Figure G4: 20µm Electron Micro-Probe Analysis for **Marcellus shale** showing **Zinc (Zn)** and **Chlorine (Cl)** surface geochemical profile of the CO<sub>2</sub>-reacted sample (top row) compared to control specimen (bottom row). Note the general depletion of elemental components that are associated with minerals that are susceptible to dissolution. These trends are only detected at the lower micron resolution presented above. The Scanning Electron Microscopy (SEM) back scatter image for these profiles is in **figure 4.28**.

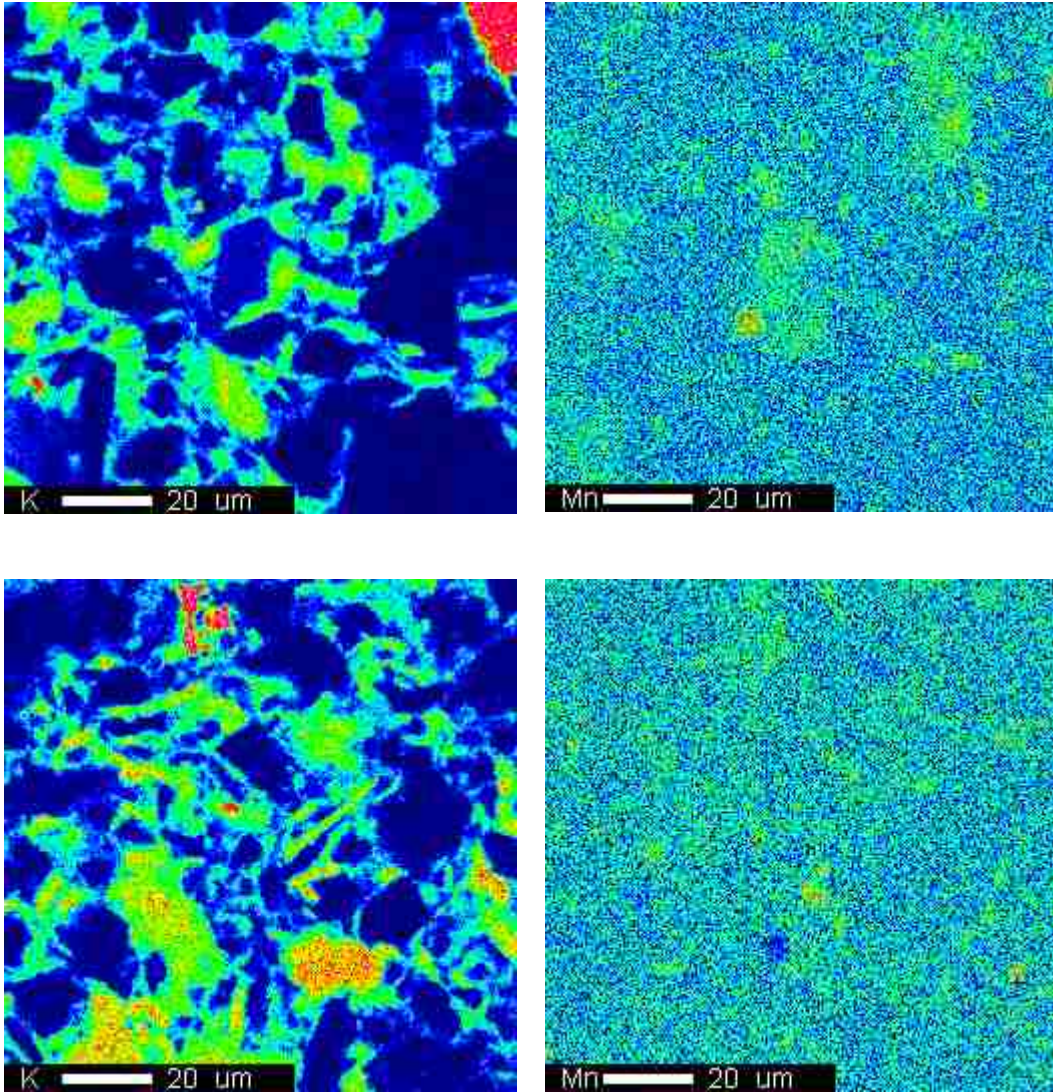


Figure G5: 20µm Electron Micro-Probe Analysis for **Pottsville shale** showing **Potassium (K)** and **Manganese (Mn)** surface geochemical profile of the CO<sub>2</sub>-reacted sample (top row) compared to control specimen (bottom row). Note the general depletion of elemental components that are associated with minerals that are susceptible to dissolution. These trends are only detected at the lower micron resolution presented above. The Scanning Electron Microscopy (SEM) back scatter image for these profiles is in **figure 4.31**.

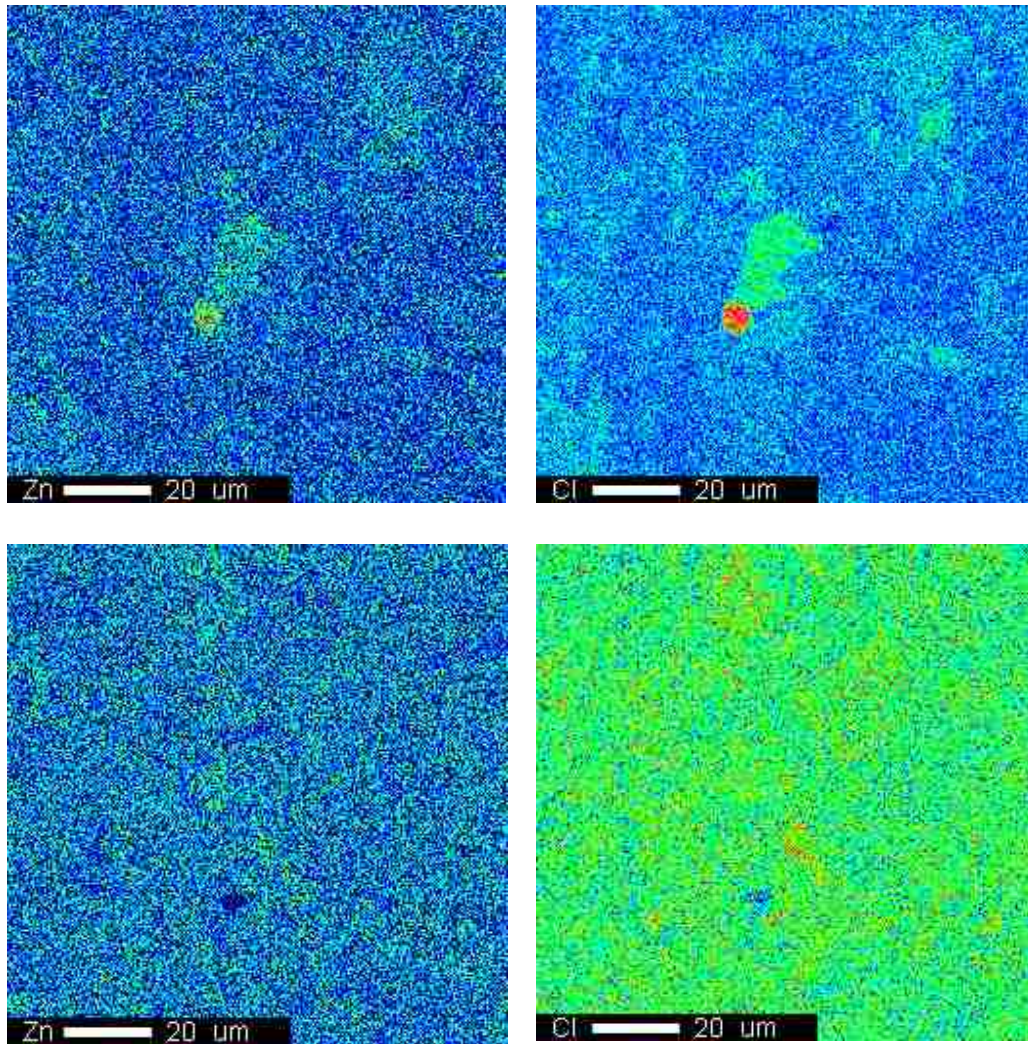


Figure G6: 20 $\mu$ m Electron Micro-Probe Analysis for **Pottsville shale** showing **Zinc (Zn)** and **Chlorine (Cl)** surface geochemical profile of the CO<sub>2</sub>-reacted sample (top row) compared to control specimen (bottom row). Note the general depletion of elemental components that are associated with minerals that are susceptible to dissolution. These trends are only detected at the lower micron resolution presented above. The Scanning Electron Microscopy (SEM) back scatter image for these profiles is in **figure 4.31**.

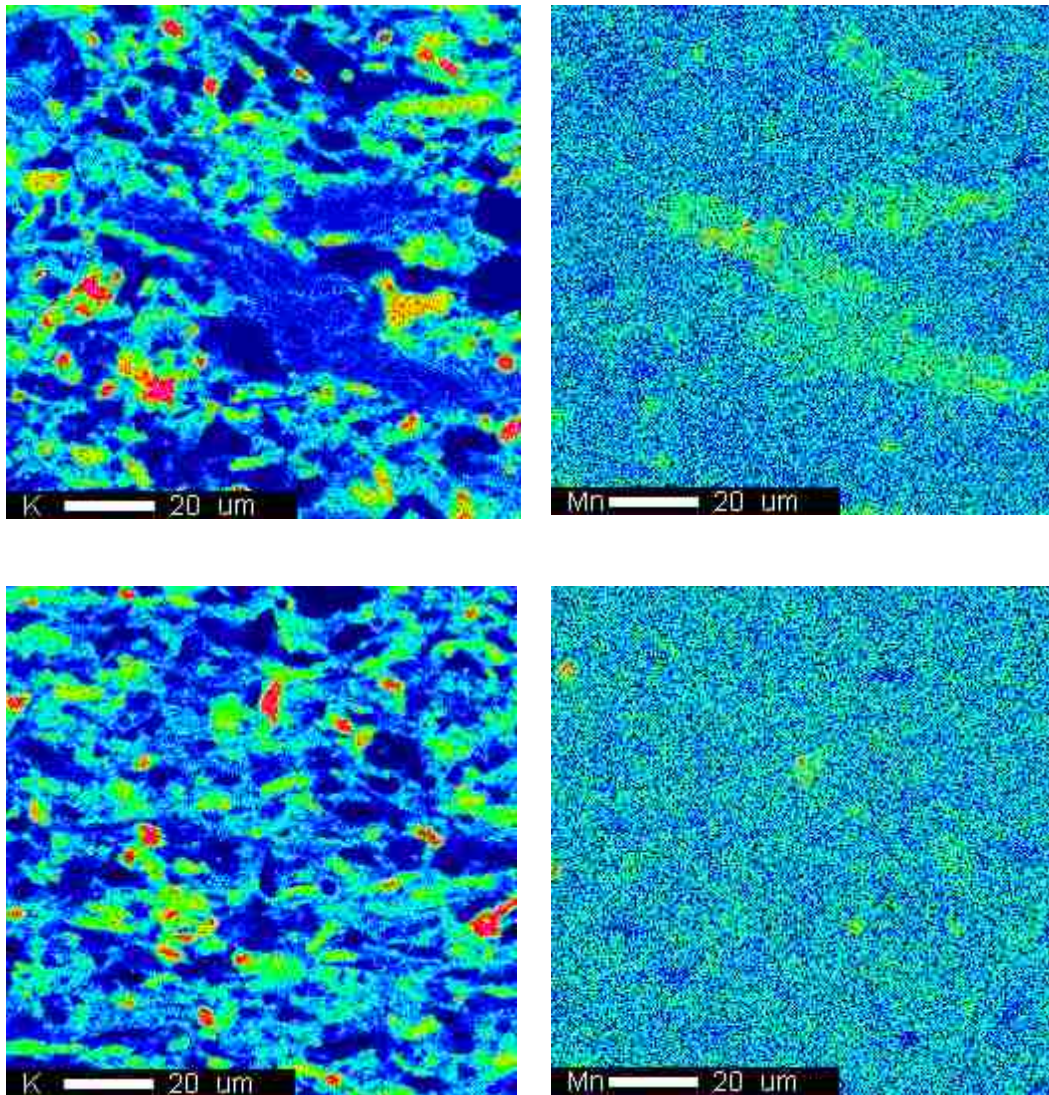


Figure G7: 20µm Electron Micro-Probe Analysis for **Wilcox shale** showing **Potassium (K)** and **Manganese (Mn)** surface geochemical profile of the CO<sub>2</sub>-reacted sample (top row) compared to control specimen (bottom row). Note the general depletion of elemental components that are associated with minerals that are susceptible to dissolution. These trends are only detected at the lower micron resolution presented above. The Scanning Electron Microscopy (SEM) back scatter image for these profiles is in **figure 4.34**.

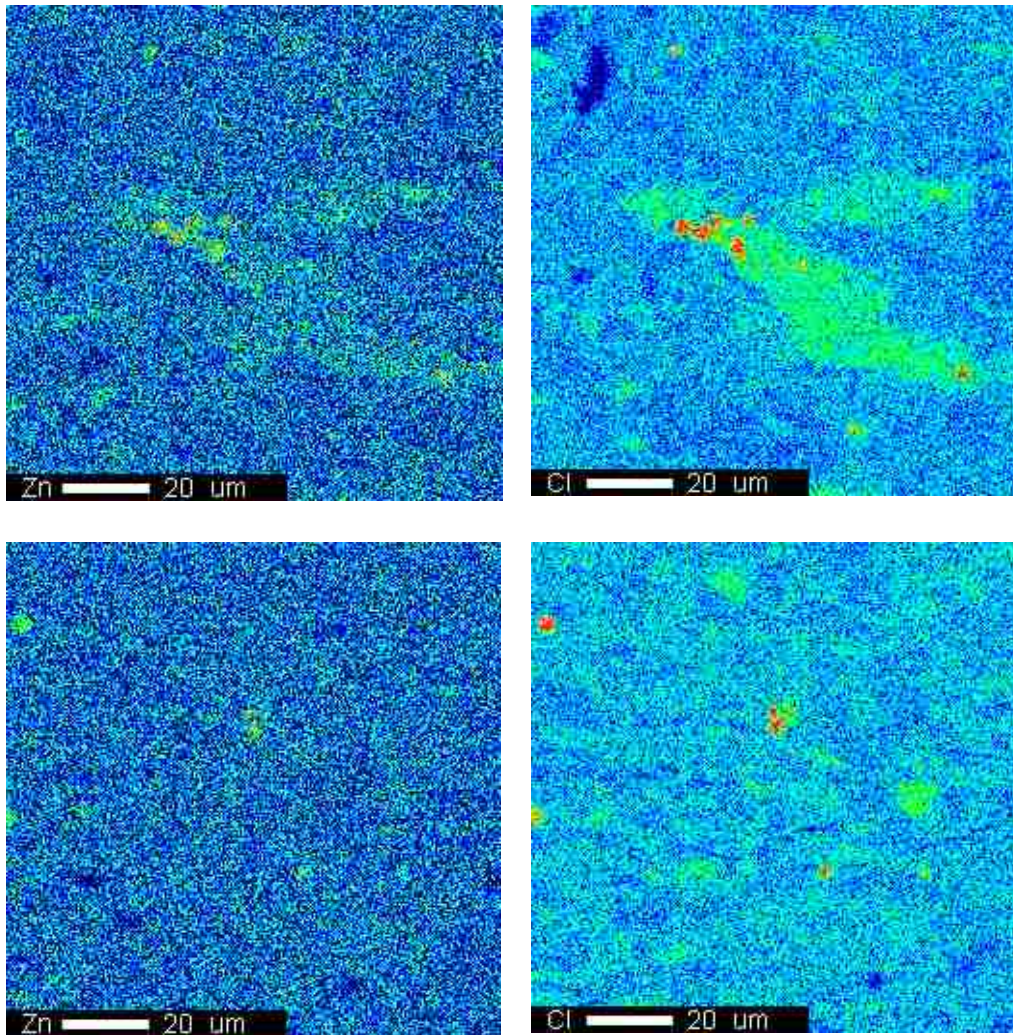


Figure G8: 20 $\mu$ m Electron Micro-Probe Analysis for **Wilcox shale** showing **Zinc (Zn)** and **Chlorine (Cl)** surface geochemical profile of the CO<sub>2</sub>-reacted sample (top row) compared to control specimen (bottom row). Note the general depletion of elemental components that are associated with minerals that are susceptible to dissolution. These trends are only detected at the lower micron resolution presented above. The Scanning Electron Microscopy (SEM) back scatter image for these profiles is in **figure 4.34**.

## APPENDIX G

### FLOW/PRESSURE DATA

Table G.1: Data for differential pressure, dP (psi) across **25 $\mu$ m** fractured core(s) for flow-through experiment using **Mancos shale**.

<b>Time (days)</b>	<b>Run1</b>	<b>Run2</b>	<b>Run3</b>	<b>Average</b>	<b>Standard Deviation</b>
<b>0.00</b>	58.71	<b>29.34</b>	<b>30.90</b>	<b>39.65</b>	<b>13.49</b>
<b>0.25</b>	77.47	34.40	40.24	50.70	19.08
<b>0.50</b>	95.19	152.69	52.59	100.16	41.01
<b>0.75</b>	132.36	153.07	177.63	154.35	18.50
<b>1.00</b>	140.74	154.47	185.84	160.35	18.88
<b>1.25</b>	172.88	156.90	186.99	172.26	12.29
<b>1.50</b>	174.86	157.41	189.98	174.09	13.31
<b>1.75</b>	180.40	159.08	190.12	176.53	12.96
<b>2.00</b>	180.48	159.15	190.67	176.76	13.13
<b>2.25</b>	181.56	163.86	191.70	179.04	11.50
<b>2.50</b>	183.05	166.88	191.78	180.57	10.32
<b>2.75</b>	183.59	168.71	192.84	181.72	9.94
<b>3.00</b>	183.93	170.48	192.86	182.42	9.20
<b>3.25</b>	184.88	171.61	193.17	183.22	8.88
<b>3.50</b>	185.65	173.94	193.52	184.37	8.04
<b>3.75</b>	186.63	175.45	194.17	185.42	7.69
<b>4.00</b>	188.26	176.86	194.45	186.52	7.29
<b>4.25</b>	188.76	177.07	195.19	187.01	7.50
<b>4.50</b>	189.18	178.52	195.84	187.85	7.13
<b>4.75</b>	190.03	179.97	196.46	188.82	6.78
<b>5.00</b>	192.00	181.10	196.49	189.86	6.46

Table G.2: Data for differential pressure, dP (psi) across **25 $\mu$ m** fractured core(s) for flow-through experiment using **Marcellus shale**.

<b>Time (days)</b>	<b>Run1</b>	<b>Run2</b>	<b>Run3</b>	<b>Average</b>	<b>Standard Deviation</b>
<b>0.00</b>	158.92	131.91	163.16	151.33	13.84
<b>0.25</b>	159.02	172.53	163.25	164.93	5.64
<b>0.50</b>	176.55	172.62	172.18	173.78	1.97
<b>0.75</b>	177.33	178.09	172.52	175.98	2.47
<b>1.00</b>	178.29	178.42	175.22	177.31	1.48
<b>1.25</b>	178.69	178.62	178.52	178.61	0.07
<b>1.50</b>	178.72	178.65	180.00	179.12	0.62
<b>1.75</b>	179.64	179.09	181.88	180.20	1.21
<b>2.00</b>	179.97	179.86	183.66	181.17	1.77
<b>2.25</b>	180.25	181.42	184.99	182.22	2.02
<b>2.50</b>	180.94	181.46	187.02	183.14	2.75
<b>2.75</b>	181.73	181.51	187.10	183.45	2.58
<b>3.00</b>	182.39	182.55	187.79	184.25	2.51
<b>3.25</b>	182.50	182.64	187.98	184.37	2.55
<b>3.50</b>	182.77	183.21	189.16	185.05	2.91
<b>3.75</b>	183.30	183.58	189.31	185.40	2.77
<b>4.00</b>	184.89	184.10	189.83	186.27	2.53
<b>4.25</b>	185.25	184.49	193.29	187.68	3.98
<b>4.50</b>	185.96	184.96	193.86	188.26	3.98
<b>4.75</b>	185.98	185.42	195.11	188.83	4.44
<b>5.00</b>	187.33	186.42	197.24	190.33	4.90

Table G.3: Data for differential pressure, dP (psi) across **25 $\mu$ m** fractured core(s) for flow-through experiment using **Pottsville shale**.

<b>Time (days)</b>	<b>Run1</b>	<b>Run2</b>	<b>Run3</b>	<b>Average</b>	<b>Standard Deviation</b>
<b>0.00</b>	41.89	41.89	32.55	38.78	4.40
<b>0.25</b>	85.83	85.83	118.89	96.85	15.58
<b>0.50</b>	99.79	99.79	121.19	106.93	10.09
<b>0.75</b>	125.53	125.53	137.63	129.56	5.70
<b>1.00</b>	126.54	126.54	157.07	136.72	14.39
<b>1.25</b>	126.84	126.84	164.56	139.41	17.78
<b>1.50</b>	128.18	128.18	166.09	140.81	17.87
<b>1.75</b>	128.35	128.35	167.68	141.46	18.54
<b>2.00</b>	128.96	128.96	168.34	142.09	18.56
<b>2.25</b>	129.45	129.45	168.49	142.47	18.40
<b>2.50</b>	130.22	130.22	168.58	143.01	18.08
<b>2.75</b>	147.43	147.43	169.07	154.65	10.20
<b>3.00</b>	147.68	147.68	169.30	154.88	10.19
<b>3.25</b>	148.83	148.83	169.59	155.75	9.79
<b>3.50</b>	149.65	149.65	170.37	156.56	9.77
<b>3.75</b>	149.69	149.69	172.03	157.14	10.53
<b>4.00</b>	150.23	150.23	172.73	157.73	10.60
<b>4.25</b>	150.78	150.78	172.90	158.15	10.43
<b>4.50</b>	152.48	152.48	175.72	160.22	10.95
<b>4.75</b>	153.50	153.50	175.98	160.99	10.60
<b>5.00</b>	154.35	154.35	177.79	162.17	11.05

Table G.4: Data for differential pressure, dP (psi) across **25 $\mu$ m** fractured core(s) for flow-through experiment using **Wilcox shale**.

<b>Time (days)</b>	<b>Run1</b>	<b>Run2</b>	<b>Run3</b>	<b>Average</b>	<b>Standard Deviation</b>
<b>0.00</b>	33.00	65.00	95.35	64.45	25.46
<b>0.25</b>	55.57	92.51	132.29	93.46	31.33
<b>0.50</b>	70.02	93.07	132.40	98.50	25.75
<b>0.75</b>	88.35	94.76	132.48	105.20	19.47
<b>1.00</b>	108.34	126.32	132.56	122.41	10.27
<b>1.25</b>	116.50	126.89	132.67	125.35	6.69
<b>1.50</b>	120.75	131.84	132.77	128.45	5.46
<b>1.75</b>	121.69	140.15	132.87	131.57	7.59
<b>2.00</b>	124.95	150.25	132.99	136.06	10.55
<b>2.25</b>	143.06	152.59	133.41	143.02	7.83
<b>2.50</b>	143.51	153.17	139.45	145.38	5.75
<b>2.75</b>	157.23	158.46	139.91	151.87	8.47
<b>3.00</b>	163.60	158.99	141.91	154.84	9.33
<b>3.25</b>	164.59	160.21	143.64	156.15	9.02
<b>3.50</b>	164.90	170.15	143.90	159.65	11.34
<b>3.75</b>	166.16	171.86	147.42	161.81	10.44
<b>4.00</b>	167.47	173.48	165.33	168.76	3.45
<b>4.25</b>	167.75	173.74	166.63	169.37	3.12
<b>4.50</b>	172.22	178.07	166.82	172.37	4.59
<b>4.75</b>	176.49	180.72	169.39	175.53	4.68
<b>5.00</b>	179.42	180.83	170.63	176.96	4.51

Table G.5: Data for differential pressure, dP (psi) across **150 $\mu$ m** fractured core(s) for flow-through experiment using **Mancos shale**.

<b>Time (days)</b>	<b>Run1</b>	<b>Run2</b>	<b>Run3</b>	<b>Average</b>	<b>Standard Deviation</b>
<b>0.00</b>	23.78	21.48	25.88	23.72	5.40
<b>0.25</b>	36.95	34.65	39.05	36.88	7.63
<b>0.50</b>	56.63	54.33	58.73	56.56	8.20
<b>0.75</b>	82.37	80.07	84.47	82.30	7.40
<b>1.00</b>	103.23	100.93	105.33	103.16	7.55
<b>1.25</b>	110.11	107.81	112.21	110.05	4.92
<b>1.50</b>	114.98	112.68	117.08	114.91	5.32
<b>1.75</b>	122.99	120.69	125.09	122.92	5.19
<b>2.00</b>	125.74	123.44	127.84	125.67	5.25
<b>2.25</b>	129.78	127.48	131.88	129.72	4.60
<b>2.50</b>	131.06	128.76	133.16	130.99	4.13
<b>2.75</b>	133.09	130.79	135.19	133.02	3.98
<b>3.00</b>	134.64	132.34	136.74	134.57	3.68
<b>3.25</b>	136.49	134.19	138.59	136.42	3.55
<b>3.50</b>	137.10	134.80	139.20	137.03	3.22
<b>3.75</b>	137.67	135.37	139.77	137.60	3.08
<b>4.00</b>	140.27	137.97	142.37	140.20	2.91
<b>4.25</b>	140.60	138.30	142.70	140.53	3.00
<b>4.50</b>	142.00	139.70	144.10	141.93	2.85
<b>4.75</b>	143.50	141.20	145.60	143.43	2.71
<b>5.00</b>	145.70	143.40	147.80	145.63	2.58

Table G.6: Data for differential pressure, dP (psi) across **150 $\mu$ m** fractured core(s) for flow-through experiment using **Marcellus shale**.

<b>Time (days)</b>	<b>Run1</b>	<b>Run2</b>	<b>Run3</b>	<b>Average</b>	<b>Standard Deviation</b>
<b>0.00</b>	32.81	30.92	34.52	32.75	6.92
<b>0.25</b>	52.25	50.36	53.96	52.19	7.90
<b>0.50</b>	91.80	89.91	93.51	91.74	2.75
<b>0.75</b>	127.10	125.21	128.81	127.04	3.45
<b>1.00</b>	135.08	133.19	136.79	135.02	2.07
<b>1.25</b>	139.68	137.79	141.39	139.62	1.28
<b>1.50</b>	143.17	141.28	144.88	143.11	1.29
<b>1.75</b>	144.10	142.21	145.81	144.04	1.69
<b>2.00</b>	145.30	143.41	147.01	145.24	2.47
<b>2.25</b>	146.70	144.81	148.41	146.64	2.83
<b>2.50</b>	147.20	145.31	148.91	147.14	3.86
<b>2.75</b>	148.90	147.01	150.61	148.84	3.61
<b>3.00</b>	149.10	147.21	150.81	149.04	3.51
<b>3.25</b>	149.80	147.91	151.51	149.74	3.57
<b>3.50</b>	149.90	148.01	151.61	149.84	4.08
<b>3.75</b>	150.30	148.41	152.01	150.24	3.87
<b>4.00</b>	150.50	148.61	152.21	150.44	3.55
<b>4.25</b>	150.60	148.71	152.31	150.54	5.57
<b>4.50</b>	150.90	149.01	152.61	150.84	5.58
<b>4.75</b>	151.30	149.41	153.01	151.24	6.22
<b>5.00</b>	151.60	149.71	153.31	151.54	6.86

Table G.7: Data for differential pressure, dP (psi) across **150 $\mu$ m** fractured core(s) for flow-through experiment using **Pottsville shale**.

<b>Time (days)</b>	<b>Run1</b>	<b>Run2</b>	<b>Run3</b>	<b>Average</b>	<b>Standard Deviation</b>
<b>0.00</b>	27.28	24.23	29.95	27.15	2.20
<b>0.25</b>	42.50	39.45	45.17	42.37	7.79
<b>0.50</b>	68.18	65.13	70.85	68.06	5.04
<b>0.75</b>	88.72	85.67	91.39	88.60	2.85
<b>1.00</b>	97.55	94.50	100.22	97.43	7.20
<b>1.25</b>	103.40	100.35	106.07	103.28	8.89
<b>1.50</b>	108.55	105.50	111.22	108.42	8.94
<b>1.75</b>	110.22	107.17	112.89	110.09	9.27
<b>2.00</b>	111.40	108.35	114.07	111.27	9.28
<b>2.25</b>	111.90	108.85	114.57	111.77	9.20
<b>2.50</b>	113.00	109.95	115.67	112.87	9.04
<b>2.75</b>	113.80	110.75	116.47	113.67	5.10
<b>3.00</b>	114.30	111.25	116.97	114.17	5.10
<b>3.25</b>	114.90	111.85	117.57	114.77	4.89
<b>3.50</b>	115.50	112.45	118.17	115.37	4.89
<b>3.75</b>	115.90	112.85	118.57	115.77	5.26
<b>4.00</b>	116.20	113.15	118.87	116.07	5.30
<b>4.25</b>	116.80	113.75	119.47	116.67	5.21
<b>4.50</b>	117.50	114.45	120.17	117.37	5.48
<b>4.75</b>	117.80	114.75	120.47	117.67	5.30
<b>5.00</b>	118.00	114.95	120.67	117.87	5.52

Table G.8: Data for differential pressure, dP (psi) across **150 $\mu$ m** fractured core(s) for flow-through experiment using **Wilcox shale**.

<b>Time (days)</b>	<b>Run1</b>	<b>Run2</b>	<b>Run3</b>	<b>Average</b>	<b>Standard Deviation</b>
<b>0.00</b>	25.78	24.54	27.89	26.07	14.76
<b>0.25</b>	39.03	37.79	41.14	39.32	9.40
<b>0.50</b>	65.40	64.16	67.51	65.69	14.94
<b>0.75</b>	87.00	85.76	89.11	87.29	11.29
<b>1.00</b>	91.94	90.70	94.05	92.23	5.96
<b>1.25</b>	94.30	93.06	96.41	94.59	3.88
<b>1.50</b>	95.74	94.50	97.85	96.03	3.17
<b>1.75</b>	99.25	98.01	101.36	99.54	4.40
<b>2.00</b>	100.94	99.70	103.05	101.23	6.12
<b>2.25</b>	102.00	100.76	104.11	102.29	4.54
<b>2.50</b>	103.90	102.66	106.01	104.19	3.34
<b>2.75</b>	105.00	103.76	107.11	105.29	4.91
<b>3.00</b>	106.40	105.16	108.51	106.69	5.41
<b>3.25</b>	107.10	105.86	109.21	107.39	5.23
<b>3.50</b>	108.00	106.76	110.11	108.29	6.58
<b>3.75</b>	108.50	107.26	110.61	108.79	6.05
<b>4.00</b>	108.90	107.66	111.01	109.19	2.00
<b>4.25</b>	109.70	108.46	111.81	109.99	1.81
<b>4.50</b>	110.10	108.86	112.21	110.39	2.66
<b>4.75</b>	111.00	109.76	113.11	111.29	2.71
<b>5.00</b>	111.90	110.66	114.01	112.19	2.62

## APPENDIX H

### FRACTURE CONDUCTIVITY DATA AND CALCULATIONS

Table H.1: Steps, equations and assumptions were made in calculating the fracture conductivity of the cores used during the experiments.

Steps	Equations	Assumptions
1. Put averaged values of dP from three experiments /per core in tabular form.	$k_f = 8.45 \times 10^9 w_f^2$	1. Flow is primarily through fractures
2. Declare and specify parameters (in approximate units) such as viscosity, fracture length, flow rate	$k_f = \frac{k_{av}A - k_m(A - w_f l)}{w_f l}$	2. Bulk fracture flow properties are captured in the experimental differential pressure measurements
3. Calculate average fracture width from experimental data	$8.45 \times 10^9 w_f^3 l - k_{av}A + k_m(A - w_f l) = 0$	3. CO <sub>2</sub> -brine viscosity is constant throughout the experiment
4. Estimate dimensionless fracture conductivity over time from fracture width and fracture length using the relationship shown in the list of equations	$q_m = \frac{k_m A \Delta P}{\mu L}$	4. Length of the core(s), for each experimental run, approximates the fracture length.
	$q_f = 9.86 \times 10^9 \frac{w_f^3 l \Delta P}{12 \mu L_f}$	
	$w_f k_f = \pi C_r k L_f$	5. Tortuosity of fracture geometry is unity
	$w_f = \sqrt[3]{\frac{q_f \times 12 \mu}{9.86 \times 10^9 \Delta P}}$	6. Effect of fracture surface roughness is negligible
	$C_r = \frac{w_f k_f}{\pi K_{av} L_f} \approx \frac{w_f}{\pi L_f}$	7. Microtubes are made of polymeric materials (PEEK), does not interfere at all with dissolution-precipitation process

## VITA

Abiola Olabode is the third child of a family of three children. He attended Government College Ibadan and Command Day Secondary School Odogbo for his secondary education. He later proceeded to Obafemi Awolowo University, Ile Ife where in 2008, he earned a Bachelor's degree in Chemical Engineering with honors. Abiola worked with Pan Ocean Oil Corporation in Lagos, Nigeria between 2008 and 2010 as a natural gas Process Engineer helping with the design of multi-stage NGL recovery systems. He joined the graduate program of the Craft & Hawkins Department of Petroleum Engineering in 2010 and obtained a Master of Science degree with Thesis in December 2012. His doctoral program began in January of 2013. He has co-authored several peer-reviewed research articles and conference papers during his graduate studies (<https://scholar.google.com/citations?user=TrkUbtQAAAAJ&hl=en>).